

**RETRIEVAL OF SOIL MOISTURE
UNDER VEGETATION USING
POLARIMETRIC RADAR**

Thesis by

Motofumi Arii

In Partial Fulfillment of the Requirements for the
degree of

Doctor of Philosophy

CALIFORNIA INSTITUTE OF TECHNOLOGY

Pasadena, California

2009

(Defended December 9, 2008)

© 2009

Motofumi Aii

All Rights Reserved

To Megumi and Raku

Acknowledgements

First of all, I would like to thank my advisors, Professor David Rutledge, Dr. Jakob van Zyl, and Yunjin Kim for their unlimited help and support. Their shrewd advice and guidance opened my eyes to the world of science and enabled me to achieve my Ph.D at Caltech.

I also would like to thank Mitsubishi Space Software Co. Ltd. for their kindness to give me a chance to study at Caltech. The opportunity definitely enhanced my life by letting me set my path to pursue this advanced degree. I am equally grateful to Prof. Yoshizumi Yasuoka for his encouragement to undertake this Ph.D course.

Before coming Caltech, I had committed myself to design a radar system at that company, and regularly referred to a book, *Spaceborne RADAR-remote-sensing*, which was written by Professor C. Elachi. This book led me to this school. I would thank not only him but also Professor P. P. Vaidyanathan and A. Emami for many helpful comments as committee members.

I am thankful to all staff members in Moore building for giving us joyful work environments, and all the other members of the Caltech RF and Microwave Group, Glenn Jones, Joe Bardin, Yu-lung Tang, Niklas Wadefalk, Ann Shen, Kent Potter, Hamdi Mani, Dr. Sanguen Jeon, Younkyu Chung, and Sander Weinreb, for sharing various things with me. I would like to extend a special thank to Dale Yee for giving my family many precious tips for life in the United States.

I am deeply grateful to Yoji and Hisako Arie, my parents, and Shizumori and Kumiko Okutsu, my in-laws. Without their understanding, I would not have achieved this ultimate goal in my life. I would like to close by expressing my deepest gratitude to Megumi Arie, my wife, for her unconditional love and ungrudging support. She provides me harmonious home environments and soothes my fatigue from Ph.D work. This thesis is dedicated to her.

Motofumi Arii

Pasadena, California

December 2008

Abstract

The unique contributions of this thesis are: 1) a polarimetric classification algorithm that is a significant improvement over an existing algorithm and 2) introduction of a cube technique to retrieve soil moisture under vegetation.

The most widely used classification algorithm is the three-component scattering technique. Even though it includes three dominant scattering mechanisms, the decomposition approach can cause a non-physical solution due to incorrect assumptions. The Adaptive Non Negative Eigenvalue Decomposition approach in this thesis produces correct solution. It appears that this new approach provides better classification results. It is a significant improvement over the existing technique.

A cube technique is introduced to retrieve soil moisture under vegetation. Using this approach, we have evaluated the retrieval accuracy of several polarimetric combinations. The effects of the incorrect vegetation model and data noise were investigated. In addition, the proposed cube algorithm can be improved by applying the classification result.

Table of Contents

List of Tables	viii
List of Figures	ix
Chapter I: Introduction	1
Chapter II: Fundamentals	5
2.1 Coordinate System	
2.2 Radar Polarimetry	
Chapter III: Polarimetric Decomposition	11
3.1 Previous Techniques	
3.2 Freeman Decomposition	
3.3 Non-Negative Eigenvalue Decomposition	
3.4 Generalization of the Volume Scattering Term	
3.5 Adaptive Non-Negative Eigenvalue Decomposition	
3.6 Experimental Results and Analysis	
Chapter IV: Scattering Mechanisms of a Vegetated Surface	63
4.1 Overview of Modeling	
4.2 Scattering from an Oriented Cylinder	
4.3 Scattering from a Cloud of Cylinders	
4.3.1 Attenuation Type I: Scattering from the Branch Layer	
4.3.2 Attenuation Type II: Scattering from the Trunk Layer	
4.3.3 Attenuation Type III: Double Bounce and Surface Scattering	
4.4 Scattering from a Surface	
4.5 Interaction between the Cylinder and the Surface	
4.6 Sensitivity Study	
Chapter V: Quantitative Analysis of the Decomposition Techniques	116
5.1 Test Scenario	
5.2 Simulation Results and Analysis	
Chapter VI: Soil Moisture Retrieval	140
6.1 Previous Algorithms	
6.2 Soil Moisture Retrieval Using an Algorithm Proposed by Dubois et al.	
6.3 A New Inversion Algorithm Using the Polarimetric Scattering Cube	
Chapter VII: Conclusions and Suggestions	156
Appendix A: Positive Eigenvalues of the Measured Covariance Matrix	158
Appendix B: Eigenvalues of the General Covariance Matrix	160
Appendix C: Direct Inversion of the General Covariance Matrix	163
Appendix D: The Appearance of a Cloud of Randomly Oriented Dipoles ...	177
Bibliography	179

List of Tables

- Table 1.1: Land classification by vegetation types [10]
- Table 3.1: Standard deviation, $p(\sigma)$, and $q(\sigma)$ in (3.64) for various n 's
- Table 4.1: Fixed simulation parameters of scattering from an oriented cylinder
- Table 4.2: Cases for simulations of scattering from an oriented cylinder
- Table 4.3: Surface parameters for Facets and Bragg scatterings
- Table 4.4: Fixed parameters for the sensitivity simulation
- Table 4.5: Cases of the sensitivity simulation
- Table 5.1: Baseline parameters for the test scenario
- Table 5.2: Variables for the test scenario
- Table 6.1: Baseline parameters for the test scenario
- Table 6.2: Variables for the reference cubes

List of Figures

- Figure 1.1: Monthly changes of NDVI (top), precipitation history (second row), and radar backscatter cross section of vertical polarization (third row and bottom) at Beja in Portugal
- Figure 2.1: Coordinate systems: Forward Scatter Alignment (FSA) (left), Backscatter Alignment (BSA) (right)
- Figure 2.2: Radar observation geometry
- Figure 3.1: Backscattering from a vegetated terrain
- Figure 3.2: L-band image of the Black Forest in Germany obtained by NASA/JPL AIRSAR system in the summer of 1991. The solid arrows indicate the name of city or area type. The dotted lines specify the direction of topographic change. The terrain slopes upward in the direction of the arrows.
- Figure 3.3: Results of the Freeman algorithm applied to three different wavelength images in Freiburg obtained by AIRSAR. From left to right, C-band (5 cm), L-band (24 cm) and P-band (68 cm) images are displayed. Green, red, and blue are assigned to volume scattering, double-bounce scattering, and ground scattering, respectively.
- Figure 3.4: Pixels with negative eigenvalue are displayed using the L-band Black Forest image. The left image is the total power image at L-band, and the left image is the result of the validation test.
- Figure 3.5: Illustration of the third eigenvalue in (3.16a)
- Figure 3.6: Illustration of the second and third eigenvalues in (3.16a). This is a specific case where x_2 is smaller than x_3 .
- Figure 3.7: Geometrical property of x_1 and x_2 on unit circle. The property in equation (3.31) determines this relationship.

- Figure 3.8: Decomposition result using NNED are shown. The original images with three different frequencies are the same as in Figure 3.2. Color assignments are the same as Figure 3.2 as well.
- Figure 3.9: Difference between the Freeman decomposition and NNED at L-band. Most of the forested area shows higher values due to overestimation of Freeman's decomposition.
- Figure 3.10: An infinitely thin cylinder on H_0-V_0 plane. The cylinder follows the vertical axis.
- Figure 3.11: An infinitely thin cylinder on rotated H_0-V_0 plane
- Figure 3.12: An oriented thin cylinder on a fixed $H-V$ plane
- Figure 3.13: Uniform distribution of oriented thin cylinders
- Figure 3.14: Cosine squared distribution of a cloud of oriented thin cylinders
- Figure 3.15: Delta function distribution of a cloud of oriented thin cylinders
- Figure 3.16: Illustration of various randomness of vegetated area. Larger randomness, medium randomness, and smaller randomness correspond to terrain covered by rainforest, coniferous forest, and cornfield vegetation types, respectively.
- Figure 3.17: n -th power cosine squared probability density function
- Figure 3.18: Definition of standard deviation of n -th power cosine squared probability density function
- Figure 3.19: Standard deviation of n -th power cosine squared distribution in (3.51) in terms of index number, n . The standard deviation is uniquely related to the index. Also the standard deviation has a limited range between 0 and 0.91, while the index can be infinitely large number.
- Figure 3.20: Plot of two coefficients in (3.64), $p(\sigma)$ (blue line), and $q(\sigma)$ (green line). These curves are obtained by fitting analytically derived points which are displayed by red asterisks.
- Figure 3.21: Scattering matrices for various elemental scatterers: Dipole (left and top); sphere, trihedral, or odd number of scattering (right and top); dihedral or even number of scattering (right and bottom); and circular (left and bottom) are displayed [17].

- Figure 3.22: Flowchart of adaptive NNED algorithm
- Figure 3.23: Results of the NNED' (dash) algorithm assuming a uniform distribution applied to three different wavelength images in Freiburg obtained by AIRSAR. Green, red, and blue are assigned to the volume, double-bounce, and ground components.
- Figure 3.24: Results of the ANNED algorithm applied to three different wavelength images in Freiburg obtained by AIRSAR. Green, red, and blue are assigned to the volume, double-bounce, and ground components.
- Figure 3.25: C_{other} of ANNED (left) for the C-band Black Forest image compared with those of NNED' (dash) using two distributions: cosine squared (center) and uniform (right) distribution. Note that the cosine squared distribution has zero orientation angle.
- Figure 3.26: C_{other} of ANNED (left) for the L-band Black Forest image compared with those of NNED' (dash) using two distributions: cosine squared (center) and uniform (right) distribution. Note that the cosine squared distribution has zero orientation angle.
- Figure 3.27: C_{other} of ANNED (left) for the P-band Black Forest image compared with those of NNED' (dash) using two distributions: the cosine squared (center) and uniform (right) distribution. Note that cosine squared distribution has zero orientation angle.
- Figure 3.28: Orientation angle (upper left) and randomness (upper right) maps derived from the C-band AIRSAR image. Histograms for each parameter are also displayed.
- Figure 3.29: Orientation angle (upper left) and randomness (upper right) maps derived from the L-band AIRSAR image. Histograms for each parameter are also displayed.
- Figure 3.30: Orientation angle (upper left) and randomness (upper right) maps derived from the P-band AIRSAR image. Histograms for each parameter are also displayed.

- Figure 4.1: Illustration of a typical forest consisting of three components: the canopy, trunk, and ground.
- Figure 4.2: Three-layer structure for the MIMICS vegetation model
- Figure 4.3: Illustration of the discrete scatterers of a forested terrain
- Figure 4.4: Scattering mechanisms for DSM
- Figure 4.5: Local coordinate system $x'y'z'$ of an oriented cylinder
- Figure 4.6: Geometry of the angle $\tilde{\varphi}$ defined in (4.11)
- Figure 4.7: Scattering from an oriented cylinder for the case 4-1-1: the 3D plot (left) and cross section at $\phi_s = 0$ (right)
- Figure 4.8: Scattering from an oriented cylinder for the case 4-1-2: the 3D plot (left) and cross section at $\phi_s = 0$ (right)
- Figure 4.9: Scattering from an oriented cylinder for the case 4-1-3: the 3D plot (left) and cross section at $\phi_s = 0$ (right)
- Figure 4.10: Scattering from a cloud of cylinders
- Figure 4.11: Illustration of extinction by a cloud of cylinders
- Figure 4.12: Scattering geometry from the trunk layer with extinction
- Figure 4.13: Parameters characterizing surface roughness
- Figure 4.14: Surface undulation and its statistical definition. A Gaussian distribution is assigned to the range angle, ψ , while a uniform distribution is assigned to azimuth angle, δ .
- Figure 4.15: Vector normal to the tilted plane
- Figure 4.16: Facets (left) and Bragg (right) scatterings. The facets scattering has an obvious peak around its specular angle (140 deg).
- Figure 4.17: Assumed double bounce scattering cases: bistatic at cylinder followed by specular on the ground (upper left), specular on the ground followed by bistatic at cylinder (upper right), specular at cylinder followed by bistatic on the ground (bottom left), and bistatic on the ground followed by specular at cylinder (bottom right)
- Figure 4.18: Definition of the angle α

- Figure 4.19: Geometry of the top-hat reflector
- Figure 4.20: Geometry of double bounce scattering from a cylinder to the ground
- Figure 4.21: Geometry of double bounce scattering from the ground to a cylinder
- Figure 4.22: Orientation angle, ψ' , within the incidence plane
- Figure 4.23: Two cases for the different azimuth orientation angle ranges
- Figure 4.24: Result of the baseline parameters with $M_v=10\%$, $W_c=1.24\text{kg}$, $kh=0.26$, $\sigma_\psi=0.56$
- Figure 4.25: Result of the case 4-6-1 with $M_v=30\%$, $W_c=1.24\text{ kg}$, $kh=0.26$, $\sigma_\psi=0.56$
- Figure 4.26: Result of the case 4-6-2 with $M_v=60\%$, $W_c=1.24\text{ kg}$, $kh=0.26$, $\sigma_\psi=0.56$
- Figure 4.27: Result of the case 4-6-3 with $M_v=10\%$, $W_c=0\text{ kg}$, $kh=0.26$, $\sigma_\psi=0.56$
- Figure 4.28: Result of the case 4-6-4 with $M_v=10\%$, $W_c=2.54\text{ kg}$, $kh=0.26$, $\sigma_\psi=0.56$
- Figure 4.29: Result of the case 4-6-5 with $M_v=10\%$, $W_c=1.24\text{ kg}$, $kh=0.5$, $\sigma_\psi=0.56$
- Figure 4.30: Result of the case 4-6-6 with $M_v=10\%$, $W_c=1.24\text{ kg}$, $kh=1.00$, $\sigma_\psi=0.56$
- Figure 4.31: Result of the case 4-6-7 with $M_v=10\%$, $W_c=1.24\text{ kg}$, $kh=0.26$, $\sigma_\psi=0.30$
- Figure 4.32: Result of the case 4-6-8 with $M_v=10\%$, $W_c=1.24\text{ kg}$, $kh=0.26$, $\sigma_\psi=0.91$
- Figure 4.33: Backscatter cross section with $M_v=10\sim 30\%$, $W_c=1.24\text{ kg}$, $kh=0.26$, $\sigma_\psi=0.56$
- Figure 4.34: Slope with $M_v=10\sim 30\%$, $kh=0.26$, $\sigma_\psi=0.56$ at $\theta_i=40\text{ deg}$
- Figure 4.35: Slope with $M_v=10\sim 30\%$, $W_c=1.24\text{kg}$, $\sigma_\psi=0.56$ at $\theta_i=40\text{ deg}$
- Figure 5.1: Cube to express the backscatter cross section in terms of the three physical parameters: the soil moisture (M_v), surface roughness (kh), and vegetation water content (W_c). The three view angles (A, B, C) are also shown.
- Figure 5.2: Input data from DSM with the given test scenario: $\sigma_\psi=0.30$. Each row corresponds to one of the view angles defined in Figure 5.1, while each column corresponds to the backscatter cross section of σ_{hhhh} (right), $\sigma_{hv hv}$ (center), and σ_{vvvv} (right), respectively.
- Figure 5.3: Input data from DSM with the given test scenario: $\sigma_\psi=0.56$. Each row corresponds to one of the view angles defined in Figure 5.1, while each column corresponds to the backscatter cross section of σ_{hhhh} (right), $\sigma_{hv hv}$ (center), and σ_{vvvv} (right), respectively.

- Figure 5.4: Input data from DSM with the given test scenario: $\sigma_v=0.91$. Each row corresponds to one of the view angles defined in Figure 5.1, while each column corresponds to the backscatter cross section of σ_{hhhh} (right), σ_{hvhv} (center), and σ_{vvvv} (right), respectively.
- Figure 5.5: Estimated randomness and mean orientation angle: $\sigma_v=0.30$. Each row corresponds to each view angle defined in Figure 5.1 while each column corresponds to the orientation angle (right) and the randomness (right), respectively.
- Figure 5.6: Estimated randomness and mean orientation angle: $\sigma_v=0.56$. Each row corresponds to each view angle defined in Figure 5.1 while each column corresponds to the orientation angle (right) and the randomness (right), respectively.
- Figure 5.7: Estimated randomness and mean orientation angle: $\sigma_v=0.91$. Each row corresponds to each view angle defined in Figure 5.1 while each column corresponds to the orientation angle (right) and the randomness (right), respectively.
- Figure 5.8: Estimated power for the volume component: $\sigma_v=0.30$. Each row corresponds to each view angle defined in Figure 5.1 while the columns correspond to the true data, results from NNED assuming the cosine squared and uniform distributions, and results from ANNED, respectively from left to right.
- Figure 5.9: Estimated power for bounce component: $\sigma_v=0.30$. Each row corresponds to each view angle defined in Figure 5.1 while the columns correspond to the true data, results from NNED assuming the cosine squared and uniform distributions, and results from ANNED, respectively from left to right.
- Figure 5.10: Estimated power for surface component: $\sigma_v=0.30$. Each row corresponds to each view angle defined in Figure 5.1 while the columns correspond to the true data, results from NNED assuming the cosine squared and uniform distributions, and results from ANNED, respectively from left to right.

- Figure 5.11: Magnitude of the phase of σ_{hhvv} from the double bounce component in terms of cylinder radius
- Figure 5.12: Backscatter cross section of the co-polarized responses and their ratio of them. All values are in dB.
- Figure 5.13: Estimated power for the volume component: $\sigma_v=0.56$. Each row corresponds to each view angle defined in Figure 5.1, while the columns correspond to the true data, results from NNED assuming the cosine squared and uniform distributions, and results from ANNED, respectively from left to right.
- Figure 5.14: Estimated power for the bounce component: $\sigma_v=0.56$. Each row corresponds to each view angle defined in Figure 5.1, while the columns correspond to the true data, results from NNED assuming the cosine squared and uniform distributions, and results from ANNED, respectively from left to right.
- Figure 5.15: Estimated power for the surface component: $\sigma_v=0.56$. Each row corresponds to each view angle defined in Figure 5.1, while the columns correspond to the true data, results from NNED assuming the cosine squared and uniform distributions, and results from ANNED, respectively from left to right.
- Figure 5.16: Estimated power for the volume component: $\sigma_v=0.91$. Each row corresponds to each view angle defined in Figure 5.1, while the columns correspond to the true data, results from NNED assuming the cosine squared and uniform distributions, and results from ANNED, respectively from left to right.
- Figure 5.17: Estimated power for the bounce component: $\sigma_v=0.91$ Each row corresponds to each view angle defined in Figure 5.1, while the columns correspond to the true data, results from NNED assuming the cosine squared and uniform distributions, and results from ANNED, respectively from left to right.

- Figure 5.18: Estimated power for the surface component: $\sigma_p=0.91$. Each row corresponds to each view angle defined in Figure 5.1, while the columns correspond to the true data, results from NNED assuming the cosine squared and uniform distributions, and results from ANNED, respectively from left to right.
- Figure 6.1: Inversion result using Dubois et al.'s algorithm without polarimetric decomposition
- Figure 6.2: Inversion result using Dubois et al.'s algorithm with the polarimetric decomposition (NNED assuming a cosine squared distribution). The decomposition makes the accuracy worse than the result without decomposition.
- Figure 6.3: A reference cube for the soil moisture retrieval. The soil moisture, surface roughness, and vegetation water content correspond to the x , y , and z axes, respectively.
- Figure 6.4: Calculated five independent cubes (20 samples for each axis). Note that $hhhv$ and $hvvv$ terms are small due to the scattering reflection symmetry.
- Figure 6.5: Inversion results using the cube technique. Inversions of soil moisture (left), roughness (center), and vegetation water content (right) are displayed.
- Figure 6.6: Inversion results using cube technique for various radii of cylinders. Inversions of soil moisture (left), roughness (center), and vegetation water content (right) are displayed.
- Figure 6.7: Inversion results using the cube technique. The -40 dB thermal noise is added to the test data in Figure 6.5. Inversions of soil moisture (left), roughness (center), and vegetation water content (right) are displayed.
- Figure 6.8: Proposed inversion strategy
- Figure C.1: Flowchart of the two-component decomposition using the direct inversion technique of the general covariance matrix
- Figure C.2: Pixels with no solution are displayed at the three wavelengths: C-band (left), L-band (center), and P-band (right). Black: no solution, white: with solution. The results are obtained from the Black Forest image used in Chapter 3.

Figure C.3: Maps of the mean orientation angle (left) and randomness (right) using the two component decomposition model for the C-band Black Forest image

Figure C.4: Maps of the mean orientation angle (left) and randomness (right) using the two component decomposition model for the L-band Black Forest image

Figure C.5: Maps of the mean orientation angle (left) and randomness (right) using the two component decomposition model for P-band of the Black Forest image

Figure D.1: Geometry of an oriented dipole on the ground and a definition of the mean orientation angle at the receiver

Figure D.2: Randomness at the receiver corresponding to that on the ground with various incidence angles

Chapter I

INTRODUCTION

Soil moisture, a medium for interaction between atmosphere and land surface, plays an important role in understanding the global climate system. Once a local precipitation event occurs, typically 40% of input water forms runoff or infiltrates underground, and 60% of input water returns to atmosphere through evapotranspiration [1]. Radiation from the sun causes soil moisture to evaporate directly from the surface. On the other hand, vegetation absorbs soil moisture through the roots, and the radiation energy induces transpiration. These examples illustrate that a solid knowledge of the dynamics of soil moisture deepens our understanding of the global energy cycle as well as the global water cycle. Therefore, soil moisture is an essential physical parameter in understanding the complex hydrologic cycle and thus a systematic technique to measure soil moisture globally and temporally with reasonable accuracy is strongly required.

Measuring soil moisture on bare surfaces has been studied for more than five decades. It is well known that radar scattering from bare soil is strongly related to surface roughness and dielectric constant, which is affected by soil moisture, and several theoretical models have been proposed and are widely used [2, 3]. Some researchers applied these models to infer the soil moisture [4, 5, 6], while others derived inversion models empirically, or semi-empirically, using experimental data sets [7, 8, 9]. Even though these inversion techniques have achieved great accuracy, they are only applicable to bare surfaces or surfaces with a small amount of vegetation having a specific structure.

Table 1.1 shows land classification by vegetation types [10]. Since the desert and tundra are considered as bare surface, using 26.2 million km² as the area covered by desert as given in [11], more than 76% of the total land surface is covered by vegetation. To understand our global climate system thoroughly, measuring soil moisture under vegetation is therefore absolutely necessary.

Table 1.1: Land classification by vegetation types [10]

Biome	Area (million km ²)
Tropical forests	17.6
Temperate zone forests	10.4
Boreal forests	13.7
Tropical savannas	22.5
Temperate grasslands	12.5
Deserts and semi-deserts	45.5
Tundra	9.5
Wetlands	3.5
Croplands	16
<i>Total</i>	<i>151.2</i>

One way to measure soil moisture from vegetated terrain would be to isolate that part of the radar return that was directly returned from the underlying soil surface. Though many researchers have tried to decompose polarimetric radar signals from vegetated terrain into several scattering mechanisms to isolate the ground scattering component [12, 13], these techniques still have not achieved practical accuracy and applicability yet due to the following difficulties. First, there are various types of vegetation (as in Table 1.1), and most of the decomposition algorithms assume a particular type of vegetation. In addition, the multiple scattering mechanisms from vegetated terrain –such as direct backscatter from the canopy, trunks, and ground; interaction between canopy and ground; and interaction between trunk and ground– are not all independent. For example, a dense canopy produces strong backscattering from the canopy while it significantly attenuates backscatter from the trunks and the ground, and all interactions between the vegetation layers and the ground.

However, using the European Remote Sensing (ERS) satellite scatterometer, Wagner et al. showed that the radar cross section from vegetated terrain at Beja in Portugal is highly sensitive to soil moisture even when using a higher frequency [14]. In Figure 1.1, monthly change in backscatter from Beja is shown with normalized differential vegetation index (NDVI) observed by the Advanced Very High Resolution Radiometer (AVHRR) and precipitation history. The NDVI indicates the amount of chlorophylls, which is equivalent to amount of vegetation covering the surface. It is obvious that backscatter cross section follows precipitation history. Hence this tells us that the radar backscatter is sensitive enough to see soil moisture under vegetation.

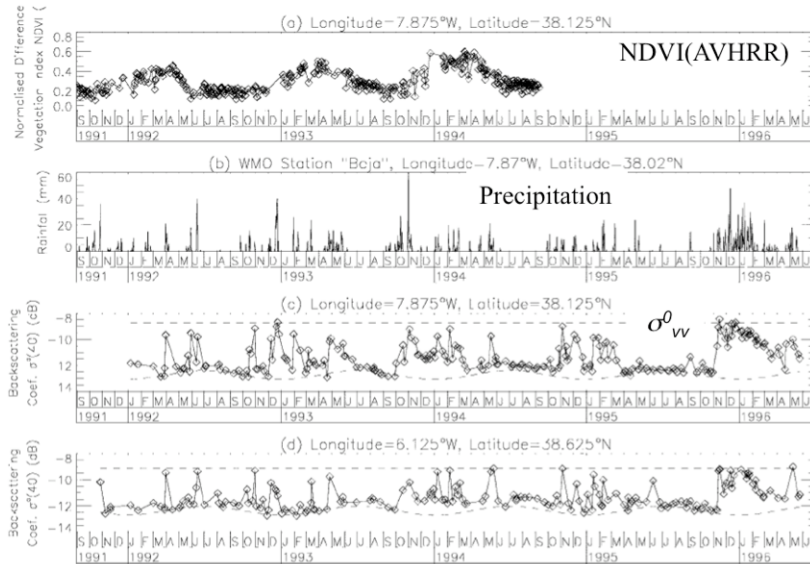


Fig. 3. Temporal evolution of the NDVI, rainfall observations, and the normalized backscattering coefficient $\sigma^0(40)$ over an agricultural region around Beja in southern Portugal. (a) Daily NDVI values degraded to match the resolution of the ERS scatterometer, (b) rainfall recorded at the synoptic station "Beja," (c) $\sigma^0(40)$ time series over Beja; the dotted lines show the backscattering coefficient for dry soil conditions, $\sigma_{dry}^0(40, t)$, and the backscattering coefficient for wet soil conditions, $\sigma_{wet}^0(40)$, and (d) $\sigma^0(40)$ series over a region about 150 km east of Beja; the dotted lines represent $\sigma_{dry}^0(40, t)$ and $\sigma_{wet}^0(40)$.

Figure 1.1: Monthly changes of NDVI (top), precipitation history (second row), and radar backscatter cross section of vertical polarization (third row and bottom) at Beja in Portugal, which were reported in [14]

The purpose of this research is to study in detail the scattering mechanisms of vegetated terrain to attempt to find a way to isolate surface scattering from other scattering mechanisms, and apply this knowledge to retrieve the soil moisture.

This thesis is organized as follows. In Chapter II, we define the coordinate systems used in this research, followed by the fundamental mathematical operations for the scattering and covariance matrices.

We follow this introductory material with a discussion of polarimetric scattering decomposition as used in this thesis. We introduce a more general decomposition technique and show how this algorithm corrects some of the deficiencies of the current decomposition schemes. Our algorithm allows one to adaptively change the assumed vegetation structure on a pixel-by-pixel basis to find the best approximation to the observed scattering.

In order to verify the decomposition algorithm, we use a numerical scattering model to simulate vegetation scattering. In Chapter IV, the forward simulation model called the Discrete Scatterer Model (DSM) [15, 16] is introduced with some modifications to the previous work. This model is then utilized to study the sensitivity of the polarimetric radar backscatter cross section to changes in the physical parameters of vegetated terrain. This provides us with a better physical understanding of the scattering in such a complicated system. In Chapter V, the proposed decomposition algorithms are applied to DSM so that we can quantitatively evaluate them. Finally, in Chapter VI, we discuss ideas for retrieving soil moisture from vegetated terrain.

Chapter II

Fundamentals

In this chapter several fundamentals are introduced for later discussion. We start with coordinate systems and radar polarimetry techniques, and follow that with a discussion of observation. We also discuss the scattering and covariance matrices and the reciprocity theorem.

2.1 Coordinate System

Two types of coordinate systems are commonly used to express electromagnetic scattering problems [17] depending on the definition of propagation direction of the scattered wave: the forward scatter alignment (FSA) convention and the backscatter alignment (BSA) convention. Figure 2.1 shows both of them. FSA is generally used to describe bistatic scattering problems while BSA is used to describe backscattering problems.

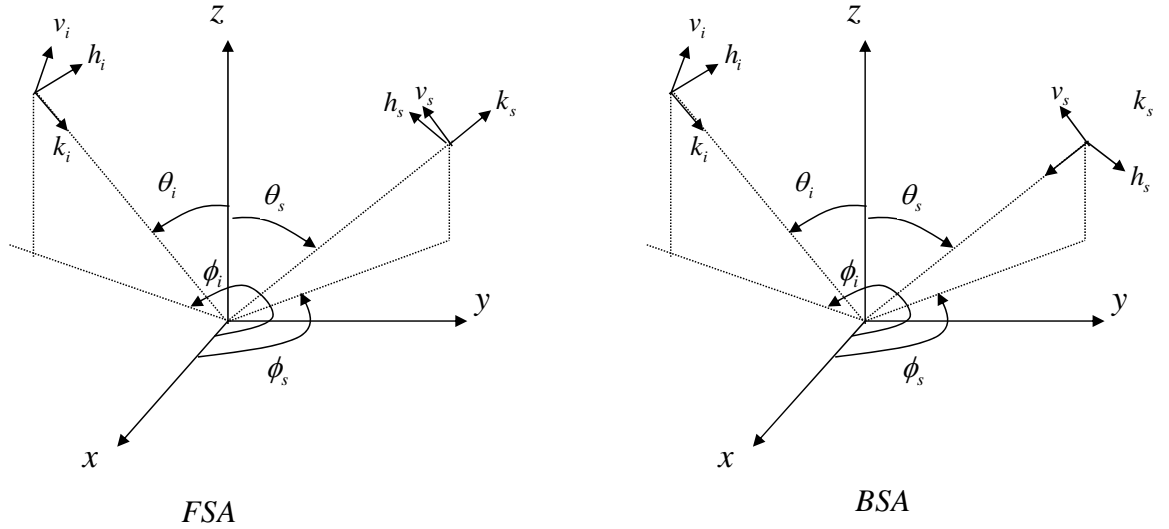


Figure 2.1: Coordinate systems: Forward Scatter Alignment (FSA) (left), Backscatter Alignment (BSA) (right)

There are several other definitions of the four angles, θ_i , θ_s , ϕ_i , and ϕ_s shown in the figure. For example, Ulaby et al. defines $\pi - \theta_i$, θ_s , $\pi + \phi_i$, and ϕ_s for θ_i , θ_s , ϕ_i , and ϕ_s , respectively [17]. To avoid further complexity using different angle definitions, we just choose simplest one, as in the figure. In a later chapter, we introduce another coordinate system to discuss natural vegetation where it makes better physical sense to define the angle from top to bottom. The definitions are exactly same as in the figure. Incidence and scattered vectors are mathematically expressed as follows.

$$\begin{pmatrix} k \\ h \\ v \end{pmatrix}^{FSA} = \begin{pmatrix} \sin \theta_s & 0 & \cos \theta_s \\ 0 & 1 & 0 \\ -\cos \theta_s & 0 & \sin \theta_s \end{pmatrix} \begin{pmatrix} \cos \phi_s & \sin \phi_s & 0 \\ -\sin \phi_s & \cos \phi_s & 0 \\ 0 & 0 & 1 \end{pmatrix} \begin{pmatrix} x \\ y \\ z \end{pmatrix} \quad (2.1)$$

$$\begin{pmatrix} k \\ h \\ v \end{pmatrix}^{BSA} = \begin{pmatrix} \sin \theta_i & 0 & -\cos \theta_i \\ 0 & 1 & 0 \\ \cos \theta_i & 0 & \sin \theta_i \end{pmatrix} \begin{pmatrix} -\cos \phi_i & -\sin \phi_i & 0 \\ \sin \phi_i & -\cos \phi_i & 0 \\ 0 & 0 & 1 \end{pmatrix} \begin{pmatrix} x \\ y \\ z \end{pmatrix} \quad (2.2)$$

The coordinate systems are easily related to those in the Ulaby et al.'s book. To avoid any further confusion, the transformation matrices are defined here.

$$\theta_i = \pi - \theta_i^{Ulaby,Elachi}, \quad \phi_i = \phi_i^{Ulaby,Elachi} + \pi \quad (2.3)$$

$$\begin{pmatrix} k \\ h \\ v \end{pmatrix}^x = \begin{pmatrix} 1 & 0 & 0 \\ 0 & 1 & 0 \\ 0 & 0 & -1 \end{pmatrix} \begin{pmatrix} k \\ h \\ v \end{pmatrix}^{Ulaby,Elachi} \quad x = BSA, FSA \quad (2.4)$$

$$\begin{pmatrix} k \\ h \\ v \end{pmatrix}^y = \begin{pmatrix} -1 & 0 & 0 \\ 0 & -1 & 0 \\ 0 & 0 & -1 \end{pmatrix} \begin{pmatrix} k \\ h \\ v \end{pmatrix}^{Ulaby,Elachi} \quad (x, y) = (BSA, FSA), (FSA, BSA) \quad (2.5)$$

Note that the inverse matrix of each transformation matrix is the same as the original one.

2.2 Radar Polarimetry

Typical radar observation geometry is shown in Figure 2.2. There are transmitting and receiving antennas which allow us to measure scattered power from a target located at a distance R_1 from the transmitting antenna and R_2 from the receiving antenna.

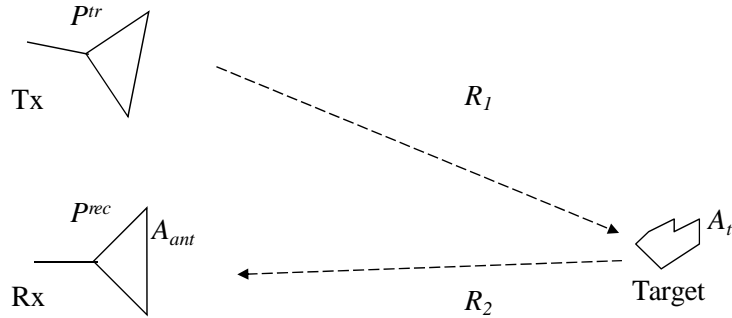


Figure 2.2: Radar observation geometry

Received power is expressed in the well known radar equation,

$$P^{rec} = \frac{P^{tr} G}{4\pi R_1^2} \sigma^0 A_t \frac{A_{ant}}{4\pi R_2^2} \quad (2.6)$$

where G is the antenna gain, and P^{tr} and P^{rec} are the transmitted power and received power, respectively. A_{ant} and A_t are the antenna effective area and target effective area, respectively. σ^0 is backscatter cross section. The radar system estimates the backscatter cross section based on the *a priori* knowledge of the other parameters in (2.6).

Now the concept is extended to polarimetric radar observation. Maxwell's equation tells us that polarization of an electromagnetic wave can be expressed using polarization bases. Horizontal and vertical linear polarizations are commonly used because they are easy to implement. These two polarization bases are physically realized by changing the antenna effective length, and the normalized antenna effective length is called the polarization state,

$$\vec{p} = \begin{pmatrix} p_h \\ p_v \end{pmatrix} \rightarrow \vec{p}_{norm} = \frac{\vec{p}}{|\vec{p}|} \quad (2.7)$$

where p_h and p_v are horizontal and vertical antenna effective length, respectively. This allows us to describe the backscatter cross section of single scatterer as

$$\sigma^0 = \left| \vec{p}_{norm}^{rec} \cdot [S] \vec{p}_{norm}^{tr} \right|^2 \quad (2.8)$$

where \vec{p}_{norm}^{tr} and \vec{p}_{norm}^{rec} are normalized antenna effective lengths for transmitting and receiving, respectively.

$$[S] = \begin{bmatrix} S_{hh} & S_{hv} \\ S_{vh} & S_{vv} \end{bmatrix} \quad (2.9)$$

The matrix S is called the scattering matrix and expresses a polarimetric scattering property of the target. S_{xy} means that a y -polarized wave is transmitted and a x -polarized wave is

received. So we can say that polarimetric radar observation is a way to measure the four elements of the scattering matrix and the target is considered as a polarimetric transformer.

A simple calculation gives us the following expressions.

$$\vec{p}_{norm}^{rec} \cdot [S] \vec{p}_{norm}^{tr} = \begin{pmatrix} p_h^{rec} \\ p_v^{rec} \end{pmatrix} \cdot \begin{bmatrix} S_{hh} & S_{hv} \\ S_{vh} & S_{vv} \end{bmatrix} \begin{pmatrix} p_h^{tr} \\ p_v^{tr} \end{pmatrix} = \begin{pmatrix} p_h^{tr} p_h^{rec} \\ p_v^{tr} p_h^{rec} \\ p_h^{tr} p_v^{rec} \\ p_v^{tr} p_v^{rec} \end{pmatrix}^T \begin{pmatrix} S_{hh} \\ S_{hv} \\ S_{vh} \\ S_{vv} \end{pmatrix} = \vec{A}^T \vec{S} = \vec{S}^T \vec{A} \quad (2.10)$$

$$\sigma^0 = (\vec{A}^T \vec{S}) (\vec{A}^T \vec{S})^{*T} = \vec{A}^T (\vec{S} \vec{S}^{*T}) \vec{A}^* = \vec{A}^T C_0 \vec{A}^*$$

where superscript T and * denote transpose and complex conjugation, respectively. Note that the vector \vec{A} consists only of antenna polarization parameters. As long as we are interested in observing natural terrain, the received diffuse scattering power is usually statistically averaged. This physical fact leads us to the following mathematical formulation,

$$C = \langle C_0 \rangle = 4\pi \begin{bmatrix} \langle |S_{hh}|^2 \rangle & \langle S_{hh} S_{hv}^* \rangle & \langle S_{hh} S_{vh}^* \rangle & \langle S_{hh} S_{vv}^* \rangle \\ \langle S_{hh}^* S_{hv} \rangle & \langle |S_{hv}|^2 \rangle & \langle S_{hv} S_{vh}^* \rangle & \langle S_{hv} S_{vv}^* \rangle \\ \langle S_{hh}^* S_{vh} \rangle & \langle S_{hv}^* S_{vh} \rangle & \langle |S_{vh}|^2 \rangle & \langle S_{vh} S_{vv}^* \rangle \\ \langle S_{hh}^* S_{vv} \rangle & \langle S_{hv}^* S_{vv} \rangle & \langle S_{vh}^* S_{vv} \rangle & \langle |S_{vv}|^2 \rangle \end{bmatrix} \quad (2.11a)$$

where $\langle \rangle$ denotes ensemble averaging. C is the so called covariance matrix and is usually used to represent polarimetric radar data. Note that this is a Hermitian matrix not only for the monostatic case but also for the bistatic case. In this thesis, the matrix is also written as

$$C = \begin{bmatrix} \sigma_{hhhh}^0 & \sigma_{hhhv}^0 & \sigma_{hhvh}^0 & \sigma_{hhvv}^0 \\ \sigma_{hhhv}^{0*} & \sigma_{hvhv}^0 & \sigma_{hvvh}^0 & \sigma_{hvvv}^0 \\ \sigma_{hhvh}^{0*} & \sigma_{hvhv}^{0*} & \sigma_{vhhv}^0 & \sigma_{vhvv}^0 \\ \sigma_{hhvv}^{0*} & \sigma_{hvvv}^{0*} & \sigma_{vhvv}^{0*} & \sigma_{vvvv}^0 \end{bmatrix} \quad (2.11b)$$

Equation (2.11) is expressed from the antenna's point of view. Now we try to express it from data user's point of view. The scattering matrix in (2.9) now corresponds to one pixel of a scene. The covariance matrix for this one pixel is as follows.

$$C_0 = \begin{bmatrix} |S_{hh}|^2 & S_{hh}S_{hv}^* & S_{hh}S_{vh}^* & S_{hh}S_{vv}^* \\ S_{hh}^*S_{hv} & |S_{hv}|^2 & S_{hv}S_{vh}^* & S_{hv}S_{vv}^* \\ S_{hh}^*S_{vh} & S_{hv}^*S_{vh} & |S_{vh}|^2 & S_{vh}S_{vv}^* \\ S_{hh}^*S_{vv} & S_{hv}^*S_{vv} & S_{vh}^*S_{vv} & |S_{vv}|^2 \end{bmatrix} \quad (2.12)$$

In order to avoid speckle-like noise caused by signal fading, averaging of the pixels, which is also called multi-looking, is commonly used in practice. This simple operation is mathematically expressed as

$$C = \langle C_0 \rangle = \frac{1}{MN} \sum_{i=1}^M \sum_{j=1}^N C_0(i, j) \quad (2.12)$$

where M and N are numbers of pixels to average in either the along track direction or the cross track direction. The resulting image is also called the M by N looks image.

If our observation can be done only in the backscattering situation, i.e. monostatic case, one can easily show that scattering symmetry gives us

$$S_{hv} = S_{vh} \quad (2.13)$$

This is called the reciprocity theorem, which plays an important role in this thesis, and reduces our 4 by 4 covariance matrix to a 3 by 3 matrix as follows.

$$[S] = \begin{bmatrix} S_{hh} & S_{hv} \\ S_{hv} & S_{vv} \end{bmatrix} \rightarrow C_0 = \begin{bmatrix} |S_{hh}|^2 & \sqrt{2}S_{hh}S_{hv}^* & S_{hh}S_{vv}^* \\ \sqrt{2}S_{hh}^*S_{hv} & 2|S_{hv}|^2 & \sqrt{2}S_{hv}S_{vv}^* \\ S_{hh}^*S_{vv} & \sqrt{2}S_{hv}^*S_{vv} & |S_{vv}|^2 \end{bmatrix} \quad (2.14)$$

Chapter III

Polarimetric Decomposition

Backscattering from a vegetated surface is typically a mixture of several scattering mechanisms such as backscattering from a canopy part, from the ground, or from interaction between the ground and trunk, as shown in Figure 3.1.

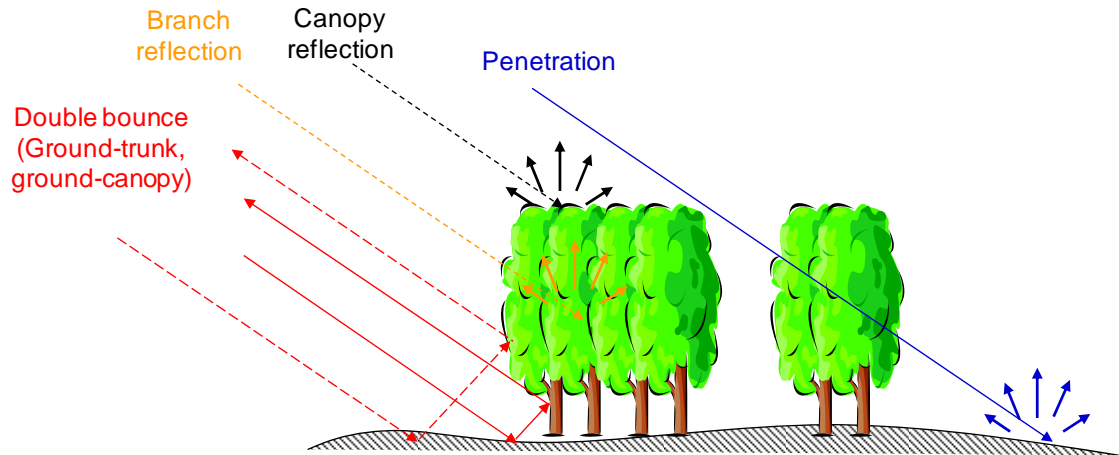


Figure 3.1: Backscattering from a vegetated terrain.

We will discuss the details of each of these scattering mechanisms in the next chapter. Extracting parameters such as amount of biomass, type of vegetation, or soil moisture from measured data requires breaking the measured data into its original scattering mechanisms.

In this chapter, we shall start by briefly introducing various decomposition techniques. One of the most popular decomposition techniques, the so-called three-component decomposition, and its potential deficiency are introduced. We propose an alternative

algorithm to improve it. Since the three-component decomposition algorithm assumes one specific type of vegetation structure, it is of limited applicability when applied to natural terrain, which usually covered by a wide variety of vegetation. In order to overcome this limitation, a generalization of the volume term is introduced and then applied. Finally some experimental results to validate those algorithms are discussed. This chapter covers only qualitative analysis; quantitative validation is deferred to Chapter V.

3.1 Previous Techniques

In order to introduce a concept of polarimetric decomposition, we shall start with the coherent case; the incoherent case will be discussed later.

The coherent decomposition model allows us to express the scattering matrix of a single scatterer by the sum of several orthogonal bases. In the backscattering case, Krogager expressed the model as

$$\begin{bmatrix} S_{hh} & S_{hv} \\ S_{hv} & S_{vv} \end{bmatrix} = a \begin{bmatrix} 1 & 0 \\ 0 & 1 \end{bmatrix} + b \begin{bmatrix} 1 & 0 \\ 0 & -1 \end{bmatrix} + c \begin{bmatrix} 0 & 1 \\ 1 & 0 \end{bmatrix} \quad (3.1)$$

where these orthogonal components are called Pauli spin matrices [18]. Each of a , b , and c , is solved for using the measured scattering matrix. An advantage of the use of these matrices is that each basis has physical meaning so that it helps with the interpretation of the decomposition results. The first term corresponds to the scattering from a trihedral corner reflector, spherical scatterer, or an odd number of reflections [17]. The second term corresponds to an even number of reflections, including the so-called double bounce reflection, and the third term usually corresponds to the amount of biomass. The choice of basis, however, is totally dependent on the purpose. Since the model is basically designed for a single deterministic scatterer, applying it to distributed scatterers is not appropriate. More recently, this coherent decomposition technique has been applied to manmade structures like bridges in [19].

For distributed targets, i.e., the coherent case, a covariance matrix in (2.12) should be used to express our observation instead of the scattering matrix. Equation (2.12) is rewritten in the backscattering case as

$$C = \begin{bmatrix} \langle |S_{hh}|^2 \rangle & \sqrt{2} \langle S_{hh} S_{hv}^* \rangle & \langle S_{hh} S_{vv}^* \rangle \\ \sqrt{2} \langle S_{hh}^* S_{hv} \rangle & 2 \langle |S_{hv}|^2 \rangle & \sqrt{2} \langle S_{hv} S_{vv}^* \rangle \\ \langle S_{hh}^* S_{vv} \rangle & \sqrt{2} \langle S_{hv}^* S_{vv} \rangle & \langle |S_{vv}|^2 \rangle \end{bmatrix}. \quad (3.2)$$

Using this 3 by 3 expression, Cloude proposed an eigenvector based decomposition in [20]. His model is expressed in the form of

$$C = \sum_{i=1}^3 \lambda_i e_i e_i^{*T} \quad (3.3)$$

where λ and e are the eigenvalue and associated eigenvector, respectively. Since the matrix is Hermitian, the eigenvectors are always an orthonormal basis, thus it provides a unique decomposition. These natural bases, however, are freely changed from pixel to pixel, thus making the interpretation more complicated because it is not guaranteed that the resulting eigenvectors always correspond to physical scatterers, as with Pauli spin matrices.

To avoid this difficulty, model based decomposition is adopted as our baseline technique in this thesis. While this model does not guarantee orthogonality of its bases, meaning the result is not unique, it provides better physical understanding of its result. Details of this model are discussed in the next section. References [21] and [22] provide an excellent review of the decomposition models mentioned in this section.

3.2 Freeman Decomposition

Although many people have studied eigenvector based decomposition recently [23, 24] and shown reasonable results, the approach may not be reliable because a result based on

purely mathematics does not provide sufficient physical insight. Therefore, it is very important to develop a decomposition technique from solid physical scattering principles. As a baseline, we start with Freeman and Durden's physics based decomposition, described in this section, and then develop it using mathematical features including eigenvalue decomposition, so that we maintain physical sense while using mathematical operations. If the reader is not familiar with scattering from vegetated terrain, we recommend reading the first section of Chapter IV.

Freeman's decomposition model expresses the measured covariance matrix as the sum of three physical components: the volume, double-bounce, and ground components,

$$C_m = xC_v + yC_d + zC_g. \quad (3.4)$$

Each term is given as

$$\begin{aligned} C_v &= \begin{bmatrix} 1 & 0 & 1/3 \\ 0 & 2/3 & 0 \\ 1/3 & 0 & 1 \end{bmatrix} \\ C_d &= \begin{bmatrix} 1 & 0 & \alpha \\ 0 & 0 & 0 \\ \alpha^* & 0 & |\alpha|^2 \end{bmatrix} \\ C_g &= \begin{bmatrix} 1 & 0 & \beta \\ 0 & 0 & 0 \\ \beta^* & 0 & |\beta|^2 \end{bmatrix} \end{aligned} \quad (3.5)$$

where α and β are variables to be fixed. These terms will be thoroughly discussed later in this chapter. So far we have four equations with five unknowns.

$$\begin{aligned}
x &= 3\sigma_{hvhv} \\
\sigma'_{hhhh} &= \sigma_{hhhh} - x = y + z \\
\sigma'_{vvvv} &= \sigma_{vvvv} - x = y|\alpha|^2 + z|\beta|^2 \\
\sigma'_{hhvv} &= \sigma_{hhvv} - \frac{1}{3}x = y\alpha + z\beta
\end{aligned} \tag{3.6}$$

Obviously we need one more condition to solve for the parameters. Freeman et al. proposed to add a constraint using a characteristic of double-bounce scattering as shown in [25]. It is known that an additional reflection flips the phase of the correlation of the co-polarizations. Van Zyl applied this characteristic to classify the scene into an odd number or even number of reflections, and obtained reasonable results. If the real part of σ'_{hhvv} is positive, we determine that surface scattering is the dominant contribution and α is fixed to -1. On the other hand, if the real part of σ'_{hhvv} is negative, we determine that double bounce scattering is the dominant contribution and β is fixed to 1. Using this condition, we can finally solve the equations as follows. If the real part of σ'_{hhvv} is positive,

$$\begin{aligned}
\alpha &= -1 \\
z &= \frac{|\sigma'_{hhvv} + \sigma'_{hhhh}|^2}{\sigma'_{hhhh} + \sigma'_{vvvv} + 2\text{Re}(\sigma'_{hhvv})} \\
\beta &= \frac{\sigma'_{hhvv} + \sigma'_{hhhh} - 1}{z} \\
y &= \sigma'_{hhhh} - z
\end{aligned} \tag{3.7}$$

Also, if it is negative,

$$\begin{aligned}
\beta &= 1 \\
y &= \frac{|\sigma'_{hhvv} - \sigma'_{hhhh}|^2}{\sigma'_{hhhh} + \sigma'_{vvvv} - 2\text{Re}(\sigma'_{hhvv})} \\
\alpha &= \frac{\sigma'_{hhvv} - \sigma'_{hhhh}}{y} + 1 \\
z &= \sigma'_{hhhh} - y
\end{aligned} \tag{3.8}$$

We shall apply the decomposition technique to a real image from the Black Forest in Germany in the summer of 1991. The L-band image is shown in Figure 3.2. The radar system illuminated from the top of the image to the bottom.

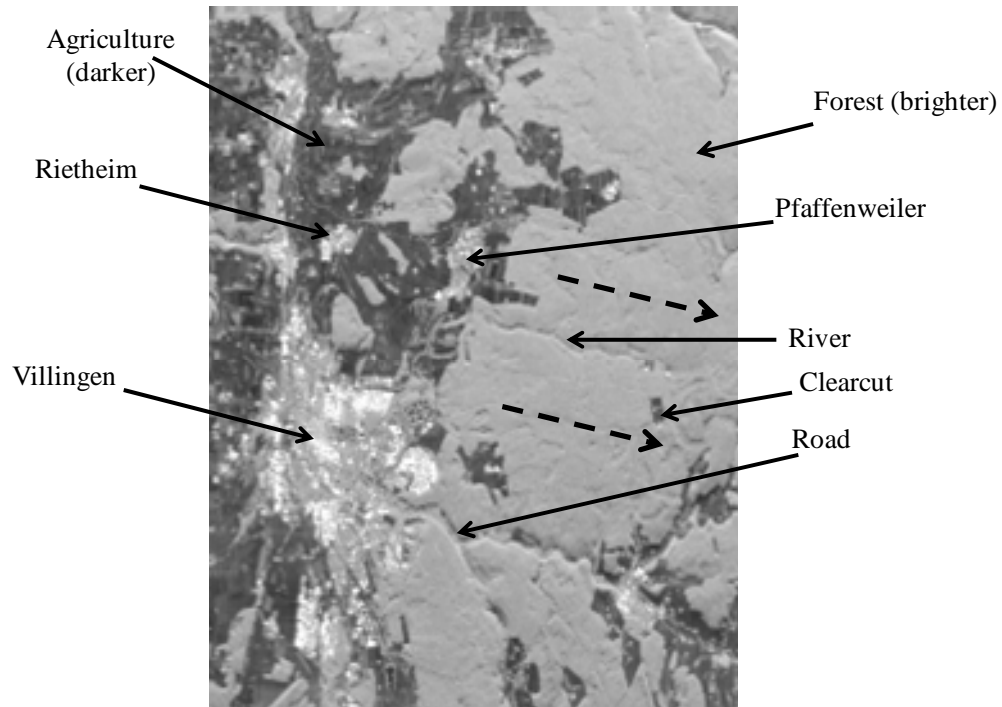


Figure 3.2: L-band image of the Black Forest in Germany obtained by NASA/JPL AIRSAR system in the summer of 1991. The solid arrows indicate the name of city or area type. The dotted lines specify the direction of topographic change. The terrain slopes upward in the direction of the arrows.

The image nicely shows urban area, agricultural area, and forested area with high contrast. There is also a river and a road from right to left. Note that the dotted lines in the forest show there is topography and the terrain slopes gradually upward from the center to the right. The forested area is a mixture of spruce, pine, and fir trees [26]. The observation was conducted at three different frequencies: C-band (6 cm), L-band (24 cm), and P-band (68 cm), and these three components are shown in Figure 3.3.

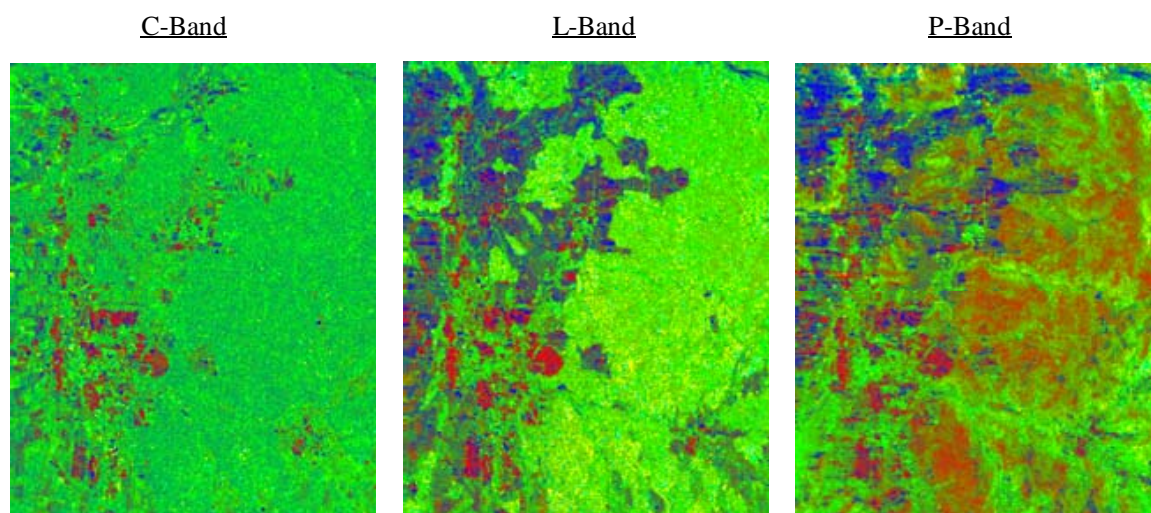


Figure 3.3: Results of the Freeman algorithm applied to three different wavelength images in Freiburg obtained by AIRSAR. From left to right, C-band (5 cm), L-band (24 cm) and P-band (68 cm) images are displayed. Green, red and blue are assigned to volume scattering, double-bounce scattering, and ground scattering, respectively.

Green, red, and blue are assigned to normalized power of the volume, double-bounce, and surface scattering components, respectively. For all wavelengths, urban areas such as Villingen and Rietheim are clearly discriminated in the double bounce component. In the agricultural area, it is clear the longer wavelengths show good penetration of canopy layer, and double-bounce scattering appears instead of the volume component. Van Zyl pointed out in [26] that the double bounce component due to the trunk-surface interaction should be replaced by the volume component if the topography is not flat. In particular, you can see this effect in the P-band image. A river exists half way down the image from right to left, and there is a steep slope on both sides toward and away from the radar. The image clearly shows that the widely spread double-bounce components are suddenly replaced by the volume component around the river. Hence the results from Freeman's model based decomposition show good agreement with our intuition.

There can be negative power associated with the Freeman decomposition. In order to remove this nonphysical quantity, we propose a different decomposition technique. The power of the covariance matrix is expressed as the sum of each diagonal element.

$$C_x = \begin{pmatrix} a & b & c \\ d & e & f \\ g & h & i \end{pmatrix} \Rightarrow P(C_x) = a + e + i \quad (3.9)$$

If double bounce and surface scattering components are removed from (3.4), and an “other” component added, the equation becomes

$$C_m = xC_v + C_{other} \quad (3.10)$$

where x is a positive real number because the observation is the sum of scattering powers, which are positive definite as shown in (2.11). The additional component is utilized as a “catch all” to collect the other terms from the decomposition so that we can always keep both the left- and right-hand side exactly equal. The equation can be written as

$$C_{other} = C_m - xC_v. \quad (3.11)$$

Conservation of energy forbids any component in (3.11) from having a negative power. Hence, we implicitly have the following conditions.

$$P(C_{other}) \geq 0, \quad P(C_m) \geq 0, \quad P(C_v) \geq 0 \quad (3.12)$$

Since Freeman’s decomposition determines the coefficient x directly from the cross polarization term of the measured covariance matrix, its value is uniquely determined. Applying (3.12) to the image, we can simply check if the decomposition is valid or not. Figure 3.4 shows the result of this validation test using the L-band Black Forest image.

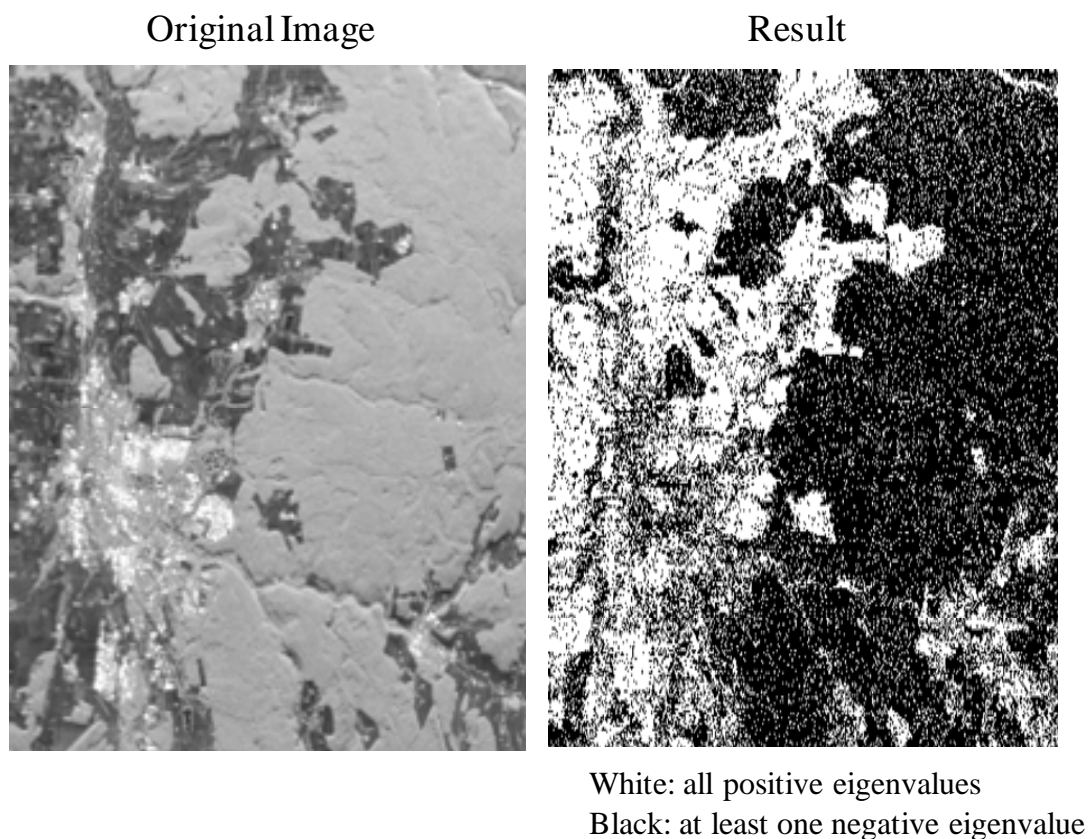


Figure 3.4: Pixels with negative eigenvalue are displayed using the L-band Black Forest image. The left image is the total power image at L-band, and the right image is the result of the validation test.

The result shows that the entire forest has negative power, which is physically unacceptable. Since Freeman's algorithm assumes that whole cross polarization term is contributed by the volume component only, it may overestimate the contribution from other scattering mechanisms. For example, the double-bounce scattering may contribute to the cross polarization term due to the fact that one of the two reflections is caused by the volume layer. This deficiency was pointed out by van Zyl et al. in [49]. We introduce the algorithm which overcomes this fatal deficiency in the next section.

3.3 Non-Negative Eigenvalue Decomposition

In order to avoid negative power, van Zyl et al. proposed an improved two-component (C_v and C_{other} in (3.11)) decomposition technique in [49]. In this section, the technique is first introduced. Then we expand to the technique to a four-component (C_v, C_d, C_g , and C_{other}) decomposition for natural terrain. For these algorithms the off-diagonal part of the measured covariance matrix in (3.11) will be set to zero, assuming scattering reflection symmetry [27].

$$C_m = \begin{pmatrix} \sigma_{hhhh} & \sqrt{2}\sigma_{hhhv} & \sigma_{hhvv} \\ \sqrt{2}\sigma_{hhhv}^* & 2\sigma_{hvhv} & \sqrt{2}\sigma_{hvvv} \\ \sigma_{hhvv} & \sqrt{2}\sigma_{hvvv}^* & \sigma_{vvvv} \end{pmatrix} \approx \begin{pmatrix} \sigma_{hhhh} & 0 & \sigma_{hhvv} \\ 0 & 2\sigma_{hvhv} & 0 \\ \sigma_{hhvv}^* & 0 & \sigma_{vvvv} \end{pmatrix} \quad (3.13)$$

Similarly, the volume component in (3.11) can be written as

$$C_v = \begin{pmatrix} p & 0 & s \\ 0 & 2q & 0 \\ s^* & 0 & r \end{pmatrix} \quad (3.14)$$

where p, q , and r are real and positive numbers while s is a complex number. Hence (3.11) is rewritten as follows.

$$C_{other} = \begin{pmatrix} \sigma_{hhhh} & 0 & \sigma_{hhvv} \\ 0 & 2\sigma_{hvhv} & 0 \\ \sigma_{hhvv}^* & 0 & \sigma_{vvvv} \end{pmatrix} - x \begin{pmatrix} p & 0 & s \\ 0 & 2q & 0 \\ s^* & 0 & r \end{pmatrix} \quad (3.15)$$

It is well known that each eigenvalue of a Hermitian matrix is real. Moreover, they are all positive as long as the measured scattering power is positive, which is the usual case (see Appendix A). These two conditions place a constraint on x in (3.15). When x is zero, C_{other} is exactly equal to the measured covariance matrix, which means that each eigenvalue of C_{other} automatically satisfies the requirements. As x is increased, the power in the second term increases, so the power in the first term necessarily decreases, which in turn reduces

the eigenvalues of the first term. If one chooses too large of an x , it is obvious that the power in C_{other} becomes negative, and hence some of the eigenvalues also become negative. Therefore, x will be constrained such that both conditions hold. We can derive this mathematically as follows.

From (3.15), each eigenvalue can be derived as

$$\begin{aligned}\lambda_1(x) &= \frac{1}{2} \left\{ (-ax + b) + \sqrt{f(x)} \right\} \\ \lambda_2(x) &= \frac{1}{2} \left\{ (-ax + b) - \sqrt{f(x)} \right\} \\ \lambda_3(x) &= 2(\sigma_{hv} - qx)\end{aligned}\tag{3.16a}$$

where,

$$\begin{aligned}f(x) &= cx^2 - 2dx + e \\ a &= p + r \\ b &= \sigma_{hhhh} + \sigma_{vvvv} \\ c &= (p - r)^2 + 4|s|^2 \\ d &= (p - r)(\sigma_{hhhh} - \sigma_{vvvv}) + 4\text{Re}(\sigma_{hvv} s^*) \\ e &= (\sigma_{hhhh} - \sigma_{vvvv})^2 + 4|\sigma_{hvv}|^2\end{aligned}\tag{3.16b}$$

Note that all values defined in (3.16b) are real, and all those values are positive except for d . Due to the fact that eigenvalues of a Hermitian matrix are always real no matter what its associated power is, we can find an implicit condition from (3.15) as follows. Obviously, the third eigenvalue is always real. In the case of the first and second eigenvalues, both eigenvalues are always real only if the real number $f(x)$ is positive so that

$$\begin{aligned}
f(x) &= c \left(x - \frac{d}{c} \right)^2 - \frac{d^2}{c} + e \geq 0 \\
&\Rightarrow -\frac{d^2}{c} + e \geq 0 \quad (\because c \geq 0) \\
&\Rightarrow |(\sigma_{hh} - \sigma_{vv})s - (p-r)\sigma_{hvv}|^2 \geq 4\{\text{Im}(\sigma_{hvv}s^*)\}
\end{aligned} \tag{3.17}$$

If this does not hold for measured data, it may imply that there is some problem with the radar system.

We can now constrain x as follows. The behavior of the third eigenvalue is shown in Figure 3.5. Note that the eigenvalue is straight line with negative slope.

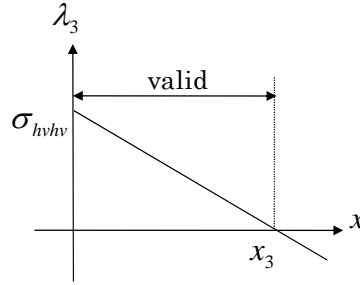


Figure 3.5: Illustration of the third eigenvalue in (3.16a)

From the figure, the x starts from σ_{hvhv} at $x=0$, and it decreases linearly with increase of x . It crosses the x axis at the point x_3 in the figure, which can be solved for using the third equation of (3.16a), yielding

$$x_3 = \frac{\sigma_{hvhv}}{q} \tag{3.18}$$

Let's move on to the first and second eigenvalues. One can easily recognize that the second one is always greater than the first one for any x . So we need only constrain the value of x from the second eigenvalue equation. The second eigenvalue in (3.16a) is rewritten as

$$\lambda_2(x) = -\frac{1}{2}(ax + \sqrt{f(x)}) + \frac{b}{2}. \quad (3.19)$$

This is a monotonously decreasing function because the first term is always negative for any x because a and $\sqrt{f(x)}$ are always positive. Setting (3.19) equal to zero, the maximum value of x can be expressed as

$$x_2 = \begin{cases} \frac{1}{a^2 - c} \left\{ (ab - d) - \sqrt{(ab - d)^2 - (b^2 - e)(a^2 - c)} \right\} & (a^2 - c \neq 0) \\ \frac{b^2 - e}{2(ab - d)} & (a^2 - c = 0) \end{cases}. \quad (3.20)$$

The behaviors of these two eigenvalues in terms of x is illustrated in Figure 3.6. Note that this is one specific case where the x_2 is smaller than the x_3 .

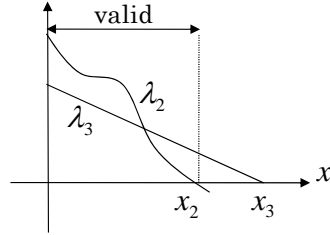


Figure 3.6: Illustration of the second and third eigenvalues in (3.16a). This is a specific case where x_2 is smaller than x_3 .

In order to find the constraints on x to satisfy both conditions on the eigenvalues, we compare x_2 and x_3 , and then choose the smaller one as

$$x_{\max} = \min(x_2, x_3). \quad (3.21)$$

This simple modification to Freeman's model, namely, the addition of the C_{other} term, corrects the potential deficiency illustrated by Figure 3.3. Although we applied it to the two-component decomposition model in (3.11), this idea can be expanded beyond this simplest case. In particular, we will further modify the decomposition model to make it

applicable to various vegetated terrains by adding two more scattering components: double bounce scattering and ground scattering. Here again, we use the *other* component to ensure that the power conservation law holds.

Equation (3.11) is modified by adding the two components as follows.

$$C_m = xC_v + yC_d + zC_g + C_{other} \quad (3.22)$$

If the two-component decomposition technique is applied, x is independently determined. The equation is then rewritten as

$$C'_m = C_m - xC_v = yC_d + zC_g + C_{other} \quad (3.23)$$

where,

$$C'_m = \begin{pmatrix} \sigma'_{hhhh} & 0 & \sigma'_{hhvv} \\ 0 & 2\sigma'_{hv hv} & 0 \\ \sigma'^*_{hhvv} & 0 & \sigma'_{vvvv} \end{pmatrix}$$

$$C_d = \begin{pmatrix} 1 & 0 & \alpha \\ 0 & 0 & 0 \\ \alpha^* & 0 & |\alpha|^2 \end{pmatrix} \quad . \quad (3.24)$$

$$C_g = \begin{pmatrix} 1 & 0 & \beta \\ 0 & 0 & 0 \\ \beta^* & 0 & |\beta|^2 \end{pmatrix}$$

Note that the (3.24) is exactly same as Freeman's model in (3.5).

Our discussion will focus on how to fix the parameters y , z , α , and β . In order to achieve this, we first introduce a similar mathematical model in which all parameters can be found, which is then combined with (3.23) to find its solutions.

A 3 by 3 Hermitian matrix, such as our measured covariance matrix, can be expressed by three real eigenvalues and three orthonormal eigenvectors as

$$C'_m = \sum_{i=1}^3 \lambda_i \bar{\mathbf{e}}_i \cdot \bar{\mathbf{e}}_i^{*T} . \quad (3.25)$$

These eigenvectors can be freely chosen as long as they are orthonormal. In [28], van Zyl pointed out that the following is a possible decomposition under the scattering reflection symmetry. First, we change the form of the measured covariance matrix to

$$C'_m = C \begin{pmatrix} 1 & 0 & \rho \\ 0 & \eta & 0 \\ \rho^* & 0 & \zeta \end{pmatrix} \quad (3.26)$$

where

$$\begin{aligned} C &= \sigma'_{hhhh} \\ \eta &= 2\sigma'_{hvhv} / \sigma'_{hhhh} \\ \zeta &= \sigma'_{vvvv} / \sigma'_{hhhh} \\ \rho &= \sigma'_{hvv} \end{aligned} . \quad (3.27)$$

The measured covariance matrix is then decomposed as

$$C'_m = \Lambda_1 \begin{pmatrix} 1 & 0 & x_1 \\ 0 & 0 & 0 \\ x_1^* & 0 & |x_1|^2 \end{pmatrix} + \Lambda_2 \begin{pmatrix} 1 & 0 & x_2 \\ 0 & 0 & 0 \\ x_2^* & 0 & |x_2|^2 \end{pmatrix} + \Lambda_3 \begin{pmatrix} 0 & 0 & 0 \\ 0 & 1 & 0 \\ 0 & 0 & 0 \end{pmatrix} \quad (3.28)$$

where,

$$\begin{aligned} \Lambda_1 &= \frac{C}{2} \left\{ \zeta + 1 + \sqrt{\Delta} \right\} \left\{ \frac{(\zeta - 1 + \sqrt{\Delta})^2}{(\zeta - 1 + \sqrt{\Delta})^2 + 4|\rho|^2} \right\} \left| \frac{2\rho}{\zeta - 1 + \sqrt{\Delta}} \right|^2 \\ \Lambda_2 &= \frac{C}{2} \left\{ \zeta + 1 - \sqrt{\Delta} \right\} \left\{ \frac{(\zeta - 1 - \sqrt{\Delta})^2}{(\zeta - 1 - \sqrt{\Delta})^2 + 4|\rho|^2} \right\} \left| \frac{2\rho}{\zeta - 1 - \sqrt{\Delta}} \right|^2 \\ \Lambda_3 &= C\eta \end{aligned} \quad (3.29)$$

and,

$$\begin{aligned}
 x_1 &= \left(\frac{\zeta - 1 + \sqrt{\Delta}}{2\rho} \right)^* \\
 x_2 &= \left(\frac{\zeta - 1 - \sqrt{\Delta}}{2\rho} \right)^* \\
 \Delta &= (\zeta - 1)^2 + 4|\rho|^2
 \end{aligned} \tag{3.30}$$

Note that

$$x_1 \cdot x_2^* = -1 . \tag{3.31}$$

So far the model has been derived purely mathematically, i.e., no physical constraints exist. Figure 3.7 shows the geometrical relationship between x_1 and x_2 on unit circle. Equation (3.31) tells us that the complex numbers x_1 and x_2 are on the straight line through the origin. If one is in the left half plane, the other is in the right half plane. Also note that if one is inside the unit circle, the other has to be outside the unit circle.

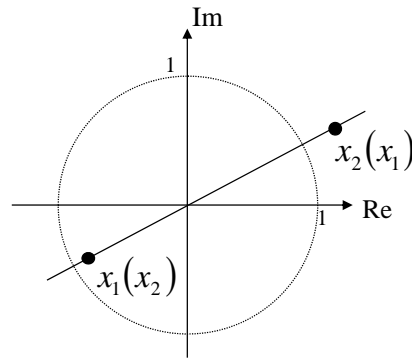


Figure 3.7: Geometrical property of x_1 and x_2 on unit circle. The property in equation (3.31) determines this relationship.

The physical model (3.23) and mathematical model (3.28) becomes

$$\begin{aligned}
C'_m &= y \begin{pmatrix} 1 & 0 & \alpha \\ 0 & 0 & 0 \\ \alpha^* & 0 & |\alpha|^2 \end{pmatrix} + z \begin{pmatrix} 1 & 0 & \beta \\ 0 & 0 & 0 \\ \beta^* & 0 & |\beta|^2 \end{pmatrix} + C_{other} \\
C'_m &= \Lambda_1 \begin{pmatrix} 1 & 0 & x_1 \\ 0 & 0 & 0 \\ x_1^* & 0 & |x_1|^2 \end{pmatrix} + \Lambda_2 \begin{pmatrix} 1 & 0 & x_2 \\ 0 & 0 & 0 \\ x_2^* & 0 & |x_2|^2 \end{pmatrix} + \Lambda_3 \begin{pmatrix} 0 & 0 & 0 \\ 0 & 1 & 0 \\ 0 & 0 & 0 \end{pmatrix}.
\end{aligned} \tag{3.32}$$

Comparing these two equations, one can easily find the following relations by ignoring the third term of both equations.

$$\begin{aligned}
\alpha &= x_1 \\
\beta &= x_2 \\
y &= \Lambda_1 \\
z &= \Lambda_2
\end{aligned} \tag{3.33}$$

If the real part of x_1 is positive, x_1 and x_2 can be interchanged so that α is always in the left half plane in Figure 3.7. This corresponds to Freeman's decomposition criterion which states that the scattering is double bounce if the real part of σ'_{hhvv} is negative. However, his decomposition model sets a fixed number to α or β depending on the sign of σ'_{hhvv} . This operation provides clear contrast between double bounce and ground scattering. On the other hand, our approach is expected to have more natural discrimination between double bounce scattering and ground scattering since it allows both parameters to be complex numbers. In this thesis, we call the decomposition technique described above Non-Negative Eigenvalue Decomposition (NNED).

Figure 3.8 shows the decomposition results using NNED where green, red, and blue are assigned to volume, double bounce, and ground scattering as in Figure 3.3. Note that the volume scattering term here is the same as Freeman's technique in (3.2), hence

$$C_v = \begin{pmatrix} p & 0 & s \\ 0 & 2q & 0 \\ s^* & 0 & r \end{pmatrix}, \quad p = r = 1, \quad q = s = 1/3. \quad (3.34)$$

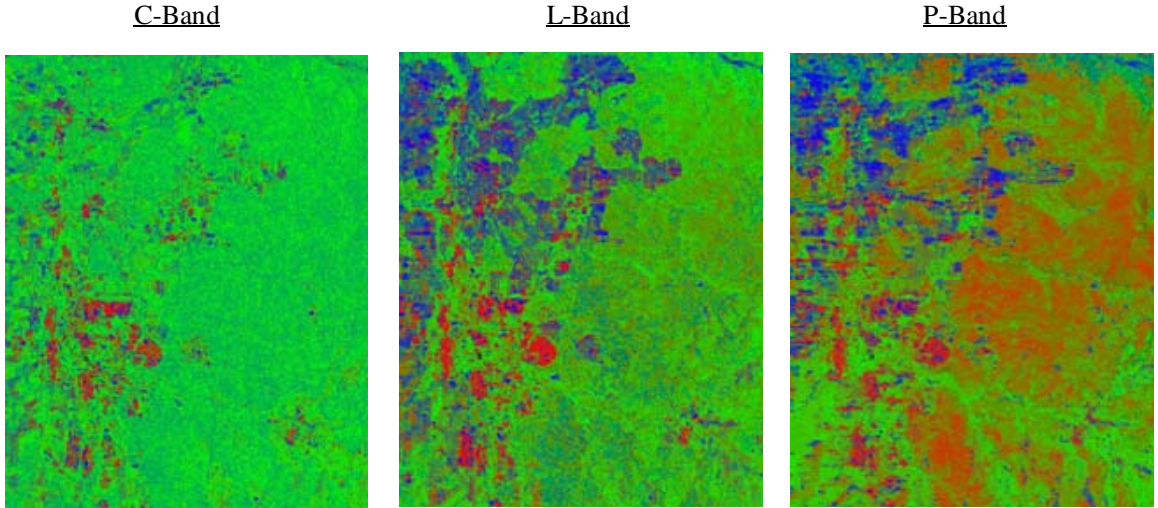


Figure 3.8: Decomposition result using NNED are shown. The original images with three different frequencies are the same as in Figure 3.2. Color assignments are the same as Figure 3.2 as well.

You can easily see that the volume component is significantly suppressed. Instead, surface scattering and double bounce scattering are emphasized in the L-band and P-band images, respectively. We can see some faint red in the middle of the Black Forest in the L-band image. The agricultural and urban areas do not show a difference between the two techniques. Also the P-band image still shows the volume scattering contribution around the river half way down the image. In order to see more clearly the suppression of the volume component, we calculate the following index for each pixel.

$$\frac{(x_{freeman} - x_{NNED})}{x_{freeman}} \times 100[\%] \quad (3.35)$$

This index indicates how much the volume scattering power decreased under our decomposition technique. In other words, the figure shows how much the volume power is overestimated by Freeman's decomposition. The value of this index applied to the L-band image is shown in Figure 3.9.

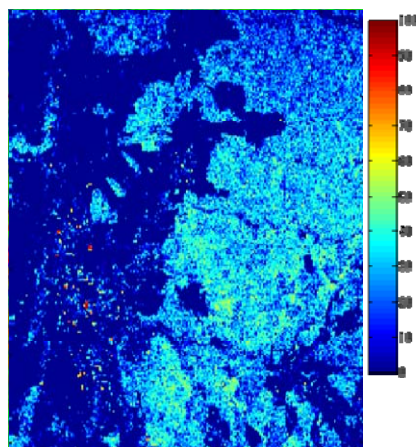


Figure 3.9: Difference between the Freeman decomposition and NNED at L-band. Most of the forested area shows higher values due to overestimation of Freeman's decomposition.

The entire forested area shows about a 30 to 40% drop in volume scattering power but this is not pronounced in agricultural area. Note that the map shows good correlation with Figure 3.3 as we expected.

We have introduced two decomposition techniques: Freeman decomposition and non-negative eigenvalue decomposition. As shown, both techniques use a fixed volume scattering term given by (3.5) for Freeman's decomposition and by (3.34) for NNED. As described in the next chapter, both models assume a uniform distribution of thin cylinders, as in the canopy of a rainforest. Clearly, this limits their applicability to scenes with a specific type of vegetation. In addition, these models show how to find the maximum value of x but this value is not necessarily optimal. It is not easy to choose the optimal value of x from our limited information. However, we have shown a better way to estimate x using a

generalized volume component. In the next two chapters, we generalize our volume scattering component first, and then suggest an adaptive decomposition technique using this generalized volume scattering component.

3.4 Generalization of the Volume Scattering Term

In the previous chapter, we used the following covariance matrix for volume scattering.

$$C_v = \begin{pmatrix} 1 & 0 & 1/3 \\ 0 & 2/3 & 0 \\ 1/3 & 0 & 1 \end{pmatrix} \quad (3.36)$$

First, we discuss how to obtain this expression as a volume term. Suppose we have an infinitely thin cylinder on a polarization plane, H_0 - V_0 , as in Figure 3.10.

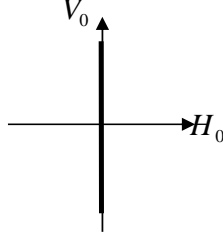


Figure 3.10: An infinitely thin cylinder on H_0 - V_0 plane. The cylinder follows the vertical axis.

Note that the cylinder exists along the vertical polarization axis, V_0 . The scattering matrix and backscatter cross section of this cylinder are calculated as

$$S_{dipole} = \begin{pmatrix} 0 & 0 \\ 0 & 1 \end{pmatrix} \quad \rightarrow \quad \sigma^0 = \left| \vec{p}_0^{recT} S_{dipole} \vec{p}_0^{tr} \right|^2 \quad (3.37)$$

where \bar{p}_0^{tr} and \bar{p}_0^{rec} are normalized antenna effective length for transmitting and receiving respectively. The polarization plane can then be rotated as in Figure 3.10.

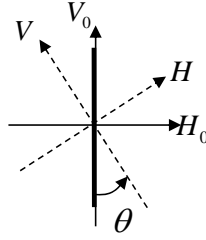


Figure 3.11: An infinitely thin cylinder on rotated H_0 - V_0 plane

The antenna effective lengths are rewritten as

$$\bar{p}^i = \begin{pmatrix} \cos \theta & \sin \theta \\ -\sin \theta & \cos \theta \end{pmatrix} \bar{p}_0^i \quad i = tr, rec . \quad (3.38)$$

One can plug this into (3.37).

$$\sigma^0 = \left| \bar{p}^{rec T} \begin{pmatrix} \cos \theta & \sin \theta \\ -\sin \theta & \cos \theta \end{pmatrix} S_{dipole} \begin{pmatrix} \cos \theta & \sin \theta \\ -\sin \theta & \cos \theta \end{pmatrix}^{-1} \bar{p}^{tr} \right|^2 \quad (3.39)$$

Of course, the situation in Figure 3.11 is exactly same as the case of an oriented cylinder on a fixed polarization plane, H - V , as shown in Figure 3.12.

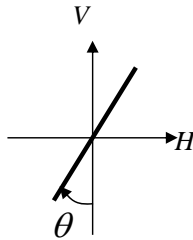


Figure 3.12: An oriented thin cylinder on a fixed H - V plane

We obtain a scattering matrix for an oriented infinitely thin cylinder as

$$S(\theta) = \begin{pmatrix} \cos \theta & \sin \theta \\ -\sin \theta & \cos \theta \end{pmatrix} S_{dipole} \begin{pmatrix} \cos \theta & \sin \theta \\ -\sin \theta & \cos \theta \end{pmatrix}^{-1} = \begin{pmatrix} \sin^2 \theta & \sin \theta \cos \theta \\ \sin \theta \cos \theta & \cos^2 \theta \end{pmatrix}. \quad (3.40)$$

The covariance matrix follows immediately

$$C_0(\theta) = \begin{pmatrix} \sin^4 \theta & \sqrt{2} \sin^3 \theta \cos \theta & \sin^2 \theta \cos^2 \theta \\ \sqrt{2} \sin^3 \theta \cos \theta & 2 \sin^2 \theta \cos^2 \theta & \sqrt{2} \sin \theta \cos^3 \theta \\ \sin^2 \theta \cos^2 \theta & \sqrt{2} \sin \theta \cos^3 \theta & \cos^4 \theta \end{pmatrix}. \quad (3.41)$$

This matrix expresses scattering from a single oriented thin cylinder. However, scattering from a natural volume layer should be close to that from many randomly oriented cylinders.

This covariance matrix is expressed as follows

$$C = \int_0^{2\pi} C_0 p(\theta) d\theta \quad (3.42)$$

where $p(\theta)$ is a probability density function (pdf) in terms of orientation angle. Note that the matrix has a slightly different form from the one used in the discrete scatterer model in (4.8) in the next chapter because of the difference in angle definitions.

Three specific cases of these equations are shown as follows. The first case is to derive a covariance matrix for uniformly distributed cylinders.

$$p_{uniform}(\theta) = \frac{1}{2\pi} \quad (3.43)$$

Figure 3.13 shows an illustration of uniformly distributed cylinders and a plot of the pdf in terms of orientation angle.

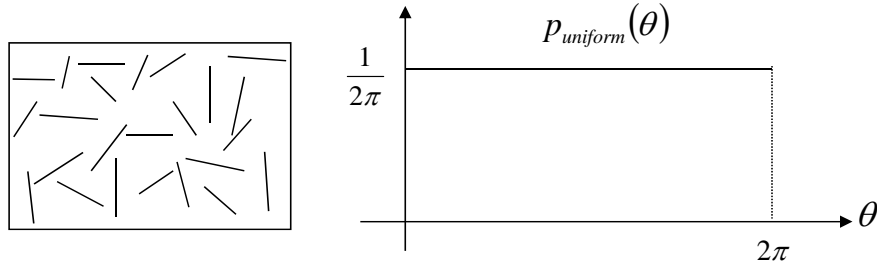


Figure 3.13: Uniform distribution of oriented thin cylinders

The covariance matrix becomes

$$C_{uniform} = \int_0^{2\pi} C_0 p_{uniform}(\theta) d\theta = \frac{1}{8} \begin{pmatrix} 3 & 0 & 1 \\ 0 & 2 & 0 \\ 1 & 0 & 3 \end{pmatrix} = \frac{3}{8} \begin{pmatrix} 1 & 0 & 1/3 \\ 0 & 2/3 & 0 \\ 1/3 & 0 & 1 \end{pmatrix}. \quad (3.44)$$

The portion inside 3 by 3 matrix of (3.44) is exactly same as that of (3.5) and (3.4). This means that we have implicitly assumed that volume layer consists of uniformly distributed oriented cylinders. This assumption may work well for complicated vegetation as in a rainforest.

The second case is a cloud of thin cylinders distributed with a cosine squared distribution. The fact that cosine squared function has two peaks with π radian interval leads us to apply it to as a pdf. This pdf is applicable to any symmetrical shape such as a cylinder because if you have a peak probability at a certain angle, another peak probability exists at π radians from the first angle. The pdf is given by

$$p_{\cos_sq}(\theta) = \frac{1}{\pi} \cos^2 \theta. \quad (3.45)$$

The illustration and plot of the pdf is in Figure 3.14.

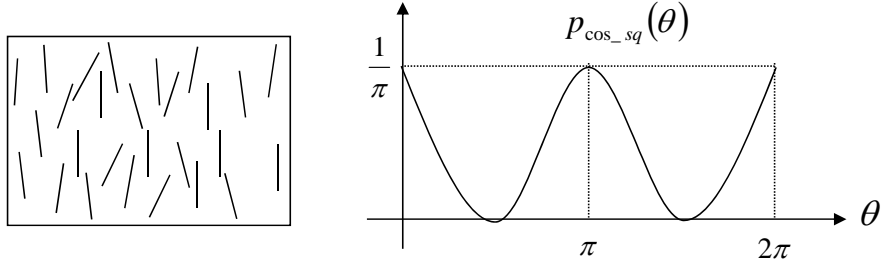


Figure 3.14: Cosine squared distribution of a cloud of oriented thin cylinders

In this case, the covariance matrix becomes

$$C_{\cos_sq} = \int_0^{2\pi} C_0 p_{\cos_sq}(\theta) d\theta = \frac{1}{8} \begin{pmatrix} 1 & 0 & 1 \\ 0 & 2 & 0 \\ 1 & 0 & 5 \end{pmatrix}. \quad (3.46)$$

This matrix shows that the backscatter cross section of the vertical co-polarization term is five times larger than the horizontal co-polarization term. This is reasonable because the cosine squared distribution assigns more probability to vertical orientation than to horizontal orientation.

If one assumes that uniform distribution is an extreme case of volume scattering, there should also be an extremely narrow distribution. The pdf should be a delta function:

$$p_{\delta}(\theta) = \frac{1}{2} \delta(\theta - m\pi) \quad m = 0, 1. \quad (3.47)$$

Figure 3.15 shows its illustration and a plot of the pdf.

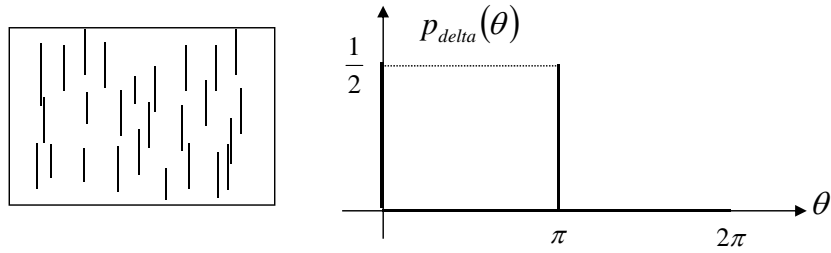


Figure 3.15: Delta function distribution of a cloud of oriented thin cylinders

The covariance matrix is

$$C_{delta} = \int_0^{2\pi} C_0 p_{delta}(\theta) d\theta = \begin{pmatrix} 0 & 0 & 0 \\ 0 & 0 & 0 \\ 0 & 0 & 1 \end{pmatrix} \quad (3.48)$$

Since the pdf assigns the probability only to the vertical orientation angle, the matrix shows that the backscattering power exists only in vertical co-polarization term.

These examples provide us two extreme cases and one intermediate case, which are illustrated in Figure 3.16.

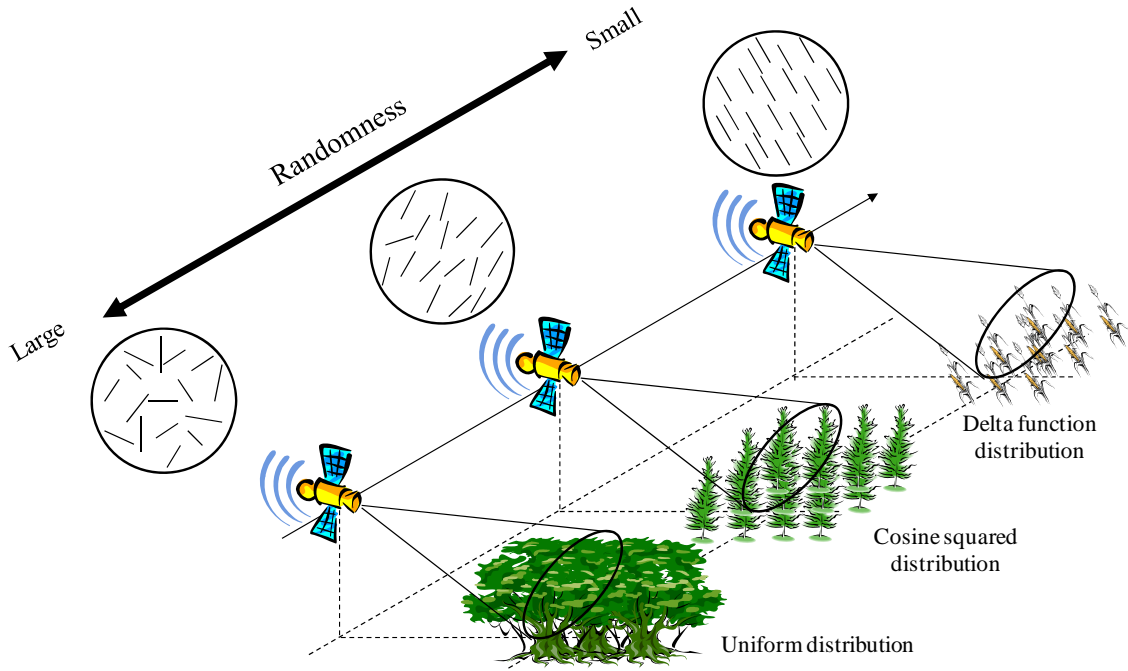


Figure 3.16: Illustration of various randomness of vegetated area. Larger randomness, medium randomness, and smaller randomness correspond to terrain covered by rainforest, coniferous forest, and cornfield vegetation types, respectively.

One might think that an n -th power cosine squared function could be used to model any type of deviation of randomly oriented cylinders between the extreme cases of a delta function and a uniform distribution. In this thesis, we use an n -th power cosine squared distribution function (pdf) for p as shown in Figure 3.16.

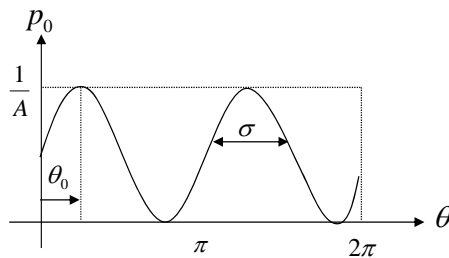


Figure 3.17: n -th power cosine squared probability density function

$$\begin{aligned}
 p_0(\theta, n) &= \frac{1}{A} \{\cos^2(\theta - \theta_0)\}^n \\
 A &= \int_0^{2\pi} (\cos^2 \theta)^n d\theta
 \end{aligned}
 \tag{3.49}$$

This pdf has two peaks separated by a π radian interval as mentioned before. Also we can easily specify any degree of randomness by changing n . For example, if one chooses $n=0$, the pdf becomes uniform distribution which has same probability for all angles. If one chooses infinitely large n , the pdf gets close to delta function with two peaks. Therefore the n -th power cosine squared function allows us to model the natural statistical properties of a cloud of cylinders. Note that the pdf can be applied not only to cylinders but also to any symmetric scatterer.

It is inconvenient to directly use n to specify the degree of randomness, because the range of the parameter is not finite. Therefore we replace it with a parameter having a limited range.

Since the pdf has two peaks, the standard deviation of the pdf should be calculated from $-\pi/2$ to $\pi/2$ radian with zero mean, $\theta_0=0$, as in Figure 3.18, to correctly measure the width of each peak.

$$\begin{aligned}
 p'_0(\theta, n) &= \frac{1}{A'} (\cos^2 \theta)^n \\
 A' &= \int_{-\pi/2}^{\pi/2} (\cos^2 \theta)^n d\theta
 \end{aligned}
 \tag{3.50}$$

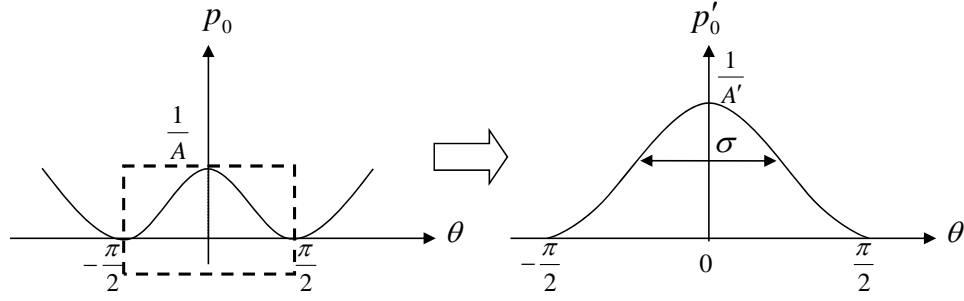


Figure 3.18: Definition of standard deviation of n-th power cosine squared probability density function

Then the standard deviation is calculated as

$$\sigma(n) = \sqrt{\int_{-\pi/2}^{\pi/2} \theta^2 p'_0(\theta, n) d\theta}. \quad (3.51)$$

Using the definition, standard deviations of uniform and delta function are easily shown to be

$$\begin{aligned} \sigma_{\text{delta}} &= \sqrt{\int_{-\pi/2}^{\pi/2} \theta^2 \delta(\theta) d\theta} = 0 \\ \sigma_{\text{uniform}} &= \sqrt{\frac{1}{\pi} \int_{-\pi/2}^{\pi/2} \theta^2 d\theta} = \sqrt{\frac{\pi^2}{12}} \approx 0.91 \end{aligned} \quad (3.52)$$

We can also numerically calculate equation (3.49) for any n between 0 and infinity as plotted in Figure 3.19.

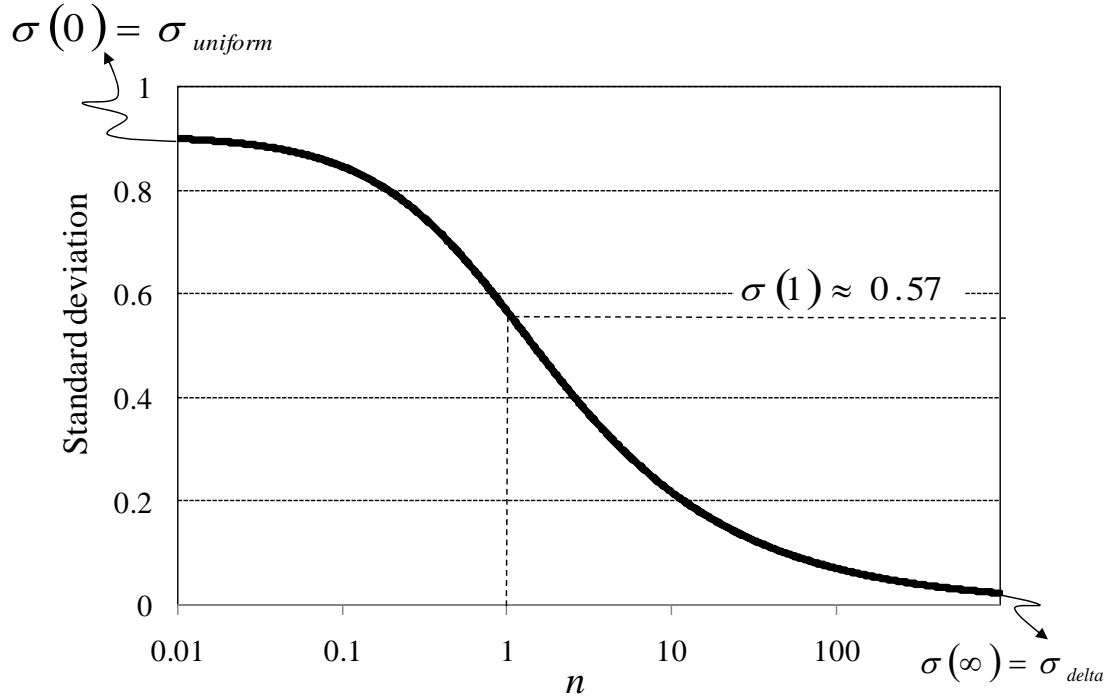


Figure 3.19: Standard deviation of n -th power cosine squared distribution in (3.51) in terms of index number, n . The standard deviation is uniquely related to the index. Also the standard deviation has a limited range between 0 and 0.91, while the index can be infinitely large number.

It is obvious that the standard deviation by equation (3.49) continuously and uniquely covers from delta function distribution to uniform distribution. Therefore the index number, n , can be completely replaced by the standard deviation of cosine squared distribution. The advantage to using this is that the parameter has limited range from 0 to 0.91 instead of that from 0 to infinity.

We shall use the standard deviation to specify the randomness of the n -th power cosine squared pdf in the rest of this thesis. Even though this does not change the mathematical property of the pdf at all, the idea plays an important role in deriving a generalized covariance matrix, which is an essential tool to adaptively decompose scattering from

vegetated terrain. We shall use the word “randomness” rather than “standard deviation” because the former word is more appropriate to express the statistical property of physical vegetation.

Starting with the covariance matrices of a cloud of dipoles for three distributions: uniform, cosine squared, and delta-function distributions, we will now attempt to find a general expression to cover any type of vegetation. To achieve this, we first modify our covariance matrices for the three cases by introducing the concept of mean orientation angle. We then try to find a hidden pattern between these covariance matrices, and extend it to cover any type of randomness and mean orientation angles.

Let us rewrite three distributions (uniform, n-th power cosine squared (3.50), and delta function distributions) with a specific mean orientation angle, ϕ .

$$\begin{aligned}
 p_{uniform}(\theta) &= \frac{1}{2\pi} \\
 p_{cos_sqn}(\theta, \phi, n) &= \frac{1}{A} \left\{ \cos^2(\theta - \phi) \right\}^n, \quad A = \int_{-\frac{\pi}{2}}^{\frac{\pi}{2}} (\cos^2 \theta)^n d\theta \\
 p_{delta}(\theta, \phi) &= \frac{1}{2} \delta(\theta - (\phi + m\pi)) \quad m = 0,1
 \end{aligned} \tag{3.53}$$

Using these pdfs in (3.53), each covariance matrix previously shown in (3.44), (3.46), and (3.48) can be rewritten as follows. First, the case of uniform distribution in (3.44) becomes

$$C(\sigma_{uniform}) = \int_0^{2\pi} C_0 p_{uniform}(\theta) d\theta = \frac{1}{8} \begin{bmatrix} 3 & 0 & 1 \\ 0 & 2 & 0 \\ 1 & 0 & 3 \end{bmatrix} \tag{3.54}$$

where $\sigma_{uniform}$ means uniform distribution and comes from (3.52). Obviously, this is exactly same as (3.44) since the uniform distribution does not have any specific mean orientation angle. Next, we derive the case of the cosine squared distribution. Note that this corresponds to a specific case of the second equation in (3.53) with $n=1$. So the pdf function has the form

$$p_{\cos_sqn}(\theta, \phi, 1) = \frac{1}{\pi} \cos^2(\theta - \phi) . \quad (3.55)$$

The covariance matrix then becomes

$$\begin{aligned} C(\sigma_{\cos_sqn}(n=1)) &= \int_0^{2\pi} C_0 p_{\cos_sqn} d\theta \\ &= \int_0^{2\pi} \begin{pmatrix} \sin^4 \theta & \sqrt{2} \sin^3 \theta \cos \theta & \sin^2 \theta \cos^2 \theta \\ \sqrt{2} \sin^3 \theta \cos \theta & 2 \sin^2 \theta \cos^2 \theta & \sqrt{2} \sin \theta \cos^3 \theta \\ \sin^2 \theta \cos^2 \theta & \sqrt{2} \sin \theta \cos^3 \theta & \cos^4 \theta \end{pmatrix} \frac{1}{\pi} \cos^2(\theta - \phi) d\theta \\ &= \frac{1}{8} \begin{pmatrix} 5 - 4 \cos^2 \phi & 2\sqrt{2} \sin \phi \cos \phi & 1 \\ 2\sqrt{2} \sin \phi \cos \phi & 2 & 2\sqrt{2} \sin \phi \cos \phi \\ 1 & 2\sqrt{2} \sin \phi \cos \phi & 1 + 4 \cos^2 \phi \end{pmatrix} \end{aligned} \quad (3.56)$$

where $\sigma_{\cos_sqn}(n=1)$ means standard deviations of n-th power cosine squared distribution with n=1. One can easily verify the matrix with two special cases: horizontal orientation angle and vertical orientation angle.

$$\begin{aligned} \phi = 0 \text{ deg} \quad C(\sigma_{\cos_sqn}(n=1)) &= \frac{1}{8} \begin{pmatrix} 1 & 0 & 1 \\ 0 & 2 & 0 \\ 1 & 0 & 5 \end{pmatrix} \\ \phi = 90 \text{ deg} \quad C(\sigma_{\cos_sqn}(n=1)) &= \frac{1}{8} \begin{pmatrix} 5 & 0 & 1 \\ 0 & 2 & 0 \\ 1 & 0 & 1 \end{pmatrix} \end{aligned} \quad (3.57)$$

As we expected, each result shows a biased weight depending on a specified mean orientation angle. Note that the first one is exactly same as (3.46). Finally the case of delta function distribution is shown.

$$\begin{aligned}
C(\sigma_{\delta}) &= \int_0^{2\pi} C_0 p_{\delta} d\theta \\
&= \int_0^{2\pi} \begin{pmatrix} \sin^4 \theta & \sqrt{2} \sin^3 \theta \cos \theta & \sin^2 \theta \cos^2 \theta \\ \sqrt{2} \sin^3 \theta \cos \theta & 2 \sin^2 \theta \cos^2 \theta & \sqrt{2} \sin \theta \cos^3 \theta \\ \sin^2 \theta \cos^2 \theta & \sqrt{2} \sin \theta \cos^3 \theta & \cos^4 \theta \end{pmatrix} \frac{1}{2} \delta(\theta - (\phi + m\pi)) d\theta \\
&= \begin{pmatrix} \sin^4 \phi & \sqrt{2} \sin^3 \phi \cos \phi & \sin^2 \phi \cos^2 \phi \\ \sqrt{2} \sin^3 \phi \cos \phi & 2 \sin^2 \phi \cos^2 \phi & \sqrt{2} \sin \phi \cos^3 \phi \\ \sin^2 \phi \cos^2 \phi & \sqrt{2} \sin \phi \cos^3 \phi & \cos^4 \phi \end{pmatrix}
\end{aligned} \tag{3.58}$$

where σ_{δ} represents the standard deviations of the delta function distribution. We can verify this equation with the same special cases as for the cosine squared distribution in (3.57).

$$\begin{aligned}
\phi = 0 \text{ deg.} \quad C(\sigma_{\delta}) &= \begin{pmatrix} 0 & 0 & 0 \\ 0 & 0 & 0 \\ 0 & 0 & 1 \end{pmatrix} \\
\phi = 90 \text{ deg.} \quad C(\sigma_{\delta}) &= \begin{pmatrix} 1 & 0 & 0 \\ 0 & 0 & 0 \\ 0 & 0 & 0 \end{pmatrix}
\end{aligned} \tag{3.59}$$

Both cases are physically acceptable.

In order to find a hidden relationship between these three covariance matrices, (3.54), (3.56), and (3.58), they are summarized here after applying some trigonometric simplifications.

$$\begin{aligned}
C(\sigma_{uniform}) &= \frac{1}{8} \begin{pmatrix} 3 & 0 & 1 \\ 0 & 2 & 0 \\ 1 & 0 & 3 \end{pmatrix} \\
C(\sigma_{\cos_sqn}(n=1)) &= \frac{1}{8} \begin{pmatrix} 3 & 0 & 1 \\ 0 & 2 & 0 \\ 1 & 0 & 3 \end{pmatrix} + \frac{1}{8} \begin{pmatrix} -2\cos 2\phi & \sqrt{2}\sin 2\phi & 0 \\ \sqrt{2}\sin 2\phi & 0 & \sqrt{2}\sin 2\phi \\ 0 & \sqrt{2}\sin 2\phi & 2\cos 2\phi \end{pmatrix} \\
C(\sigma_{delta}) &= \frac{1}{8} \begin{pmatrix} 3 & 0 & 1 \\ 0 & 2 & 0 \\ 1 & 0 & 3 \end{pmatrix} + 2 \cdot \frac{1}{8} \begin{pmatrix} -2\cos 2\phi & \sqrt{2}\sin 2\phi & 0 \\ \sqrt{2}\sin 2\phi & 0 & \sqrt{2}\sin 2\phi \\ 0 & \sqrt{2}\sin 2\phi & 2\cos 2\phi \end{pmatrix} \\
&\quad + \frac{1}{8} \begin{pmatrix} \cos 4\phi & -\sqrt{2}\sin 4\phi & -\cos 4\phi \\ -\sqrt{2}\sin 4\phi & -2\cos 4\phi & \sqrt{2}\sin 4\phi \\ -\cos 4\phi & \sqrt{2}\sin 4\phi & \cos 4\phi \end{pmatrix}
\end{aligned} \tag{3.59}$$

By defining,

$$\begin{aligned}
C_\alpha &= \frac{1}{8} \begin{pmatrix} 3 & 0 & 1 \\ 0 & 2 & 0 \\ 1 & 0 & 3 \end{pmatrix} \\
C_\beta &= \frac{1}{8} \begin{pmatrix} -2\cos 2\phi & \sqrt{2}\sin 2\phi & 0 \\ \sqrt{2}\sin 2\phi & 0 & \sqrt{2}\sin 2\phi \\ 0 & \sqrt{2}\sin 2\phi & 2\cos 2\phi \end{pmatrix} \\
C_\gamma &= \frac{1}{8} \begin{pmatrix} \cos 4\phi & -\sqrt{2}\sin 4\phi & -\cos 4\phi \\ -\sqrt{2}\sin 4\phi & -2\cos 4\phi & \sqrt{2}\sin 4\phi \\ -\cos 4\phi & \sqrt{2}\sin 4\phi & \cos 4\phi \end{pmatrix}
\end{aligned} \tag{3.60}$$

the three covariance matrices can be compactly rewritten as

$$\begin{aligned}
C(\sigma_{uniform}) &= C_\alpha \\
C(\sigma_{\cos_sqn}(n=1)) &= C_\alpha + C_\beta \ . \\
C(\sigma_{delta}) &= C_\alpha + 2C_\beta + C_\gamma
\end{aligned} \tag{3.61}$$

Remember that the first (uniform distribution) and the third (delta function distribution) equations are two extreme cases, and the second (cosine squared distribution) is one specific point between those two extreme cases, as in Figure 3.15. These equations suggest to us that it may be possible to express any type of distribution using only the third equation. It may be easier to understand this idea by first considering the delta function distribution, which corresponds to zero randomness. The second and third components of the delta function distribution decrease gradually as the randomness increases. When the randomness becomes equivalent to cosine squared distribution, the covariance matrix is the same as the second equation. The third component is gone and the second component is just half of that in the third equation. As the randomness continues to increase, the second component decreases further until finally it is also gone, which then corresponds to the uniform distribution as given by the first equation. Note that the component of uniform distribution, C_α , is common to all cases. We have already shown that the randomness of the two extreme cases, the uniform distribution and delta function distribution, can be expressed as special cases of the cosine squared distribution as in (3.18).

$$\begin{aligned}\sigma(n = \infty) &= \sigma_{\text{delta}} \\ \sigma(n = 0) &= \sigma_{\text{uniform}}\end{aligned}\quad (3.62)$$

where we indicate the randomness by $\sigma(n)$. (3.61) is then rewritten as

$$\begin{aligned}C(\sigma(n = \infty)) &= C_\alpha \\ C(\sigma(n = 1)) &= C_\alpha + C_\beta \\ C(\sigma(n = 0)) &= C_\alpha + 2C_\beta + C_\gamma\end{aligned}\quad (3.63)$$

The idea described above is mathematically represented by

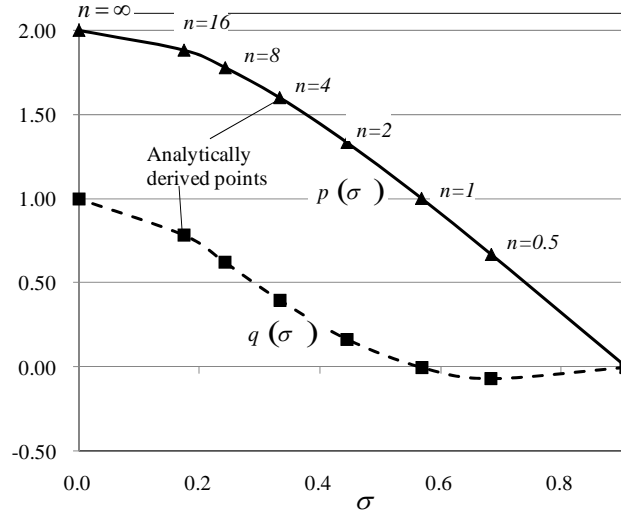
$$C(\sigma) = C_\alpha + p(\sigma)C_\beta + q(\sigma)C_\gamma \quad (3.64)$$

where $p(\sigma)$ and $q(\sigma)$ are some functions of the randomness. The function p has a value between 0 and 2, and the function q has a value between 0 and 1. Next we try to identify those functions. Some values of $p(\sigma)$ and $q(\sigma)$ are shown in Table 3.1.

Table 3.1: Standard deviation, $p(\sigma)$, and $q(\sigma)$ in (3.64) for various n 's

n	0	0.5	1	2	4	8	16	<i>infinity</i>
σ	0.9069	0.6837	0.5679	0.4444	0.3327	0.2424	0.1741	0.0000
$p(\sigma)$	0.0000	0.6667	1.0000	1.3333	1.6000	1.7778	1.8824	2.0000
$q(\sigma)$	0.0000	-0.0667	0.0000	0.1667	0.4000	0.6222	0.7843	1.0000

Red points of the Figure 3.20 show the plots of samples in Table 3.1. Since they vary smoothly with respect to randomness, we can fit polynomials to these calculated points.

**Figure 3.20:** Plot of two coefficients in (3.64), $p(\sigma)$ (blue line) and $q(\sigma)$ (green line).

These curves are obtained by fitting analytically calculated points which are displayed by red asterisks.

The following are 6th order polynomials which provide accuracy around 1e-13 on given n 's.

$$\begin{aligned}
 p(\sigma) &= 2.0806\sigma^6 - 6.3350\sigma^5 + 6.3864\sigma^4 \\
 &\quad - 0.4431\sigma^3 - 3.9638\sigma^2 - 0.0008\sigma + 2.000 \\
 q(\sigma) &= 9.0166\sigma^6 - 18.7790\sigma^5 + 4.9590\sigma^4 \\
 &\quad + 14.5629\sigma^3 - 10.8034\sigma^2 + 0.1902\sigma + 1.000
 \end{aligned} \tag{3.65}$$

Figure 3.20 shows a plot of the fitted curves with given points.

Using these two fitted curves, (3.64) can be used to model any type of vegetation in between the uniform and delta function distribution with any mean orientation angle. It can easily be shown that the following more organized expressions are exactly same as (3.64).

$$C_{dipole}(\sigma) = (\vec{\alpha} + p\vec{\beta} + q\vec{\gamma}) \cdot \vec{V} \quad (3.66)$$

where

$$\begin{aligned} \vec{\alpha} &= \frac{1}{8}(3 \ 1 \ 2 \ 0 \ 0 \ 0)^T \\ \vec{\beta} &= \frac{1}{8}(0 \ 0 \ 0 \ -2\cos 2\phi \ \sqrt{2}\sin 2\phi \ \sqrt{2}\sin 2\phi)^T \\ \vec{\gamma} &= \frac{1}{8}(\cos 4\phi \ -\cos 4\phi \ -2\cos 4\phi \ 0 \ -\sqrt{2}\sin 4\phi \ \sqrt{2}\sin 4\phi)^T \end{aligned} \quad (3.67)$$

and

$$\vec{V} = \left(\begin{pmatrix} 1 & 0 & 0 \\ 0 & 0 & 0 \\ 0 & 0 & 1 \end{pmatrix} \begin{pmatrix} 0 & 0 & 1 \\ 0 & 0 & 0 \\ 1 & 0 & 0 \end{pmatrix} \begin{pmatrix} 0 & 0 & 0 \\ 0 & 1 & 0 \\ 0 & 0 & 0 \end{pmatrix} \begin{pmatrix} 1 & 0 & 0 \\ 0 & 0 & 0 \\ 0 & 0 & -1 \end{pmatrix} \begin{pmatrix} 0 & 1 & 0 \\ 1 & 0 & 0 \\ 0 & 0 & 0 \end{pmatrix} \begin{pmatrix} 0 & 0 & 0 \\ 0 & 0 & 1 \\ 0 & 1 & 0 \end{pmatrix} \right)^T \quad (3.68)$$

where T means transpose. Since the covariance matrix was derived for thin cylinders (dipoles), it is explicitly named as so. Note that each element of \vec{V} is orthogonal each other.

We have developed an expression for a cloud of thin cylinders with various randomness and mean orientation angles. The expression will now be generalized to any elementary scatterer.

Our derivation of (3.66) starts from the scattering matrix of dipole, given in (3.69)

$$S_{dipole} = \begin{pmatrix} 0 & 0 \\ 0 & 1 \end{pmatrix}. \quad (3.69)$$

There are several more known scattering matrices as in Figure 3.21 [17].

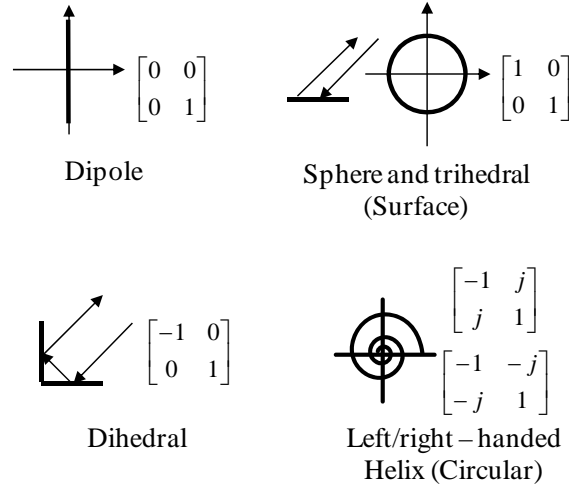


Figure 3.21: Scattering matrices for various elemental scatterers: Dipole (left and top); sphere, trihedral, or odd number of scattering (right and top); dihedral or even number of scattering (right and bottom); and circular (left and bottom) are displayed [17].

In order to encompass any type of elementally scatterers, we try to replace the scattering matrix (3.69) with a general scattering matrix

$$S = \begin{pmatrix} a & c \\ c & b \end{pmatrix} \quad (3.70)$$

where a , b , and c are any complex number. The only limitation is that the matrix still obeys the reciprocity theorem in which $S_{hv} = S_{vh}$. Starting with this generalized covariance matrix one can derive an equivalent expression to (3.70), which has the same basic form as (3.66),

$$C(\sigma) = (\bar{\alpha} + p\bar{\beta} + q\bar{\gamma}) \cdot \bar{V} \quad (3.71)$$

where p and q are exactly same as (3.65). However, (3.67) is modified as

$$\begin{aligned}
\vec{\alpha} &= \frac{1}{8} \{ K_{+ab} \vec{\alpha}_1 + L_{\text{Re}ab} \vec{\alpha}_2 + 4K_c \vec{\alpha}_3 + 2(L_{\text{Im}ac} - L_{\text{Im}bc}) \vec{\alpha}_4 \} \\
\vec{\beta} &= \frac{1}{8} \{ K_{-ab} \vec{\beta}_1 + L_{\text{Im}ab} \vec{\beta}_2 + 2(L_{\text{Re}ac} + L_{\text{Re}bc}) \vec{\beta}_3 \\
&\quad - 2(L_{\text{Im}ac} + L_{\text{Im}bc}) \vec{\beta}_4 + L_{abc} \vec{\beta}_5 + L_{cab} \vec{\beta}_6 \} \\
\vec{\gamma} &= \frac{1}{8} \{ (K_{+ab} - L_{\text{Re}ab} - 4K_c) \vec{\gamma}_1 + 2(L_{\text{Re}ac} - L_{\text{Re}bc}) \vec{\gamma}_2 \} \\
K_{+ab} &= |a|^2 + |b|^2 \\
K_{-ab} &= |a|^2 - |b|^2 \\
K_c &= |c|^2 \\
L_{abc} &= (a+b)c^* \\
L_{cab} &= c(a+b)^* \\
L_{\text{Re}ab} &= ab^* + ba^* \\
L_{\text{Im}ab} &= ab^* - ba^* \\
L_{\text{Re}bc} &= bc^* + cb^* \\
L_{\text{Im}bc} &= bc^* - cb^* \\
L_{\text{Re}ac} &= ac^* + ca^* \\
L_{\text{Im}ac} &= ac^* - ca^* \\
\vec{\alpha}_1 &= (3 \ 1 \ 2 \ 0 \ 0 \ 0 \ 0 \ 0 \ 0) \\
\vec{\alpha}_2 &= (1 \ 3 \ -2 \ 0 \ 0 \ 0 \ 0 \ 0 \ 0) \\
\vec{\alpha}_3 &= (1 \ -1 \ 2 \ 0 \ 0 \ 0 \ 0 \ 0 \ 0) \\
\vec{\alpha}_4 &= (0 \ 0 \ 0 \ 0 \ 0 \ 0 \ 0 \ \sqrt{2} \ -\sqrt{2}) \\
\vec{\beta}_1 &= (0 \ 0 \ 0 \ 2 \cos 2\phi \ -\sqrt{2} \sin 2\phi \ -\sqrt{2} \sin 2\phi \ 0 \ 0 \ 0) \\
\vec{\beta}_2 &= (0 \ 0 \ 0 \ 0 \ 0 \ 0 \ 2 \cos 2\phi \ \sqrt{2} \sin 2\phi \ \sqrt{2} \sin 2\phi) \\
\vec{\beta}_3 &= (0 \ 0 \ 0 \ \sin 2\phi \ 0 \ 0 \ 0 \ 0 \ 0) \\
\vec{\beta}_4 &= (0 \ 0 \ 0 \ 0 \ 0 \ 0 \ \sin 2\phi \ 0 \ 0) \\
\vec{\beta}_5 &= (0 \ 0 \ 0 \ 0 \ \sqrt{2} \cos 2\phi \ \sqrt{2} \cos 2\phi \ 0 \ \sqrt{2} \cos 2\phi \ \sqrt{2} \cos 2\phi) \\
\vec{\beta}_6 &= (0 \ 0 \ 0 \ 0 \ \sqrt{2} \cos 2\phi \ \sqrt{2} \cos 2\phi \ 0 \ -\sqrt{2} \cos 2\phi \ -\sqrt{2} \cos 2\phi) \\
\vec{\gamma}_1 &= (\cos 4\phi \ -\cos 4\phi \ -2 \cos 4\phi \ 0 \ -\sqrt{2} \sin 4\phi \ \sqrt{2} \sin 4\phi \ 0 \ 0 \ 0) \\
\vec{\gamma}_2 &= (\sin 4\phi \ -\sin 4\phi \ -2 \sin 4\phi \ 0 \ \sqrt{2} \cos 4\phi \ -\sqrt{2} \cos 4\phi \ 0 \ 0 \ 0) .
\end{aligned} \tag{3.72}$$

The vector of orthogonal matrices in (3.68) becomes

$$\vec{V} = \left(\begin{pmatrix} 1 & 0 & 0 \\ 0 & 0 & 0 \\ 0 & 0 & 1 \end{pmatrix} \begin{pmatrix} 0 & 0 & 1 \\ 0 & 0 & 0 \\ 1 & 0 & 0 \end{pmatrix} \begin{pmatrix} 0 & 0 & 0 \\ 0 & 1 & 0 \\ 0 & 0 & 0 \end{pmatrix} \begin{pmatrix} 1 & 0 & 0 \\ 0 & 0 & 0 \\ 0 & 0 & -1 \end{pmatrix} \begin{pmatrix} 0 & 1 & 0 \\ 1 & 0 & 0 \\ 0 & 0 & 0 \end{pmatrix} \right. \\ \left. \begin{pmatrix} 0 & 0 & 0 \\ 0 & 0 & 1 \\ 0 & 1 & 0 \end{pmatrix} \begin{pmatrix} 0 & 0 & 1 \\ 0 & 0 & 0 \\ -1 & 0 & 0 \end{pmatrix} \begin{pmatrix} 0 & 1 & 0 \\ -1 & 0 & 0 \\ 0 & 0 & 0 \end{pmatrix} \begin{pmatrix} 0 & 0 & 0 \\ 0 & 0 & -1 \\ 0 & 1 & 0 \end{pmatrix} \right)^T . \quad (3.73)$$

These are still an orthogonal basis. The equations from (3.71) to (3.73) can be applied not only to scattering from a cloud of dipoles but also to that from a cloud of any type of scatterer. As a way to validate the equation, we tried to derive its characteristic equation (see Appendix B). We eventually found that the eigenvalues are not affected by mean orientation angle, i.e., rotation regarding line of sight. Eigenvector based decomposition shown earlier in this chapter takes advantage of this property to remove the one dimension (the orientation angle) which is not related to intrinsic characteristics of the target.

A way to determine unknown parameters directly from measured data is given in Appendix C. The derivation, however, is purely mathematical, so further verification is needed for solid interpretation.

In the next section, the equation (3.66) will be added to our decomposition model, and a method of implementing the decomposition process will be shown with some results.

3.5 Adaptive Non-Negative Eigenvalue Decomposition

In this section, we add a generalized volume scattering model (3.66) to the NNED model, and explain how to find the optimal coefficients to decompose the scattering power from natural terrain.

Our decomposition model is still the same as (3.22). However, the volume scattering term in (3.14) should be replaced by the new one given in (3.66). Though we have ignored off-diagonal terms such as σ_{hhv} and σ_{hvv} in the previous model, they have to be taken into account here since the generalized model consists of all elements of the 3 by 3 matrix. Equation (3.22) can be explicitly rewritten as

$$C_m = xC_v(\phi, \sigma) + yC_d(\alpha) + zC_g(\beta) + C_{other} \quad (3.74)$$

where measured covariance matrix has a form

$$C_m = \begin{pmatrix} \sigma_{hhhh} & \sqrt{2}\sigma_{hhhv} & \sigma_{hhvv} \\ \sqrt{2}\sigma_{hhhv}^* & 2\sigma_{hvhv} & \sqrt{2}\sigma_{hvvv} \\ \sigma_{hhvv}^* & \sqrt{2}\sigma_{hvvv}^* & \sigma_{vvvv} \end{pmatrix}. \quad (3.75)$$

Once the mean orientation angle, ϕ , and randomness, σ , are given, the maximum limit for x is found as described previously. The double bounce and surface scattering terms do not affect the maximum value of x . However, since the covariance matrices for the measured data and the volume layer are full 3 by 3 matrices, (3.20) cannot be used to derive the maximum value of x . If we can assume that the correlation terms between the co- and cross-polarizations are small relative to the other elements, the eigenvalues in terms of x still follow the same trend as shown in Figure 3.6. This is true in practice due to scattering symmetry. The eigenvalues decrease monotonically, so there exists some maximum value of x which minimizes all three eigenvalues subject to the constraint that they remain non-negative. An analytical expression of the three eigenvalues derived from the full 3 by 3 covariance matrix is extremely complicated, so we directly calculate them for various values of x and then numerically find the maximum value of x which makes all of them non-negative. The covariance matrix for eigenvalue decomposition then becomes

$$C_m - xC_v(\phi, \sigma) = \begin{pmatrix} \sigma_{hhhh} & \sqrt{2}\sigma_{hhhv} & \sigma_{hhvv} \\ \sqrt{2}\sigma_{hhhv}^* & 2\sigma_{hvhv} & \sqrt{2}\sigma_{hvvv} \\ \sigma_{hhvv}^* & \sqrt{2}\sigma_{hvvv}^* & \sigma_{vvvv} \end{pmatrix} \approx \begin{pmatrix} \sigma_{hhhh} & 0 & \sigma_{hhvv} \\ 0 & 2\sigma_{hvhv} & 0 \\ \sigma_{hhvv}^* & 0 & \sigma_{vvvv} \end{pmatrix}. \quad (3.76)$$

We have shown how to derive the maximum x as in (3.21) so far. However, it is not necessary that the x in (3.74) is always the maximum x . Here we try to find the best x in the range between 0 and the maximum x . From (3.32) and (3.16a), a power of C_{other} can be derived as follows.

$$P(C_{other}) = P\left(\Lambda_3 \begin{pmatrix} 0 & 0 & 0 \\ 0 & 1 & 0 \\ 0 & 0 & 0 \end{pmatrix}\right) = \lambda_3 = 2(\sigma_{hvhv} - qx_{best}) \quad (3.77)$$

where, x_{best} means the best x in the range. The best x makes the power minimize so that the condition for the x becomes

$$P(C_{other}) = 0 \Rightarrow x_{best} = \frac{\sigma_{hvhv}}{q} = x_3. \quad (3.78)$$

To avoid the negative eigenvalue, the best fit x should be

$$x_{best} = x_{max}. \quad (3.79)$$

This means that our best fit x for this type of decomposition is exactly same as the maximum x .

Equation (3.74) tells us that if the parameters perfectly match the measured data, the power in C_{other} will be zero. This implies that in reality we can find the optimal parameter set which minimizes the power in C_{other} . The optimization is performed by varying the values of the randomness and orientation angle. A new algorithm, named adaptive NNED (ANNED), is proposed here and summarized in Figure 3.22.

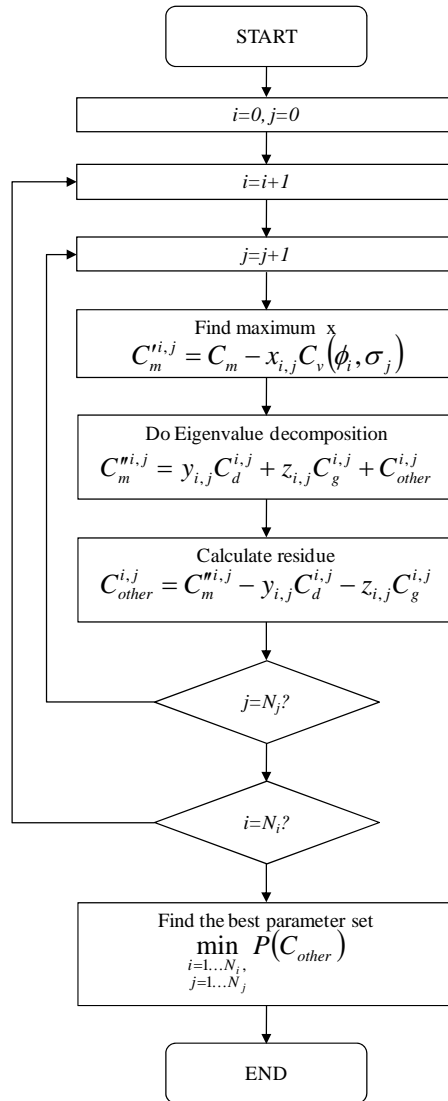


Figure 3.22: Flowchart of adaptive NNED algorithm

3.6 Experimental Results and Analysis

To see how the ANNED algorithm shown in Figure 3.22 adjusts to various types of vegetation, its results will be compared with those obtained from NNED shown in Figure 3.8. There is a difference between these two algorithms which might add complexity to the

discussion. It exists in the operation (3.13). By assuming scattering reflection symmetry, we can drop the four off-diagonal elements as in (3.13). The NNED algorithm uses this assumption as shown in Section 3.5. ANNED, however, uses the full matrix to derive the maximum x , and then it drops those four elements to obtain parameters for double-bounce and surface scattering. This difference is illustrated here with an example. We have the following covariance matrix from the Black Forest image.

$$C_m = \begin{pmatrix} 0.0278 & 0.003 + j0.007 & 0.0083 - j0.0032 \\ 0.003 - j0.007 & 0.0041 & -0.0009 + j0.0006 \\ 0.0083 + j0.0032 & -0.0009 + j0.0006 & 0.0188 \end{pmatrix} \quad (3.80)$$

This becomes an input to the maximum x determination processing in ANNED in (3.80). When we assume that the randomness is cosine squared distribution and the orientation angle is zero, the covariance matrix component is

$$C_v = \frac{1}{8} \begin{pmatrix} 1 & 0 & 1 \\ 0 & 2 & 0 \\ 1 & 0 & 5 \end{pmatrix}. \quad (3.81)$$

Then the maximum x for ANNED is calculated as 0.0156. On the other hand, assuming scattering symmetry the (3.80) is approximated for NNED as

$$C_m \approx \begin{pmatrix} 0.0278 & 0 & 0.0083 - j0.0032 \\ 0 & 0.0041 & 0 \\ 0.0083 + j0.0032 & 0 & 0.0188 \end{pmatrix}. \quad (3.82)$$

Using the same volume component in (3.81), the obtained maximum value of x is calculated to be 0.0165. The maximum value of x from ANNED is 0.0009 smaller than from NNED. Thus the off-diagonal elements in (3.82) add extra constraints to the decomposition so that the range of x is constrained. It is important to note that the maximum x by NNED is not allowed in ANNED because of the difference arising from the symmetry approximation. To avoid this difference, we turn ANNED one step back to

where the orientation angle and randomness are simply fixed. We call this NNED' (dash), and use this modified algorithm only to explore the applicability of ANNED.

Figures 3.23 and 3.24 show the decomposition results given by NNED' and ANNED, respectively. Green, red, and blue are assigned to volume, double bounce, and ground component, respectively.

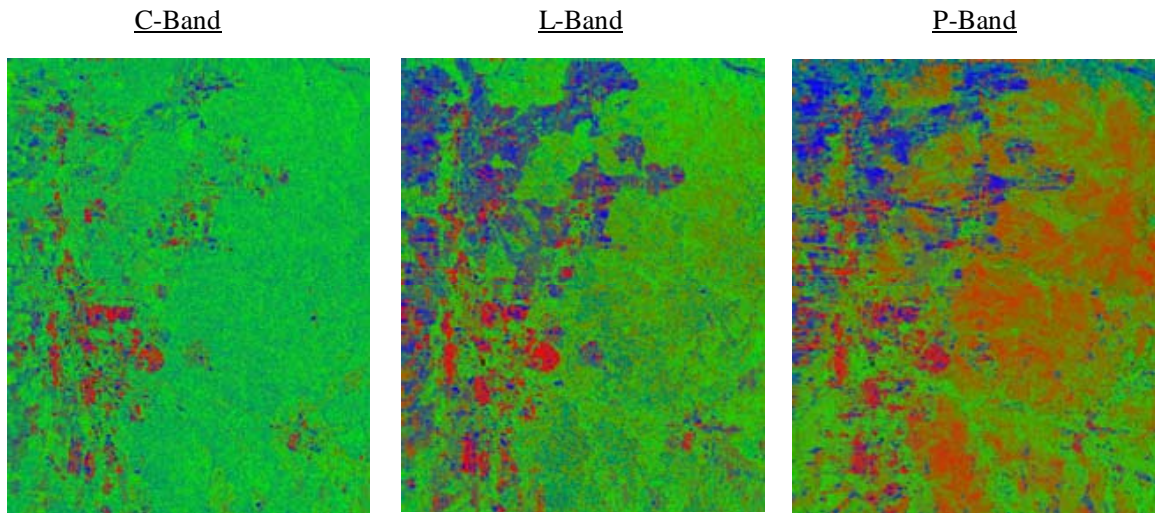


Figure 3.23: Results of the NNED' (dash) algorithm assuming a uniform distribution applied to three different wavelength images in Freiburg obtained by AIRSAR. Green, red, and blue are assigned to the volume, double bounce, and ground components.

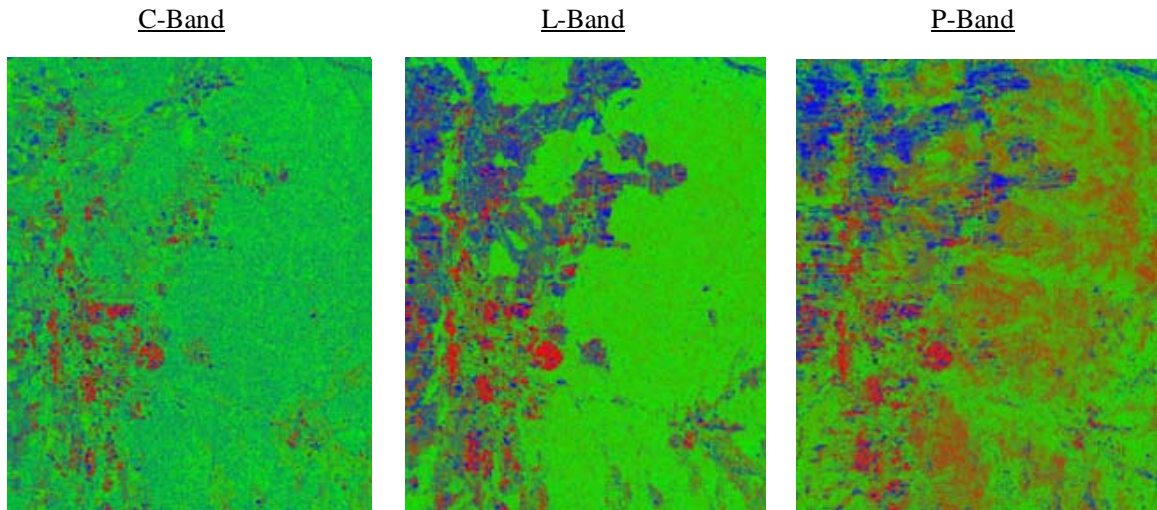


Figure 3.24: Results of the ANNED algorithm applied to three different wavelength images in Freiburg obtained by AIRSAR. Green, red, and blue are assigned to the volume, double bounce, and ground components.

From the L-band results, one can easily recognize that much more of the volume component appears in the forested area in ANNED than in NNED'. The P-band results also show a similar tendency. Focusing on the river halfway down the image, ANNED assigns more volume component than NNED' which means the effect of trunk-surface interaction due to topographic change shown in section 3.2 is less pronounced in ANNED. To more closely examine the applicability of ANNED, the remainder term of (3.74), C_{other} , is mapped in Figures 3.25 to 3.27 for the different wavelengths. In each figure, the result of ANNED is compared with those of NNED', assuming two distributions: uniform and cosine squared with zero orientation angle. From the model, the smaller pixel value is interpreted as the better fit to the chosen parameters of the model.

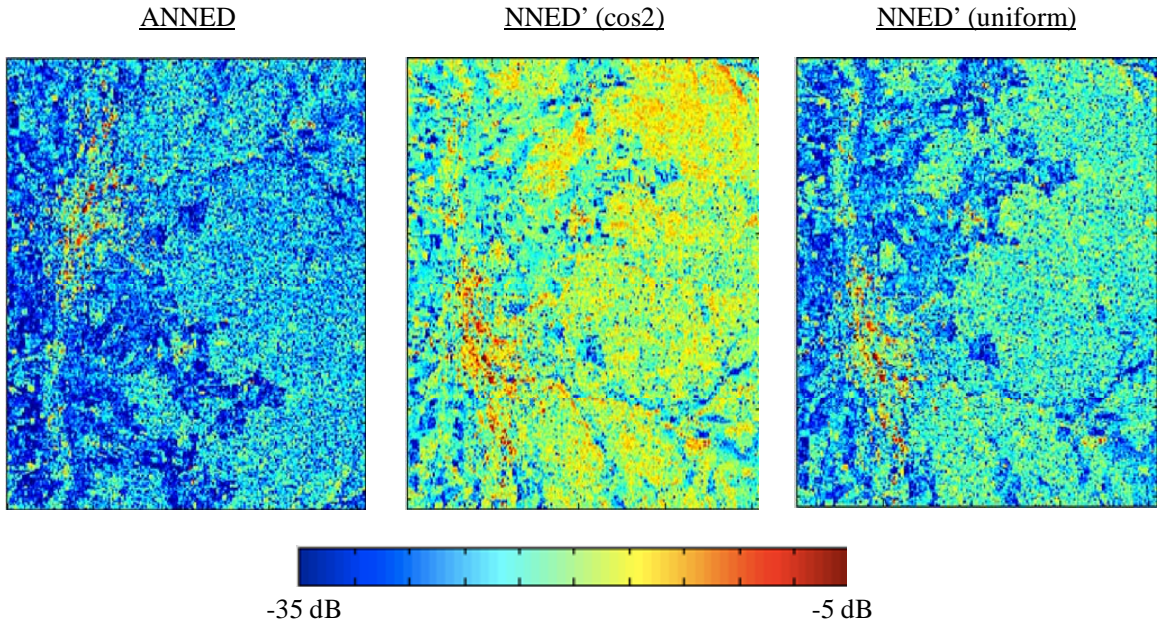


Figure 3.25: C_{ther} of ANNED (left) for the C-band Black Forest image compared with those of NNED' (dash) using two distributions: cosine squared (center) and uniform (right) distribution. Note that the cosine squared distribution has zero orientation angle.

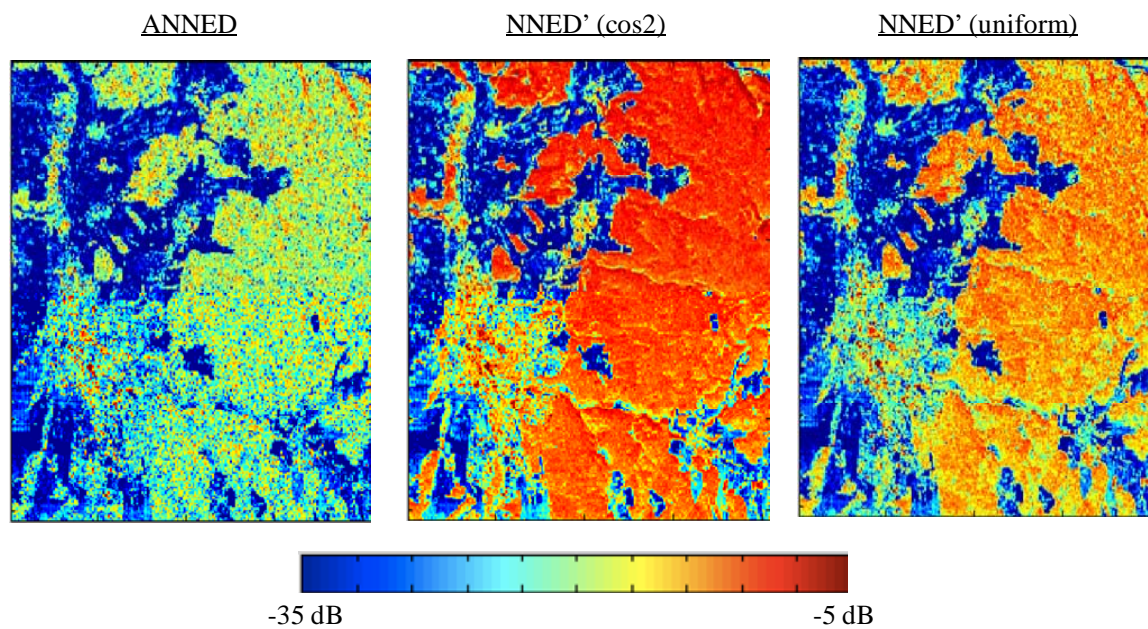


Figure 3.26: C_{oster} of ANNED (left) for the L-band Black Forest image compared with those of NNED' (dash) using two distributions: cosine squared (center) and uniform (right) distribution. Note that the cosine squared distribution has zero orientation angle.

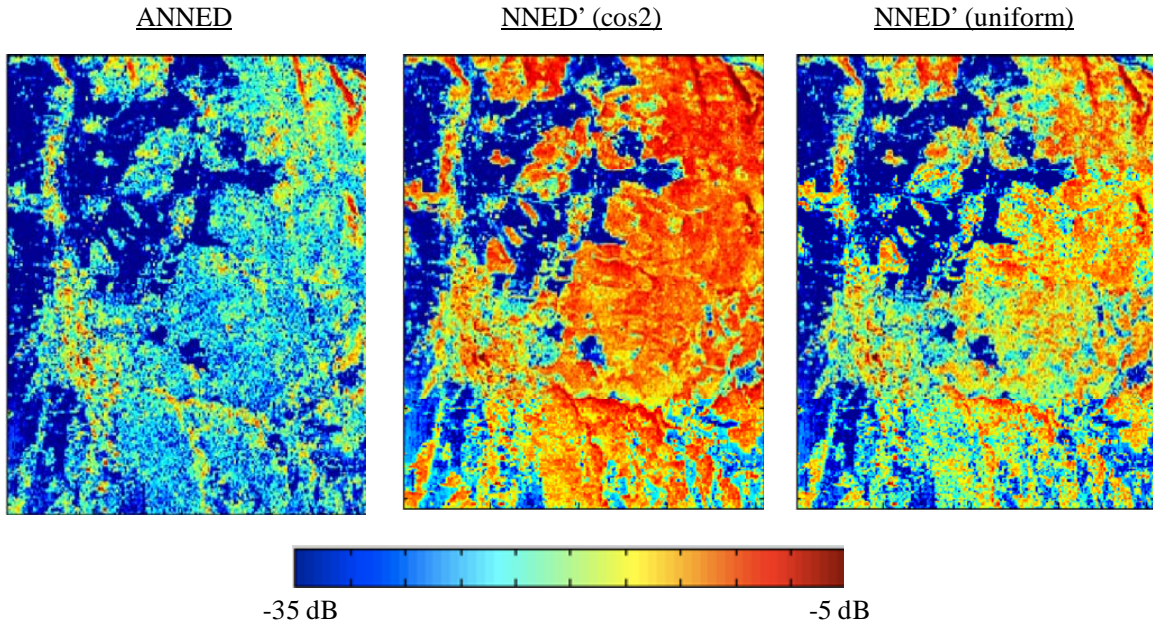


Figure 3.27: C_{ther} of ANNED (left) for the P-band Black Forest image compared with those of NNED' (dash) using two distributions: cosine squared (center) and uniform (right) distribution. Note that cosine squared distribution has zero orientation angle.

This clearly shows that ANNED can find the best fit parameter set, and the effect is significant in the forested area. Hence, we can conclude that ANNED has good applicability to the variation of vegetated area, as we expected. However we still have some mismatch area in the urban and some in the forest. The mismatch in the urban area is expected because our decomposition model was developed for vegetated terrain. The two thick reddish lines from the top to the bottom in P-band image might be topography under the forest. Because our ground scattering term only assumes a slightly rough surface (which will be thoroughly discussed in the next chapter) the other scattering mechanisms from the terrain degrade the parameter estimation. Even though the L-band shows significantly better parameter fits than the other wavelengths, there are points with relatively high mismatch widely distributed in the forest. This mismatch leads us to suspect that the thin cylinder approximation in (3.69) may not be appropriate for L-band. However, further investigation is required to be sure.

Finally, we analyze randomness and mean orientation angle obtained from the ANNEED decomposition process. Figure 3.28 shows the maps of these two parameters with their histograms from the C-band AIRSAR data.

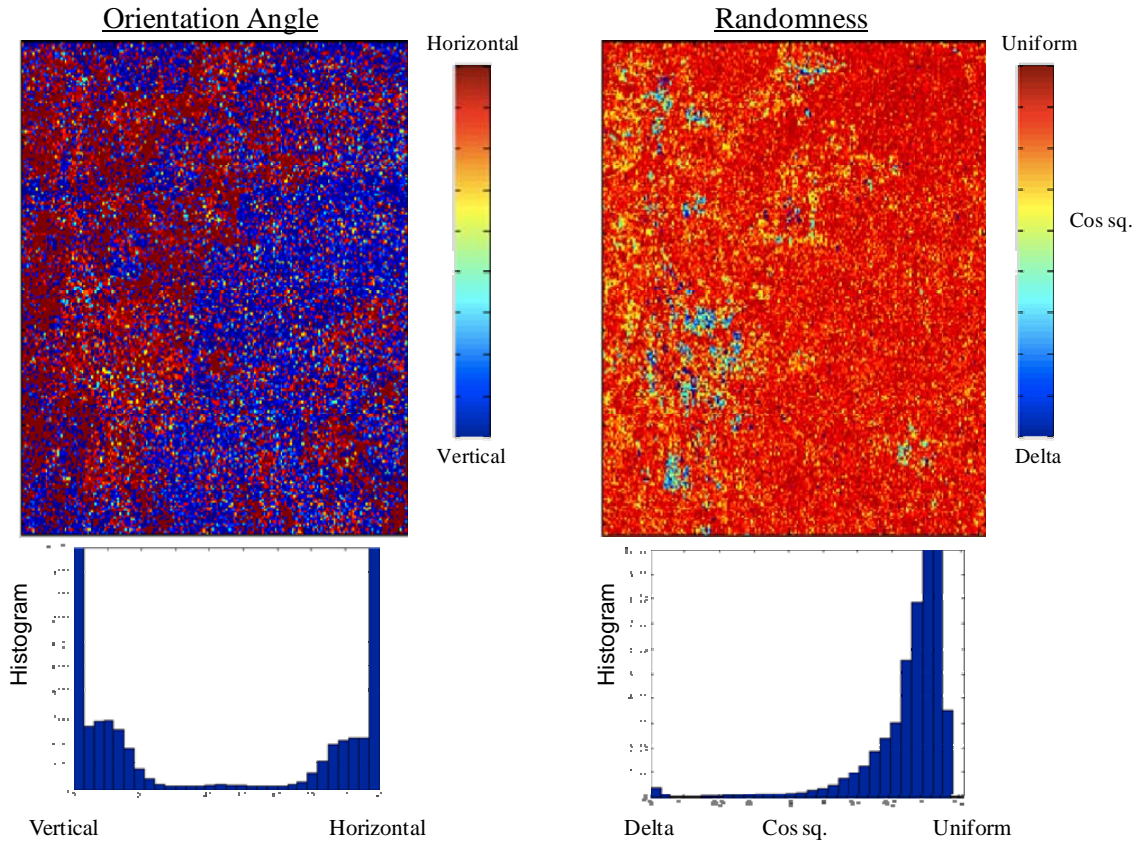


Figure 3.28: Orientation angle (upper left) and randomness (upper right) maps derived from the C-band AIRSAR image. Histograms for each parameter are also displayed.

Orientation angle is displayed from vertical (blue) to horizontal (red) orientation angle. Randomness varies from a delta function distribution (blue) to a uniform distribution (red). Since the randomness map shows mostly reddish pixels, the vegetation distribution of the corresponding area is estimated to be close to a uniform distribution. Since the forested

area of the image is widely covered with spruce, pine, and fir trees, the C-band wave may interact more strongly with their leaves and twigs, which usually have more complicated distribution than the other elements in a forested area. Even though the orientation angle map indicates mostly vertical orientation (blue pixels) in that area, this does not have physical meaning because the uniform distribution has no mean orientation angle. On the other hand, the agricultural area shows less randomness (yellowish color). This means that the incident wave interacts with crops which are expected to be more methodically distributed (less randomness) than the forested area. Results at L-band and P-band are shown in Figures 3.29 and 3.30, respectively.

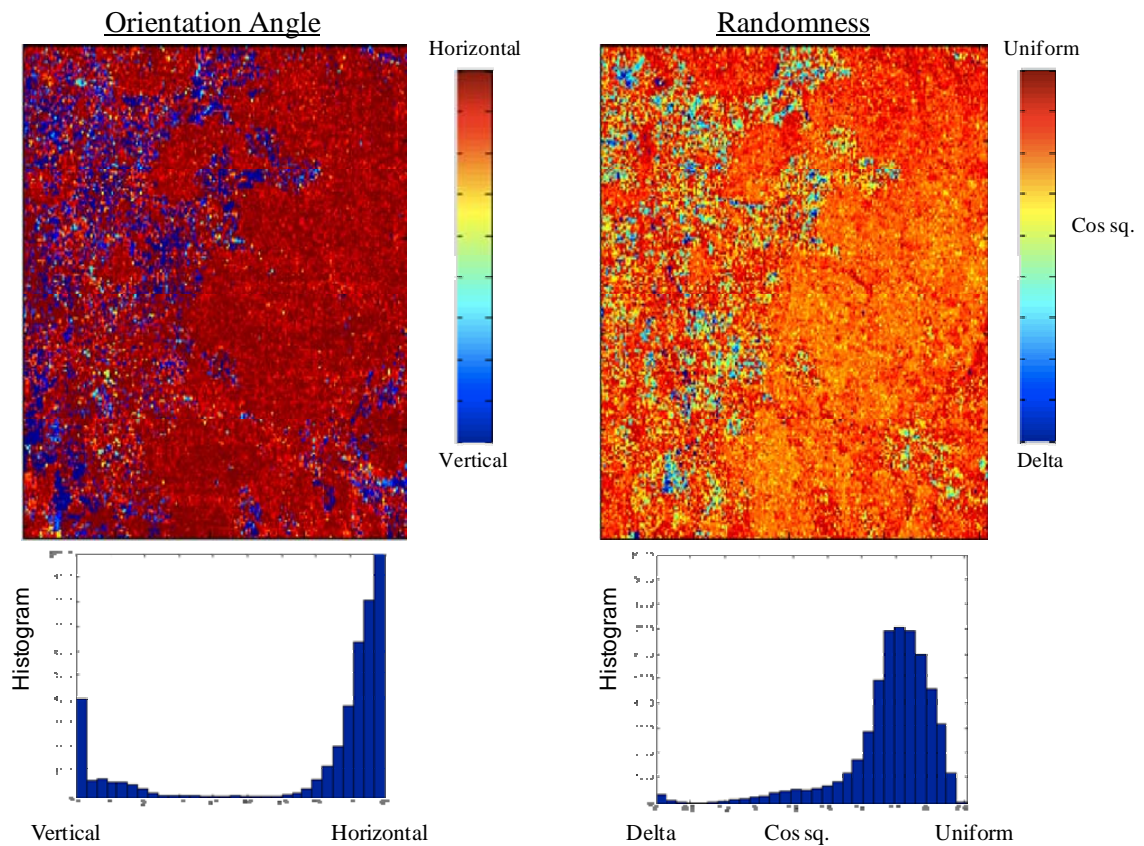


Figure 3.29: Orientation angle (upper left) and randomness (upper right) maps derived from the L-band AIRSAR image. Histograms for each parameter are also displayed.

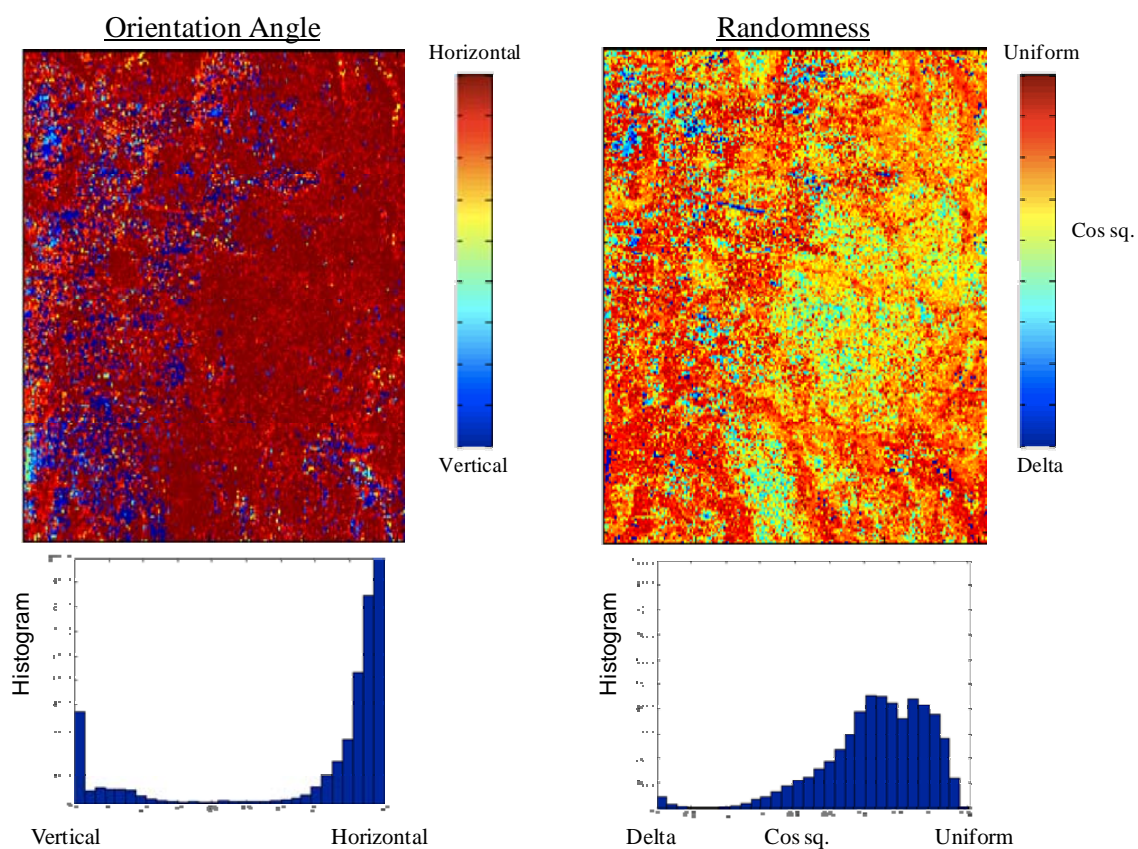


Figure 3.30: Orientation angle (upper left) and randomness (upper right) maps derived from the P-band AIRSAR image. Histograms for each parameter are also displayed.

Both wavelengths show that the randomness in the forested area is higher than that in the urban or agricultural area for all bands. This agrees with our interpretation for C-band. Focusing on the forested area, randomness decreases with increasing wavelength. The histograms numerically show that the peak in the forested area goes down from 0.9 at C-band to 0.8 at L-band, and finally reaches to around 0.7 at P-band. This is because the longer wavelengths can penetrate the volume layer, and are scattered by thick branches, trunks or the ground. Since the randomness at L-band and P-band are smaller than for a uniform distribution, the mean orientation angles are meaningful. Since the orientation

angles are mostly horizontal with some amount of randomness at L-band, the 24 cm wavelength signal mainly interacts with the branches. However, the interpretation of P-band image in the forested area is not straightforward. Its randomness is significantly lower than L-band, while the orientation angle is almost identical to that of L-band image. If the orientation angle were vertical, we could conclude that the trunk-ground interaction contributes to that area. We need to further investigate the scattering mechanism in this area.

In this chapter, several decomposition techniques were introduced, and qualitatively verified. Due to insufficient ground truth data for the decomposition models, quantitative validation has not been done so far. However, we will attempt the quantitative validation of the models by introducing the Discrete Scatterer Model (DSM) in this thesis. The DSM will be thoroughly discussed in the next chapter, and the decomposition techniques will be applied using the DSM in Chapter V.

Chapter IV

Scattering Mechanisms of a Vegetated Surface

This chapter will discuss modeling the scattering from a vegetated area. Each scattering mechanism occurring from natural terrain will be thoroughly discussed with the mathematical model for numerical simulations. This will be used for the quantitative validation of the decomposition models shown in the previous chapter.

4.1 Overview of Modeling

In order to express scattering from a vegetated terrain, two models are widely used. One is a radiative transfer model, and the other is a discrete scatterer model. Let us assume that there is a typical forest consisting of three components: the canopy, trunk, and ground.

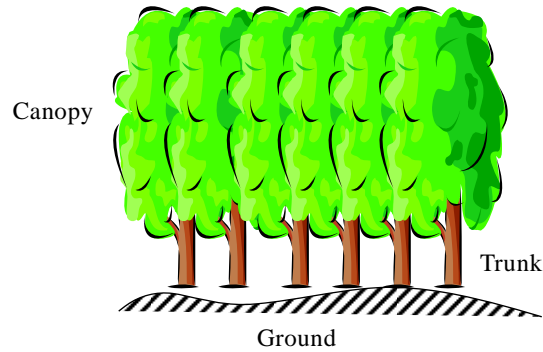


Figure 4.1: Illustration of a typical forest consisting of three components: the canopy, trunk, and ground.

The radiative transfer theory was originally introduced by Chandrasekhar [29]. Ulaby et al. then successfully applied the concept to scattering from vegetated terrain [30]. The model is the so called Michigan Microwave Canopy Scattering (MIMICS) model, and assumes that a typical forest has a three-layer structure as shown in Figure 4.2.

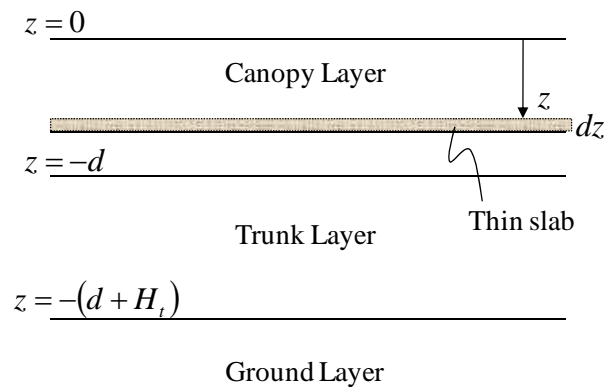


Figure 4.2: Three-layer structure for the MIMICS vegetation model

Based on the law of conservation of energy for the infinitely thin slab dz shown in the figure, we can form the following differential equations to express the net intensity for each of the upward and downward directions.

$$\begin{aligned} \frac{d}{dz} I_m^+(\mu, \phi, z) &= -\frac{\kappa_m^+}{\mu} I_m^+(\mu, \phi, z) + F_m^+(\mu, \phi, z) \\ -\frac{d}{dz} I_m^-(\mu, \phi, z) &= -\frac{\kappa_m^-}{\mu} I_m^-(\mu, \phi, z) + F_m^-(\mu, \phi, z) \end{aligned} \quad (4.1)$$

where

$$\begin{aligned} \mu &= \cos \theta \\ -\mu &= \cos(\pi - \theta) \end{aligned} \quad (4.2)$$

m is either of the canopy or trunk, and $+$ and $-$ indicate the upward and downward components, respectively. I represents the intensity, and F is the source function. κ is the attenuation coefficient which will be discussed in later in this chapter. θ and ϕ are angles corresponding to those in Figure 2.1. The second term on the right-hand side expresses the total incident intensity from all directions onto the slab in the specific direction, and is reduced by its attenuated intensity. The left-hand side shows the net intensity. These differential equations are integrated in terms of z with four boundary conditions: canopy top, canopy bottom (upward), canopy bottom (downward), and ground level.

$$\begin{aligned} I_{canopy}^+(-\mu, \phi, 0) &= I_0 \delta(\mu - \mu_0) \delta(\phi - \phi_0) \\ I_{canopy}^+(\mu, \phi, -d) &= I_{trunk}^+(\mu, \phi, -d) \\ I_{trunk}^-(-\mu, \phi, -d) &= I_{canopy}^-(-\mu, \phi, -d) \\ I_{trunk}^+(\mu, \phi, -(d + H_t)) &= R(\mu) I_{trunk}^-(-\mu, \phi, -(d + H_t)) \end{aligned} \quad (4.3)$$

where,

$$R(\mu) = \begin{pmatrix} |R_v|^2 & 0 & 0 & 0 \\ 0 & |R_h|^2 & 0 & 0 \\ 0 & 0 & \text{Re}(R_v R_h^*) & -\text{Im}(R_v R_h^*) \\ 0 & 0 & \text{Im}(R_v R_h^*) & \text{Re}(R_v R_h^*) \end{pmatrix}. \quad (4.4)$$

R_v and R_h are the well-known Fresnel coefficients which will be discussed in (4.38). I_0 is the total incident wave with incidence direction of θ_0 and ϕ_0 . The backscatter cross section is then obtained as

$$\sigma_{pq}^0 = 4\pi T_{pq}(\theta_0, \phi_0) \cos \theta_0 \quad (4.5)$$

where p and q are either h or v , and the 2 by 2 transformation matrix $T(\theta_0, \phi_0)$ is obtained from

$$I_s = T(\theta_0, \phi_0) I_0. \quad (4.6)$$

The equations are iteratively solved depending upon the number of times that the incident wave changes its direction due to particle interaction. The zero-th-order solution has no change direction so the solution only takes into account extinction. This is then employed to solve for the first-order solution in which the scattered wave is a sum of the five cases: direct particle scattering, direct ground scattering, particle-ground scattering, ground-particle scattering, and ground-particle-ground scattering. Though there is no limitation of this order, the calculation complexity is generally reasonable only up to the second order, which corresponds to two changes of direction by particle interaction. The advantage of using MIMICS is that taking into account multiple scattering leads to higher accuracy than using the discrete scatterer model. Conversely, it does not provide physical insight because of its complexity.

Durden et al. proposed the Discrete Scatterer Model (DSM) in 1989 [16]. The model assumes the model for vegetated terrain as shown in Figure 4.3.

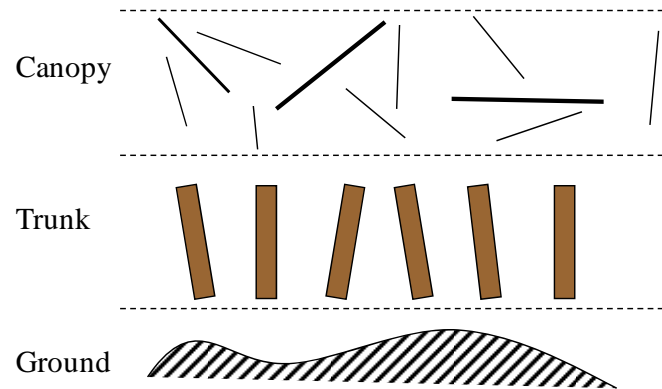


Figure 4.3: Illustration of the discrete scatterers of a forested terrain

The model does not have a layer structure, instead discrete scatterers. The multiple scattering is ignored by assuming that the scatterers inside the vegetation are usually sparsely distributed so that the scattered wave is well attenuated through multiple scatterings. With this assumption, the model is expressed by the only five distinct scattering mechanisms as illustrated in Figure 4.4: the backscatter from canopy, backscatter from trunk, backscatter from the ground, interaction between the ground and trunk, and interaction between the ground and canopy.

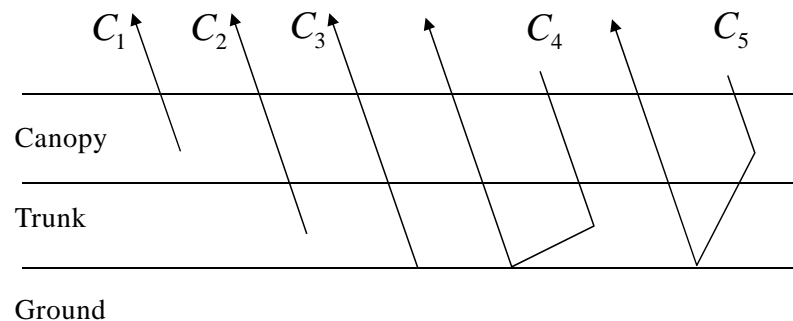


Figure 4.4: Scattering mechanisms for DSM

The total power at the receiver is simply expressed as a sum of the power from each scattering mechanism. The model is significantly simpler than the MIMICS model and

yields physical insights. However, the accuracy is not as good as that of MIMICS because it ignores multiple scatterings.

In this thesis, we introduce a scattering model for vegetated terrain to validate our proposed algorithms, such as decomposition technique shown in the previous chapter and the soil moisture inversion algorithms shown in Chapter IV. It is required that the model be simple enough but with reasonable accuracy so that we can easily understand the behavior of our algorithms. Therefore, DSM is adopted for the baseline scatter model for the vegetated terrain.

Specific characteristics of the scatter from the canopy part are highly dependent upon the wavelength of the incident wave. For example, if one uses the shorter wavelength C-band (6 cm), the wave interacts with leaves and twigs, whereas longer wavelengths such as L-band (24 cm) penetrate the canopy layer for the most part. At L-band, the wave interacts mostly with branches [31].

Many shapes, such as a disc or blade, have been proposed for the discrete scatterer in [32, 17]. However, in this thesis, a dielectric cylinder in various sizes is used to present natural properties of the scatterers due to the simplicity in the scattering calculation. There are two reasons. First, a simple cylindrical shape avoids additional complexity. Secondly, the shape should be a good model for a trunk, branch, and twig [16]. So the cylinder is good enough for the calculation. The model may not be appropriate for shorter wavelength such as C-band or X-band (3 cm) if the targeted terrain includes round-shape leaves. If this is the case, one may need to add a disk-shape elemental scatterer. Nonetheless, the model is still valid for these shorter wavelengths if the leaves have a thinner shape.

4.2 Scattering from an Oriented Cylinder

There are many publications describing scattering from an arbitrarily oriented cylinder, as in [33, 34, 35]. They usually start by solving Maxwell's equation for scatter from an

oriented infinitely long cylinder, and then move onto a case of a finite cylinder. The scattering from this is derived using Huygen's principle, in which the infinite cylinder is considered as a cluster of many small antennas, and each contribution is then synthesized. The idea uses exactly the same principle as an antenna array. In this thesis, the cylinder scattering model given in [17] is adopted as a baseline model because it is widely used and more rigorous, including edge contributions, the surface wave, and the interaction between them.

We will use two different coordinate systems to treat the scattering problem. One is a global coordinate system used to describe the incident and scattered wave vectors. The other is a local coordinate system to describe the scattering matrix of the cylinder. Once these wave vectors and the orientation angle of the cylinder are defined in the global coordinate system and transformed to the local coordinate system, the scattering matrix of an oriented cylinder can be calculated in its own local coordinate system. Then the power at the receiver is transformed back to the global coordinate system.

The global coordinate system can be shown using the FSA convention of Figure 2.1. The local coordinate system is defined in Figure 4.5. The z' axis is along the cylinder's length direction.

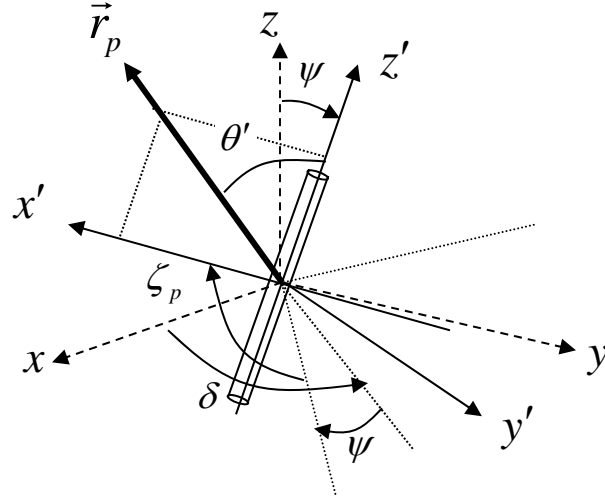


Figure 4.5: Local coordinate system $x'y'z'$ of an oriented cylinder

It is mathematically expressed as

$$\begin{pmatrix} x' \\ y' \\ z' \end{pmatrix}^p = \begin{pmatrix} \cos \zeta_p & -\sin \zeta_p & 0 \\ \sin \zeta_p & \cos \zeta_p & 0 \\ 0 & 0 & 1 \end{pmatrix} \begin{pmatrix} \cos \psi & 0 & -\sin \psi \\ 0 & 1 & 0 \\ \sin \psi & 0 & \cos \psi \end{pmatrix} \begin{pmatrix} \cos \delta & \sin \delta & 0 \\ -\sin \delta & \cos \delta & 0 \\ 0 & 0 & 1 \end{pmatrix} \begin{pmatrix} x \\ y \\ z \end{pmatrix} \quad (4.7)$$

$p = i, s$

where \vec{r}_p is

$$\vec{r}_p = \begin{pmatrix} r_x \\ r_y \\ r_z \end{pmatrix} = \begin{pmatrix} \sin \theta_p \cos \phi_p \\ \sin \theta_p \sin \phi_p \\ \cos \theta_p \end{pmatrix} \quad p = i, s \quad (4.8)$$

$\vec{r}_i = -k_i, \quad \vec{r}_s = k_s$

Since the incident wave is defined in x' - z' plane, \vec{r}_p and y' have to be orthogonal.

$$\vec{r}_p \cdot y' = 0 \quad (4.9)$$

ζ_p can be calculated under this condition.

$$\tan \zeta = \frac{r_x \sin \delta - r_y \cos \delta}{r_x \cos \psi \cos \delta + r_y \cos \psi \sin \delta - r_z \sin \psi} \quad (4.10)$$

With these definitions, the scattering matrix from an oriented cylinder can be expressed as

$$S_0 = \begin{pmatrix} S_{hh}^0 & S_{hv}^0 \\ S_{vh}^0 & S_{vv}^0 \end{pmatrix} = -i \frac{l}{\pi \sin^2(\pi - \theta')} \frac{\sin V}{V} \begin{pmatrix} A_{hh} & A_{hv} \\ A_{vh} & A_{vv} \end{pmatrix}.$$

$$A_{hh} = \sum_{m=-\infty}^{\infty} (-1)^m \left\{ [C_m^{TM}(h_i \cdot z') - i\bar{C}_m(v_i \cdot z')] (h_s \cdot z') \right. \\ \left. + [C_m^{TE}(v_i \cdot z') + i\bar{C}_m(h_i \cdot z')] (v_s \cdot z') \right\} e^{im\tilde{\phi}}$$

$$A_{hv} = \sum_{m=-\infty}^{\infty} (-1)^m \left\{ [C_m^{TM}(v_i \cdot z') + i\bar{C}_m(h_i \cdot z')] (h_s \cdot z') \right. \\ \left. - [C_m^{TE}(h_i \cdot z') - i\bar{C}_m(v_i \cdot z')] (v_s \cdot z') \right\} e^{im\tilde{\phi}} \quad (4.11)$$

$$A_{vh} = \sum_{m=-\infty}^{\infty} (-1)^m \left\{ [C_m^{TM}(h_i \cdot z') - i\bar{C}_m(v_i \cdot z')] (v_s \cdot z') \right. \\ \left. - [C_m^{TE}(v_i \cdot z') + i\bar{C}_m(h_i \cdot z')] (h_s \cdot z') \right\} e^{im\tilde{\phi}}$$

$$A_{vv} = \sum_{m=-\infty}^{\infty} (-1)^m \left\{ [C_m^{TM}(v_i \cdot z') + i\bar{C}_m(h_i \cdot z')] (v_s \cdot z') \right. \\ \left. + [C_m^{TE}(h_i \cdot z') - i\bar{C}_m(v_i \cdot z')] (h_s \cdot z') \right\} e^{im\tilde{\phi}}$$

$$\begin{aligned}
C_m^{TM} &= -\frac{V_m P_m - q_m^2 J_m(x_0) H_m^{(1)}(x_0) J_m^2(x_1)}{P_m N_m - [q_m H_m^{(1)}(x_0) J_m(x_1)]^2} = C_{-m}^{TM} \\
C_m^{TE} &= -\frac{M_m N_m - q_m^2 J_m(x_0) H_m^{(1)}(x_0) J_m^2(x_1)}{P_m N_m - [q_m H_m^{(1)}(x_0) J_m(x_1)]^2} = C_{-m}^{TE} \\
\bar{C}_m &= i \frac{2}{\pi x_0 \sin(\pi - \theta')} \frac{q_m J_m^2(x_1)}{P_m N_m - [q_m H_m^{(1)}(x_0) J_m(x_1)]^2} = -\bar{C}_{-m} \\
V &= \frac{1}{2} k_0 l (k_i - k_s) \cdot z', \quad \cos(\pi - \theta') = k_i \cdot z', \quad \sin(\pi - \theta') = -k_i \cdot x' \\
x_0 &= k_0 a \sin(\pi - \theta'), \quad x_1 = k_0 a \sqrt{\varepsilon - \cos^2(\pi - \theta')} \\
q_m &= m k_0 a \cos(\pi - \theta') \left(\frac{1}{x_1^2} - \frac{1}{x_0^2} \right) \\
k_0 &= \frac{2\pi}{\lambda} \\
V_m &= k_0 a \left\{ \frac{\varepsilon}{x_1} J_m(x_0) J'_m(x_1) - \frac{1}{x_0} J'_m(x_0) J_m(x_1) \right\} \\
P_m &= k_0 a \left\{ \frac{1}{x_1} H_m^{(1)}(x_0) J'_m(x_1) - \frac{1}{x_0} H_m^{(1)'}(x_0) J_m(x_1) \right\} \\
N_m &= k_0 a \left\{ \frac{\varepsilon}{x_1} H_m^{(1)}(x_0) J'_m(x_1) - \frac{1}{x_0} H_m^{(1)'}(x_0) J_m(x_1) \right\} \\
M_m &= k_0 a \left\{ \frac{1}{x_1} J_m(x_0) J'_m(x_1) - \frac{1}{x_0} J'_m(x_0) J_m(x_1) \right\}
\end{aligned}$$

where a and l are the radius and length of a cylinder, respectively, and ε is the dielectric constant. Also φ is the angle shown in Figure 4.3.

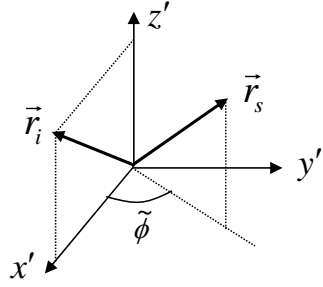


Figure 4.6: Geometry of the angle $\tilde{\phi}$ defined in (4.11)

This can be calculated as

$$\tilde{\phi} = \zeta_s - \zeta_i. \quad (4.12)$$

Bessel functions are calculated for a positive integer ν .

$$\begin{aligned}
 J_{-\nu}(x) &= (-1)^\nu J_\nu(x) \\
 J'_\nu(x) &= \frac{\nu}{x} J_\nu(x) - J_{\nu+1}(x) \\
 J'_{-\nu}(x) &= (-1)^\nu J'_\nu(x) \\
 H_\nu^{(1)}(x) &= J_\nu(x) + iY_\nu(x) \\
 H_{-\nu}^{(1)}(x) &= (-1)^\nu H_\nu^{(1)}(x) \\
 H_\nu^{(1)'}(x) &= \frac{\nu}{x} H_\nu^{(1)}(x) - H_{\nu+1}^{(1)}(x) \\
 H_{-\nu}^{(1)'}(x) &= (-1)^\nu H_\nu^{(1)'}(x) \\
 J'_{-\nu}(x) &= \frac{\nu}{x} J_{-\nu}(x) + J_{-\nu-1}(x) \\
 H_{-\nu}^{(1)'}(x) &= \frac{\nu}{x} H_{-\nu}^{(1)}(x) + H_{-\nu-1}^{(1)}(x)
 \end{aligned} \quad (4.13)$$

Since the scattering matrix above is stated using the coordinate system defined in Ulaby et al.'s book, backscattering and forward scattering in our coordinate system should be transformed using the transformation matrices defined in section 2.1.

$$\begin{aligned} S_{back} &= \begin{pmatrix} -1 & 0 \\ 0 & -1 \end{pmatrix} S_0 \begin{pmatrix} 1 & 0 \\ 0 & -1 \end{pmatrix} \\ S_{forward} &= \begin{pmatrix} 1 & 0 \\ 0 & -1 \end{pmatrix} S_0 \begin{pmatrix} 1 & 0 \\ 0 & -1 \end{pmatrix} \end{aligned} \quad (4.14)$$

Using the scattering matrices in (4.11), simulation results with different orientation angles and different wavelengths are demonstrated as follows. Fixed simulation parameters are shown in Table 4.1.

Table 4.1: Fixed simulation parameters of scattering from an oriented cylinder

θ_i (deg.)	ϕ_i (deg.)	a (cm)	l (m)	ϵ
40	0	10	1	13+j5

Also Table 4.2 shows specific simulation cases.

Table 4.2: Cases for simulations of scattering from an oriented cylinder

case	ψ (deg.)	δ (deg.)	λ (cm)
4-1-1	0	0	24
4-1-2	10	180	24
4-1-3	0	0	67

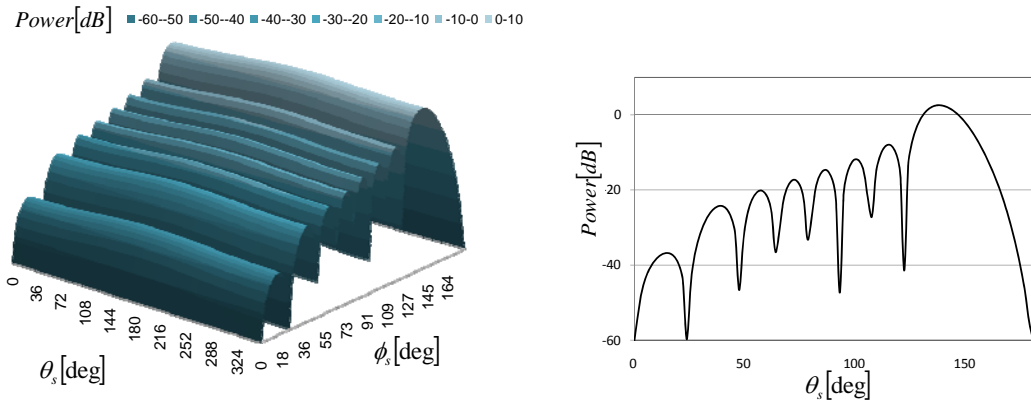


Figure 4.7: Scattering from an oriented cylinder for the case 4-1-1: the 3D plot (left) and cross section at $\phi_s = 0$ (right)

Figure 4.7 has a maximum reflection at $\theta_s = 140$ degrees and $\phi_s = 0$ degrees. This corresponds to a specular reflection from the incidence angle $\theta_i = 40$ degrees. Similarly, the maximum reflection occurs at $\theta_s = 140$ degrees and $\phi_s = 180$ degrees. The scattering corresponds to transmission, and is important when considering the attenuation effect as shown in the next chapter. Comparing the power at $\theta_s = 40$ degrees and $\phi_s = 0$ degrees with that at $\theta_s = 140$ and $\phi_s = 0$, it is clear that the forward scattering is much stronger than backscattering. This characteristic plays an important role understanding a contribution to double bounce scattering in a forested area, as shown in a later chapter.

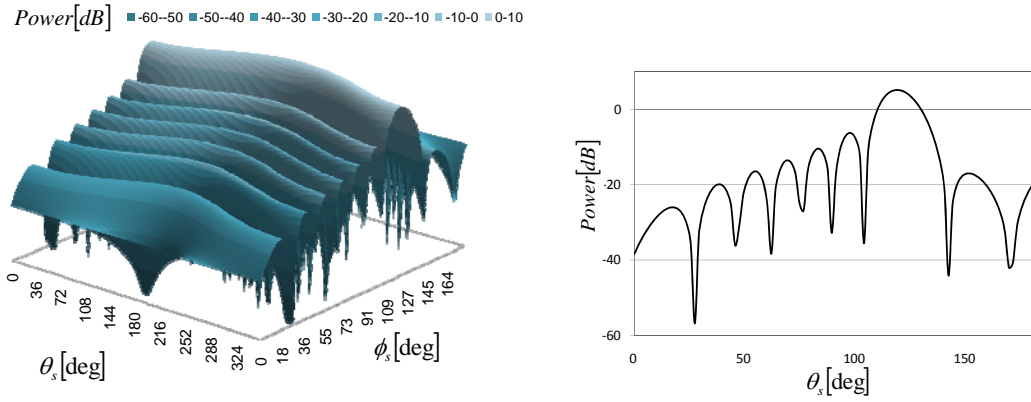


Figure 4.8: Scattering from an oriented cylinder for the case 4-1-2: the 3D plot (left) and cross section at $\phi_s = 0$ (right)

Figure 4.8 shows the results with the same parameters as the previous simulation but with varying the orientation angle of the cylinder. The orientation angle makes the incidence angle to the cylinder close to orthogonal. So the incidence angle to the cylinder becomes 50 degrees instead of 40 degrees. Therefore the specular angle for this oriented cylinder is now $\theta_s = 120$ degrees and $\phi_s = 0$ degrees, as shown in the figure.

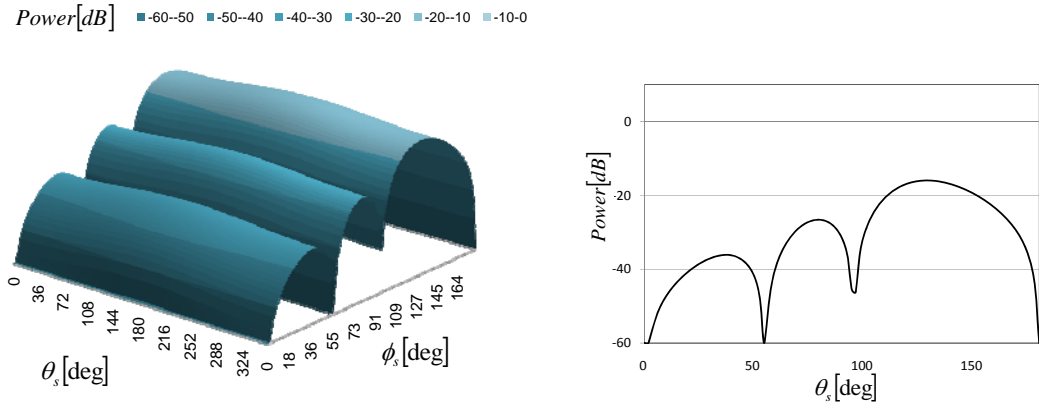


Figure 4.9: Scattering from an oriented cylinder for the case 4-1-3: the 3D plot (left) and cross section at $\phi_s = 0$ (right)

The last case is shown in Figure 4.9. The same parameters are used as in the first case except with varying wavelength. The longer wavelength makes the total scattering power much less than that in the previous case. This is because the 67 cm wavelength penetrates the cylinder (10 cm radius and 1 m length).

4.3 Scattering from a Cloud of Cylinders

In the previous section, we discussed how to calculate a scattering from arbitrarily oriented cylinder. Now we move on to scattering from a cloud of cylinders, as in Figure 4.10.

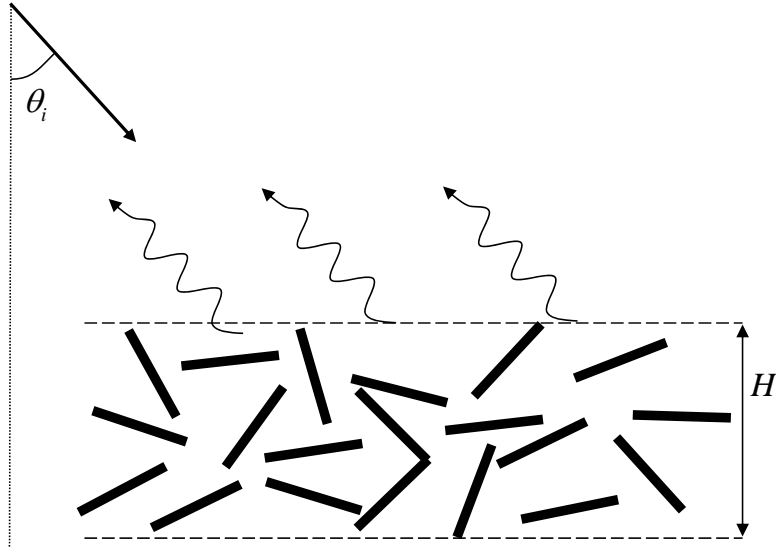


Figure 4.10: Scattering from a cloud of cylinders

We consider a layer filled with cloud cylinders that are oriented following a statistical distribution, $p(\psi, \delta)$. Each cylinder reflects back to the receiver so that the total receiving power is obtained by averaging all of them. A mathematical expression of the model can be derived from equation (2.11).

$$\begin{aligned}
 C_{no_att} &= \rho H \int_0^{2\pi} \int_0^{\pi} C_0 p(\psi, \delta) \sin \psi d\psi d\delta \\
 &= \begin{pmatrix} \sigma_{hhhh}^{no_att} & \sigma_{hhhv}^{no_att} & \sigma_{hhvh}^{no_att} & \sigma_{hhvv}^{no_att} \\ \sigma_{hhhv}^{no_att*} & \sigma_{hvhv}^{no_att} & \sigma_{hvhv}^{no_att} & \sigma_{hvvv}^{no_att} \\ \sigma_{hhvh}^{no_att*} & \sigma_{hvvh}^{no_att*} & \sigma_{vhvh}^{no_att} & \sigma_{vhvv}^{no_att} \\ \sigma_{hhvv}^{no_att*} & \sigma_{hvvv}^{no_att*} & \sigma_{vhvv}^{no_att*} & \sigma_{vvvv}^{no_att} \end{pmatrix} \quad (4.15)
 \end{aligned}$$

where ρ is the density of cylinders. As discussed in 3.4, we use the n-th power cosine squared distribution, and apply it to express the two-dimensional pdf, $p(\psi, \delta)$, as

$$p(\psi, \delta) = p_0(\psi)p_0(\delta). \quad (4.16)$$

Note that multiplying by $\sin\psi$ is important. This works as a regulator of the scatterer population to keep the same density on any part of the surface of a virtual sphere. One might think that there is no backscatter when all cylinders stand up perfectly (any $\psi=0$). However, the equation guarantees that there will be the backscatter, no matter what ψ is, because the pdf becomes delta function.

Now attenuation of the electromagnetic waves by the volume layer should be considered. As in many textbooks, such as [35, 36, 17], this is based on the *optical theorem*. Let us assume a layer with statistically distributed cylinders as shown in Figure 4.11.

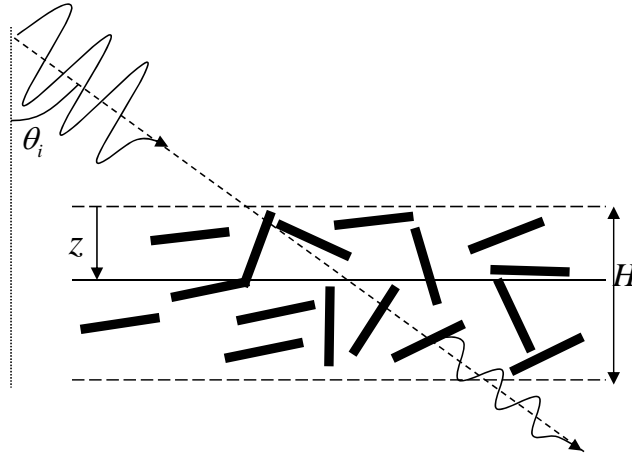


Figure 4.11: Illustration of extinction by a cloud of cylinders

The coefficients can be described in a form of the following scattering matrix.

$$S_{ext}(z) = \begin{pmatrix} T_{hh} & 0 \\ 0 & T_{vv} \end{pmatrix} = \begin{pmatrix} \exp\left(-\frac{1}{2}\alpha_{ext}^{hh} \frac{z}{\cos\theta_i}\right) & 0 \\ 0 & \exp\left(-\frac{1}{2}\alpha_{ext}^{vv} \frac{z}{\cos\theta_i}\right) \end{pmatrix} \quad (4.17)$$

$$\alpha_{ext}^{pp} = \frac{4\pi}{k} \langle \text{Im}\{S_{pp}^{fwd}\} \rangle, \quad p = h, v$$

The incident wave is disturbed by the cylinders, but some of the incident power survives and exits the layer. The optical theorem derives the attenuation coefficient using the scattering in the incidence direction. Therefore more interaction between the wave and cylinders causes a higher extinction rate α_{ext}^{pp} . Using this idea, S_{pp}^{fwd} is given by

$$\langle S_{pp}^{fwd} \rangle = \rho \int_0^{2\pi} \int_0^\pi S_{pp}(\theta_i, \phi_s = \pi, \psi, \delta) p(\psi, \delta) \sin \psi d\psi d\delta. \quad (4.18)$$

To apply the theory to our physical layer structure, we can categorize the five scatterings in Figure 4.3 into the following three types.

Type I: Scattering from the branch layer (C1)

Type II: Scattering from the trunk layer (C2)

Type III: Double bounce and surface scattering (C3, C4, and C5)

Each type has distinguishing characteristics for their calculations as follows.

4.3.1 Attenuation Type I: Scattering from the Branch Layer

From (2.8), the voltage measured by a polarimetric radar system for a single branch in a layer is expressed as

$$V = \vec{E}_0^{recT} S_0^b \vec{E}_0^{tr} \quad (4.19)$$

$$\vec{E}_0 = (E_h \quad E_v)^T$$

where \vec{E}_0^{tr} and \vec{E}_0^{rec} are the electric fields of transmitting and receiving, respectively. S_0^b is the scattering matrix of the branch layer. The attenuation coefficient in (4.17) affects not only the incident wave but also the scattered wave so that \vec{E}_0 should be replaced by

$$\vec{E} = S_{ext}^b(z) \vec{E}_0 = \begin{pmatrix} T_{hh}^b(z) & 0 \\ 0 & T_{vv}^b(z) \end{pmatrix} \vec{E}_0. \quad (4.20)$$

Then the voltage can be rewritten as

$$V(z) = \vec{E}^{recT} S_{ext}^b(z) S_0^b S_T^b(z) \vec{E}^{tr} \quad \left(\because S_{ext}^{bT} = S_{ext}^b \right). \quad (4.21)$$

The updated scattering matrix with attenuation and the associated covariance matrix are

$$S_0^{b-ext} = S_{ext}^b S_0^b S_{ext}^b \rightarrow C_0^{b-ext}(z). \quad (4.22)$$

Finally the covariance matrix from the branch layer with the attenuation is obtained with the layer height H_b .

$$C^{b-ext} = \rho \int_0^{H_b} \int_0^{2\pi} \int_0^{2\pi} C_0^{b-ext} p(\psi, \delta) \sin \psi d\psi d\delta dz \quad (4.23)$$

This is also written as

$$C^{b-ext} = \int_0^{H_b} \begin{pmatrix} T_{hh}^{b4} \sigma_{hhhh}^{no_att} & T_{hh}^{b3} T_{vv}^b \sigma_{hhhv}^{no_att} & T_{hh}^{b3} T_{vv}^b \sigma_{hhvh}^{no_att} & T_{hh}^{b2} T_{vv}^{b2} \sigma_{hhvv}^{no_att} \\ T_{hh}^{b3} T_{vv}^b \sigma_{hhhv}^{no_att*} & T_{hh}^{b2} T_{vv}^{b2} \sigma_{hhvv}^{no_att} & T_{hh}^{b2} T_{vv}^{b2} \sigma_{hhvh}^{no_att} & T_{hh}^{b2} T_{vv}^{b3} \sigma_{hhvv}^{no_att} \\ T_{hh}^{b3} T_{vv}^b \sigma_{hhvh}^{no_att*} & T_{hh}^{b2} T_{vv}^{b2} \sigma_{hhvh}^{no_att*} & T_{hh}^{b2} T_{vv}^{b2} \sigma_{hhvh}^{no_att} & T_{hh}^{b2} T_{vv}^{b3} \sigma_{hhvv}^{no_att} \\ T_{hh}^{b2} T_{vv}^{b2} \sigma_{hhvv}^{no_att*} & T_{hh}^{b2} T_{vv}^{b3} \sigma_{hhvv}^{no_att*} & T_{hh}^{b2} T_{vv}^{b3} \sigma_{hhvv}^{no_att*} & T_{vv}^{b4} \sigma_{vvvv}^{no_att} \end{pmatrix} dz. \quad (4.24)$$

Since the radar cross section is not a function of z , $hhhh$ component, for example, can be expressed as

$$\int_0^{H_b} T_{hh}^{b4} \sigma_{hhhh}^{no_att} dz = \sigma_{hhhh}^{no_att} \int_0^{H_b} T_{hh}^{b4} dz. \quad (4.25)$$

Each term is then calculated using

$$\begin{aligned}
\int_0^{H_b} T_{hh}^{b^4} dz &= \int_0^{H_b} e^{-2\alpha_{ext}^{hh} \frac{z}{\cos \theta_i}} dz = \frac{\cos \theta_i}{2\alpha_{ext}^{hh}} \left(1 - e^{-2\alpha_{ext}^{hh} \frac{H_b}{\cos \theta_i}} \right) \\
\int_0^{H_b} T_{hh}^{b^2} T_{vv}^{b^2} dz &= \int_0^{H_b} e^{-\left(\alpha_{ext}^{hh} + \alpha_{ext}^{vv}\right) \frac{z}{\cos \theta_i}} dz = \frac{\cos \theta_i}{\alpha_{ext}^{hh} + \alpha_{ext}^{vv}} \left(1 - e^{-\left(\alpha_{ext}^{hh} + \alpha_{ext}^{vv}\right) \frac{H_b}{\cos \theta_i}} \right) \\
\int_0^{H_b} T_{vv}^{b^4} dz &= \int_0^{H_b} e^{-2\alpha_{ext}^{vv} \frac{z}{\cos \theta_i}} dz = \frac{\cos \theta_i}{2\alpha_{ext}^{vv}} \left(1 - e^{-2\alpha_{ext}^{vv} \frac{H_b}{\cos \theta_i}} \right) \\
\int_0^{H_b} T_{hh}^{b^3} T_{vv}^b dz &= \int_0^{H_b} e^{-\frac{1}{2}\left(3\alpha_{ext}^{hh} + \alpha_{ext}^{vv}\right) \frac{z}{\cos \theta_i}} dz = \frac{2 \cos \theta_i}{3\alpha_{ext}^{hh} + \alpha_{ext}^{vv}} \left(1 - e^{-\frac{1}{2}\left(3\alpha_{ext}^{hh} + \alpha_{ext}^{vv}\right) \frac{H_b}{\cos \theta_i}} \right) \\
\int_0^{H_b} T_{hh}^b T_{vv}^{b^3} dz &= \int_0^{H_b} e^{-\frac{1}{2}\left(\alpha_{ext}^{hh} + 3\alpha_{ext}^{vv}\right) \frac{z}{\cos \theta_i}} dz = \frac{2 \cos \theta_i}{\alpha_{ext}^{hh} + 3\alpha_{ext}^{vv}} \left(1 - e^{-\frac{1}{2}\left(\alpha_{ext}^{hh} + 3\alpha_{ext}^{vv}\right) \frac{H_b}{\cos \theta_i}} \right)
\end{aligned} \tag{4.26}$$

These equations tell us that the covariance matrix can be obtained by calculating the radar scatter cross section portion and the attenuation coefficient separately.

4.3.2 Attenuation Type II: Scattering from the Trunk Layer

The attenuated incident wave from the branch layer now reaches to the trunk layer, and this layer also attenuates the wave power. From the scattering geometry in Figure 4.12, the attenuation matrix of the branch and trunk layers are expressed as

$$\begin{aligned}
S_{ext}^b(z = H_b) &= \begin{pmatrix} T_{hh}^b(H_b) & 0 \\ 0 & T_{vv}^b(H_b) \end{pmatrix} \\
S_{ext}^t(z) &= \begin{pmatrix} T_{hh}^t(z) & 0 \\ 0 & T_{vv}^t(z) \end{pmatrix}
\end{aligned} \tag{4.27}$$

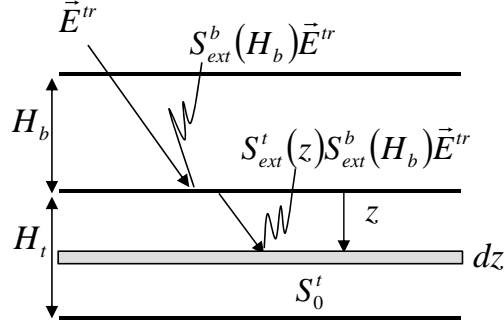


Figure 4.12: Scattering geometry from the trunk layer with extinction

The extinction by the trunk layer is a function of the layer depth. The covariance matrix of a scatterer from the trunk layer is derived from its scattering matrix with attenuation.

$$S_0^{t-ext} = S_{ext}^t S_{ext}^b S_0^t S_{ext}^b S_{ext}^t \rightarrow C_0^{t-ext}(z) \quad (4.28)$$

The covariance matrix of the trunk layer is

$$C^{t-ext} = \rho \int_0^{H_t} \int_0^{2\pi} \int_0^{2\pi} C_0^{t-ext} p(\psi, \delta) \sin \psi d\psi d\delta dz. \quad (4.29)$$

This can be rewritten as

$$C^{b-ext} = \int_0^{H_t} \left(\begin{array}{cc} T_{hh}^{b4} T_{hh}^{t4} \sigma_{hhhh}^{no_att} & T_{hh}^{b3} T_{vv}^{b3} T_{hh}^{t3} T_{vv}^{t3} \sigma_{hhhv}^{no_att} \\ T_{hh}^{b3} T_{vv}^{b3} T_{hh}^{t3} T_{vv}^{t3} \sigma_{hhhv}^{no_att*} & T_{hh}^{b2} T_{vv}^{b2} T_{hh}^{t2} T_{vv}^{t2} \sigma_{hvhv}^{no_att} \\ T_{hh}^{b3} T_{vv}^{b3} T_{hh}^{t3} T_{vv}^{t3} \sigma_{hhvh}^{no_att*} & T_{hh}^{b2} T_{vv}^{b2} T_{hh}^{t2} T_{vv}^{t2} \sigma_{hvvh}^{no_att*} \\ T_{hh}^{b2} T_{vv}^{b2} T_{hh}^{t2} T_{vv}^{t2} \sigma_{hhvv}^{no_att*} & T_{hh}^{b3} T_{vv}^{b3} T_{hh}^{t3} T_{vv}^{t3} \sigma_{hvvh}^{no_att*} \\ T_{hh}^{b3} T_{vv}^{b3} T_{hh}^{t3} T_{vv}^{t3} \sigma_{hvhv}^{no_att} & T_{hh}^{b2} T_{vv}^{b2} T_{hh}^{t2} T_{vv}^{t2} \sigma_{hhvv}^{no_att} \\ T_{hh}^{b2} T_{vv}^{b2} T_{hh}^{t2} T_{vv}^{t2} \sigma_{hvvh}^{no_att} & T_{hh}^{b3} T_{vv}^{b3} T_{hh}^{t3} T_{vv}^{t3} \sigma_{hvvh}^{no_att} \\ T_{hh}^{b2} T_{vv}^{b2} T_{hh}^{t2} T_{vv}^{t2} \sigma_{vvhv}^{no_att} & T_{hh}^{b3} T_{vv}^{b3} T_{hh}^{t3} T_{vv}^{t3} \sigma_{vhvv}^{no_att} \\ T_{hh}^{b3} T_{vv}^{b3} T_{hh}^{t3} T_{vv}^{t3} \sigma_{vhvv}^{no_att*} & T_{vv}^{b4} T_{vv}^{t4} \sigma_{vvvv}^{no_att} \end{array} \right) dz. \quad (4.30)$$

Since the attenuation coefficient of the branch layer is a constant, the calculation for *hhhh* polarization is as follows.

$$\int_0^{H_t} T_{hh}^{b^4} T_{hh}^{t^4} \sigma_{hhhh}^{no-att} dz = \sigma_{hhhh}^{no-att} T_{hh}^{b^4} \int_0^{H_t} T_{hh}^{t^4} dz. \quad (4.31)$$

While *Type I* has only σ_{hhhh}^{no-att} as a constant, *Type II* has one more constant, T_{hh}^b . The full covariance matrix is obtained similarly using (4.26).

4.3.3 Attenuation Type III: Double Bounce and Surface Scattering

The scatterings of this type penetrate both the branch and trunk layers. Now the attenuation matrix for each layer is expressed as

$$\begin{aligned} S_{ext}^b(z = H_b) &= \begin{pmatrix} T_{hh}^b(H_b) & 0 \\ 0 & T_{vv}^b(H_b) \end{pmatrix} \\ S_{ext}^t(z = H_t) &= \begin{pmatrix} T_{hh}^t(H_t) & 0 \\ 0 & T_{vv}^t(H_t) \end{pmatrix}. \end{aligned} \quad (4.32)$$

The covariance matrix of a single element is expressed as

$$S_0^{x-ext} = S_{ext}^t S_{ext}^b S_0^x S_{ext}^b S_{ext}^t \rightarrow C_0^{x-ext} \quad (4.33)$$

where x is double bounce or surface. The covariance matrix for a cloud of scatterers becomes

$$C^{x_ext} = \begin{pmatrix} T_{hh}^b T_{hh}^t \sigma_{hhhh}^{no_att} & T_{hh}^b T_{vv}^b T_{hh}^t T_{vv}^t \sigma_{hhhv}^{no_att} \\ T_{hh}^b T_{vv}^b T_{hh}^t T_{vv}^t \sigma_{hhhv}^{no_att*} & T_{hh}^b T_{vv}^b T_{hh}^t T_{vv}^t \sigma_{hhvv}^{no_att} \\ T_{hh}^b T_{vv}^b T_{hh}^t T_{vv}^t \sigma_{hhvh}^{no_att*} & T_{hh}^b T_{vv}^b T_{hh}^t T_{vv}^t \sigma_{hhvh}^{no_att} \\ T_{hh}^b T_{vv}^b T_{hh}^t T_{vv}^t \sigma_{hhvv}^{no_att*} & T_{hh}^b T_{vv}^b T_{hh}^t T_{vv}^t \sigma_{hhvv}^{no_att*} \\ T_{hh}^b T_{vv}^b T_{hh}^t T_{vv}^t \sigma_{hhvh}^{no_att} & T_{hh}^b T_{vv}^b T_{hh}^t T_{vv}^t \sigma_{hhvv}^{no_att} \\ T_{hh}^b T_{vv}^b T_{hh}^t T_{vv}^t \sigma_{hhvv}^{no_att} & T_{hh}^b T_{vv}^b T_{hh}^t T_{vv}^t \sigma_{hhvv}^{no_att} \\ T_{hh}^b T_{vv}^b T_{hh}^t T_{vv}^t \sigma_{hhvh}^{no_att} & T_{hh}^b T_{vv}^b T_{hh}^t T_{vv}^t \sigma_{hhvv}^{no_att} \\ T_{hh}^b T_{vv}^b T_{hh}^t T_{vv}^t \sigma_{hhvv}^{no_att} & T_{hh}^b T_{vv}^b T_{hh}^t T_{vv}^t \sigma_{hhvv}^{no_att} \\ T_{hh}^b T_{vv}^b T_{hh}^t T_{vv}^t \sigma_{hhvh}^{no_att} & T_{hh}^b T_{vv}^b T_{hh}^t T_{vv}^t \sigma_{hhvv}^{no_att} \\ T_{hh}^b T_{vv}^b T_{hh}^t T_{vv}^t \sigma_{hhvv}^{no_att} & T_{hh}^b T_{vv}^b T_{hh}^t T_{vv}^t \sigma_{hhvv}^{no_att} \end{pmatrix}. \quad (4.34)$$

4.4 Scattering from a Surface

Surface scattering is characterized by two parameters: dielectric constant and roughness. The dielectric constant is strongly related to soil moisture (see 4.6). If a bare surface is observed and its roughness property is known, we can directly infer the dielectric constant from the backscatter cross section. However, it is difficult to have accurate knowledge about roughness for a specific area in practice so that the estimation will be degraded depending on the degree of accuracy. The roughness is characterized by height deviation and correlation length, as shown in Figure 4.13.

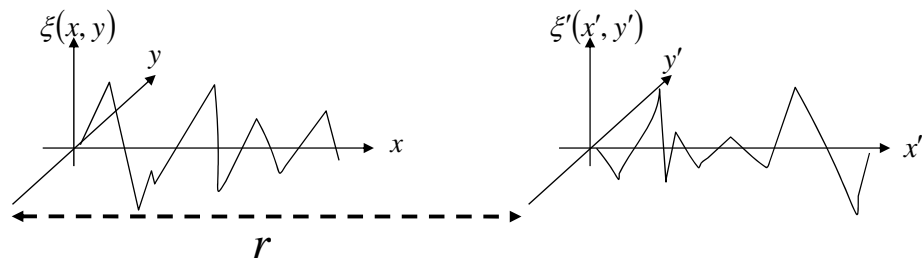


Figure 4.13: Parameters characterizing surface roughness

The figure shows that there are two local areas separated in the distance of r . Both areas have the same height deviation, which is also called root mean square (RMS) height. The height is mathematically written as

$$h = \langle \xi^2(x, y) \rangle = \langle \xi'^2(x', y') \rangle \quad (4.35)$$

where $\langle \rangle$ denotes an ensemble average. Also the surface correlation function is defined by the separation r between two independent local areas. This characterizes the similarity of the surface pattern of different two areas.

$$\rho(r) = \frac{\langle \xi(x, y)\xi'(x', y') \rangle}{h^2}. \quad (4.36)$$

Instead of the correlation function, the following roughness spectrum function is also used. It is just a Fourier transform of (4.36) as

$$\begin{aligned} W(k_x, k_y) &= \frac{1}{2\pi} \int_{-\infty}^{\infty} \int_{-\infty}^{\infty} \rho(x, y) \exp(-jk_x x) \exp(-jk_y y) dx dy \\ &= \int_0^{\infty} r \rho(r) J_0(kr) dr \end{aligned} \quad (4.37)$$

where the 0th order Bessel function is as given in (4.14), and the other parameters are

$$\begin{aligned} x &= r \cos \alpha \\ y &= r \sin \alpha \\ r &= \sqrt{x^2 + y^2} \end{aligned} \quad (4.38)$$

k_x and k_y are the wave numbers in the x direction and y direction, respectively. The following Gaussian and exponential spectrum functions are most commonly used for the roughness spectrum function.

$$W_g(p, q) = \frac{l^2}{2} e^{-\frac{(p^2+q^2)^2}{4}} \quad (4.39)$$

and

$$W_e(p, q) = \frac{l^2}{\{1 + (p^2 + q^2)l^2\}^{\frac{3}{2}}} \quad (4.40)$$

where l is the correlation length. A rougher surface generally has higher RMS height and shorter correlation length.

There are the two popular surface scattering models: the small perturbation model (SPM) [2] and the integral equation model (IEM) [3]. The SPM appeared in 1957 and has been widely validated by many researchers [37]. A mathematical expression of the first-order SPM is shown below.

$$\begin{aligned} \sigma_{ppqq}^g &= 8k^4 h^2 \cos^4 \theta_i (\alpha_{pp} \cdot \alpha_{qq}^*) W(2k \sin \theta_i, 0) \\ \alpha_{hh} &= \frac{1 - \varepsilon}{\left(\cos \theta_i + \sqrt{\varepsilon - \sin^2 \theta_i}\right)^2}, \\ \alpha_{vv} &= (1 - \varepsilon) \frac{\sin^2 \theta_i - \varepsilon(1 + \sin^2 \theta_i)}{\left(\varepsilon \cos \theta_i + \sqrt{\varepsilon - \sin^2 \theta_i}\right)^2} \end{aligned} \quad (4.41)$$

where p and q are either of h or v .

The IEM came about more recently in 1991, and is expressed as follows.

$$\sigma_{qp}^g = \frac{k^2}{2} \exp(-2k_z^2 h^2) \sum_{n=1}^{\infty} h^{2n} |I_{qp}^n|^2 \frac{W^n(-2k_x, 0)}{n!} \quad (4.42)$$

where,

$$\begin{aligned}
I_{qp}^n &= (2k_z)^n f_{qp} \exp(-k_z^2 h^2) + \frac{k_z^n \{F_{qp}(-k_x, 0) + F_{qp}(k_x, 0)\}}{2} \\
f_{hh} &= -\frac{2R_h}{\cos \theta_i} \\
f_{vv} &= \frac{2R_v}{\cos \theta_i} \\
f_{hv} &= f_{vh} = 0 \\
F_{vv}(-k_x, 0) + F_{vv}(k_x, 0) &= \frac{2 \sin^2 \theta_i (1 + R_h)^2}{\cos \theta_i} \left[\left(1 - \frac{1}{\varepsilon}\right) + \frac{\mu \varepsilon - \sin^2 \theta_i - \varepsilon \cos^2 \theta_i}{\varepsilon^2 \cos^2 \theta_i} \right] \\
F_{hh}(-k_x, 0) + F_{hh}(k_x, 0) &= -\frac{2 \sin^2 \theta_i (1 + R_v)^2}{\cos \theta_i} \left[\left(1 - \frac{1}{\mu}\right) + \frac{\mu \varepsilon - \sin^2 \theta_i - \mu \cos^2 \theta_i}{\mu^2 \cos^2 \theta_i} \right] \\
F_{hv}(-k_x, 0) + F_{hv}(k_x, 0) &= F_{vh}(-k_x, 0) + F_{vh}(k_x, 0) = 0
\end{aligned} \tag{4.43}$$

where μ is the permeability and k_z is a wave number in z direction. Fresnel coefficients are given as

$$\begin{aligned}
m &= \sqrt{\varepsilon}, \quad \theta_0 = \sin^{-1} \left(\frac{\sin \theta_i}{m} \right) \\
R_h &= \frac{\cos \theta_i - m \cos \theta_0}{\cos \theta_i + m \cos \theta_0}, \quad R_v = \frac{m \cos \theta_i - \cos \theta_0}{m \cos \theta_i + \cos \theta_0}
\end{aligned} \tag{4.44}$$

Under the small perturbation approximation where kh is much less than 1, the model becomes identical to the SPM. Also with a rougher surface ($kh > 3$ reported in [3]) the scattering is dominated by the Kirchoff term (shown in the next section) and is in agreement with the geometric optics model. Clearly, one of the main advantages of the model is its wider applicability than that of SPM. We, however, adopt SPM as the surface scattering model for DSM because the full covariance matrix of IEM has not been derived yet. In order to expand the applicability of SPM to higher roughness, we may introduce the concept of statistical surface tilt. However, all numerical calculations in this thesis use SPM for a surface scattering component

Topographical undulation affects the incidence and scattered angles of the surface scattering, and makes the backscatter cross section change drastically. The frequency of the surface undulation is assumed to be much lower than the limitation of SPM. As with the angle definitions for an oriented cylinder, the surface orientation angle is defined in Figure 4.14.

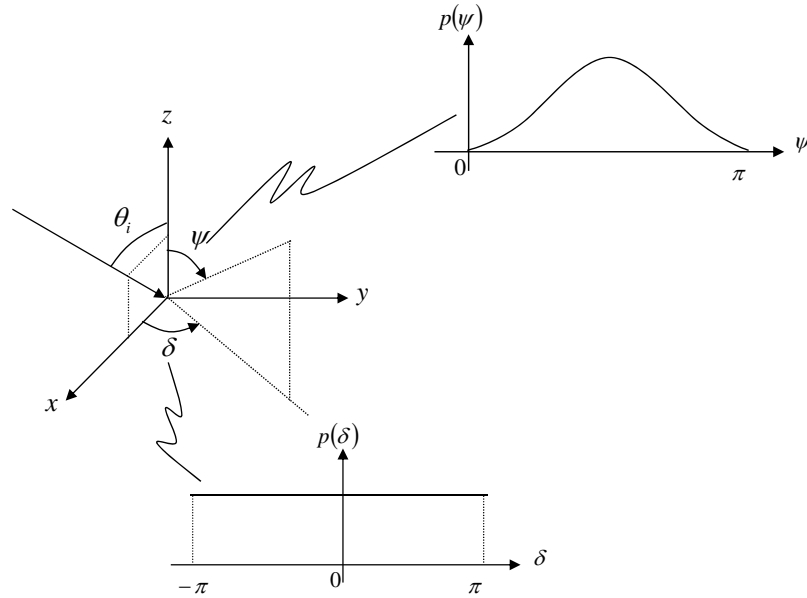


Figure 4.14: Surface undulation and its statistical definition. A Gaussian distribution is assigned to the range angle, ψ , while a uniform distribution is assigned to azimuth angle, δ .

Note that the pdf for angle ψ is a Gaussian distribution instead of a cosine squared distribution used for the cylinder. From these angle definitions, a tilted SPM, also known as a tilted Bragg surface model, can be expressed as follows. First, the voltage of nontilted surface scattering is written in scattering matrix form.

$$V = \vec{E}_0^{recT} S^g \vec{E}_0^{tr}$$

$$S^g = \begin{pmatrix} 0 & 0 & 0 \\ 0 & S_{hh}^g & S_{hv}^g \\ 0 & S_{vh}^g & S_{vv}^g \end{pmatrix} \quad (4.45)$$

Then the transmitted and received electric fields are transformed with the surface tilt. These coordinate transformations are derived from the geometry in Figure 4.5 and Figure 4.14.

$$\vec{E}^{tr} = D_i \vec{E}_0^{tr}$$

$$D_i = \left\{ \begin{pmatrix} -\cos \zeta & -\sin \zeta & 0 \\ \sin \zeta & -\cos \zeta & 0 \\ 0 & 0 & 1 \end{pmatrix} \begin{pmatrix} \sin \theta'_i & 0 & \cos \theta'_i \\ 0 & 1 & 0 \\ -\cos \theta'_i & 0 & \sin \theta'_i \end{pmatrix} \right\}^{-1} \begin{pmatrix} \cos \psi & 0 & -\sin \psi \\ 0 & 1 & 0 \\ \sin \psi & 0 & \cos \psi \end{pmatrix}$$

$$\begin{pmatrix} \cos \delta & \sin \delta & 0 \\ -\sin \delta & \cos \delta & 0 \\ 0 & 0 & 1 \end{pmatrix} \begin{pmatrix} -\cos \phi_i & \sin \phi_i & 0 \\ -\sin \phi_i & -\cos \phi_i & 0 \\ 0 & 0 & 1 \end{pmatrix} \begin{pmatrix} \sin \theta_i & 0 & \cos \theta_i \\ 0 & 1 & 0 \\ -\cos \theta_i & 0 & \sin \theta_i \end{pmatrix} \quad (4.46)$$

$$\vec{E}^{rec} = D_s \vec{E}_0^{rec}$$

$$D_s = \left\{ \begin{pmatrix} -\cos \zeta & -\sin \zeta & 0 \\ \sin \zeta & -\cos \zeta & 0 \\ 0 & 0 & 1 \end{pmatrix} \begin{pmatrix} \sin \theta'_s & 0 & \cos \theta'_s \\ 0 & 1 & 0 \\ -\cos \theta'_s & 0 & \sin \theta'_s \end{pmatrix} \right\}^{-1} \begin{pmatrix} \cos \psi & 0 & -\sin \psi \\ 0 & 1 & 0 \\ \sin \psi & 0 & \cos \psi \end{pmatrix}$$

$$\begin{pmatrix} \cos \delta & \sin \delta & 0 \\ -\sin \delta & \cos \delta & 0 \\ 0 & 0 & 1 \end{pmatrix} \begin{pmatrix} -\cos \phi_s & \sin \phi_s & 0 \\ -\sin \phi_s & -\cos \phi_s & 0 \\ 0 & 0 & 1 \end{pmatrix} \begin{pmatrix} \sin \theta_s & 0 & \cos \theta_s \\ 0 & 1 & 0 \\ -\cos \theta_s & 0 & \sin \theta_s \end{pmatrix}$$

ζ comes from equation (4.10) and θ' is obtained by

$$\cos \theta' = r_x \sin \psi \cos \delta + r_y \sin \psi \sin \delta + r_z \cos \psi . \quad (4.47)$$

The voltage from the tilted surface should be

$$V_{ilt} = \left(D_s \vec{E}_0^{rec} \right)^T S^g D_i \vec{E}_0^{tr} = \vec{E}_0^{recT} D_s^T S^g D_i \vec{E}_0^{tr} . \quad (4.48)$$

Then the scattering matrix and covariance matrix for the tilted surface become

$$\begin{aligned}
S_{\text{tilt}}^g &= D_s^T S^g D_i \Rightarrow C_{\text{tilt}_0}^{g_no_att} \\
C_{\text{tilt}}^{g_no_att} &= \int_{-\pi}^{\pi} \int_0^{\pi} C_{\text{tilt}_0}^{g_no_att} p(\psi, \delta) \sin \psi d\psi d\delta \\
&= \begin{pmatrix} \sigma_{hhhh}^{\text{tiltg_no_att}} & \sigma_{hhhv}^{\text{tiltg_no_att}} & \sigma_{hhvh}^{\text{tiltg_no_att}} & \sigma_{hhvv}^{\text{tiltg_no_att}} \\ \sigma_{hhhv}^{\text{tiltg_no_att}*} & \sigma_{hvhv}^{\text{tiltg_no_att}} & \sigma_{hvvh}^{\text{tiltg_no_att}} & \sigma_{hvvv}^{\text{tiltg_no_att}} \\ \sigma_{hhvh}^{\text{tiltg_no_att}*} & \sigma_{hvhv}^{\text{tiltg_no_att}*} & \sigma_{vhvh}^{\text{tiltg_no_att}} & \sigma_{vhvv}^{\text{tiltg_no_att}} \\ \sigma_{hhvv}^{\text{tiltg_no_att}*} & \sigma_{hhvv}^{\text{tiltg_no_att}*} & \sigma_{vhvv}^{\text{tiltg_no_att}*} & \sigma_{vvvv}^{\text{tiltg_no_att}} \end{pmatrix} \quad (4.49)
\end{aligned}$$

Finally the covariance matrix with the attenuation effect is derived using (4.31) as

$$\begin{aligned}
C_{\text{tilt}}^g &= \begin{pmatrix} T_{hh}^{b^4} T_{hh}^{t^4} \sigma_{hhhh}^{\text{tiltg_no_att}} & T_{hh}^{b^3} T_{vv}^b T_{hh}^{t^3} T_{vv}^t \sigma_{hhhv}^{\text{tiltg_no_att}} \\ T_{hh}^{b^3} T_{vv}^b T_{hh}^{t^3} T_{vv}^t \sigma_{hhhv}^{\text{tiltg_no_att}*} & T_{hh}^{b^2} T_{vv}^{b^2} T_{hh}^{t^2} T_{vv}^t \sigma_{hvhv}^{\text{tiltg_no_att}} \\ T_{hh}^{b^3} T_{vv}^b T_{hh}^{t^3} T_{vv}^t \sigma_{hhvh}^{\text{tiltg_no_att}*} & T_{hh}^{b^2} T_{vv}^{b^2} T_{hh}^{t^2} T_{vv}^t \sigma_{hhvh}^{\text{tiltg_no_att}*} \\ T_{hh}^{b^2} T_{vv}^{b^2} T_{hh}^{t^2} T_{vv}^t \sigma_{hhvv}^{\text{tiltg_no_att}*} & T_{hh}^b T_{vv}^{b^3} T_{hh}^t T_{vv}^t \sigma_{hhvv}^{\text{tiltg_no_att}*} \\ \\ T_{hh}^{b^3} T_{vv}^b T_{hh}^{t^3} T_{vv}^t \sigma_{hhvh}^{\text{tiltg_no_att}} & T_{hh}^{b^2} T_{vv}^{b^2} T_{hh}^{t^2} T_{vv}^t \sigma_{hhvv}^{\text{tiltg_no_att}} \\ T_{hh}^{b^2} T_{vv}^{b^2} T_{hh}^{t^2} T_{vv}^t \sigma_{hvhv}^{\text{tiltg_no_att}} & T_{hh}^b T_{vv}^{b^3} T_{hh}^t T_{vv}^t \sigma_{hvvv}^{\text{tiltg_no_att}} \\ T_{hh}^{b^2} T_{vv}^{b^2} T_{hh}^{t^2} T_{vv}^t \sigma_{vhvh}^{\text{tiltg_no_att}} & T_{hh}^b T_{vv}^{b^3} T_{hh}^t T_{vv}^t \sigma_{vhvv}^{\text{tiltg_no_att}} \\ T_{hh}^b T_{vv}^{b^3} T_{hh}^t T_{vv}^t \sigma_{vhvv}^{\text{tiltg_no_att}*} & T_{vv}^{b^4} T_{vv}^{t^4} \sigma_{vvvv}^{\text{tiltg_no_att}} \end{pmatrix}. \quad (4.50)
\end{aligned}$$

This equation tells us that the covariance matrix is obtained by calculating surface backscattering first and then multiplying by the attenuation coefficients. However, there are some cases where (4.40) cannot be applied such as an oriented cylinder. For physically realizable cases, the dot product of a vector expressed by \vec{r}_i in (4.8) and a vector \vec{r}_g in Figure 4.15 has to always be positive.

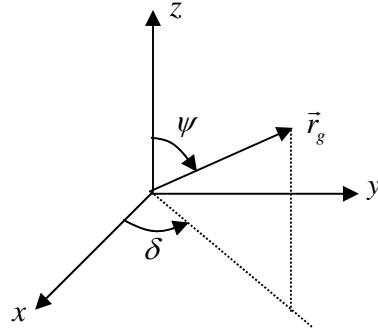


Figure 4.15: Vector normal to the tilted plane

The condition is

$$\vec{r}_i \cdot \vec{r}_g \geq 0. \quad (4.51)$$

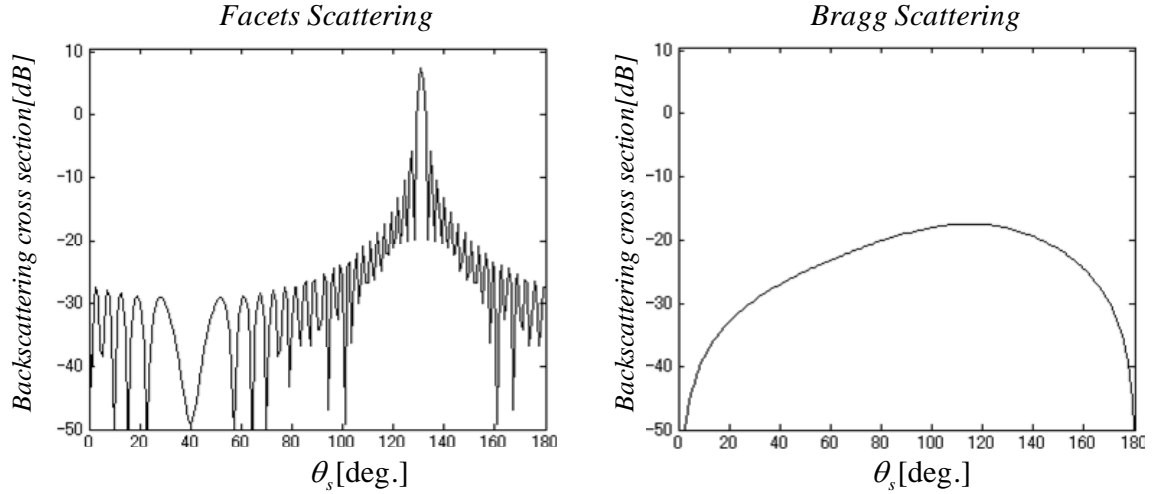
Therefore, the integration in (4.49) is only valid when equation (4.51) is satisfied.

4.5 Interaction between the Cylinders and the Surface

The interaction between the cylinders and a surface is also known as the double bounce reflection. For this type of scattering, we are interested in forward scattering instead of backscattering. It is well known that rough surface scattering consists of coherent and incoherent parts [31]. The coherent part is equivalent to the specular reflection from a smooth surface, also called facets scattering. The incoherent part is equivalent to the Bragg scattering, as discussed in the previous section. Using the surface parameters shown in Table 4.3, Figure 4.16 shows these two types of scatterings.

Table 4.3: Surface parameters for Facets and Bragg scatterings

θ_i (deg.)	λ (m)	h (m)	l (m)	ϵ
40	0.06	0.001	0.01	16+j1

**Figure 4.16:** Facet (left) and Bragg (right) scatterings. Facet scattering has an obvious peak around its specular angle (140 deg).

Facet scattering clearly shows a peak at specular reflection around 140 degrees while the Bragg scattering does not have a similar peak. It is reasonable for the double bounce scattering to take into account only specular scattering. This drastically reduces our computational cost compared with calculating for over all scattering angles. In addition, the simulation results of the cylinder scatterings in Figures 4.7, 4.8, and 4.9 clearly show that the maximum scattering occurs at the specular angle. Therefore we treat the following four cases shown in Figure 4.17. Note that the surface tilt is just ignored for simplicity.

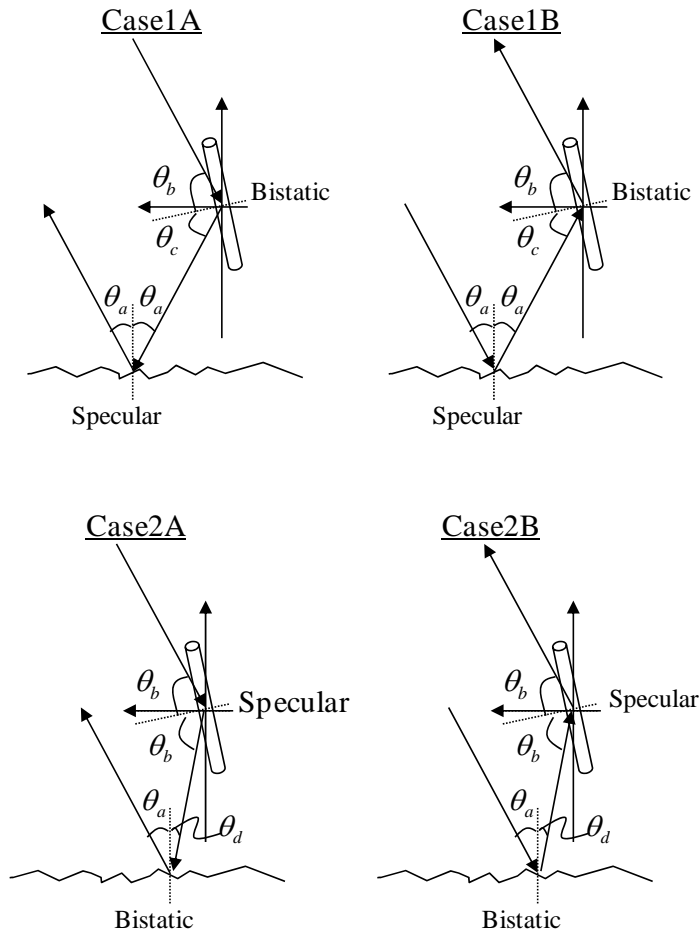


Figure 4.17: Assumed double bounce scattering cases: bistatic at cylinder followed by specular on the ground (upper left), specular on the ground followed by bistatic at cylinder (upper right), specular at cylinder followed by bistatic on the ground (bottom left), and bistatic on the ground followed by specular at cylinder (bottom right)

There are two commonly used facets scattering models: the Kirchoff model [16] and the physical optics (PO) model [17]. Since an infinitely large scattering area on the ground is assumed by PO, the Kirchoff model will be used for the double bounce scattering model in this thesis. The scattering area from the vegetated terrain is usually so limited by various plants such as trunks or grasses. The model is expressed in [26, 36] as

$$r_x = R_x \exp(-2h^2 k^2 \cos^2 \theta_i) \frac{\sin U}{U} \frac{\sin W}{W}, \quad x = h, v \quad (4.52)$$

$$U = \frac{1}{2} kb \sin \alpha, \quad W = \frac{1}{2} kb \sin \beta$$

where R_x is the Fresnel reflection coefficient in (4.44). α is an angle difference between θ_i and θ_s in the incidence plane as in Figure 4.18, and β is an angle in the out-of-incidence plane.

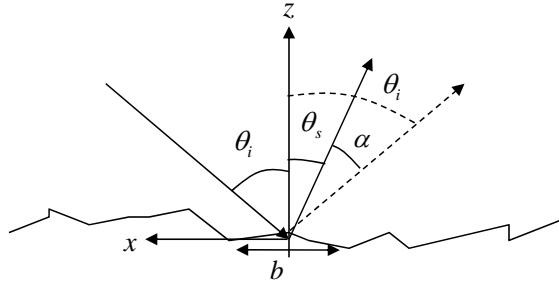


Figure 4.18: Definition of the angle α

Note that the incidence angle always lies in x - z plane. In this thesis, we ignore scattering out of the incidence plane to avoid further complexity. As in [26], this is a reasonable approximation for a first-order model. Therefore β is set to zero. The last parameter to be considered is the facet width b . We assume that the optimal b maximizes multiple scatterings between a cylinder and the ground. To find this solution, a top-hat reflector (as in [38]) should be taken into account. The geometry of a top-hat reflector is shown in Figure 4.19,

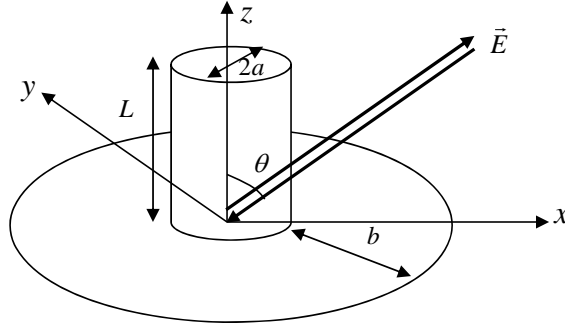


Figure 4.19: Geometry of the top-hat reflector

and the backscatter cross section is obtained in the following form.

$$\begin{aligned} \tan \theta \geq \frac{b}{L} & \quad \sigma = \frac{8\pi a}{\lambda} \sin \theta \cdot \left(\frac{b}{\tan \theta} \right)^2 \\ \tan \theta < \frac{b}{L} & \quad \sigma = \frac{8\pi a}{\lambda} \sin \theta \cdot L^2 \end{aligned} \quad (4.53)$$

We are interested in a condition on the facet width that maximizes scattering.

$$b = L \tan \theta \quad (4.54)$$

Finally the surface scattering matrix is

$$S_g^{db} = \begin{pmatrix} 0 & 0 & 0 \\ 0 & r_h & 0 \\ 0 & 0 & r_v \end{pmatrix}. \quad (4.55)$$

Note that this matrix is expressed in the FSA convention.

To express the double bounce scattering matrix between a cylinder and the ground, two parts of the wave propagation should be considered. Figure 4.20 shows one path of the wave propagation from cylinder to ground.

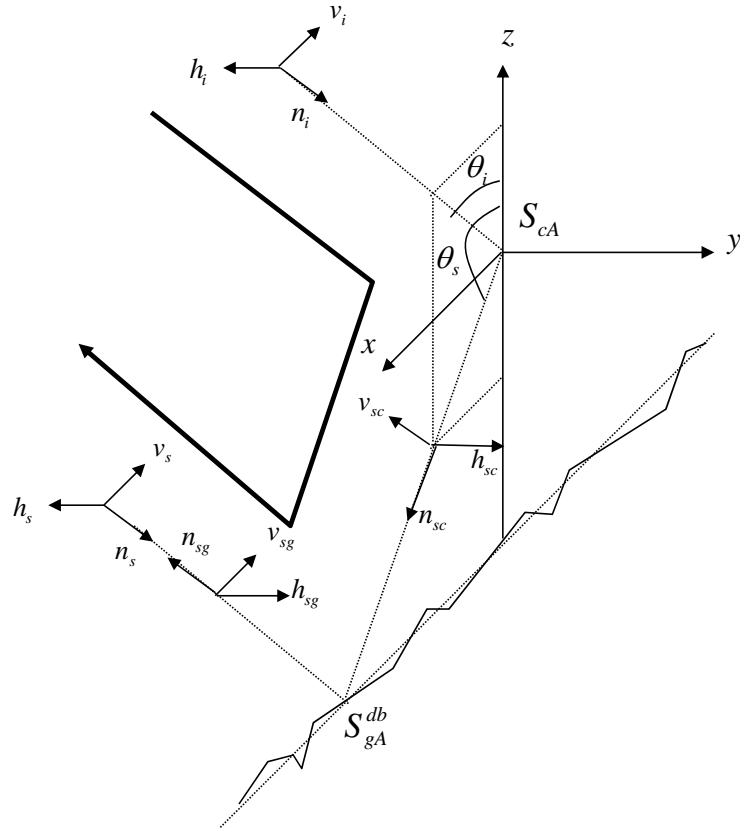


Figure 4.20: Geometry of double bounce scattering from a cylinder to the ground

The scattering matrix for this case is

$$\begin{pmatrix} n_s \\ h_s \\ v_s \end{pmatrix} = \begin{pmatrix} -1 & 0 & 0 \\ 0 & -1 & 0 \\ 0 & 0 & 1 \end{pmatrix} S_{gA}^{db} S_{cA} \begin{pmatrix} n_i \\ h_i \\ v_i \end{pmatrix} = S^{c2g} \begin{pmatrix} n_i \\ h_i \\ v_i \end{pmatrix}. \quad (4.56)$$

On the other hand, Figure 4.21 shows another path of wave propagation from the ground to a cylinder.

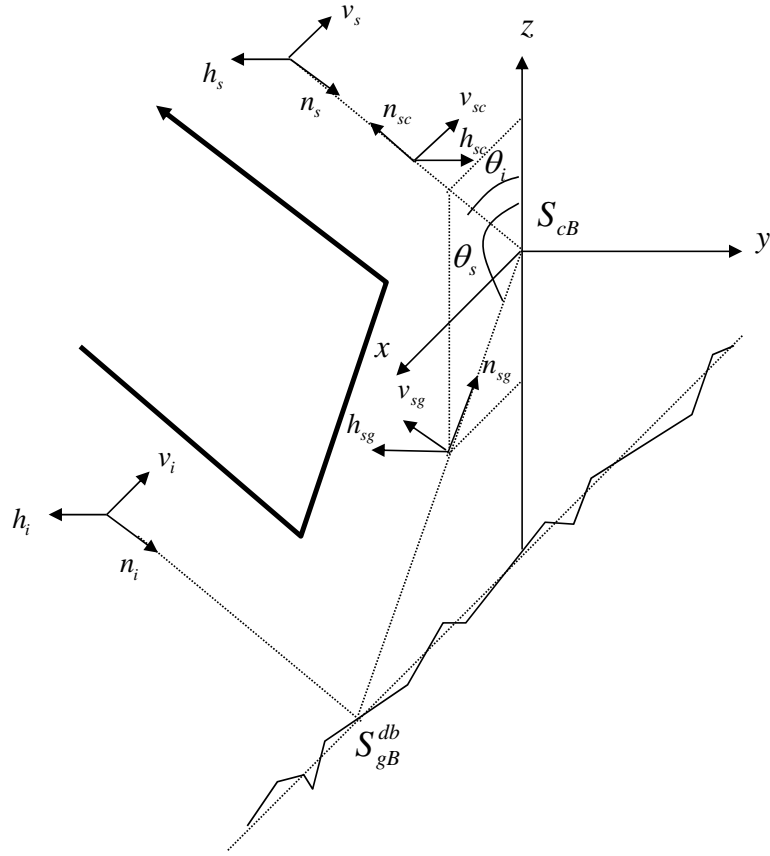


Figure 4.21: Geometry of double bounce scattering from the ground to a cylinder

The scattering matrix for this path is

$$\begin{pmatrix} n_s \\ h_s \\ v_s \end{pmatrix} = \begin{pmatrix} -1 & 0 & 0 \\ 0 & -1 & 0 \\ 0 & 0 & 1 \end{pmatrix} S_{cB} S_{gB}^{db} \begin{pmatrix} n_i \\ h_i \\ v_i \end{pmatrix} = S^{g2c} \begin{pmatrix} n_i \\ h_i \\ v_i \end{pmatrix}. \quad (4.57)$$

The scattering and covariance matrices between a cylinder and the ground can be found by taking an average of these two scattering matrices.

$$S_0^{db} = S^{c2g} + S^{g2c} \Rightarrow C_0^{db} \quad (4.58)$$

Now the total covariance matrix without the attenuation coefficients is obtained by the following operation.

$$\begin{aligned}
C^{db_no_att} &= \rho \int_0^{2\pi} \int_0^{\pi} C_0^{db} p(\psi, \delta) \sin \psi d\psi d\delta \\
&= \begin{pmatrix} \sigma_{hhhh}^{db_no_att} & \sigma_{hhhv}^{db_no_att} & \sigma_{hhvh}^{db_no_att} & \sigma_{hhvv}^{db_no_att} \\ \sigma_{hhhv}^{db_no_att*} & \sigma_{hvhv}^{db_no_att} & \sigma_{hvvh}^{db_no_att} & \sigma_{hvvv}^{db_no_att} \\ \sigma_{hhvh}^{db_no_att*} & \sigma_{hvvh}^{db_no_att*} & \sigma_{vhvh}^{db_no_att} & \sigma_{vhvv}^{db_no_att} \\ \sigma_{hhvv}^{db_no_att*} & \sigma_{hvvv}^{db_no_att*} & \sigma_{vhvv}^{db_no_att*} & \sigma_{vvvv}^{db_no_att} \end{pmatrix} \quad (4.59)
\end{aligned}$$

Finally the expression becomes

$$\begin{aligned}
C^{db} &= \begin{pmatrix} T_{hh}^b T_{hh}^t \sigma_{hhhh}^{db_no_att} & T_{hh}^b T_{vv}^b T_{hh}^t T_{vv}^t \sigma_{hhhv}^{db_no_att} \\ T_{hh}^b T_{vv}^b T_{hh}^t T_{vv}^t \sigma_{hhhv}^{db_no_att*} & T_{hh}^b T_{vv}^b T_{hh}^t T_{vv}^t \sigma_{hvhv}^{db_no_att} \\ T_{hh}^b T_{vv}^b T_{hh}^t T_{vv}^t \sigma_{hhvh}^{db_no_att*} & T_{hh}^b T_{vv}^b T_{hh}^t T_{vv}^t \sigma_{hvvh}^{db_no_att*} \\ T_{hh}^b T_{vv}^b T_{hh}^t T_{vv}^t \sigma_{hhvv}^{db_no_att*} & T_{hh}^b T_{vv}^b T_{hh}^t T_{vv}^t \sigma_{hvvv}^{db_no_att*} \\ T_{hh}^b T_{vv}^b T_{hh}^t T_{vv}^t \sigma_{hhvh}^{db_no_att} & T_{hh}^b T_{vv}^b T_{hh}^t T_{vv}^t \sigma_{hhvv}^{db_no_att} \\ T_{hh}^b T_{vv}^b T_{hh}^t T_{vv}^t \sigma_{hvhv}^{db_no_att} & T_{hh}^b T_{vv}^b T_{hh}^t T_{vv}^t \sigma_{hvvv}^{db_no_att} \\ T_{hh}^b T_{vv}^b T_{hh}^t T_{vv}^t \sigma_{hhvh}^{db_no_att*} & T_{hh}^b T_{vv}^b T_{hh}^t T_{vv}^t \sigma_{hvvv}^{db_no_att*} \\ T_{hh}^b T_{vv}^b T_{hh}^t T_{vv}^t \sigma_{hhvv}^{db_no_att*} & T_{hh}^b T_{vv}^b T_{hh}^t T_{vv}^t \sigma_{vvvv}^{db_no_att} \end{pmatrix}. \quad (4.60)
\end{aligned}$$

However, we cannot achieve a complete specular scattering at the cylinder at some orientation angles. There is a possible range for the incidence and orientation angles, so we conduct the operation only in that range. The cylinder orientation angle, ψ' , within the incidence plane (x-z plane) is shown in Figure 4.22.

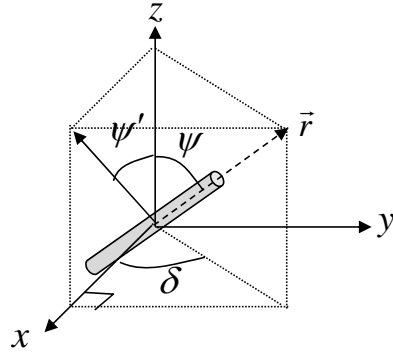


Figure 4.22: Orientation angle, ψ' , within the incidence plane

It is defined as

$$\tan \psi' = \frac{\vec{r}_x}{\vec{r}_z} = \cos \delta \tan \psi . \tag{4.61}$$

For the calculation of the specular scattering at cylinder (Case2A and 2B in the Figure 4.17), there are two cases we need to consider as shown in Figure 4.23.

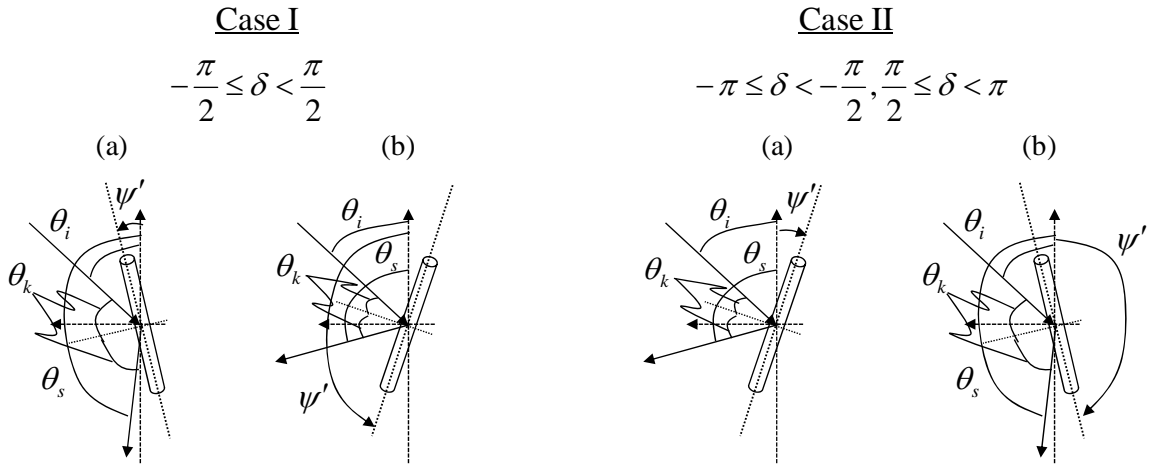


Figure 4.23: Two cases for the different azimuth orientation angle ranges

In the Case I(a), for example, if the orientation angle, ψ' , is slightly larger than the incidence angle, θ_i , the specular scattering happens behind the cylinder so that it does not come back to the sensor. We also take into account only the forward scattering on the ground. The angle, θ_k , for each case in the figure is expressed as

$$\begin{aligned}
 \text{Case I(a): } \theta_k &= \frac{\pi}{2} - (\theta_i - \psi') \\
 \text{Case I(b): } \theta_k &= \frac{\pi}{2} - \{\theta_i + (\pi - \psi')\} \\
 \text{Case II(a): } \theta_k &= \frac{\pi}{2} - (\theta_i + \psi') \\
 \text{Case II(b): } \theta_k &= \frac{\pi}{2} - \{\theta_i - (\pi - \psi')\}.
 \end{aligned} \tag{4.62}$$

For all cases, the scattered angles become

$$\theta_s = 2\theta_k + \theta_i, \quad \phi_s = 0. \tag{4.63}$$

The possible incidence and scattered angle ranges are

$$\begin{aligned}
 \text{Case I(a): } \psi' < \theta_i, \frac{\pi}{2} < \theta_s \leq \pi \\
 \text{Case I(b): } \psi' < \theta_i + \frac{\pi}{2}, \frac{\pi}{2} < \theta_s \leq \pi \\
 \text{Case II(a): } \psi' + \theta_i < \frac{\pi}{2}, \frac{\pi}{2} < \theta_s \leq \pi \\
 \text{Case II(b): } \psi' + \theta_i > \pi, \frac{\pi}{2} < \theta_s \leq \pi.
 \end{aligned} \tag{4.64}$$

(4.59) and (4.60) are calculated with angles satisfying these conditions.

4.6 Sensitivity Study

Using DSM, we will see how the backscatter cross section is affected by various physical parameters: the soil moisture, surface roughness, and vegetation water content. In this section, σ_{hhhh} , σ_{hvhv} , and σ_{vvvv} are simply called HH, HV, and VV, respectively.

There are several fixed parameters in Table 4.4. To make the situation simple, we assume the surface has no topography.

Table 4.4: Fixed parameters for the sensitivity simulation

θ_i (deg.)	λ (m)	L (m)	h_{layer} (m)	a (m)	l (cm)	ψ_0 (deg.)	σ_δ	ρ (cylinders/m ³)
0-90	0.24	0.5	0.5	0.002	5	0	0.91	900

h_{layer} is a layer height, ψ_0 is a mean orientation angle, and σ_δ is the randomness in the angle δ . 0.91 corresponding to a uniform distribution. The variables such as the soil moisture M_v , vegetation water content W_c , surface roughness kh , and randomness of the vegetation are assigned in Table 4.5.

Table 4.5: Cases of the sensitivity simulation

case	M_v (%)	W_c (kg/m ²)	kh	σ_ψ
baseline	10	1.24	0.26	0.56
4-6-1	30	1.24	0.26	0.56
4-6-2	60	1.24	0.26	0.56
4-6-3	10	0	0.26	0.56
4-6-4	10	2.54	0.26	0.56
4-6-5	10	1.24	0.50	0.56
4-6-6	10	1.24	1.00	0.56
4-6-7	10	1.24	0.26	0.30
4-6-8	10	1.24	0.26	0.91

Note that σ_ψ is assumed to have a small randomness distribution ($\sigma_\psi=0.30$), cosine squared distribution ($\sigma_\psi=0.56$), or uniform distribution ($\sigma_\psi=0.91$).

The real part of the dielectric constant of dry sand is about 3, while it is 80 for water. Soil moisture is clearly related to its dielectric constant, and generally they are characterized by a nonlinear relationship. Wang et al. proposed an empirical model in [39]. The model was derived based on measurements at 1.4 and 5 GHz. If we assume a typical loam soil, the expression is given by

$$\varepsilon = \begin{cases} 3.25 + 2.2M_v + 147.05M_v^2 & \text{for } M_v < 22\% \\ -6.8216 + 78.5M_v & \text{for } M_v > 22\% \end{cases}. \quad (4.65)$$

Hallikainen found a relationship between the real part of the dielectric constant of the soil and its moisture in percentage [40] as

$$\varepsilon_{soil} = 2.2575 + 22.9925M_v + 101.8015M_v^2. \quad (4.66)$$

This empirical model assumes a typical loam soil, and is derived from measurements from 1.4 to 18 GHz. The expression is applicable at 1.4 GHz. Dobson et al. also reported a semi-empirical model with a more complicated form [41, 42]. The model takes into account a relationship between the relaxation time for the water and temperature. These algorithms are expressions of the dielectric constant for the given soil moisture. Conversely, the soil moisture can be calculated from a measured dielectric constant [43] as follows.

$$M_v = -0.0278 + 0.0280\varepsilon_{soil} - 0.000586\varepsilon_{soil}^2 + 0.00000503\varepsilon_{soil}^3 \quad (4.67)$$

In this thesis, we use the model proposed by Hallikainen to relate the dielectric constant to the soil moisture, and also use Brisco's model for the reverse case because they have similar characteristics between the dielectric constant and soil moisture, as pointed out in [22].

We also have an expression to relate the dielectric constant of the vegetation to its water content percentage [44] by

$$\varepsilon_v = \varepsilon_r + v_{fw} \left(4.9 + \frac{75.0}{1 + jf/18} - j \frac{18\sigma_v}{f} \right) + v_b \left(2.9 + \frac{55.0}{1 + \sqrt{jf/0.18}} \right) \quad (4.68)$$

where f is the frequency in GHz, and

$$\begin{aligned} \sigma_v &= 0.16S - 0.0013S^2 \\ \varepsilon_r &= 1.7 + 3.2W_c + 6.5W_c^2 \\ v_{fw} &= (0.82W_c + 0.166)W_c . \\ v_b &= \frac{31.4W_c^2}{1 + 59.5W_c^2} \end{aligned} \quad (4.69)$$

where S is the salinity of the vegetation. It is defined as the total mass of solid salt in grams dissolved in 1 kg of solution and is expressed in parts per thousand on a weight basis. In this chapter, the salinity is assumed to be zero for the simple calculation.

Once vegetation water content percentage is obtained, it can be transformed to the weight per area as follows.

$$W_c [kg / m^2] = 1000 \rho \pi a^2 L h_{layer} W_c [\%] \quad (4.70)$$

First, the soil moisture contribution to the radar backscatter cross section in terms of the incidence angle is shown in Figures 4.24, 4.25, and 4.26. In each legend, DB_xy means a double bounce scattering for the xy polarization.

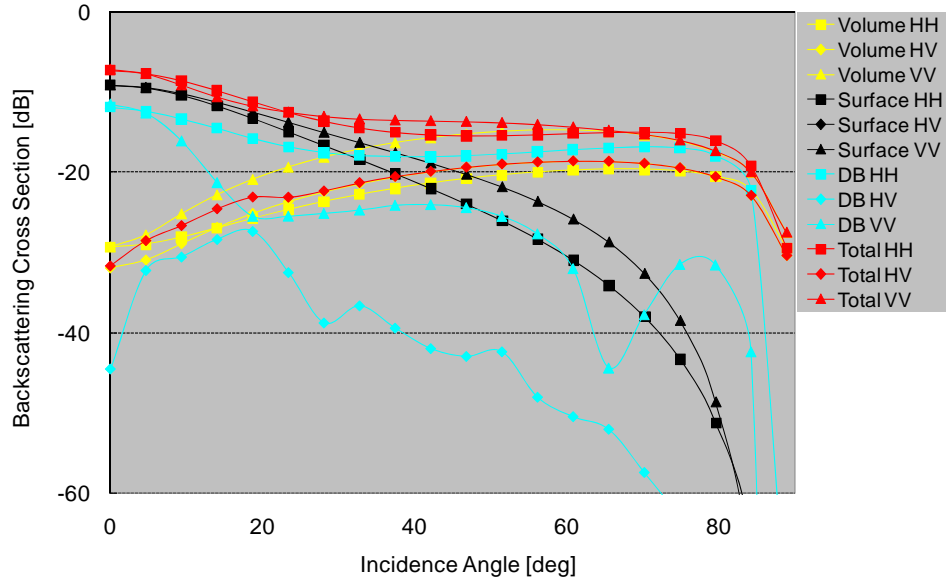


Figure 4.24: Result of the baseline parameters with $M_v=10\%$, $W_c=1.24$ kg, $kh=0.26$, $\sigma_\psi=0.56$

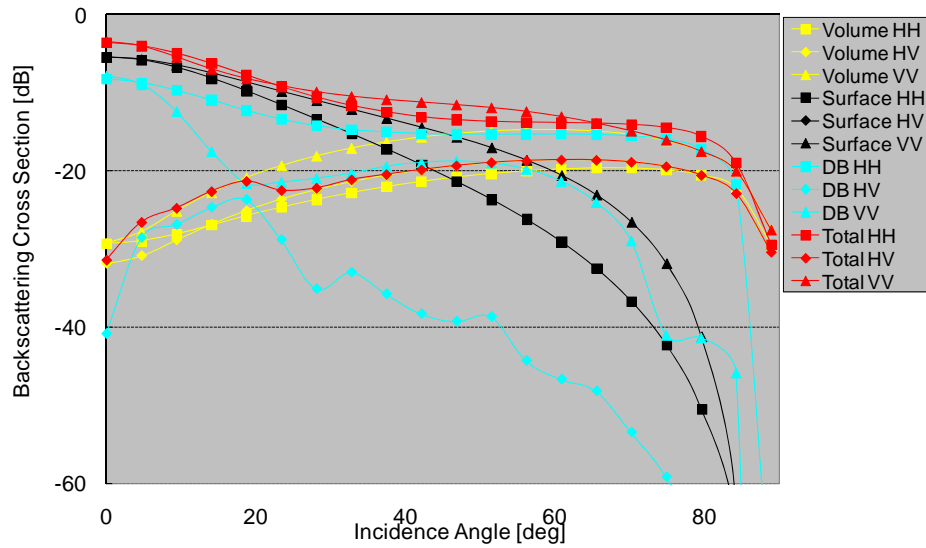


Figure 4.25: Result of the case 4-6-1 with $M_v=30\%$, $W_c=1.24$ kg, $kh=0.26$, $\sigma_\psi=0.56$

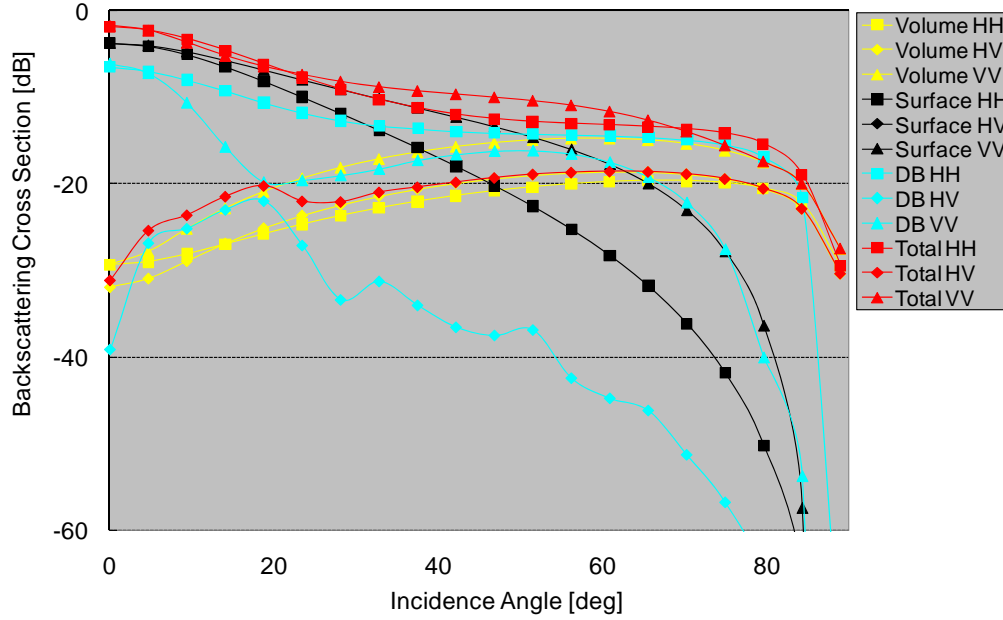


Figure 4.26: Result of the case 4-6-2 with $M_v=60\%$, $W_c=1.24$ kg, $kh=0.26$, $\sigma_v=0.56$

Both the backscattering from the surface and double bounce increase with soil moisture, while the backscattering from the volume stays the same. Since the soil moisture raises the scattering power from the ground, it also increases the double bounce scattering within the same volume layer. The co-polarization responses of the total power are a mixture of the three scattering mechanisms depending on the incidence angle. The cross polarized response, however, comes from contributions by the volume scattering only. This implies to us that the cross polarization can be used to estimate the biomass. Another important feature is the double bounce scattering in Figure 4.24. Its VV polarization response shows a distinct drop at around 65 degrees, while HH does not. This is due to the well known Brewster’s angle of the ground [45]. 10, 30, and 60% of soil moisture correspond to 67, 76, and 82 degree Brewster’s angles, respectively, as shown in Figures 4.24 to 4.26. At the smaller incidence angle, we have another drop of around 20 degrees, even though it is not as clear. This is due to the Brewster’s angle of the cloud of the

cylinders. The important thing is that VV is affected by two Brewster’s angles, and as a consequence VV can be much smaller than the HH at the incidence angle between the two Brewster’s angles. This becomes a critical issue on the dry surface. For example, at 40 degrees in Figures 4.24 and 4.26, VV on the wet surface (Figure 4.26) is about 2dB while the one on dry surface (Figure 4.24) is around 6 dB. The dry surface is more affected by the Brewster’s angles.

Figures 4.24, 4.27, and 4.28 show the contribution of the vegetation water content to the backscatter cross section in terms of the incidence angle.

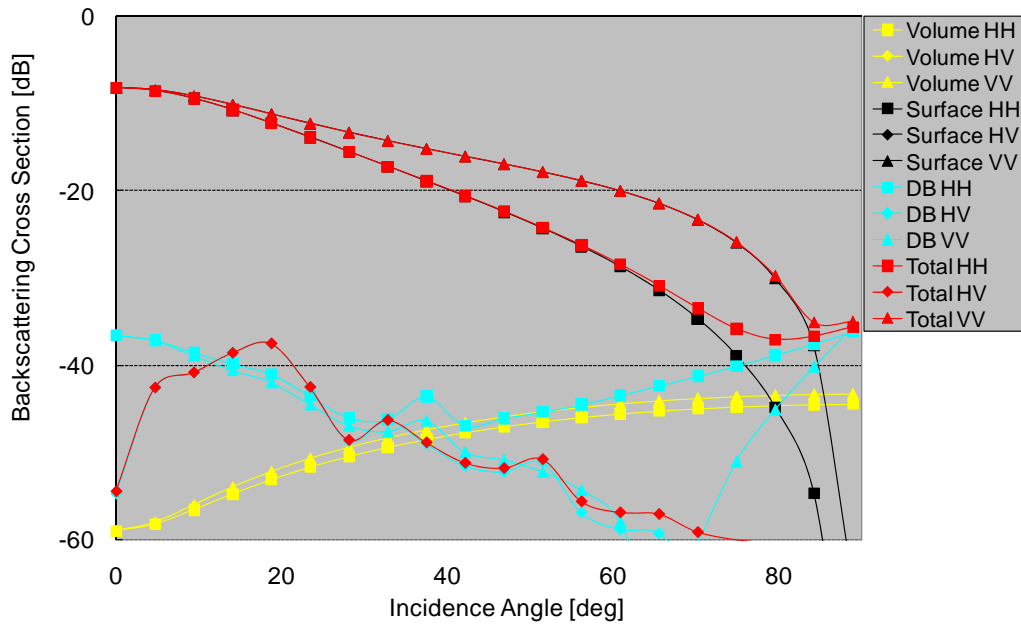


Figure 4.27: Result of the case 4-6-3 with $M_v=10\%$, $W_c=0\text{ kg}$, $kh=0.26$, $\sigma_{\psi}=0.56$

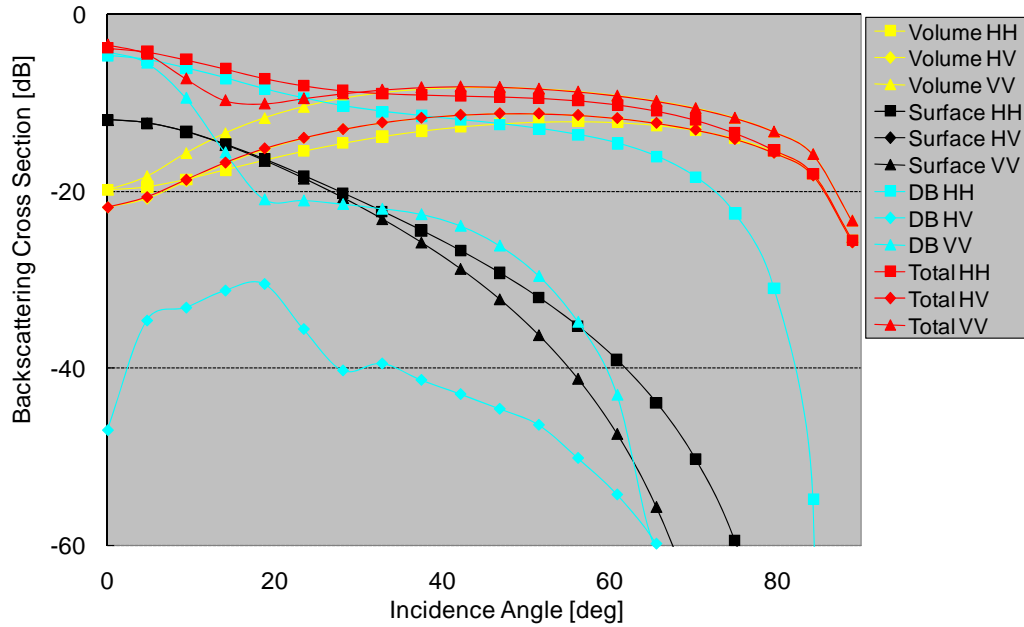


Figure 4.28: Result of the case 4-6-4 with $M_v=10\%$, $W_c=2.54$ kg, $kh=0.26$, $\sigma_\psi=0.56$

As expected, the volume scattering is dominant at the higher vegetation water content, and the total scattering increases as the amount of vegetation increases. The surface scattering is diminished due to the higher extinction caused by strong interaction with the volume component. Though the attenuation coefficient also affects the double bounce scattering, it is not clearly shown, since the strong volume scattering increases the double bounce contribution.

Figures 4.24, 4.29, and 4.30 show the contribution of the surface roughness to the backscatter cross section.

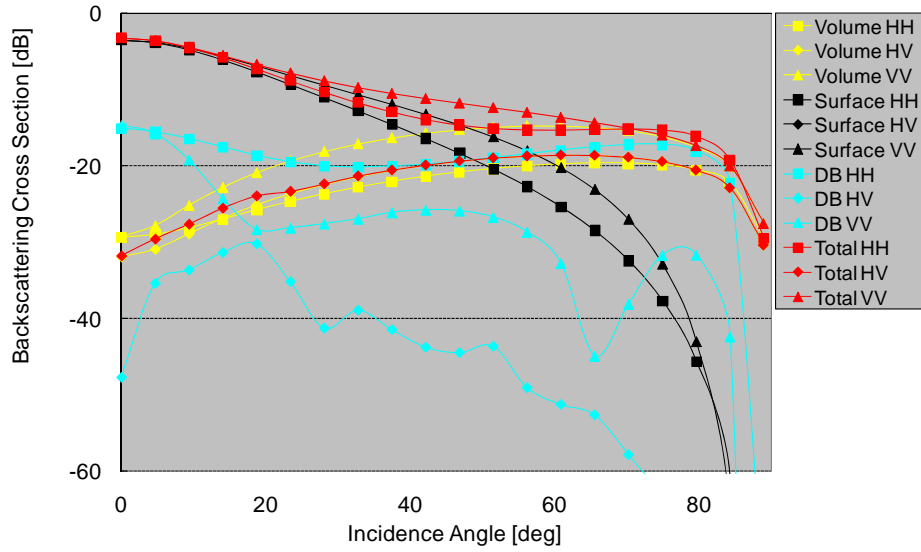


Figure 4.29: Result of the case 4-6-5 with $M_v=10\%$, $W_c=1.24$ kg, $kh=0.5$, $\sigma_\psi=0.56$

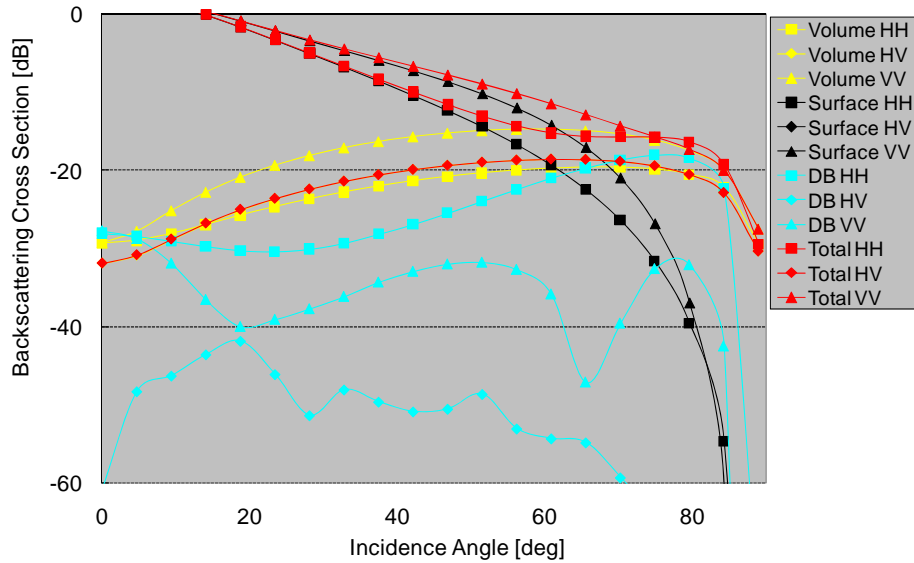


Figure 4.30: Result of the case 4-6-6 with $M_v=10\%$, $W_c=1.24$ kg, $kh=1$, $\sigma_\psi=0.56$

The surface roughness variation does not affect the volume scattering, but the surface scattering is increased. The tendency is similar to the results in terms of the soil moisture. However, the double bounce scattering decreases even though the surface scattering is raised. The Kirckhoff model in (4.47) clearly shows that the forward scattering power is attenuated by the higher value of the surface roughness, kh .

Finally, the scattering power in terms of the cylinder's distribution is shown in Figures 4.24, 4.31, and 4.32.

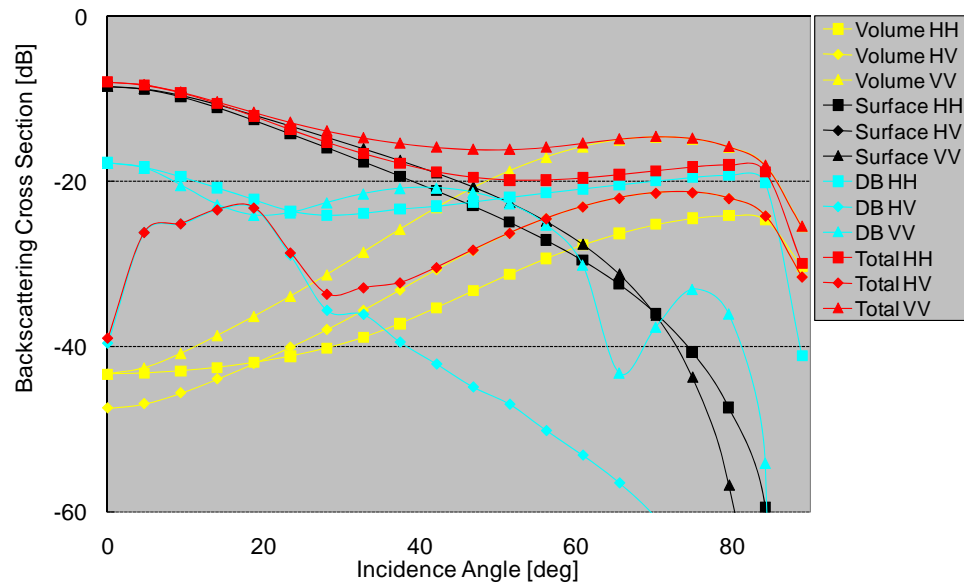


Figure 4.31: Result of the case 4-6-7 with $M_v=10\%$, $W_c=1.24$ kg, $kh=0.26$, $\sigma_\psi=0.30$

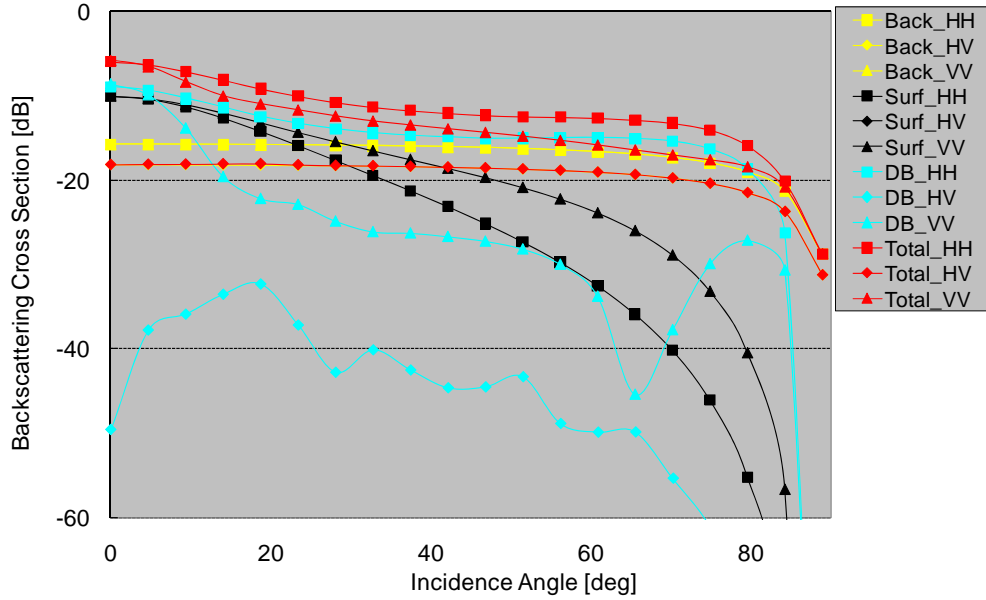


Figure 4.32: Result of the case 4-6-8 with $M_v=10\%$, $W_c=1.24$ kg, $kh=0.26$, $\sigma_\psi=0.91$

These plots show that the backscatter cross section does not change much at an incidence angle larger than 50 degrees. On the other hand, scattering from the volume layer at incidence angle smaller than 50 degrees is significantly increased in terms of the vegetation randomness. This is because the higher randomness of the volume component provides more chances that the incident wave is orthogonal to the cylinder. The backscattering from the oriented cylinder is maximized when the incident wave direction is orthogonal to the length direction of the cylinder. Also the chances are increased more with higher randomness than with lower randomness when the mean orientation angle is close to zero. Conversely, the chances are decreased when the mean angle is close to 90 degrees.

As in [46], DSM allows us to see how the backscattering from vegetated terrain is sensitive to soil moisture with various physical conditions, such as the amount of vegetation. Van Zyl defined the slope of backscattering from a vegetated area with a

specific soil moisture. For example, a plot of the total backscatter cross sections for HH, HV, and VV at $W_c=1.24\text{ kg}$ is shown in Figure 4.33. Note that the incidence angle is fixed at 40 degrees.

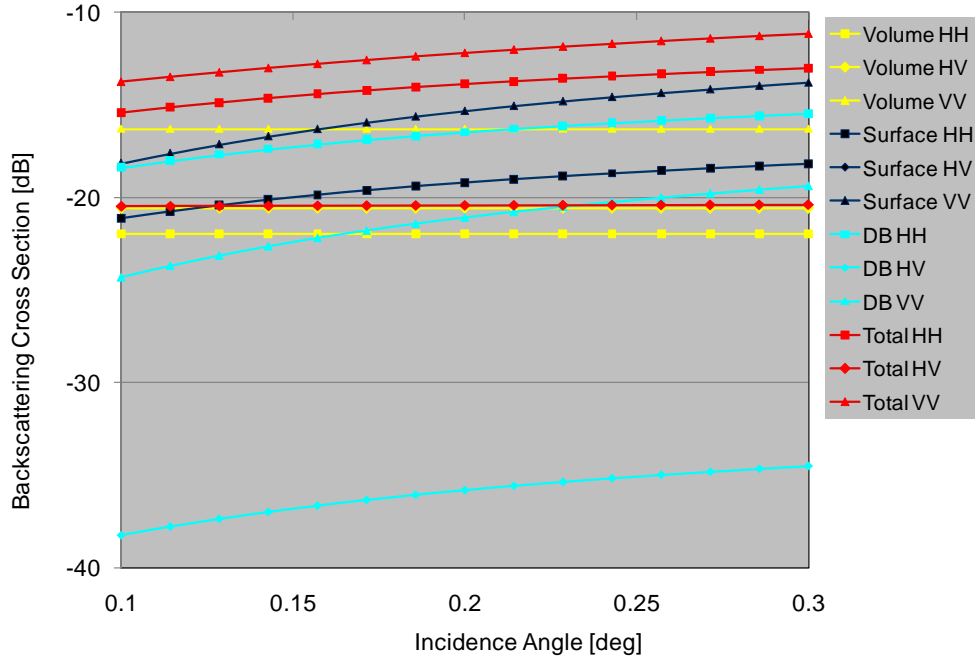


Figure 4.33: Backscatter cross section with $M_v=10\sim30\%$, $W_c=1.24\text{ kg}$, $kh=0.26$, $\sigma_\psi=0.56$

Ulaby et al. points out that the backscatter cross section can be related to the soil moisture using the following expression in [37].

$$\sigma_{xy}[dB] = A_{xy}M_v + B_{xy} \tag{4.71}$$

where x and y are h or v. Note that the backscatter cross section is in dB (decibels). The slope A expresses how the radar reflection is sensitive to the soil moisture. In the example in Figure 4.33, they are calculated to be

$$\begin{aligned}
 A_{hh} &= 11.8 \\
 A_{hv} &= 0.49 \\
 A_{vv} &= 12.8
 \end{aligned}
 \tag{4.72}$$

You can see the sensitivity of the slope to the vegetation water content in Figure 4.34.

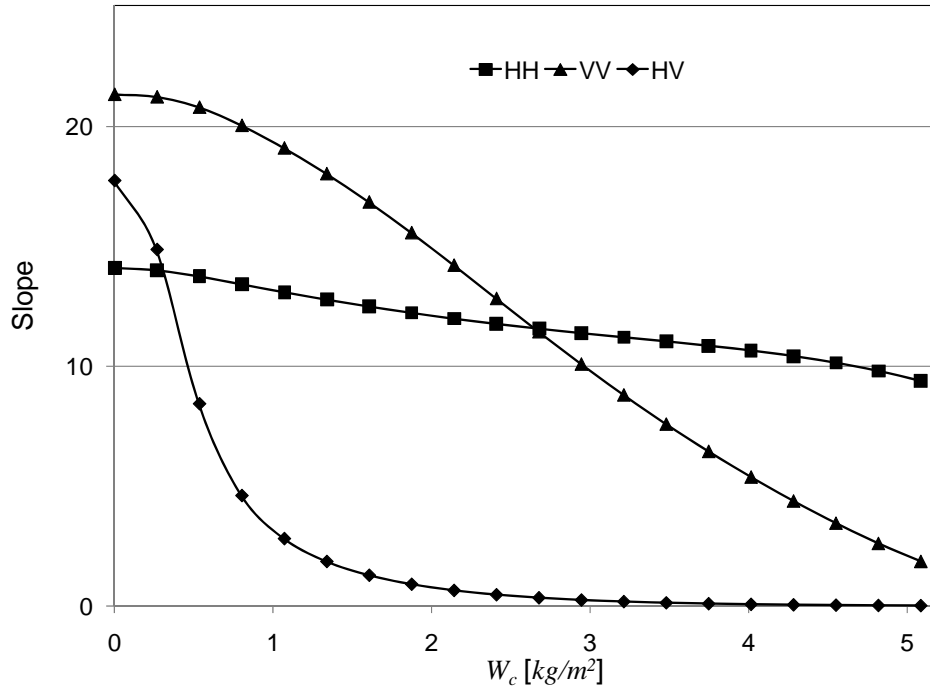


Figure 4.34: Slope with $M_v=10\sim30\%$, $kh=0.26$, $\sigma_\psi=0.56$ at $\theta_i=40$ deg

This result shows that the sensitivities for both co-polarization ratios gradually decrease, while the one for cross polarization suddenly drops and is then close to zero after $W_c=1$ kg/m^2 . This implies that the cross polarization may not be appropriate to infer the soil moisture because the effective range is quite narrow between 0 and 0.5 kg/m^2 . Another feature of the plot is that the slope of VV is larger than HH at first, and then becomes smaller than VV after around $W_c=1.3$ kg/m^2 . With the lower vegetation water content, the surface scattering mechanism is the main contributor to the total scattering, so that VV is

more sensitive than HH. The vegetation component decreases both contributions in terms of the amount of the vegetation. The cosine squared distribution with zero mean orientation angle is biased to the vertical direction on the ground. Since such vegetation interacts with the vertically polarized wave more than the horizontal one, it eventually attenuates the vertically polarized wave more. The effect of the vegetation becomes pronounced with higher vegetation water content. Therefore VV achieves higher sensitivity at lower levels of vegetation water content and is then flipped after a certain amount of the vegetation water content.

Similarly, Figure 4.35 provides the sensitivity plot in terms of the surface roughness.

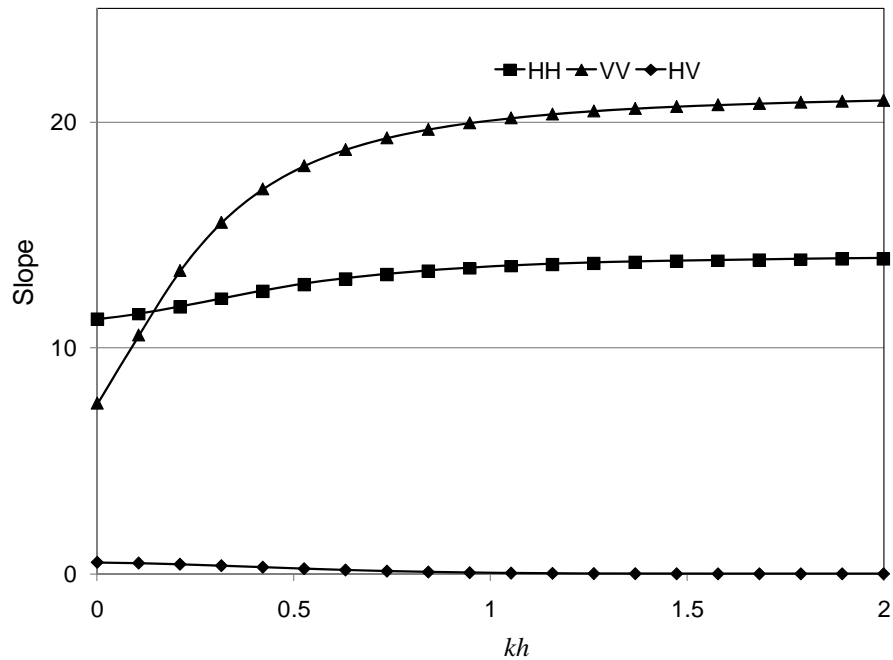


Figure 4.35: Slope with $M_v=10\sim30\%$, $W_c=1.24$ kg, $\sigma_v=0.56$ at $\theta_i=40$ deg

HV is significantly lower over the entire range of roughness, since the first-order surface scattering model tells that the cross polarized response is zero. The co-polarizations increase in sensitivity in terms of roughness until $kh=1$, and they do not change much

afterward. In addition, VV is lower than HH at kh less than 0.1. Due to the distribution of the vegetation, VV scattering is more attenuated than HH at kh lower than 0.1. At higher values of kh , VV increases in sensitivity in terms of roughness. HH also grows in sensitivity but the rate is much less than VV. This is because vegetation with a cosine squared distribution does not affect HH much, so that the increase in sensitivity is not as pronounced as that of VV. Above $kh = 1$ most of the interference from the vegetation is gone, and the slopes for both co-polarizations are affected primarily by surface roughness.

Chapter V

Quantitative Analysis of the Decomposition Techniques

Two decomposition techniques and the discrete scatterer model have been thoroughly discussed. In this chapter, NNED and ANNED will be applied to various types of vegetated terrains generated by DSM, and the effectiveness of each decomposition algorithm will be evaluated quantitatively. A cube technique, which will be used to retrieve soil moisture in Chapter VI, is also used to display the results.

5.1 Test Scenario

Backscattering from a bare surface can be expressed as a function of the surface roughness and dielectric constant (i.e., soil moisture), as shown in Section 4.4. If a surface is covered by vegetation, the backscattering from it is affected by this structure and the statistical distribution of branches or leaves. In this chapter, we will model such a vegetated terrain by varying four of the influential parameters: the soil moisture, surface roughness, vegetation water content, and randomness of the volume component. For simplicity, we use a grassland model for the baseline parameters as shown in Table 5.1.

Table 5.1: Baseline parameters for the test scenario

θ_i (deg.)	λ (m)	L (m)	h_{layer} (m)	a (m)	l (cm)	ψ_0 (deg.)	σ_δ	ρ (cylinders/m ³)
40	0.24	0.5	0.5	0.002	5	0	0.91	900

The four variables are given in Table 5.2.

Table 5.2: Variables for the test scenario

M_v (%)	W_c (kg/m ²)	kh	σ
0-60	0-2.54	0.1-2	0.30, 0.56, 0.91

Note that $\sigma_v=0.56$ and 0.91 correspond to a cosine squared distribution and uniform distribution, respectively.

The cube in Figure 5.1 neatly displays the backscatter cross section in terms of the three variables. The axes are assigned to the soil moisture (M_v), surface roughness (kh), and vegetation water content (W_c). The figure also defines three view angles covering all dimensions of the cube. One of these view angles (A, B, or C) will be specified to indicate the view angle used to display the data.

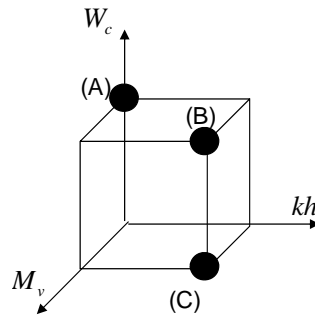


Figure 5.1: Cube to express the backscatter cross section in terms of the three physical parameters: the soil moisture (M_v), surface roughness (kh), and vegetation water content (W_c). The three view angles (A, B, C) are also shown.

The backscatter cross sections for the co- and cross polarizations are shown in Figures 5.2 ($\sigma_v=0.30$), 5.3 ($\sigma_v=0.56$), and 5.4 ($\sigma_v=0.91$). The columns and rows show the different polarizations and different view angles, respectively. Note that the color range for each cube is shown in the associated color bar.

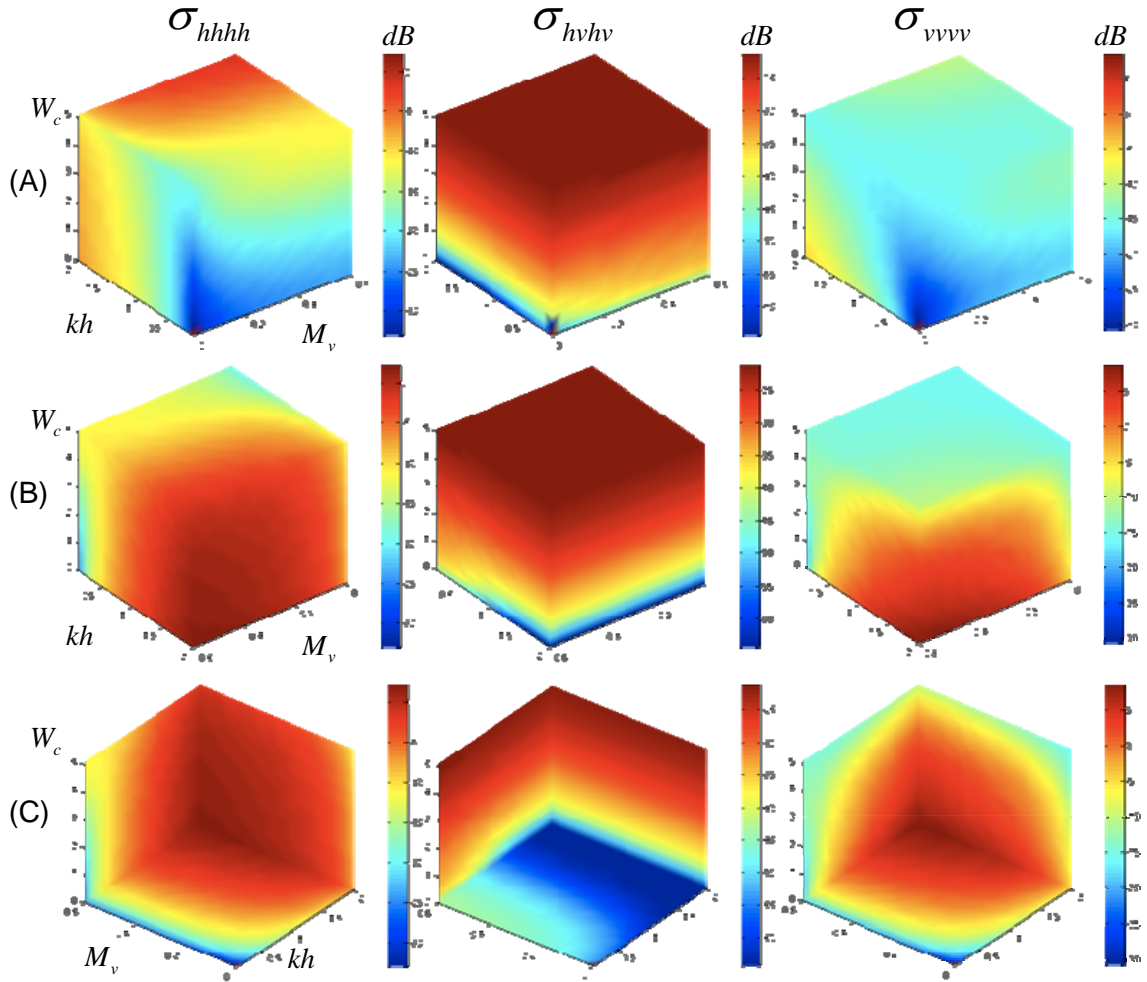


Figure 5.2: Input data from DSM with the given test scenario: $\sigma_v=0.30$. Each row corresponds to one of the view angles defined in Figure 5.1, while each column corresponds to the backscatter cross section of σ_{hhhh} (right), $\sigma_{hv hv}$ (center), and σ_{vvvv} (right), respectively.

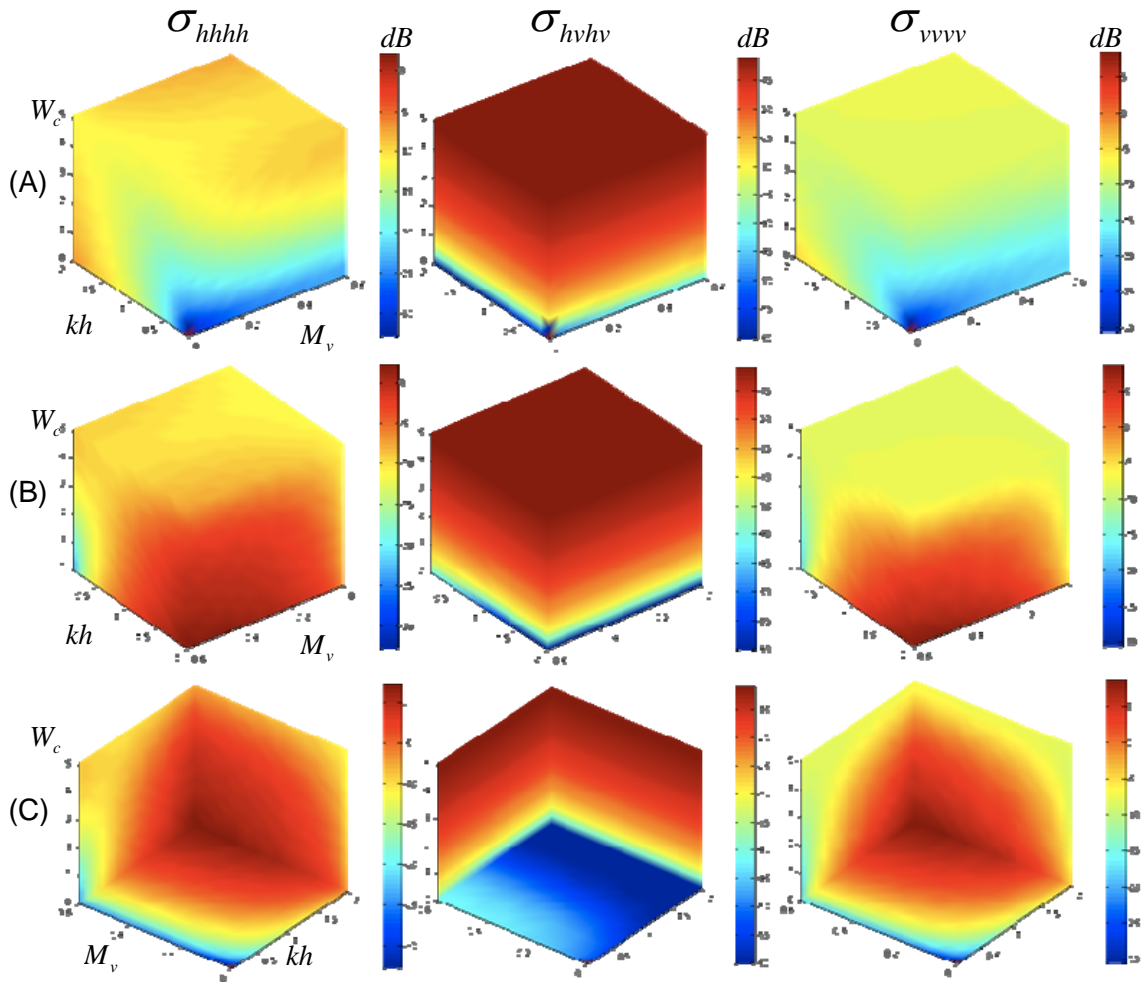


Figure 5.3: Input data from DSM with the given test scenario: $\sigma_v=0.56$. Each row corresponds to one of the view angles defined in Figure 5.1, while each column corresponds to the backscatter cross section of σ_{hhhh} (left), $\sigma_{hv hv}$ (center), and σ_{vvvv} (right), respectively.

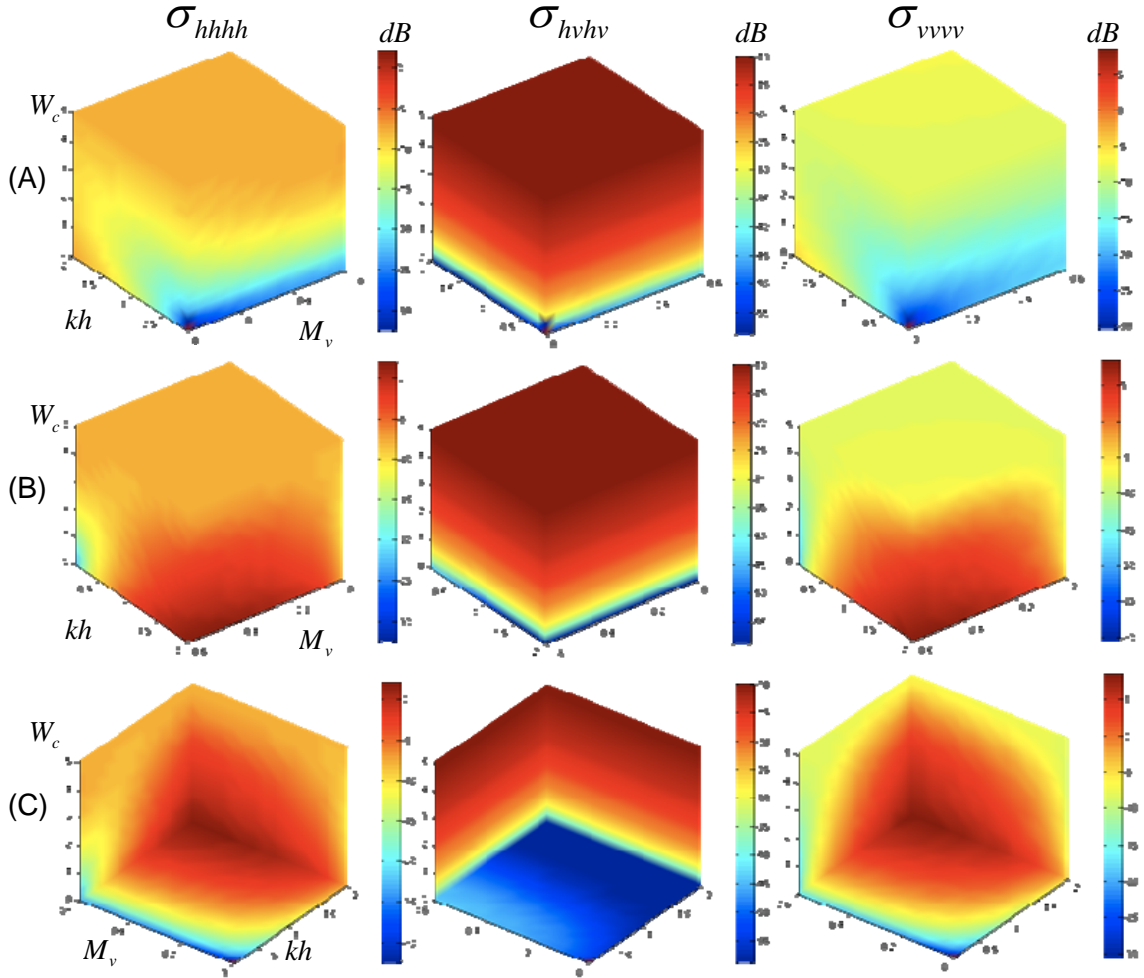


Figure 5.4: Input data from DSM with the given test scenario: $\sigma_v=0.91$. Each row corresponds to one of the view angles defined in Figure 5.1, while each column corresponds to the backscatter cross section of σ_{hhhh} (left), $\sigma_{hv hv}$ (center), and $\sigma_{vv vv}$ (right), respectively.

It is clear that the cross polarization is highly sensitive to the amount of vegetation, but is not sensitive to the other two variables. This implies that the polarization is a key parameter to estimate the amount of vegetation, as pointed out in [12]. The results from the view angle (A) of the co-polarizations show that the lowest power occurs at their origin, and it spherically increases in terms of each variable. This follows from the characteristics of SPM, which is strongly a function of the surface roughness and soil moisture, and also

demonstrates the properties discussed in Section 4.6 (Figures 4.27 and 4.28). However, results from the view angles (B) and (C) exhibit the opposite behavior, where the maximum power occurs at the center (the maxima of the roughness and soil moisture and the minimum of the vegetation water content), and spherically decreases as the roughness and soil moisture decrease and the vegetation water content increases. The maximum scattering occurs when both the soil moisture and surface roughness are maximized. One may also expect to have the maximum scattering occur with maximum vegetation water content as in view angle (A), but it does not. The reason lies in attenuation of the volume layer. We know the scattering from the volume layer increases as the vegetation water content increases. At the same time, the strong interaction between the incoming wave and the volume layer increases the attenuation coefficient, as discussed in Section 4.3.1. At middle values of vegetation water content and the maximum of the surface roughness and soil moisture, the scatterings from the surface and double bounce are still larger than the backscattering from the volume layer. However, at the maximum vegetation water content, the volume scattering is significant compared to scattering from the other scattering mechanisms, so the volume layer attenuates much of the scattering from the surface and double bounce.

Another important feature exists at the top of the cubes. The case with the uniform distribution in Figure 5.4 does not show a specific texture in the area, and the case of the cosine squared distribution in Figure 5.3 shows some texture but it is vague. However, the case with lower roughness in Figure 5.2 shows the clear pattern on the top of the horizontal polarization. The pattern is almost the same as that at the bottom, so the scattering at the top is contributed by the scattering from the surface and double bounce. Due to its statistical properties (zero orientation angle and the narrower distribution), most of the vertically polarized response from the surface and double bounce are significantly attenuated while the horizontally polarized response survives. This fact is important because we can see the ground scattering well even with significant vegetation, depending on the randomness.

5.2 Simulation Results and Analysis

First, the randomness and mean orientation angle of the volume component estimated by ANNED are shown. Figures 5.5, 5.6, and 5.7 correspond to the cases of $\sigma_\psi=0.30$, cosine squared distribution, and uniform distribution, respectively. Each orientation angle cube has a range between 0 and 90 degrees, which correspond to vertical ($\phi_\psi=0$) and horizontal orientation angles ($\phi_\psi=90$), respectively. Also the minimum and maximum values on the randomness cubes are related to the delta function ($\sigma_\psi=0$) and uniform distributions ($\sigma_\psi=0.91$), respectively.

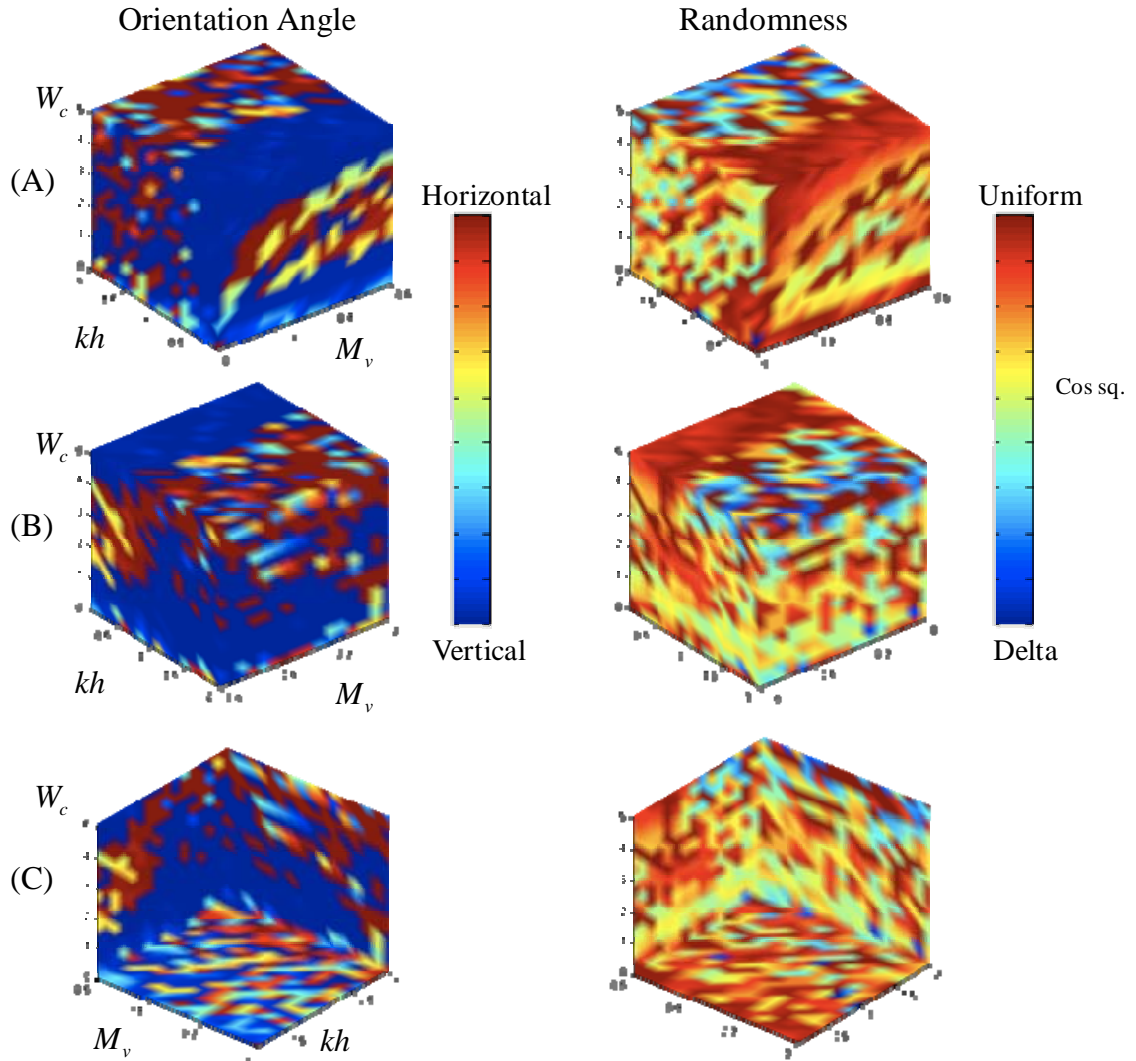


Figure 5.5: Estimated randomness and mean orientation angle: $\sigma_\psi=0.30$. Each row corresponds to each view angle defined in Figure 5.1 while each column corresponds to the orientation angle (right) and the randomness (right), respectively.

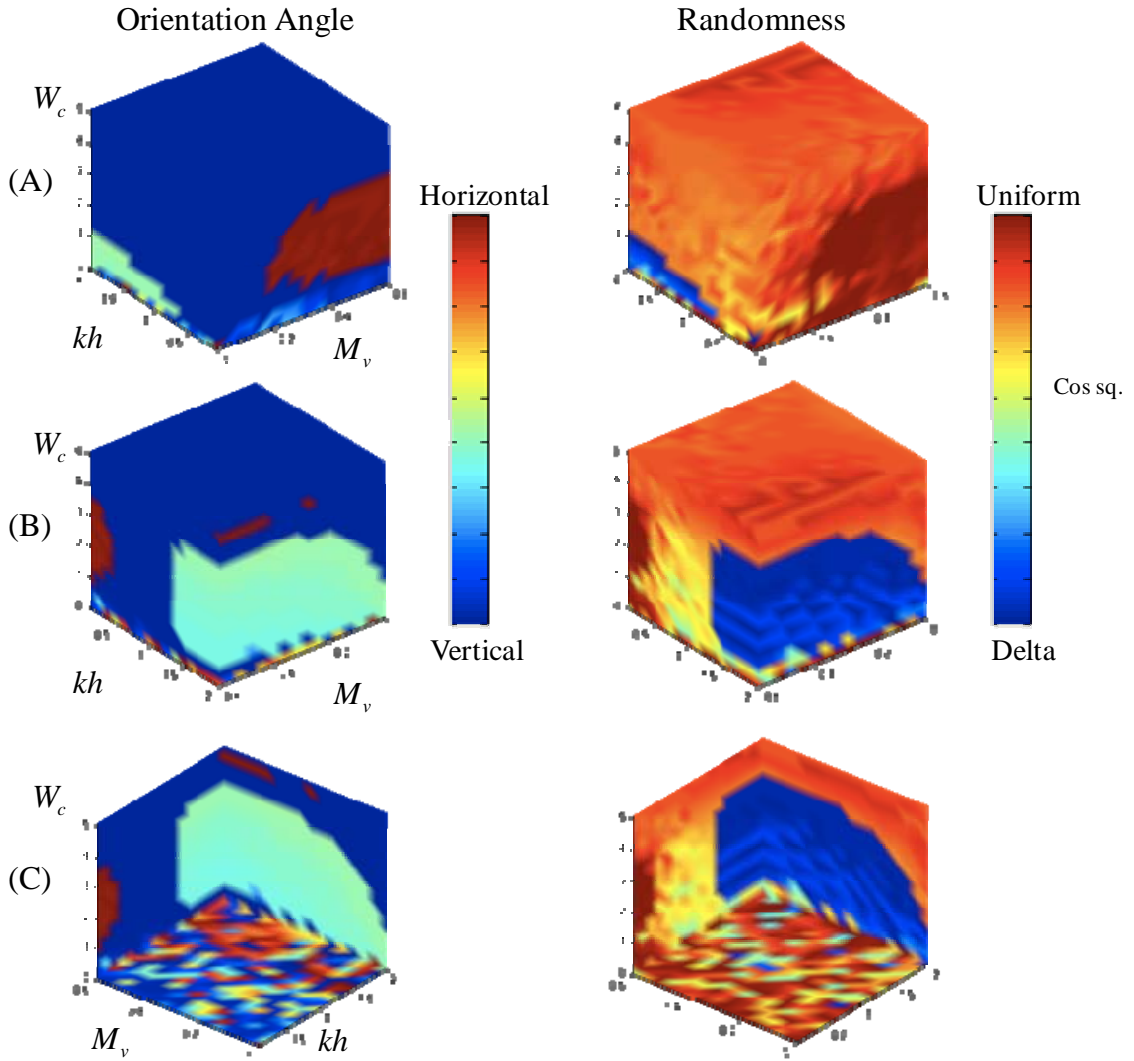


Figure 5.6: Estimated randomness and mean orientation angle: $\sigma_\psi=0.56$. Each row corresponds to each view angle defined in Figure 5.1 while each column corresponds to the orientation angle (right) and the randomness (right), respectively.

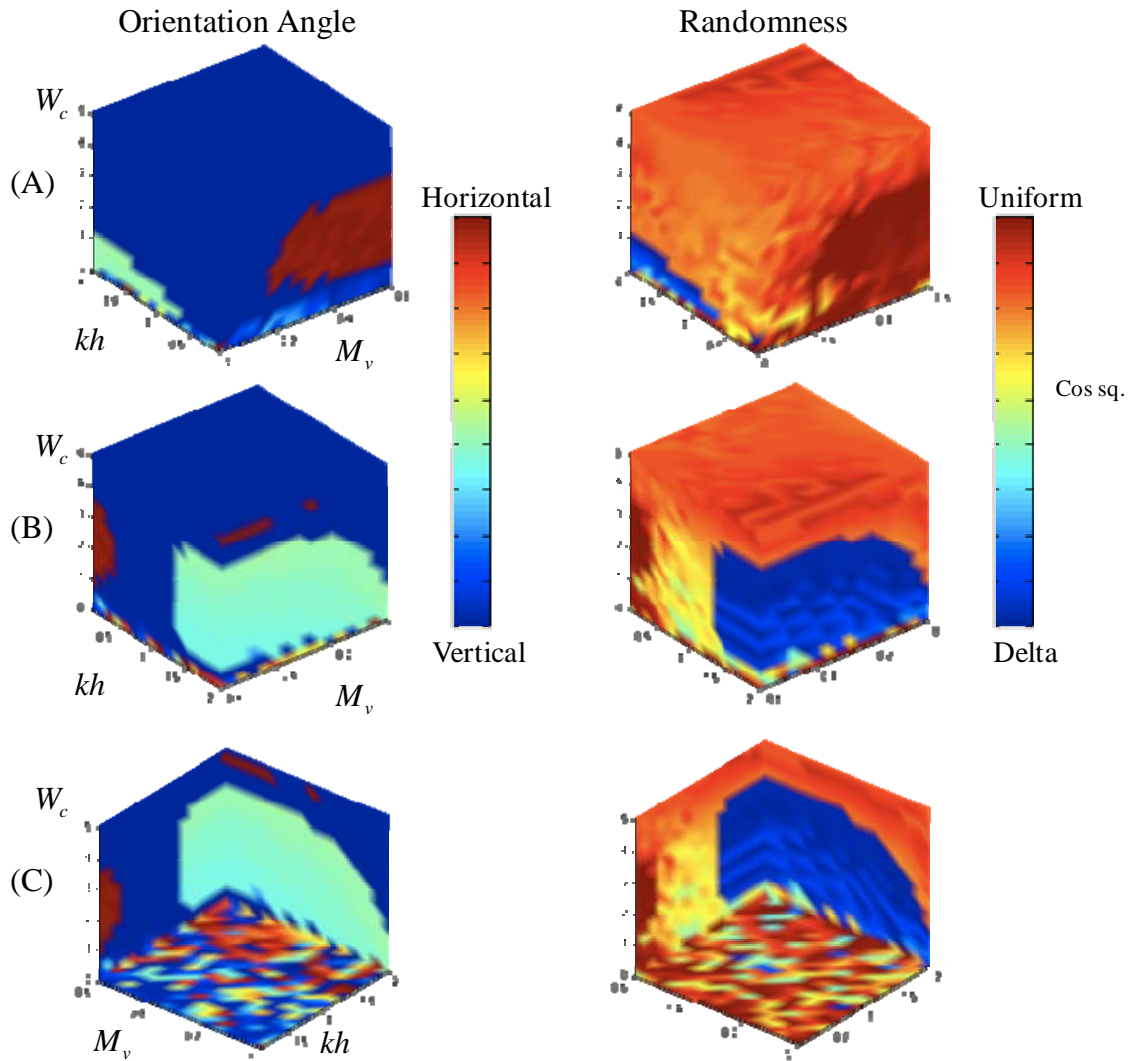


Figure 5.7: Estimated randomness and mean orientation angle: $\sigma_\psi=0.91$. Each row corresponds to each view angle defined in Figure 5.1 while each column corresponds to the orientation angle (right) and the randomness (right), respectively.

The result of the lower randomness in Figure 5.5 is highly unstable, due to the small amount of power from the volume component. As discussed in Section 4.6 (Figures 4.31 and 4.32), the lower randomness with the zero orientation angle of the volume component causes lower backscattering. On the other hand, the results from the cosine squared distribution in Figure 5.6 seem stable. The region dominated by volume scattering yields

zero as the mean orientation angle and around 0.75 as the randomness. One may expect the randomness should be around 0.56, as defined in the scenario. This discrepancy comes from the fact that the angle definition on the ground is different from the one at the receiver, as shown in Figure D.2, which shows that the randomness 0.56 on the ground corresponds to 0.75 at the receiver at $\theta_i=40$ deg. For the case of the uniform distribution in Figure 5.7, the randomness cube is at around 0.9, as we expected. The mean orientation angle cube is unstable because the uniform distribution has no mean orientation angle.

Both NNED and ANNED are expressed as

$$C_m = xC_v + yC_d + zC_g \quad (5.1)$$

and the power in each component normalized by the total power is defined as follows.

$$P_v = \frac{xP(C_v)}{P(C_m)}, P_d = \frac{yP(C_d)}{P(C_m)}, P_g = \frac{zP(C_g)}{P(C_m)} \quad (5.2)$$

Figures 5.8, 5.9, and 5.10 correspond to the estimated power for the volume, double bounce and surface components, respectively, at $\sigma_v=0.30$. Four cubes are shown for each view angle: the true data, two results from NNED assuming cosine squared and uniform distributions, and result from ANNED.

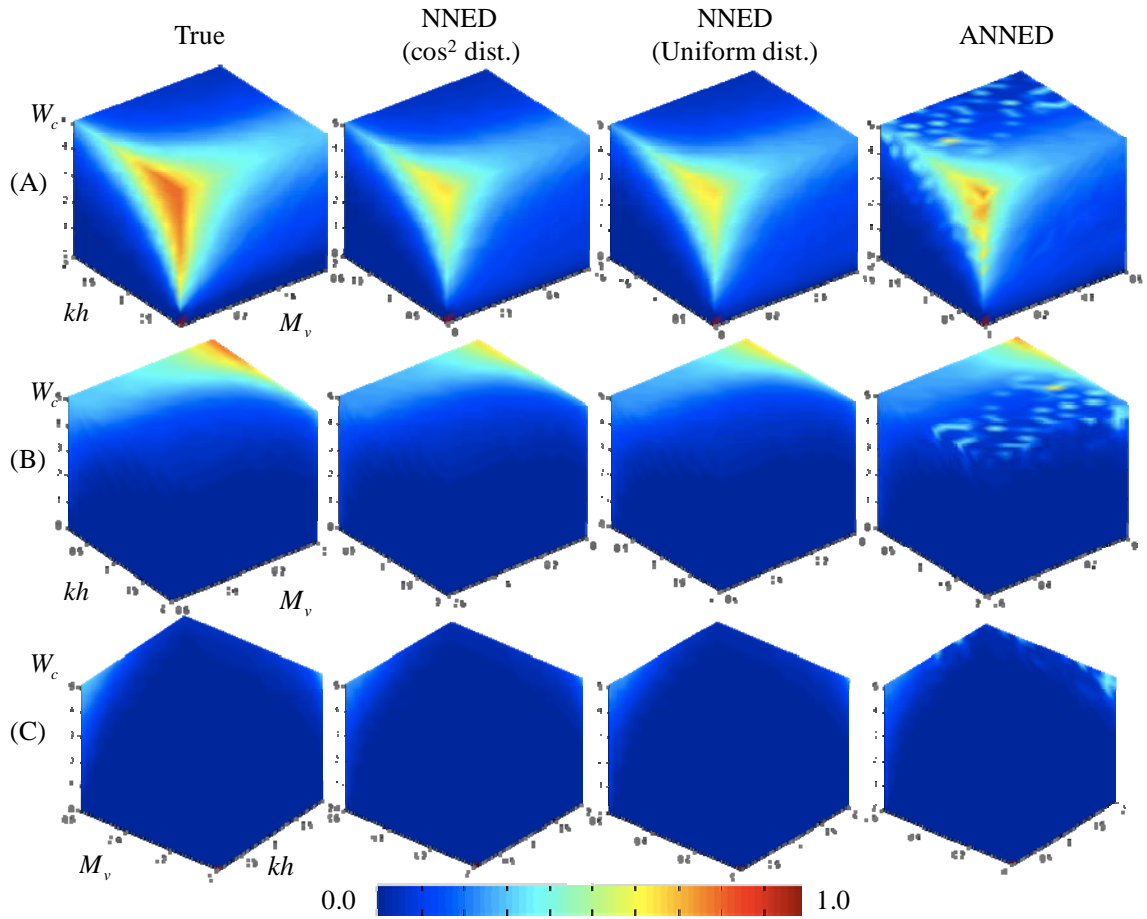


Figure 5.8: Estimated power for the volume component: $\sigma_v=0.30$. Each row corresponds to each view angle defined in Figure 5.1 while the columns correspond to the true data, results from NNED assuming the cosine squared and uniform distributions, and results from ANNED, respectively from left to right.

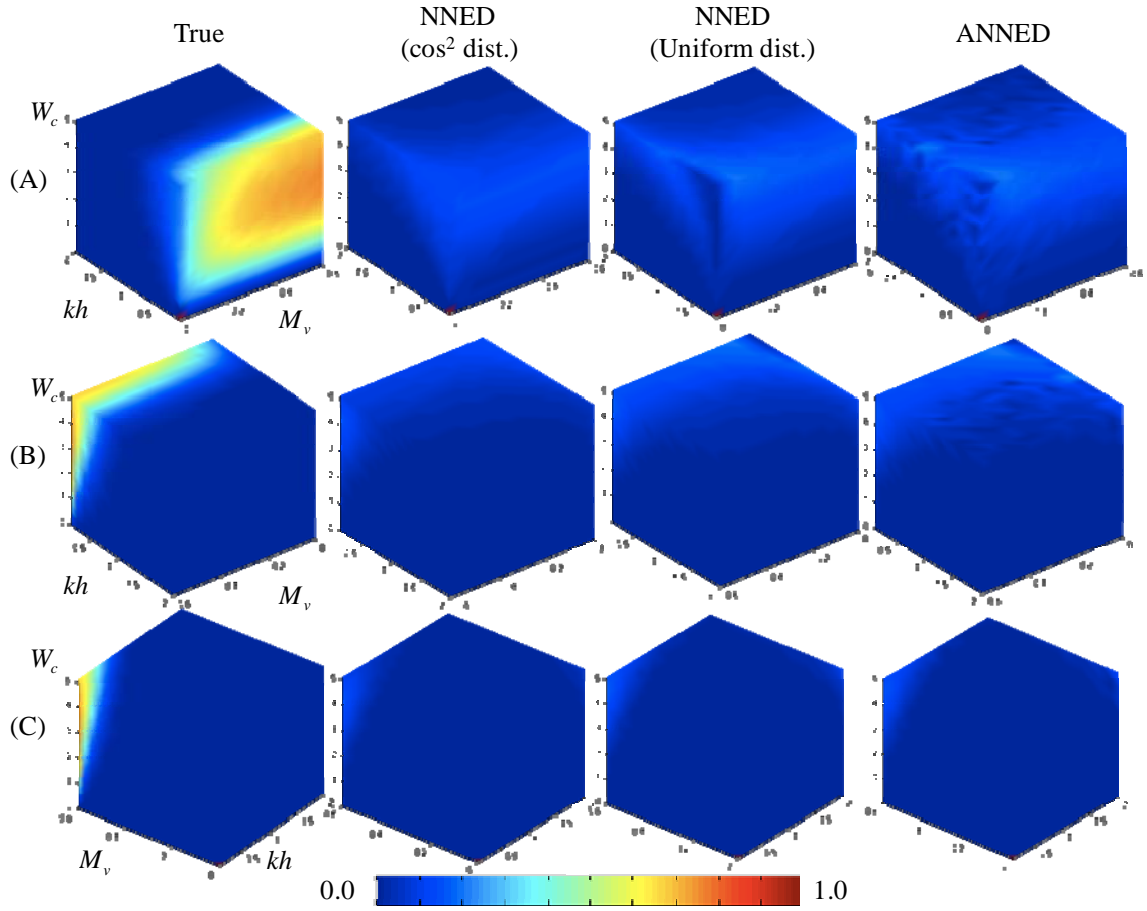


Figure 5.9: Estimated power for the double bounce component: $\sigma_\psi=0.30$. Each row corresponds to each view angle defined in Figure 5.1 while the columns correspond to the true data, results from NNED assuming the cosine squared and uniform distributions, and results from ANNED, respectively from left to right.

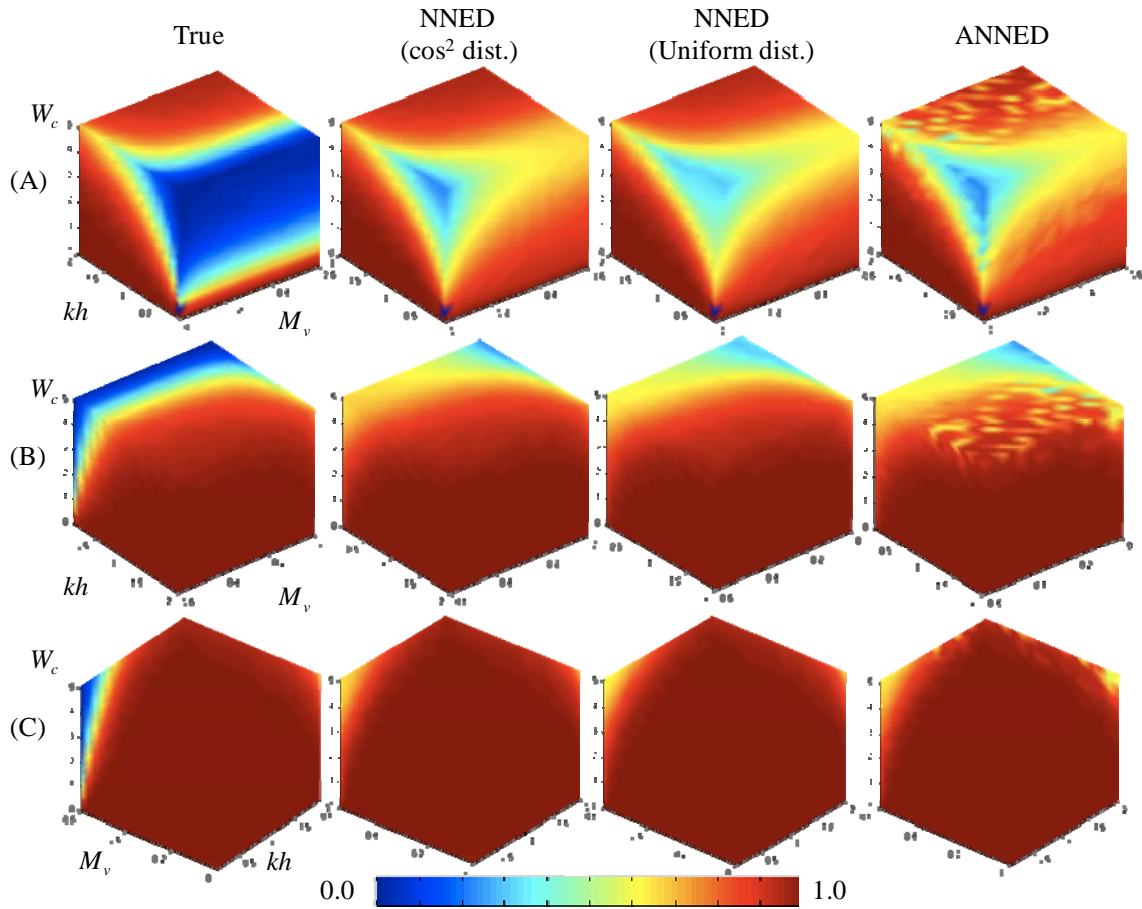


Figure 5.10: Estimated power for the surface component: $\sigma_v=0.30$. Each row corresponds to each view angle defined in Figure 5.1 while the columns correspond to the true data, results from NNED assuming the cosine squared and uniform distributions, and results from ANNED, respectively from left to right.

The true data in Figure 5.8 tells that a strong volume contribution occurs only in the limited area around the center of view angle (A). This causes oscillations shown in the result from ANNED. The ANNED estimation of the volume component is disturbed by the strong scattering from the surface and double bounce even at higher vegetation water content. Nonetheless, ANNED can extract a relatively strong volume contribution compared to the others.

The true data in Figure 5.9 shows that the primary double bounce contribution occurs at only lower roughness. This is because the surface scattering model, the Kirchoff approximation, attenuates scattering as the surface roughness increases as shown in (4.52). All three techniques fail to extract this double bounce contribution. The criterion to determine the double bounce component is that the phase of σ_{hhvv} should be more than 90 degrees or less than -90 degrees, as discussed in Section 3.3. Figure 5.11 shows the phase history of the double bounce component in terms of the radius of the cylinder. The simulation parameters are the same as above with a variable number of cylinders used to keep $W_c=1.7 \text{ kg/m}^2$ so that the dielectric constants of the cylinders stay the same. The other variables are fixed at $M_v=60 \%$ and $kh=0.13$.

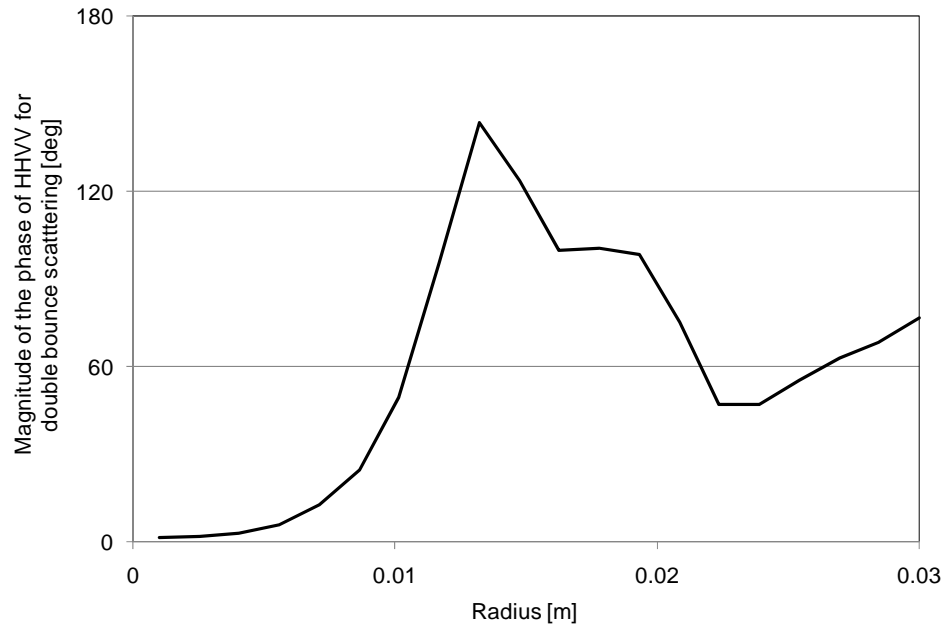


Figure 5.11: Magnitude of the phase of σ_{hhvv} from the double bounce component in terms of cylinder radius

The phase is unstable, and it is often out of the angle range that we expected. The radius 2 mm is close to zero so that the criterion cannot be used to judge the signal to be double bounce scattering. Figure 5.12 shows the backscatter cross sections of the co-

polarizations from a single cylinder with the ratio of the two co-polarizations. Note that it displays the result from direct backscattering, not double bounce.

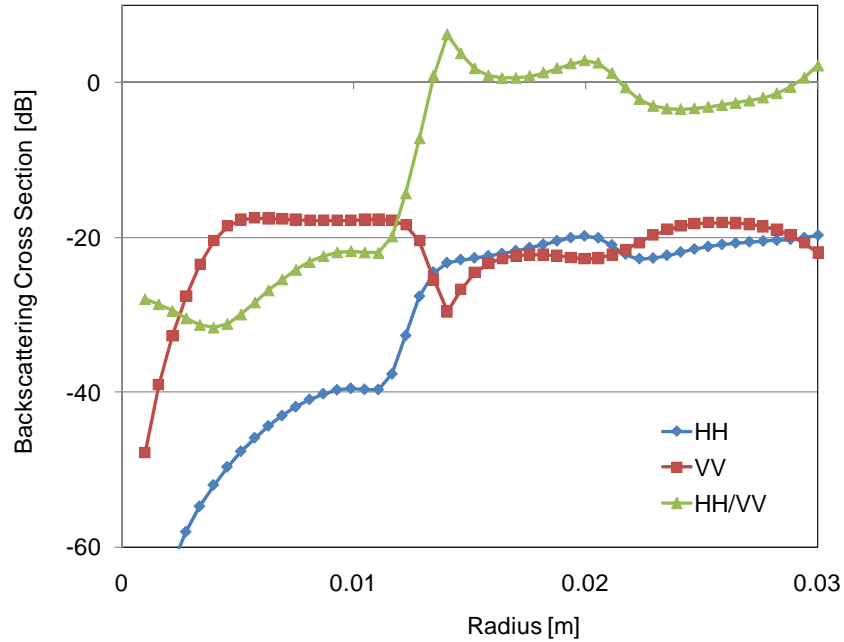


Figure 5.12: Backscatter cross section of the co-polarized responses and their ratio of them. All values are in dB.

Clearly, the phase history shows a strong correlation to the ratio of the co-polarizations. This tells us two important things. First, the radius of the cylinder strongly affects the phase of σ_{hhvv} . Second, a large difference between the two co-polarized responses may not flip the phase. This is shown at radii between 0 and 0.01 m in the figure. Remember that the Brewster’s angle pulls the vertical polarized scattering down, as discussed in Section 4.6, and causes the larger gap between the two co-polarizations as seen for radii between 0 and 0.01 m. We need further investigation to determine the best criteria to discriminate the double bounce and ground scatterings. The three techniques do not show much difference because they use the same criterion for this discrimination.

Figures 5.13, 5.14, and 5.15 correspond to the estimated power for the volume, double bounce, and surface, respectively, in the case of $\sigma_v=0.56$.

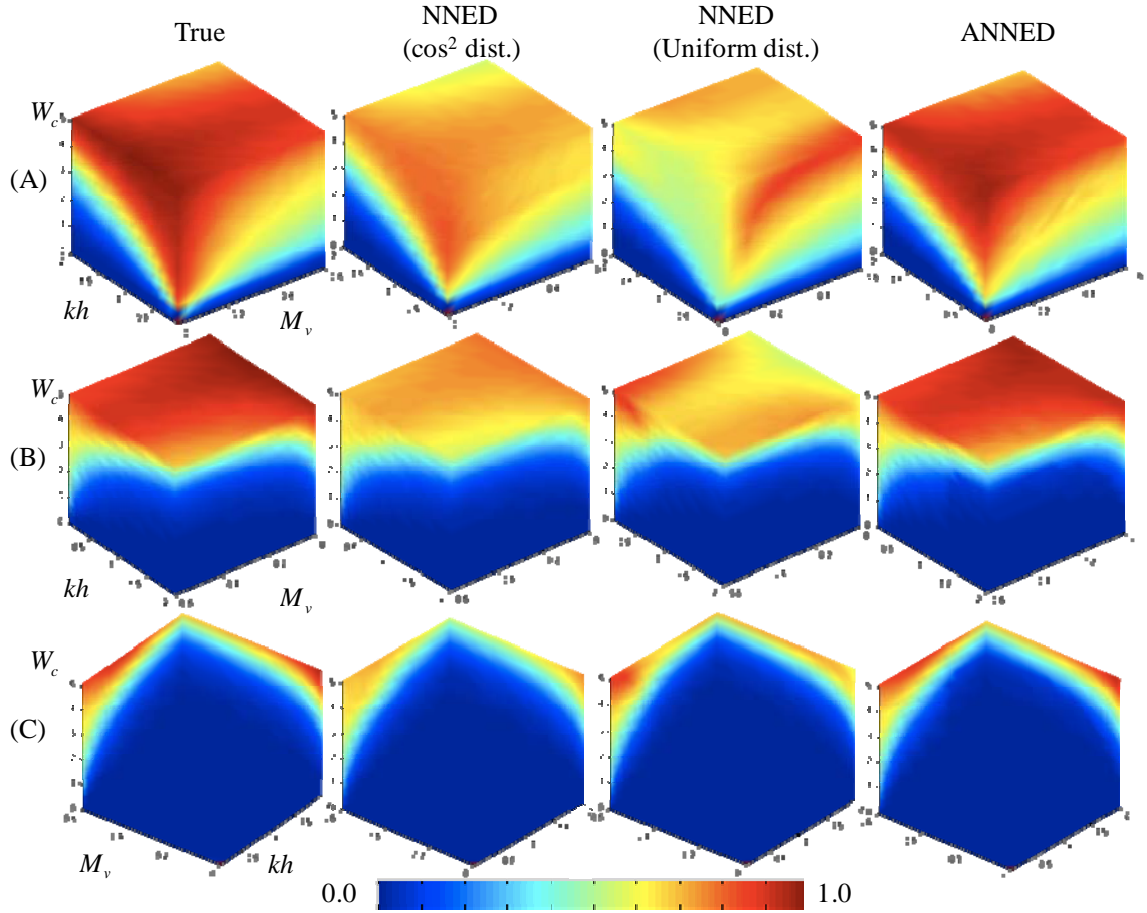


Figure 5.13: Estimated power for the volume component: $\sigma_v=0.56$. Each row corresponds to each view angle defined in Figure 5.1, while the columns correspond to the true data, results from NNED assuming the cosine squared and uniform distributions, and results from ANNED, respectively from left to right.

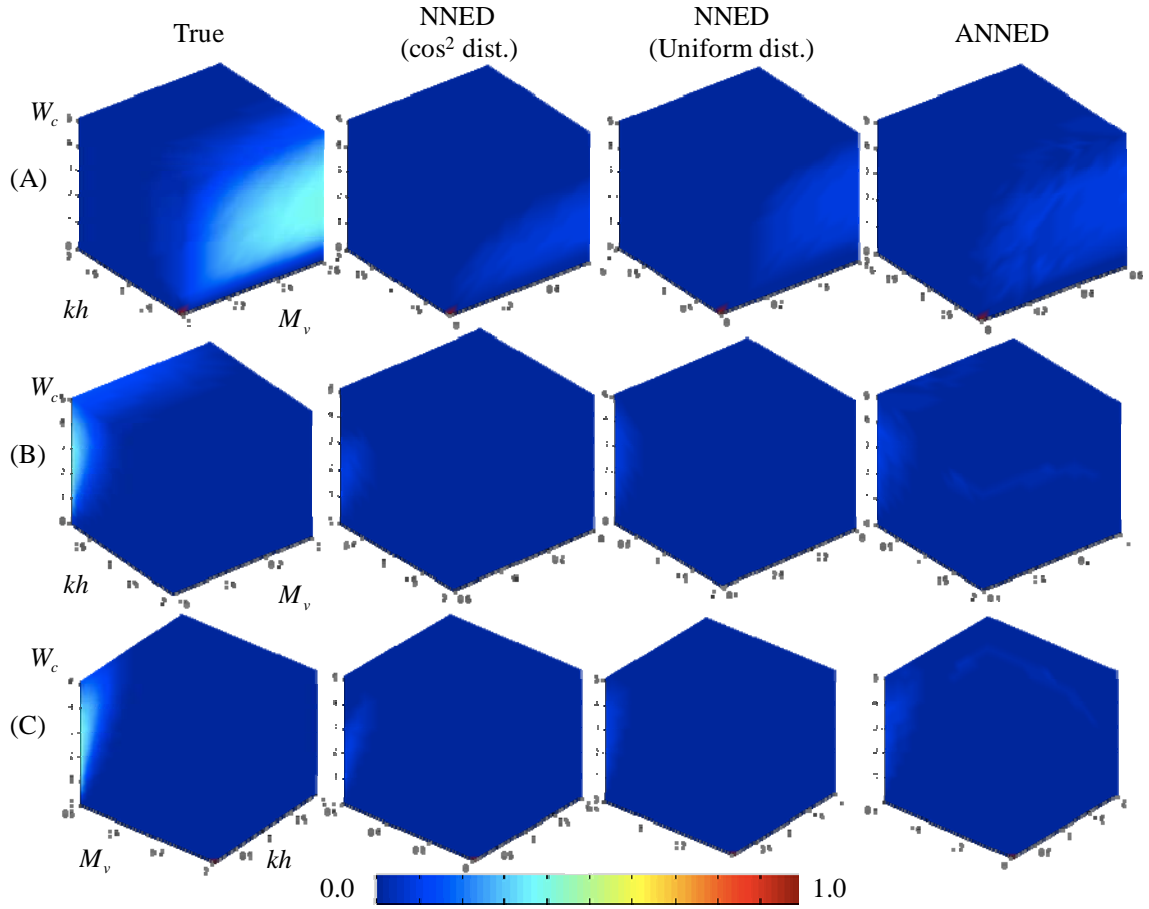


Figure 5.14: Estimated power for the double bounce component: $\sigma_v=0.56$. Each row corresponds to each view angle defined in Figure 5.1, while the columns correspond to the true data, results from NNED assuming the cosine squared and uniform distributions, and results from ANNED, respectively from left to right.

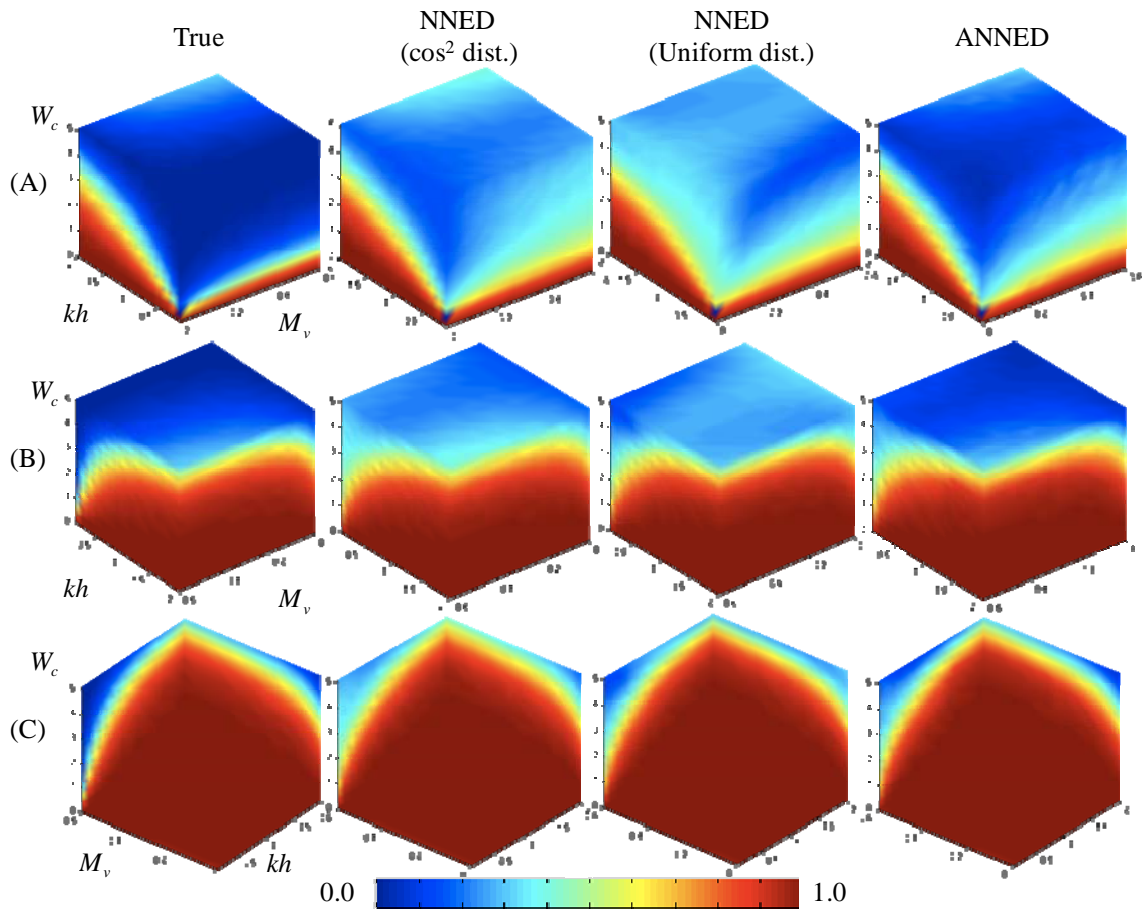


Figure 5.15: Estimated power for the surface component: $\sigma_v=0.56$. Each row corresponds to each view angle defined in Figure 5.1, while the columns correspond to the true data, results from NNED assuming the cosine squared and uniform distributions, and results from ANNED, respectively from left to right.

ANNED extracts the volume component very well compared to the other algorithms as shown in Figure 5.13. NNED, assuming a cosine squared distribution, also shows a reasonable texture match, but the contrast is lower than in the true data. NNED, assuming a uniform distribution, fails to extract the contribution. For the double bounce component in Figure 5.14, ANNED seems better than the others. Thus, the adaptive technique is the best way to extract the surface scattering component, as shown in Figure 5.15, while there is some blurriness at lower roughness due to the double bounce criterion discussed before.

Figure 5.16, 5.17 and 5.18 correspond to the estimated power for the volume, double bounce and surface, respectively, in the case of $\sigma_v=0.91$.

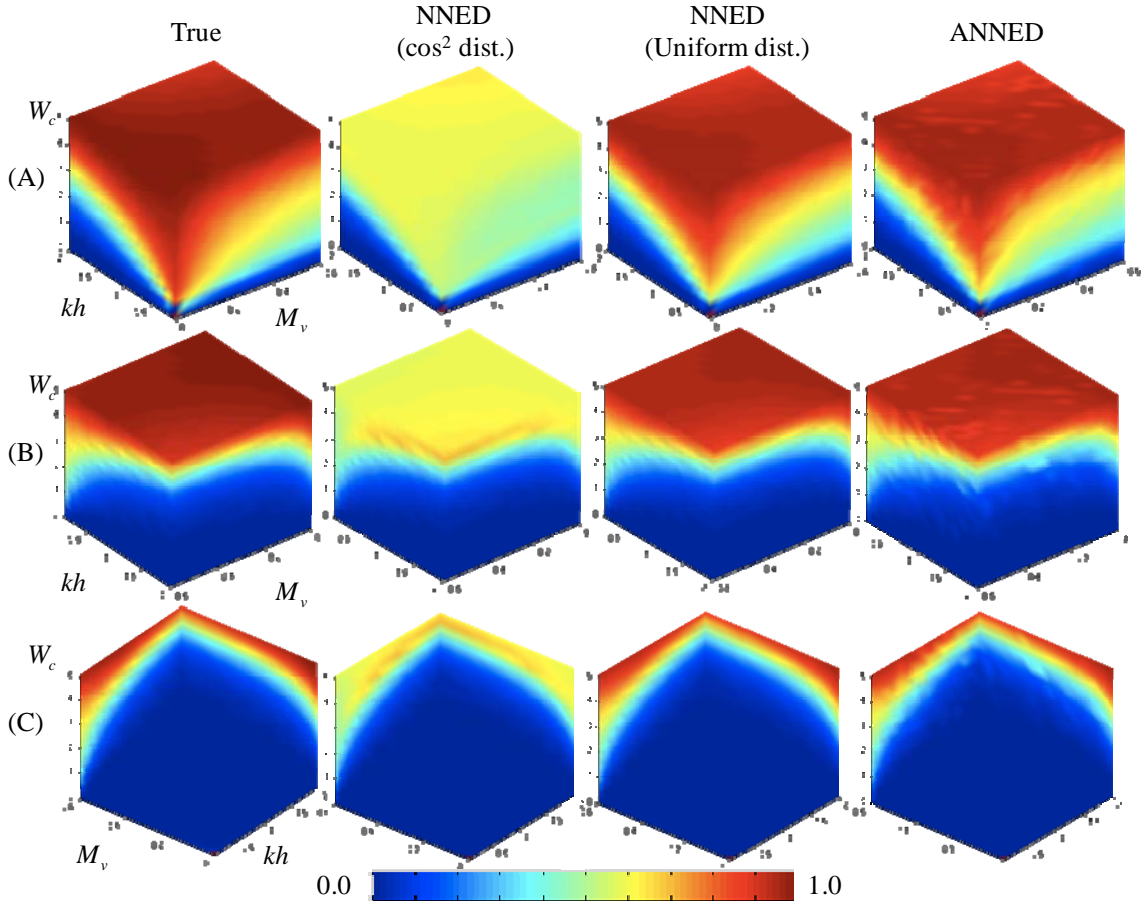


Figure 5.16: Estimated power for the volume component: $\sigma_v=0.91$. Each row corresponds to each view angle defined in Figure 5.1, while the columns correspond to the true data, results from NNED assuming the cosine squared and uniform distributions, and results from ANNED, respectively from left to right.

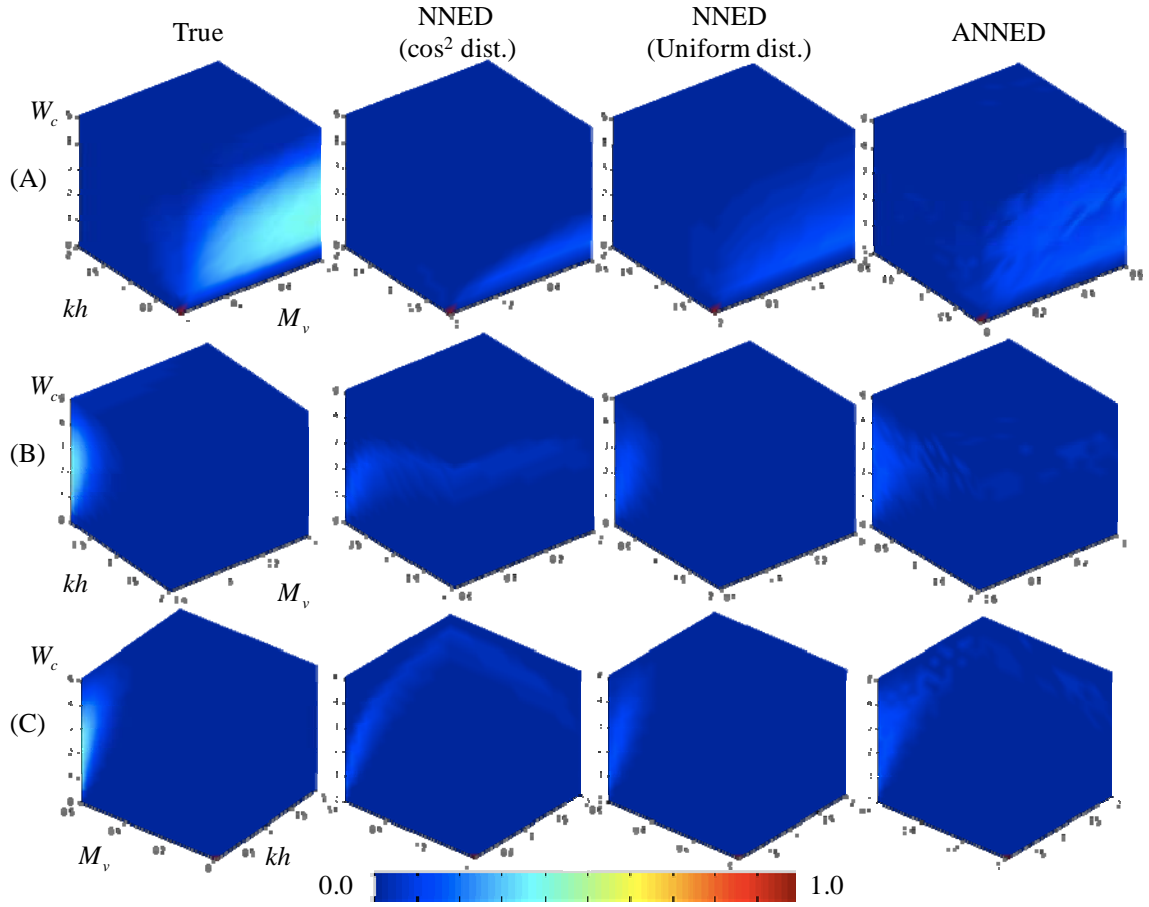


Figure 5.17: Estimated power for the double bounce component: $\sigma_v=0.91$. Each row corresponds to each view angle defined in Figure 5.1, while the columns correspond to the true data, results from NNED assuming the cosine squared and uniform distributions, and results from ANNED, respectively from left to right.

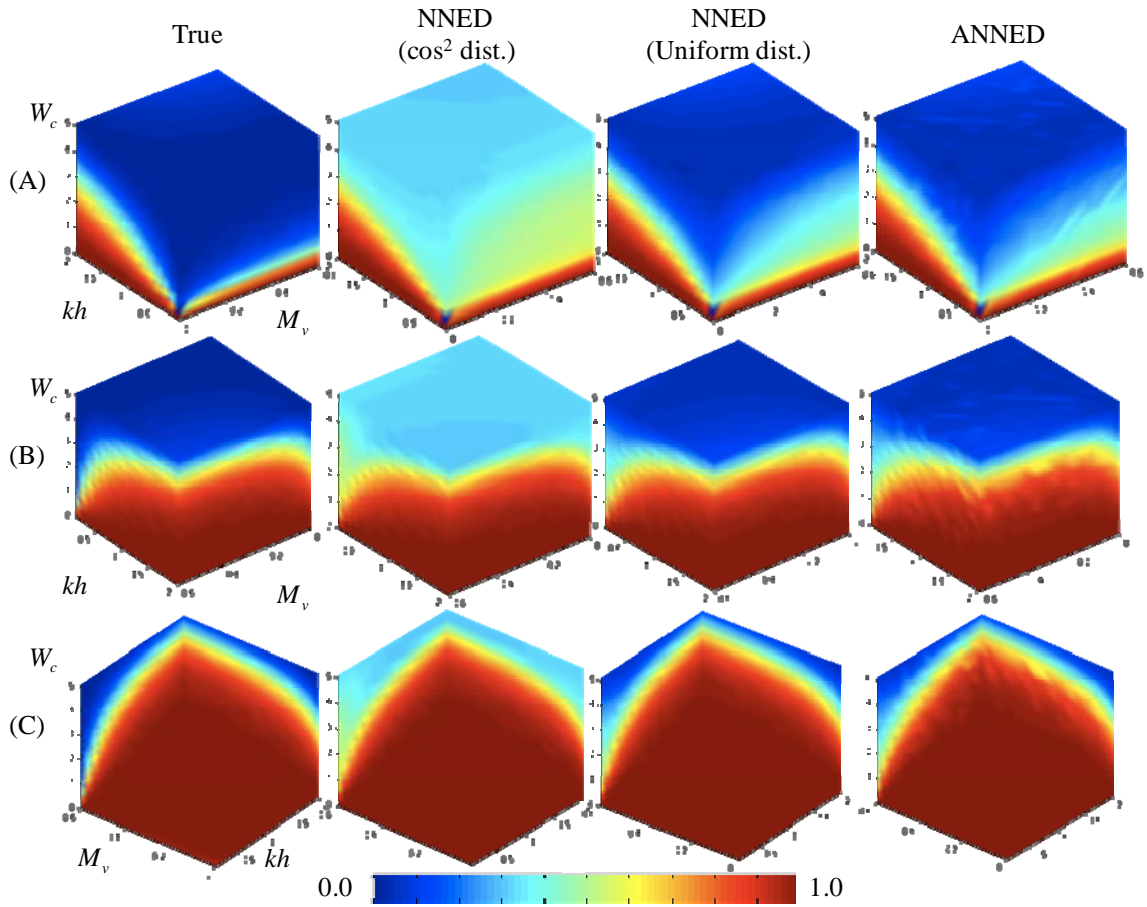


Figure 5.18: Estimated power for the surface component: $\sigma_v=0.91$. Each row corresponds to each view angle defined in Figure 5.1, while the columns correspond to the true data, results from NNED assuming the cosine squared and uniform distributions, and results from ANNED, respectively from left to right.

NNED, assuming a cosine squared distribution, is clearly inappropriate for this case. For the volume component, NNED, assuming a uniform distribution, is slightly better than ANNED, which shows some oscillations while the texture and contrast are almost same. Figure 5.17 shows that ANNED extracts the double bounce contribution in the view angle (A) slightly better than NNED, assuming a uniform distribution.

From the results presented in this section, ANNED clearly shows better applicability than the other techniques.

Chapter VI

Soil Moisture Retrieval

In this chapter, we will apply the decomposition techniques to retrieve the soil moisture from measured data. We shall start by introducing Dubois et al.'s inversion algorithm [8] as a representative of previous algorithms. This algorithm will then be applied to DSM to see how vegetation degrades our inversion accuracy. We will attempt to combine the algorithm with the decomposition technique, and verify the effectiveness. This quantitative simulation, however, reveals a potential deficiency of the decomposition technique. To overcome this problem, a brand new inversion technique will be introduced with simulation results.

6.1 Previous Algorithms

Several previous algorithms for soil moisture retrieval will be briefly introduced, along with a discussion of their applicability to vegetated terrain in this section.

Suppose we have a flat surface having a specific dielectric property. One transmits a light at specific incidence angle, and another receives scattered light in the specular direction. Since the surface is perfectly flat, the scattered power is dictated by the Fresnel coefficient, and so one can easily invert the dielectric constant. Next, consider the case of a surface with some roughness. The scattered power in the specular direction, which is called the coherent component, is decreased, and the rest of the power in the other directions, which is called the incoherent component, is increased as the surface roughness increases. Therefore the scattering from a bare surface is strongly related to dielectric constant and

roughness. In other words, the roughness is a noise source in the inversion of the dielectric constant. Vegetation is also a noise source. Therefore, a key point of the soil moisture inversion algorithms focuses on how to suppress the effects of the surface roughness and vegetation. Several theoretical and empirical models have been proposed as follows.

The first-order small perturbation model [2] in (4.28) can be a soil moisture estimator by taking the ratio of co-polarized responses as

$$\frac{\sigma_{hhhh}}{\sigma_{vvvv}} = \left| \frac{\alpha_{hh}}{\alpha_{vv}} \right|^2 = \left| \frac{\left(\varepsilon \cos \theta_i + \sqrt{\varepsilon - \sin^2 \theta_i} \right)^2}{\left(\cos \theta_i + \sqrt{\varepsilon - \sin^2 \theta_i} \right)^2 \left\{ \sin^2 \theta_i - \varepsilon (1 + \sin^2 \theta_i) \right\}} \right|^2$$

$$\alpha_{hh} = \frac{1 - \varepsilon}{\left(\cos \theta_i + \sqrt{\varepsilon - \sin^2 \theta_i} \right)^2} \quad (6.1)$$

$$\alpha_{vv} = (1 - \varepsilon) \frac{\sin^2 \theta_i - \varepsilon (1 + \sin^2 \theta_i)}{\left(\varepsilon \cos \theta_i + \sqrt{\varepsilon - \sin^2 \theta_i} \right)^2}$$

where θ_i and ε are the incidence angle and dielectric constant, respectively. This simple operation reduces the dependency on roughness. However, the applicability is limited to only small roughness compared with the wavelength. The co-polarizations approach each other at larger roughness, and equation (6.1) then underestimates the dielectric constant. More recently Kim et al. expanded the applicability by taking into account an undulation of the local topography (see [6]).

Oh et al. proposed an empirical model in [9]. This model relates both the co-polarization and cross polarization ratios to the dielectric constant, surface roughness, and wavelength.

$$\begin{aligned}
\frac{\sigma_{hhhh}}{\sigma_{vvvv}} &= \left\{ 1 - \left(\frac{2\theta}{\pi} \right)^{1/3\Gamma_0} \exp(-kh) \right\}^2 \\
\frac{\sigma_{hv hv}}{\sigma_{vvvv}} &= 0.23\sqrt{\Gamma_0} \{1 - \exp(-kh)\} \\
\Gamma_0 &= \left| \frac{1 - \sqrt{\varepsilon}}{1 + \sqrt{\varepsilon}} \right|^2
\end{aligned} \tag{6.2}$$

where k is a wave number. The authors found this using data sets from the bare surfaces with different roughness measured by the University of Michigan's truck-mounted network-analyzer-based scatterometer [47], which operates fully polarimetrically over L-, C-, and X-bands. With respect to surface roughness, wider applicability is expected compared to SPM. Note that the cross polarization term is significantly sensitive to the existence of vegetation, as discussed in 5.1. So the use of the cross polarization term may degrade the inversion accuracy.

To minimize the effect of vegetation, Dubois et al. reported the following model in [8].

$$\begin{aligned}
\sigma_{hhhh} &= 10^{-2.75} \frac{\cos^{1.5} \theta_i}{\sin^5 \theta_i} 10^{0.028\varepsilon \tan \theta_i} (kh \sin \theta_i)^{1.4} \lambda[cm]^{0.7} \\
\sigma_{vvvv} &= 10^{-2.35} \frac{\cos^3 \theta_i}{\sin^3 \theta_i} 10^{0.046\varepsilon \tan \theta_i} (kh \sin \theta_i)^{1.1} \lambda[cm]^{0.7}
\end{aligned} \tag{6.3}$$

This model relates co-polarized backscatter cross sections to dielectric constant and surface roughness, and ignores the cross-polarization. This ignorance gives the algorithm robustness to a certain amount of vegetation. This empirical model was derived by the same data set with Oh et al. and data sets measured by The University of Berne's truck-mounted radiometer-scatterometer [8], which operates fully polarimetrically at six frequencies between 2.5 and 11 GHz. One can rewrite (6.3) to solve for the dielectric constant and surface roughness as

$$\hat{\varepsilon} = 3.5469 \left\{ 14 \log \left(\frac{\sigma_{vvvv}}{\sigma_{hhhh}} \right) + 3 \log \sigma_{hhhh} \right\} + 18.4374 \quad (6.4a)$$

$$\log(kh) = \log \left(\frac{\sigma_{hhhh}^{1.37}}{\sigma_{vvvv}^{0.83}} \right) + 1.9854 \quad (6.4b)$$

where we assume that $\theta_i = 40$ degrees and $\lambda = 24$ cm (L-band). The first equation shows that not only the ratio $\frac{\sigma_{vvvv}}{\sigma_{hhhh}}$ but also the absolute value σ_{hhhh} affect the soil moisture inversion. One of the main advantages of this algorithm is the simple implementation of the inversion procedure.

There are three parameters to characterize surface roughness: the RMS height, correlation length, and roughness spectrum function, as discussed in 4.4. Both algorithms consider only RMS height. Shi et al. proposed an algorithm taking into account the rest of the parameters [4]. Their algorithm was developed by fitting single scattering IEM –based numerical simulations (described in (4.42)) for a wide range of surface roughness and soil moisture conditions. After considering various combinations of the polarizations, he found the following two co-polarization sets to show reasonable agreement with the Little Washita watershed images measured by AIRSAR and Shuttle Imaging Radar C (SIR-C).

$$\begin{aligned} 10 \log_{10} \left(\frac{|\alpha_{vv}|^2}{\sigma_{vvvv}} \right) &= a_{vv}(\theta_i) + b_{vv}(\theta_i) 10 \log_{10} \left(\frac{1}{S_R} \right) \\ 10 \log_{10} \left(\frac{|\alpha_{vv}|^2 + |\alpha_{hh}|^2}{\sigma_{vvvv} + \sigma_{hhhh}} \right) &= a_{vh}(\theta_i) + b_{vh}(\theta_i) 10 \log_{10} \left(\frac{|\alpha_{vv}| |\alpha_{hh}|}{\sqrt{\sigma_{vvvv} + \sigma_{hhhh}}} \right) \end{aligned} \quad (6.5)$$

$$\begin{aligned} S_R &= (kh)^2 W \\ a_{vv}(\theta_i) &= 6.901 + 5.492 \tan \theta_i - 1.051 \log(\sin \theta_i) \\ b_{vv}(\theta_i) &= 0.515 + 0.896 \sin \theta_i - 0.475 \sin^2 \theta_i \\ a_{vh}(\theta_i) &= \exp(-12.37 + 37.206 \sin \theta_i - 41.187 \sin^2 \theta_i + 18.898 \sin^3 \theta_i) \\ b_{vh}(\theta_i) &= 0.649 + 0.659 \cos \theta_i - 0.306 \cos^2 \theta_i \end{aligned}$$

where W is a roughness spectrum function in (4.37).

In this chapter, we choose an algorithm proposed by Dubois et al. as a representative of the previous algorithms because of its simple implementation with reasonable robustness to the effect of vegetation.

[48] and [22] also provide excellent reviews and comparison of the soil moisture inversion algorithms.

6.2 Soil Moisture Retrieval Using an Algorithm Proposed by Dubois et al.

As discussed in the previous section, the algorithm proposed by Dubois et al. in (6.4) is chosen as a representative of current algorithms. Note that we directly evaluate the dielectric constant in this section, instead of transforming to soil moisture as discussed in Section 4.6. Because each model shown in Section 4.6 is not simple linear function, this may add further complication. Since the algorithm is basically valid for bare surface, we use $\hat{\epsilon}_{bare}$ for the estimated dielectric constant.

Table 6.1 shows simulation parameters. Note that the vegetation structure corresponds to a cosine squared distribution.

Table 6.1: Baseline parameters for the test scenario

θ_i (deg.)	λ (m)	L (m)	h_{layer} (m)	a (m)	h (cm)	l (cm)	ψ_0 (deg.)	σ_ψ	σ_δ	ρ (cylinders/m ³)
40	0.24	0.5	0.5	0.002	1	5	0	0.56	0.91	900

Soil moisture is in range between 10 and 60%, and vegetation water content is varied from 0 to 2.54 kg/m². The inversion result is shown in Figure 6.1. ϵ_{true} is a dielectric constant corresponding to the true soil moisture. To emphasize the effect of vegetation, the dielectric constant of a dry surface ($W_c=0$) is subtracted from the inverted dielectric constant.

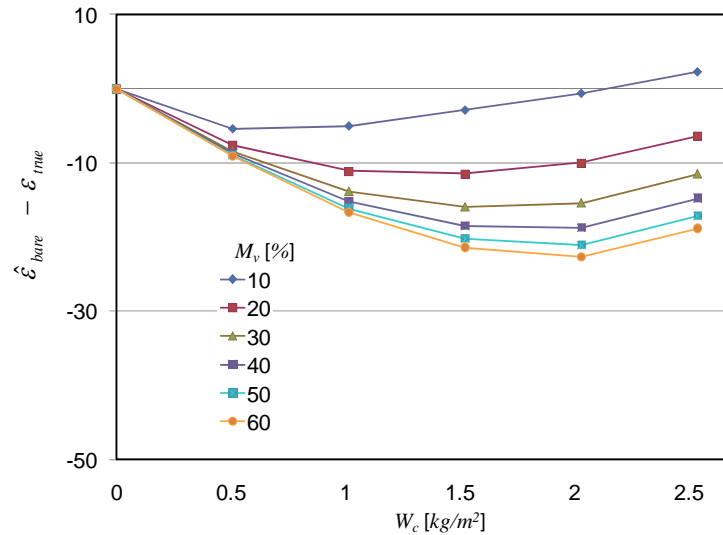


Figure 6.1: Inversion result using Dubois et al.'s algorithm without polarimetric decomposition

As we expected, the estimation error increases as the vegetation water content increases. However, it begins to decrease above a certain amount of vegetation, depending on the soil moisture. For example, the 30% soil moisture line gradually increases up to $W_c=3$ kg/m², and it then starts to decrease. Due to the vegetation type (cosine squared distribution with the zero orientation angle), the vertically polarized returns from the surface and double bounce are more attenuated than the horizontally polarized one. So the vertical returns from the surface and double bounce continue to decrease as the vegetation increases. From the first term of (6.4a), the smaller vertically polarized response results in the underestimation of the dielectric constant. On the other hand, the horizontal double bounce scattering increases as the vegetation water content increases, as shown in Figures 4.27, 4.24, and 4.28. From the second term of (6.4a), the larger horizontally polarized

response causes an overestimation of the dielectric constant. For the vegetation water content up to $W_c=1.5 \text{ kg/m}^2$, the vertical response from the surface and double bounce dominates the total scattering power due to the lower level of vegetation water content. However, at higher values of W_c , the horizontal double bounce scattering dominates the vertical scattering so that the estimated dielectric constant increases.

Next, the polarimetric decomposition technique is combined with the inversion algorithm. In this section, NNED assuming a cosine-squared distribution is used instead of ANNED to make our interpretation simpler. The dielectric constant is inverted from the decomposed surface data. Figure 6.2 shows the results.

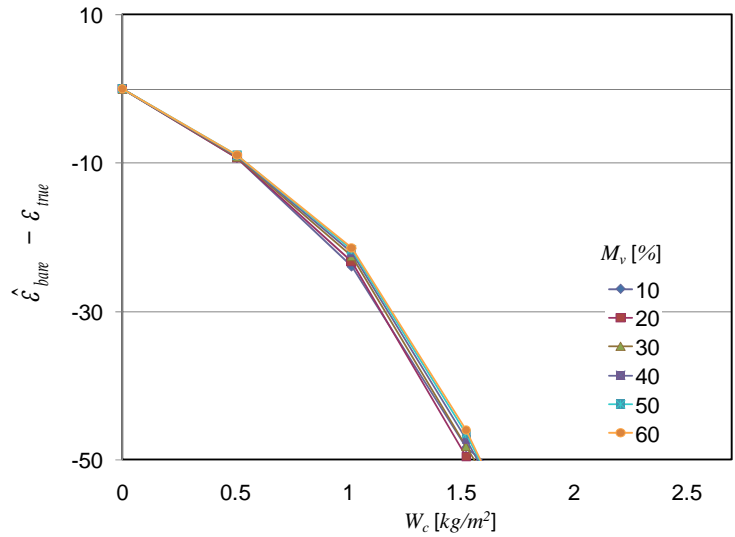


Figure 6.2: Inversion result using Dubois et al.’s algorithm with the polarimetric decomposition (NNED assuming a cosine squared distribution). The decomposition makes the accuracy worse than the result without decomposition.

First, an advantage of the use of the polarimetric decomposition is shown in the narrower variation of the estimated lines in Figure 6.2. The technique removes the vegetation effect which changes the total backscattering depending on soil moisture. Secondly, the inversion curves are monotonically decreasing functions. From the first term

of (6.4a), the underestimation of the dielectric constant comes from the smaller vertical polarization. To see the detail analytically, suppose we have received signals attenuated by the volume as in (4.17).

$$\begin{aligned}\sigma_{hhhh} &= \sigma_{hhhh}^{no_att} e^{-2\alpha_{ext}^{hh}H / \cos \theta_i} \\ \sigma_{vvvv} &= \sigma_{vvvv}^{no_att} e^{-2\alpha_{ext}^{vv}H / \cos \theta_i}\end{aligned}\quad (6.6)$$

Then the expressions are plugged into (6.4a) as

$$\hat{\varepsilon}' = \hat{\varepsilon} + 3.5469 \left\{ 14 \log \left(\frac{e^{-2\alpha_{ext}^{vv}H / \cos \theta_i}}{e^{-2\alpha_{ext}^{hh}H / \cos \theta_i}} \right) + 3 \log e^{-2\alpha_{ext}^{hh}H / \cos \theta_i} \right\} \quad (6.7)$$

For simplicity, let us take logarithm natural and assume the same attenuation coefficients between co-polarizations.

$$\hat{\varepsilon}' \approx \hat{\varepsilon} - 3.5469 \cdot 3 \cdot 2\alpha_{ext}^{hh}H / \cos \theta_i \quad (6.8)$$

This clearly tells us that the inferred dielectric constant decreases with an increase of the amount of vegetation. This estimation error comes from ignorance of the attenuation coefficients in the decomposition technique. What we can do with the decomposition technique is to estimate the *attenuated* surface scattering power. This is a potential deficiency of the decomposition technique. Freeman proposed a decomposition technique taking into account attenuation coefficients in [45]. The technique, however, requires *a priori* knowledge, such as the forest height which is one of the most difficult parameters to estimate from the measured data.

To overcome this fatal problem, we propose a brand new technique in the next section.

6.3 A New Inversion Algorithm Using the Polarimetric Scattering Cube

The forward scattering model (DSM), which already takes into account the volume attenuation, can be utilized for a new inversion algorithm. As mentioned in the previous chapter, we can make a polarimetric scattering cube for each element of the covariance matrix, as shown in Figure 6.3.

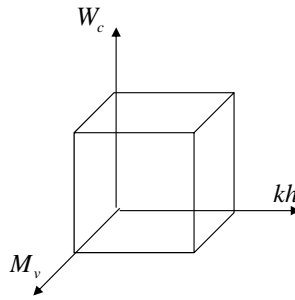


Figure 6.3: A reference cube for the soil moisture retrieval. The soil moisture, surface roughness, and vegetation water content correspond to the x , y and z axes, respectively.

The value on the cube is obtained by taking natural logarithm instead of expressing the value on dB. This operation allows us to express a complex number by splitting it into the magnitude part and the phase part.

$$\sigma_{pqrs}^{cube} = \ln \sigma_{pqrs} = \ln |\sigma_{pqrs}| + \phi_{pqrs} \quad (6.9)$$

p , q , r , and s correspond to either h or v . Each off-diagonal element consists of a pair of cubes in (6.9). Therefore nine independent cubes are obtained as follows.

$$\begin{aligned}
\sigma^{ref}(x, y, z) &= \begin{pmatrix} \sigma_{hhhh}^{ref}(x, y, z) & \sigma_{hhhv}^{ref}(x, y, z) & \sigma_{hhvv}^{ref}(x, y, z) \\ \sigma_{hhhv}^{ref*}(x, y, z) & \sigma_{hvhv}^{ref}(x, y, z) & \sigma_{hvvv}^{ref}(x, y, z) \\ \sigma_{hhvv}^{ref*}(x, y, z) & \sigma_{hvvv}^{ref*}(x, y, z) & \sigma_{vvvv}^{ref}(x, y, z) \end{pmatrix} \\
\Rightarrow \ln \sigma^{ref}(x, y, z) &= \begin{pmatrix} \ln \sigma_{hhhh}^{ref}(x, y, z) & \ln |\sigma_{hhhv}^{ref}(x, y, z)| & \ln |\sigma_{hhvv}^{ref}(x, y, z)| \\ \ln |\sigma_{hhhv}^{ref}(x, y, z)| & \ln \sigma_{hvhv}^{ref}(x, y, z) & \ln |\sigma_{hvvv}^{ref}(x, y, z)| \\ \ln |\sigma_{hhvv}^{ref}(x, y, z)| & \ln |\sigma_{hvvv}^{ref}(x, y, z)| & \ln \sigma_{vvvv}^{ref}(x, y, z) \end{pmatrix} \\
&\quad + \begin{pmatrix} 0 & \phi_{hhhv}^{ref}(x, y, z) & \phi_{hhvv}^{ref}(x, y, z) \\ -\phi_{hhhv}^{ref}(x, y, z) & 0 & \phi_{hvvv}^{ref}(x, y, z) \\ -\phi_{hhvv}^{ref}(x, y, z) & -\phi_{hvvv}^{ref}(x, y, z) & 0 \end{pmatrix}
\end{aligned} \tag{6.10}$$

x , y , and z are the axes of soil moisture, surface roughness, and vegetation water content, respectively. Similarly, the measured covariance matrix is calculated as

$$\begin{aligned}
\sigma^m &= \begin{pmatrix} \sigma_{hhhh}^m & \sigma_{hhhv}^m & \sigma_{hhvv}^m \\ \sigma_{hhhv}^{m*} & \sigma_{hvhv}^m & \sigma_{hvvv}^m \\ \sigma_{hhvv}^{m*} & \sigma_{hvvv}^{m*} & \sigma_{vvvv}^m \end{pmatrix} \\
\Rightarrow \ln \sigma^m &= \begin{pmatrix} \ln \sigma_{hhhh}^m & \ln |\sigma_{hhhv}^m| & \ln |\sigma_{hhvv}^m| \\ \ln |\sigma_{hhhv}^m| & \ln \sigma_{hvhv}^m & \ln |\sigma_{hvvv}^m| \\ \ln |\sigma_{hhvv}^m| & \ln |\sigma_{hvvv}^m| & \ln \sigma_{vvvv}^m \end{pmatrix} + \begin{pmatrix} 0 & \phi_{hhhv}^m & \phi_{hhvv}^m \\ -\phi_{hhhv}^m & 0 & \phi_{hvvv}^m \\ -\phi_{hhvv}^m & -\phi_{hvvv}^m & 0 \end{pmatrix}.
\end{aligned} \tag{6.11}$$

Using these descriptions, we can calculate a distance between the measured data and any specific point in the cubes as

$$\begin{aligned}
d(x, y, z) &= \sum_i w_i \sqrt{(\ln \sigma_i^m - \ln \sigma_i^{ref}(x, y, z))^2} \\
&\quad + \sum_j w_j \sqrt{(\ln |\sigma_j^m| - \ln |\sigma_j^{ref}(x, y, z)|)^2} + \sum_k w_k \sqrt{(\phi_k^m - \phi_k^{ref}(x, y, z))^2}
\end{aligned} \tag{6.12}$$

where i is either $hhhh$, $hvhv$, or $vvvv$, and j and k are either $hhhv$, $hhvv$ or $hvvv$. Also, w_i , w_j and w_k are weighting functions that you can change sensitivity of each polarization. You can arbitrarily choose the combination of polarizations. After calculating the distance for all x , y , and z of the referential cubes, one can find a set of (x, y, z) which minimizes the distance. If a combination (x_0, y_0, z_0) achieves the minimum distance, x_0 , y_0 , and z_0

correspond to the inversion results for the soil moisture, surface roughness, and vegetation water content, respectively. This simple operation is one of the main advantages. Now the technique will be applied to the case of the grassland.

First, the reference cubes are calculated using DSM with baseline parameters and variables shown in Tables 6.1 and 6.2, respectively.

Table 6.2: Variables for the reference cubes

M_v (%)	W_c (kg/m ²)	kh
0-60	0-2.54	0.1-2

For this demonstration, 20 samples for each axis of the cube (8000 samples in total) are calculated. The resulting five cubes are displayed in Figure 6.4. Due to the gradual change of the textures on the cube surfaces, we can increase the number of samples by simple interpolation techniques. In this case the number of samples is increased from 20 to 280 samples for each axis (21,952,000 samples in total) using cubic spline interpolation. Note that hhv and hvv are small compared with the other elements, due to the scattering reflection symmetry, and so we ignore them.

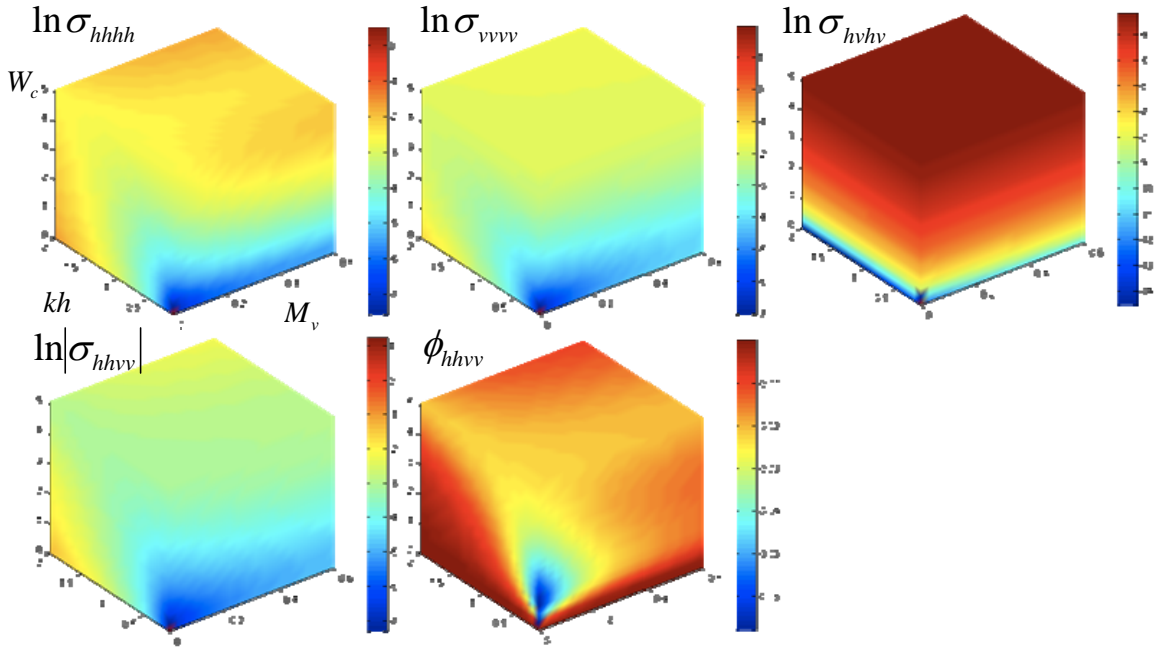


Figure 6.4: Calculated five independent cubes (20 samples for each axis). Note that hhhv and hvvv terms are small due to the scattering reflection symmetry.

For simplicity, the test data sets are assumed to have the same parameters as in Table 6.1, and the variables (soil moisture, surface roughness, and vegetation water content) are randomly chosen in the range shown in Table 6.2. In this simulation, we use two different combinations for the distance calculation: (hhhh, hvhv, vvvv) and (hhhh, hvhv, vvvv, hhvv). Figure 6.5 shows inversion results for the three parameters. In each case the y-axis is the Root Mean Squared Error (RMSE) of each parameter. The x-axis shows the amount of vegetation water content between 0 and the specified value on the axis. For example, if you pick $W_c=1.5 \text{ kg/m}^2$, the data samples are generated from uniformly distributed vegetation water contents between 0 and 1.5 kg/m^2 . Note that the error comes from the number of samples of the cubes.

$$w_{hhhh} = w_{hv hv} = w_{vvvv} = 1$$

$$w_{hhhv} = w_{hvvv} = 0$$

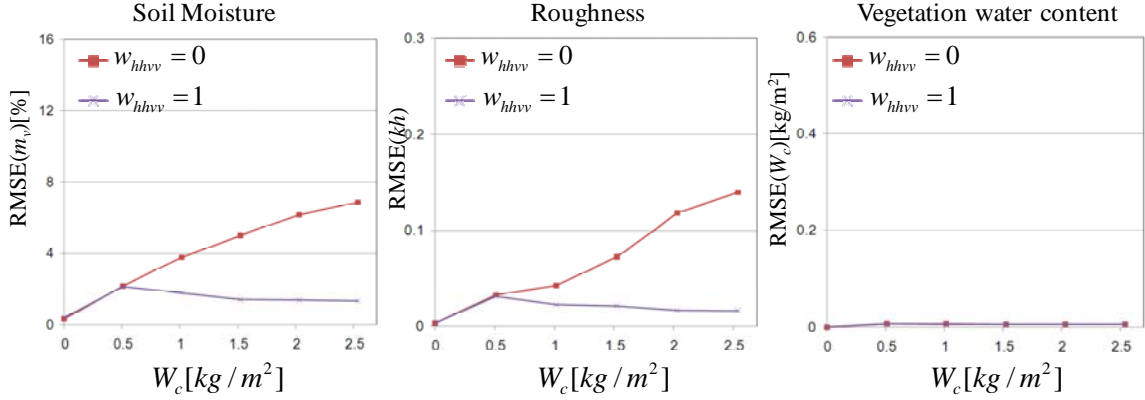


Figure 6.5: Inversion results using the cube technique. Inversions of soil moisture (left), roughness (center), and vegetation water content (right) are displayed.

The error source of this inversion is the limited sample number of the cube. The inversion result of the vegetation water content shows both lines are identical so that $hhvv$ term does not affect this inversion process at all. As discussed in Section 5.2, the cross-polarization term plays an important role in inverting the vegetation water content. The results of the soil moisture and roughness share similar characteristics. Both lines are identical up to $W_c = 0.5 \text{ kg/m}^2$, and then they diverge and the results using the $hhvv$ term achieve significantly better accuracy in both cases. Since Figure 4.34 shows the cross polarized response has effective sensitivity only up to 0.5 kg/m^2 , this term contributes to the inversion of the soil moisture and surface roughness at the lower level of vegetation water content. Another feature is that the inversion accuracies of the soil moisture and surface roughness increase as the vegetation water content increases. This tendency is opposite to that of Dubois et al.'s algorithm which ignores $hhvv$. Hence, the proposed cube inversion algorithm shows strong robustness to scattering from vegetated terrain.

Next, the inversion accuracy will be shown by varying the vegetation structure. The test data is generated with various radii of cylinders between 2 and 3 mm. The inversion results are shown in Figure 6.6.

$$w_{hhhh} = w_{hvhv} = w_{vvvv} = w_{hhvv} = 1$$

$$w_{hhhv} = w_{hvvv} = 0$$

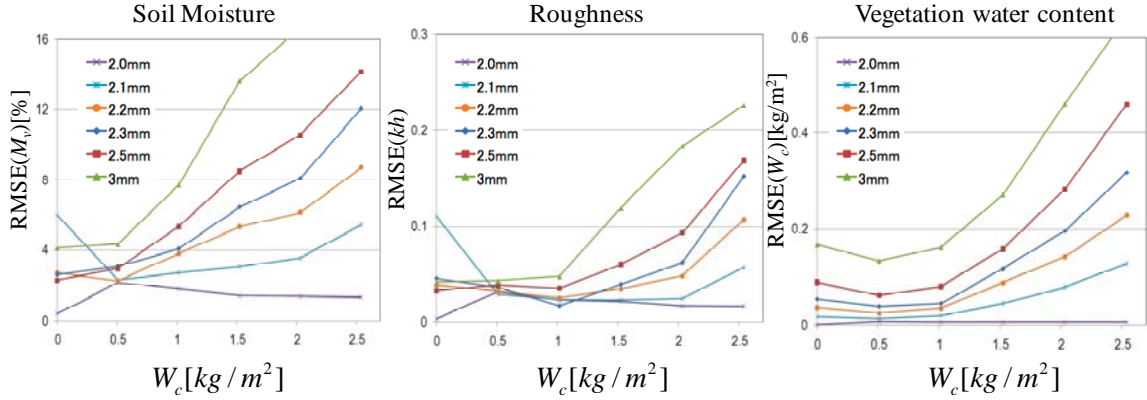


Figure 6.6: Inversion results using cube technique for various radii of cylinders. Inversions of soil moisture (left), roughness (center), and vegetation water content (right) are displayed.

Due to the existence of dried plants with various radii, the estimation at $W_c=0$ has some variation. In each case the error increases as the radius range increases. At smaller ranges of radii, the effect of the vegetation is suppressed. This implies that different reference cubes depending on the vegetation structure should be prepared to achieve the best accuracy. Since the implementation of the algorithm is simple, a large number of cubes is not a problem. Further investigation is needed to choose the most appropriate cube for a given data set *a priori*.

To see an effect of the weighting function, thermal noise (-40 dB) is added to the test data. The inversion is operated by varying the weighting function of cross-polarization. The results are shown in Figure 6.7.

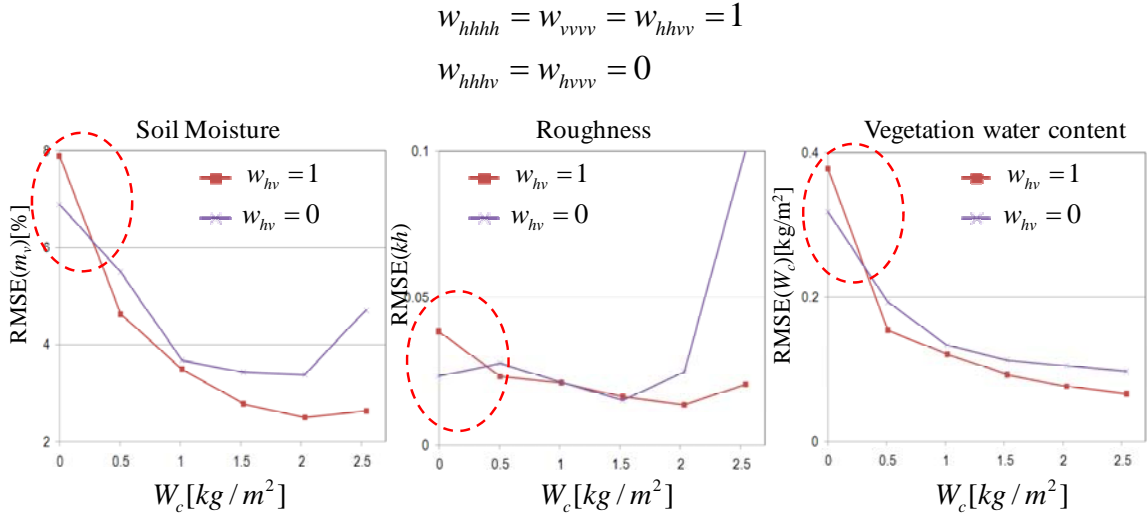


Figure 6.7: Inversion results using the cube technique. The -40 dB thermal noise is added to the test data in Figure 6.5. Inversions of soil moisture (left), roughness (center), and vegetation water content (right) are displayed.

Significantly lower accuracy is achieved in a range of smaller vegetation water content around 0 to 0.5 kg/m². The surface scattering is dominant in this range, and the cross-polarized scattering from the surface is close to zero without any topographic undulation as you can see in the analytical models (4.41) or (4.42). This means that our cross-polarized data is only contributed by thermal noise, and the use of the term degrades the accuracy. Therefore, you can perform better estimation without using the cross-polarized term in the range of smaller vegetation water content. The change of weighting function improves the results for not only soil moisture but also roughness and vegetation water content. However, the ignorance of the term does not work in the range of higher vegetation water content since the surface scattering is not dominant any more. This implies us that the sensitivity to each polarization should be determined by the class of vegetation.

From the results above, we can propose the following inversion strategy in Figure 6.8.

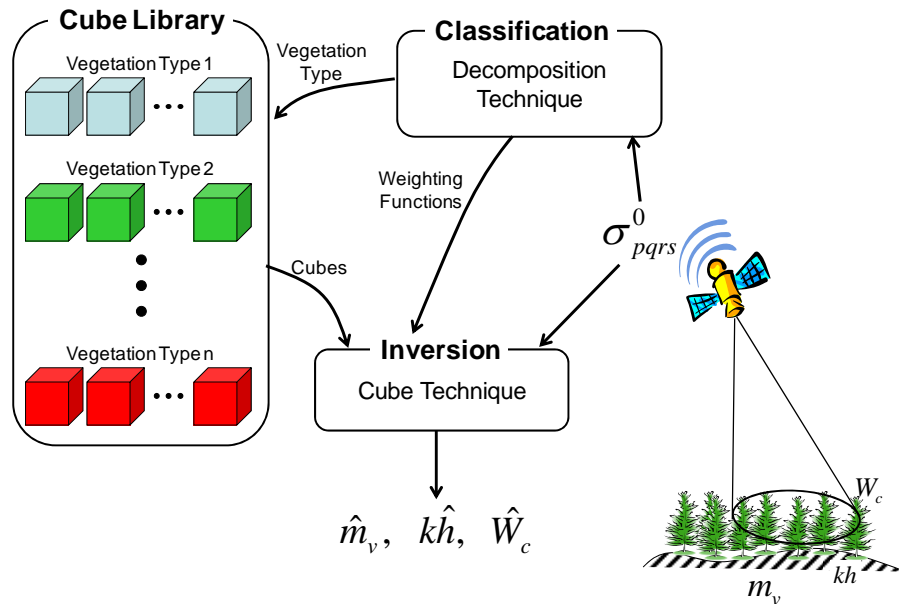


Figure 6.8: Proposed inversion strategy

Once we obtain the measured polarimetric radar data, the vegetation type and weighting functions should be identified using the decomposition technique shown in Chapter III. Here the various cube sets are developed by DSM in the Cube Library in advance so that a cube set corresponding to the estimated vegetation type can be chosen for the inversion process. Finally, the inversion for soil moisture, surface roughness or vegetation water content can be performed by (6.12). The advantages of this strategy are as follows.

- Easy implementation
- Including the attenuation effect
- Easy to achieve higher applicability by increasing the number of different cube sets.

Chapter VII

Conclusions and Suggestions

In this thesis, we conducted a detailed study of the scattering mechanisms of vegetated terrain to attempt to find a way to isolate surface scattering from other scattering mechanisms, and to apply this knowledge to the retrieval of soil moisture.

We started by pointing out a deficiency in the Freeman decomposition model [12] regarding energy conservation. An improved algorithm, Non-Negative Eigenvalue Decomposition (NNED), revealed that Freeman decomposition overestimated the volume scattering power by 30 to 40% more than that estimated by NNED. These numbers were obtained from an image of Black Forest, Germany, acquired by L-band AIRSAR. The NNED is only applicable to a specific type of vegetation due to the limitation of the volume scattering component. To overcome this limitation, the following scattering component was generalized by introducing two parameters: the randomness and the mean orientation angle. This generalized component was then applied to create the adaptive NNED (ANNED) technique. We qualitatively verified the decomposition techniques by showing how they react to various types of vegetation using the Black Forest image. ANNED proved to be most applicable.

In order to validate the decomposition models quantitatively, we introduced the Discrete Scatterer Model (DSM) [15, 16] with some modifications. Prior to applying the decomposition model, DSM was employed to study the sensitivity of the physical parameters characterizing vegetated terrain. Soil moisture, surface roughness, and vegetation water content were chosen as the variables. Through the simulation in the case of grassland, we demonstrated how the vegetation and surface roughness affect the

backscatter cross section. In particular, the attenuation coefficients derived from the vegetation structure had an important effect on the sensitivity.

Quantitative analysis of the decomposition models was conducted. Three different types of vegetations were generated using DSM. The adaptive decomposition technique showed the best applicability compared to others.

Separating the double bounce and ground scattering, however, is still an open problem. In the case of very regular vegetation structure, the criterion that the real part of HHVV be negative for double bounce scattering sometimes failed.

We attempted to employ the decomposition technique to the inversion algorithm proposed by Dubois et al. in [8]. The data was generated by DSM so that the result could be quantitatively validated. The decomposition technique did not improve the inversion accuracy due to ignorance of the attenuation effect by the volume layer. To overcome this difficulty, a new soil moisture inversion technique utilizing polarimetric scattering cubes was proposed. Each cube is calculated using DSM. The simulations with various radii of cylinders showed its effect on inversion accuracy, and implied that multiple cubes for various vegetation structures are needed. One of the main advantages of the algorithm is its easy implementation, so that having a large number of cubes does not affect the efficiency.

In the framework of the retrieval of soil moisture we are convinced that the proposed cube algorithm can achieve higher accuracy and applicability than other algorithms and is easily implemented. However, further investigations will be needed to fully demonstrate it. The dependence of the accuracy on various vegetation parameters such as the cylinder radius or distribution function has to be studied. This may help to determine what type of cube is needed for particular observation. The algorithm should be validated with numerical simulation data under various noise situations. Finally, and most importantly, it should be validated using sufficient reliable data.

Appendix A

Positive Eigenvalues of the Measured Covariance Matrix

In this section, we will prove all eigenvalues of a measured covariance matrix are always non-negative. The power of the measured covariance matrix is always non-negative,

$$P(C_m) \geq 0. \quad (\text{A.1})$$

From equation (2.10), the backscatter cross section is

$$\sigma^0 = \bar{A}^T C_m \bar{A}^* \quad (\text{A.2})$$

where the vector \bar{A} consists of antenna polarization parameters. We can diagonalize the covariance matrix by finding its eigenvalues and associated eigenvectors as

$$C'_m = \begin{pmatrix} \lambda_1 & 0 & 0 & 0 \\ 0 & \lambda_2 & 0 & 0 \\ 0 & 0 & \lambda_3 & 0 \\ 0 & 0 & 0 & \lambda_4 \end{pmatrix} = Q^{-1} C_m Q \Rightarrow C_m = Q C'_m Q^{-1} \quad (\text{A.3})$$

$$Q = (\bar{v}_1 \quad \bar{v}_2 \quad \bar{v}_3 \quad \bar{v}_4)$$

where λ_i and \bar{v}_i are eigenvalues and associated orthonormal eigenvectors, respectively.

Note that the Q has the following characteristic.

$$Q^{*T}Q = I \Rightarrow Q^{*T} = Q^{-1} \quad (\text{A.4})$$

We can project \vec{A} into the same space of C'_m using Q .

$$\vec{A}' = Q^{-1}\vec{A} \Rightarrow \vec{A} = Q\vec{A}' \quad (\text{A.5})$$

By substituting (A.3), (A.4), and (A.5) into (A.2), the backscatter cross section can be rewritten as

$$\sigma^0 = (Q\vec{A}')^T Q C'_m Q^{-1} (Q\vec{A}')^* = \vec{A}'^T C'_m \vec{A}'^* \quad (\text{A.6})$$

Since the backscatter cross section, i.e., the power, has to be positive for any \vec{A}' , each eigenvalue of a measured covariance matrix has to be positive.

Appendix B

Eigenvalues of the General Covariance Matrix

In this section, it is shown that the eigenvalues of the general covariance matrix in (3.71) are not affected by mean orientation angle, i.e., rotation angle of the target about the line of sight.

As a first step, the form of equation (3.71) is simply rewritten as

$$C = \vec{T} \cdot \vec{V} = \begin{bmatrix} T_1 + T_4 & \sqrt{2}(T_5 + T)_8 & T_2 + T_7 \\ \sqrt{2}(T_5 - T)_8 & 2T_3 & \sqrt{2}(T_6 - T_9) \\ T_2 - T_7 & \sqrt{2}(T_6 + T_9) & T_1 - T_4 \end{bmatrix}^T \quad (\text{B.1})$$

where

$$\vec{T} = (\vec{\alpha} + p\vec{\beta} + q\vec{\gamma}) = [T_1 \quad T_2 \quad 2T_3 \quad T_4 \quad \sqrt{2}T_5 \quad \sqrt{2}T_6 \quad T_7 \quad \sqrt{2}T_8 \quad \sqrt{2}T_9]^T. \quad (\text{B.2})$$

The characteristic equation becomes

$$\det|C - \lambda I| = -\lambda^3 + \frac{1}{8} f_1 \lambda^2 + \frac{1}{8^2} f_2 \lambda + \frac{1}{8^3} f_3 \quad (\text{B.3})$$

where

$$\begin{aligned}
f_1 &= 8 \cdot 2 \cdot (T_1 + T_3) \\
f_2 &= 8^2 \cdot [(T_2 - T_7)(T_2 + T_7) + 2\{(T_5 - T_8)(T_5 + T_8) + (T_6 - T_9)(T_6 + T_9)\} \\
&\quad - \{(T_1 + T_4)(T_1 - T_4) + 4T_1T_3\}] \\
f_3 &= 8^3 \cdot 2\{(T_5 + T_8)(T_6 - T_9)(T_2 - T_7) + (T_5 - T_8)(T_6 + T_9)(T_2 + T_7) \\
&\quad - T_3(T_2 - T_7)(T_2 + T_7) - (T_5 - T_8)(T_5 + T_8)(T_1 - T_4) \\
&\quad - (T_6 - T_9)(T_6 + T_9)(T_1 + T_4) + T_3(T_1 + T_4)(T_1 - T_4)\}
\end{aligned} \tag{B.4}$$

We also know that the covariance matrix is obtained from a scattering matrix, as shown in Chapter II.

$$S_0 = \begin{pmatrix} a_0 & c_0 \\ c_0 & b_0 \end{pmatrix} \rightarrow C_0 \tag{B.5}$$

This equation is then rewritten by factoring out b_0 .

$$S_0 = b_0 \begin{pmatrix} \frac{a_0}{b_0} & \frac{c_0}{b_0} \\ \frac{c_0}{b_0} & 1 \end{pmatrix} = b_0 S \rightarrow C_0 = |b_0|^2 C \tag{B.6}$$

We are interested only in C in (B.6). Ignoring the scale factor $|b_0|^2$, the updated scattering matrix is rewritten as

$$S = \begin{pmatrix} a & c \\ c & 1 \end{pmatrix} \tag{B.7}$$

where

$$a = \frac{a_0}{b_0}, \quad c = \frac{c_0}{b_0}. \tag{B.8}$$

From (B.3), the coefficient of each term, f_1 , f_2 , and f_3 , is not a function of orientation angle.

$$\begin{aligned}
f_1 &= 8(K_{+ab} + 2K_c) \\
f_2 &= \left[-4(K_{+ab} - L_{Reab} + 4K_c)(5K_{+ab} + 3L_{Reab} + 4K_c) - 16(L_{Imac} - L_{Imbc})^2 \right. \\
&\quad \left. + 4p^2(K_{-ab}^2 - L_{Imab}^2 + 4L_{abc}L_{cab}) + 4q^2 \left\{ (K_{+ab} - L_{Reab} - 4K_c)^2 + 4(L_{Reac} - L_{Rebc})^2 \right\} \right] \\
f_3 &= 2 \left[8(K_{+ab} + L_{Reab}) \left\{ (K_{+ab} - L_{Reab} + 4K_c)^2 + 4(L_{Imac} - L_{Imbc})^2 \right\} \right. \\
&\quad - 4p^2(K_{+ab} - L_{Reab} + 4K_c)(K_{-ab}^2 - L_{Imab}^2 + 4L_{abc}L_{cab}) \\
&\quad - 16p^2(L_{Imac} - L_{Imbc}) \left\{ K_{-ab}(L_{Imac} + L_{Imbc}) + L_{Imab}(L_{Reac} + L_{Rebc}) \right\} \\
&\quad + 4p^2q \left[(K_{-ab}^2 - L_{Imab}^2 - 4L_{abc}L_{cab})(K_{+ab} - L_{Reab} - 4K_c) \right. \\
&\quad \left. + 4 \left\{ K_{-ab}(L_{Reac} + L_{Rebc}) + L_{Imab}(L_{Imac} + L_{Imbc}) \right\} (L_{Reac} - L_{Rebc}) \right] \\
&\quad \left. - 8q^2(K_{+ab} + L_{Reab}) \left\{ (K_{+ab} - L_{Reab} - 4K_c)^2 + 4(L_{Reac} - L_{Rebc})^2 \right\} \right]
\end{aligned} \tag{B.9}$$

where,

$$\begin{aligned}
K_{+ab} &= |a|^2 + 1, \\
K_{-ab} &= |a|^2 - 1, \\
K_c &= |c|^2, \\
L_{abc} &= (a+1)c^*, \\
L_{cab} &= c(a^*+1), \\
L_{Reab} &= a + a^*, \\
L_{Imab} &= a - a^*, \\
L_{Rebc} &= c^* + c, \\
L_{Imbc} &= -(c - c^*), \\
L_{Reac} &= ac^* + ca^*, \\
L_{Imac} &= ac^* - ca^*
\end{aligned} \tag{B.10}$$

This means that all three eigenvalues of the general covariance matrix are not a function of the rotation angle about the line of sight.

Appendix C

Direct Inversion of the General Covariance Matrix

In this section, the direct inversion technique is mathematically derived and applied.

We shall assume that the observed area is covered by only a single type of scatterers with a single scattering mechanism, so that the measured covariance matrix is expressed by a general covariance matrix in (3.71) as

$$C_m = C_{gen} \quad (C.1)$$

where C_{gen} is a general covariance matrix, and is calculated from the following scattering matrix.

$$S_{gen} = \begin{pmatrix} a_{gen} & c_{gen} \\ c_{gen} & b_{gen} \end{pmatrix} \rightarrow C_{gen} \quad (C.2)$$

As discussed in equation (B.6) in Appendix B, the scale factor is explicitly expressed as

$$C_m = |b_{gen}|^2 C \quad (C.3)$$

where

$$S = \begin{pmatrix} a & c \\ c & 1 \end{pmatrix} \rightarrow C$$

$$a = \frac{a_{gen}}{b_{gen}}, \quad c = \frac{c_{gen}}{b_{gen}}.$$
(C.4)

Then we can rewrite (C.1) as

$$C'_m = \frac{C_m}{|b_{gen}|^2} = C(\sigma, \phi, a, c).$$
(C.5)

Our tentative goal is to find a way to determine four unknown parameters: the randomness σ , mean orientation angle ϕ , and two elements of the simplified scattering matrix, a and c . After determining these parameters, the scaling factor $|b_{gen}|^2$ will be considered. Note that both a and c are complex numbers, so that there are 6 unknown real numbers:

$$S = \begin{bmatrix} a & c \\ c & 1 \end{bmatrix} = \begin{bmatrix} |a|(a_r + ja_i) & |c|(c_r + jc_i) \\ |c|(c_r + jc_i) & 1 \end{bmatrix}$$
(C.6)

where subscripts r and i are real and imaginary parts, respectively. If C'_m is expressed as

$$C'_m = \begin{bmatrix} \sigma'_{hhhh} & \sqrt{2}\sigma'_{hhv} & \sigma'_{hhvv} \\ \sqrt{2}\sigma'^*_{hhv} & 2\sigma'_{hvhv} & \sqrt{2}\sigma'_{hvvv} \\ \sigma'^*_{hhv} & \sqrt{2}\sigma'^*_{hvv} & \sigma'_{vvvv} \end{bmatrix}$$
(C.7)

the following known parameters are defined.

$$\begin{aligned}
\alpha &= \frac{C^2 + D^2}{A^2 + B^2} \\
\beta &= \frac{BD - AC}{AD + BC} \\
A &= (\sigma'_{hhhv} - \sigma'^*_{hhhv}) - (\sigma'_{hvvv} - \sigma'^*_{hvvv}) \\
B &= (\sigma'_{hhvv} - \sigma'^*_{hhvv}) \\
C &= (\sigma'_{hhhv} + \sigma'^*_{hhhv}) + (\sigma'_{hvvv} + \sigma'^*_{hvvv}) \\
D &= (\sigma'_{hhhh} - \sigma'_{vvvv}) \\
U &= (\sigma'_{hhhv} - \sigma'^*_{hhhv}) + (\sigma'_{hvvv} - \sigma'^*_{hvvv}) \\
V &= \sigma'_{hhhh} + 2\sigma'_{hvhv} + \sigma'_{vvvv} \\
W &= \sigma'_{hhvv} - 2\sigma'_{hvhv} + \sigma'^*_{hhvv}
\end{aligned} \tag{C.8}$$

To simplify the equations, the following unknown parameters are defined.

$$\begin{aligned}
K_{+ab} &= |a|^2 + 1 \\
K_{-ab} &= |a|^2 - 1 \\
K_c &= |c|^2 \\
Q &= (a - 1)(a^* - 1) \\
J &= \sqrt{4|c|^2 Q + U^2} \\
L_{abc} &= (a + 1)c^* \\
L_{cab} &= c(a^* + 1) \\
L_{Re ab} &= a + a^* = 2a_r \\
L_{Im ab} &= a - a^* = j2a_i \\
L_{Re bc} &= c^* + c = 2c_r \\
L_{Im bc} &= -(c - c^*) = -j2c_i \\
L_{Re ac} &= ac^* + ca^* \\
L_{Im ac} &= ac^* - ca^*
\end{aligned} \tag{C.9}$$

By substituting them into (3.71), we have

$$\begin{aligned}
C(\sigma) &= (\bar{\alpha} + p\bar{\beta} + q\bar{\gamma}) \cdot \bar{V} \\
\bar{\alpha} &= \frac{1}{8} \begin{bmatrix} 3K_{+ab} + L_{\text{Re } ab} + 4K_c & 2\sqrt{2}(L_{\text{Im } ac} - L_{\text{Im } bc}) & K_{+ab} + 3L_{\text{Re } ab} - 4K_c \\ -2\sqrt{2}(L_{\text{Im } ac} - L_{\text{Im } bc}) & 2(K_{+ab} - L_{\text{Re } ab} + 4K_c) & 2\sqrt{2}(L_{\text{Im } ac} - L_{\text{Im } bc}) \\ K_{+ab} + 3L_{\text{Re } ab} - 4K_c & -2\sqrt{2}(L_{\text{Im } ac} - L_{\text{Im } bc}) & 3K_{+ab} + L_{\text{Re } ab} + 4K_c \end{bmatrix} \\
\bar{\beta} &= \frac{2}{8} \begin{bmatrix} K_{-ab} & \sqrt{2}L_{abc} & L_{\text{Im } ab} \\ \sqrt{2}L_{cab} & 0 & \sqrt{2}L_{cab} \\ -L_{\text{Im } ab} & \sqrt{2}L_{abc} & -K_{-ab} \end{bmatrix} \cos 2\phi \\
&\quad + \frac{1}{8} \begin{bmatrix} 2(L_{abc} + L_{cab}) & -\sqrt{2}(K_{-ab} - L_{\text{Im } ab}) & -2(L_{abc} - L_{cab}) \\ -\sqrt{2}(K_{-ab} + L_{\text{Im } ab}) & 0 & -\sqrt{2}(K_{-ab} + L_{\text{Im } ab}) \\ 2(L_{abc} - L_{cab}) & -\sqrt{2}(K_{-ab} - L_{\text{Im } ab}) & -2(L_{abc} + L_{cab}) \end{bmatrix} \sin 2\phi \quad (\text{C.10}) \\
\bar{\gamma} &= \frac{1}{8} (K_{+ab} - L_{\text{Re } ab} - 4K_c) \begin{bmatrix} \cos 4\phi & -\sqrt{2} \sin 4\phi & -\cos 4\phi \\ -\sqrt{2} \sin 4\phi & -2 \cos 4\phi & \sqrt{2} \sin 4\phi \\ -\cos 4\phi & \sqrt{2} \sin 4\phi & \cos 4\phi \end{bmatrix} \\
&\quad + \frac{2}{8} (L_{\text{Re } ac} - L_{\text{Re } bc}) \begin{bmatrix} \sin 4\phi & \sqrt{2} \cos 4\phi & -\sin 4\phi \\ \sqrt{2} \cos 4\phi & -2 \sin 4\phi & -\sqrt{2} \cos 4\phi \\ -\sin 4\phi & -\sqrt{2} \cos 4\phi & \sin 4\phi \end{bmatrix}
\end{aligned}$$

Using equations (C.8) and (C10), U , V , and W are rewritten as

$$\begin{aligned}
U &= L_{\text{Im } ac} - L_{\text{Im } bc} \\
V &= K_{+ab} + 2K_c \\
W &= L_{\text{Re } ab} - 2K_c = 2a_r - 2|c|^2
\end{aligned} \quad (\text{C.11})$$

By defining X as

$$X = |a|^2 \quad (\text{C.12})$$

V in (C.11) becomes

$$V = (|a|^2 + 1) + 2|c|^2 = (X + 1) + 2|c|^2 . \quad (\text{C.13})$$

the following expressions are then obtained.

$$|c|^2 = -\frac{1}{2}(X - V + 1) \quad (\text{C.14})$$

$$a_r = -\frac{1}{2}(X - W - V + 1) \quad (\text{C.15})$$

$$a_i^2 = X - a_r^2$$

Since U can also be written as

$$U = (a - 1)c^* - (a^* - 1)c \quad (\text{C.16})$$

two polynomials involving the complex number c are derived.

$$\begin{aligned} c^2 + \frac{U}{a^* - 1}c - \frac{a - 1}{a^* - 1}|c|^2 &= 0 \\ c^{*2} - \frac{U}{a^* - 1}c^* - \frac{a^* - 1}{a - 1}|c|^2 &= 0 \end{aligned} \quad (\text{C.17})$$

($\because |c|^2 = cc^*$)

Hence,

$$\begin{aligned} c &= \frac{-1}{2(a^* - 1)}\{U + (\mp J)\} \\ c^* &= \frac{1}{2(a - 1)}\{U + (\pm J)\} . \end{aligned} \quad (\text{C.18})$$

From these expressions, we have

$$\begin{aligned}
L_{abc} + L_{cab} &= (a+1)c^* + c(a^* + 1) = -\frac{1}{Q} \{L_{\text{Im}ab}U + K_{-ab}(\mp J)\} \\
L_{abc} - L_{cab} &= (a+1)c^* - c(a^* + 1) = \frac{1}{Q} \{K_{-ab}U + L_{\text{Im}ab}(\mp J)\}
\end{aligned} \tag{C.19}$$

Equations (C.8) and (C.10) provide the following expressions regarding the phase 2ϕ .

$$\begin{aligned}
p(L_{abc} - L_{cab})\cos 2\phi + pL_{\text{Im}ab} \sin 2\phi &= A \\
pL_{\text{Im}ab} \cos 2\phi - p(L_{abc} - L_{cab})\sin 2\phi &= B
\end{aligned} \tag{C.20}$$

$$\begin{aligned}
p(L_{abc} + L_{cab})\cos 2\phi - pK_{-ab} \sin 2\phi &= C \\
pK_{-ab} \cos 2\phi + p(L_{abc} + L_{cab})\sin 2\phi &= D
\end{aligned} \tag{C.21}$$

Considering equation (C.19) and

$$\begin{aligned}
K_{-ab}^2 &= (X - 1)^2 \\
L_{\text{Im}ab}^2 &= -4a_i^2 = X^2 - 2(W + V + 1)X + (W + V - 1)^2 \quad (\because (C.15))
\end{aligned} \tag{C.22}$$

equation (C.20) provides two parameters.

$$\begin{aligned}
\tan 2\phi &= \frac{L_{\text{Im}ab}A - (L_{abc} - L_{cab})B}{(L_{abc} - L_{cab})A + L_{\text{Im}ab}B} \\
p &= \sqrt{\frac{A^2 + B^2}{L_{\text{Im}ab}^2 + (L_{abc} - L_{cab})^2}}
\end{aligned} \tag{C.23}$$

Equation (C.21) also provides the same parameters in different forms.

$$\begin{aligned}
\tan 2\phi &= \frac{-K_{-ab}C + (L_{abc} + L_{cab})D}{(L_{abc} + L_{cab})C + K_{-ab}D} \\
p &= \sqrt{\frac{C^2 + D^2}{(L_{abc} + L_{cab})^2 + K_{-ab}^2}}
\end{aligned} \tag{C.24}$$

Note that p is always real, as in Figure 3.20, and varies between 0 and 2. Since equations (C.23) and (C.24) have to be equal, the following two important expressions are obtained.

$$\tan 2\phi = \frac{L_{\text{Im}ab}A - (L_{abc} - L_{cab})B}{(L_{abc} - L_{cab})A + L_{\text{Im}ab}B} = \frac{-K_{-ab}C + (L_{abc} + L_{cab})D}{(L_{abc} + L_{cab})C + K_{-ab}D} \quad (\text{C.25})$$

$$p = \sqrt{\frac{A^2 + B^2}{L_{\text{Im}ab}^2 + (L_{abc} - L_{cab})^2}} = \sqrt{\frac{C^2 + D^2}{(L_{abc} + L_{cab})^2 + K_{-ab}^2}} \quad (\text{C.26})$$

$$\Rightarrow (L_{abc} + L_{cab})^2 + K_{-ab}^2 = \alpha \{L_{\text{Im}ab}^2 + (L_{abc} - L_{cab})^2\}$$

Equation (C.26) is an 8th-order polynomial in X , so there are 8 possible values of X . For each solution to equation (C.26), we can fix unknown parameters in (C.5) as follows. Using (C.25) with (C.19), the imaginary part of a is expressed as a function of $\pm J$.

$$a_i(\pm J) = \frac{L_{\text{Im}ab}}{2j} = \frac{\beta(K_{-ab}^2 - L_{\text{Im}ab}^2)QU - (K_{-ab}^2 + L_{\text{Im}ab}^2)U \cdot (\pm J)}{2jK_{-ab}(Q^2 + U^2 + J^2)} \quad (\text{C.27})$$

Given X and (C.15), the complex number a is

$$a = a_r + ja_i(\pm J). \quad (\text{C.28})$$

The sign of J can be determined by comparing each of $|a(+J)|^2$ and $|a(-J)|^2$ with (C.12).

Once the sign is determined, the complex number a is fixed. We then move on to find c .

From equation (C.9), we can obtain the following expressions.

$$\begin{aligned} L_{\text{Re}ac} &= ac^* + ca^* = (a + a^*)c_r - j(a - a^*)c_i = c_r L_{\text{Re}ab} - jc_i L_{\text{Im}ab} \\ &\Rightarrow L_{\text{Re}ac} - L_{\text{Re}bc} = c_r L_{\text{Re}ab} - jc_i L_{\text{Im}ab} - 2c_r = c_r (L_{\text{Re}ab} - 2) - jc_i L_{\text{Im}ab} \\ L_{\text{Im}ac} &= ac^* - ca^* = (a - a^*)c_r - j(a + a^*)c_i = c_r L_{\text{Im}ab} - jc_i L_{\text{Re}ab} \\ &\Rightarrow L_{\text{Im}ac} - L_{\text{Im}bc} = c_r L_{\text{Im}ab} - jc_i (L_{\text{Re}ab} - 2) = U \end{aligned} \quad (\text{C.29})$$

(C.18) allows us to calculate

$$L_{\text{Re}ac} - L_{\text{Re}bc} = (ac^* + ca^*) - (c + c^*) = (a^* - 1)c + (a - 1)c^* = \pm J. \quad (\text{C.30})$$

From (C.29) and (C.30), the following two equations involving c are obtained.

$$\begin{aligned}
c_r (L_{\text{Re}ab} - 2) - jc_i L_{\text{Im}ab} &= \pm J \\
c_r L_{\text{Im}ab} - jc_i (L_{\text{Re}ab} - 2) &= U
\end{aligned} \tag{C.31}$$

Now we can solve them for c as

$$\begin{aligned}
c &= c_r + jc_i \\
c_r &= \frac{UL_{\text{Im}ab} + (L_{\text{Re}ab} - 2)(\mp J)}{L_{\text{Im}ab}^2 - (L_{\text{Re}ab} - 2)^2} \\
c_i &= -j \frac{U(L_{\text{Re}ab} - 2) + L_{\text{Im}ab}(\mp J)}{L_{\text{Im}ab}^2 - (L_{\text{Re}ab} - 2)^2}
\end{aligned} \tag{C.32}$$

Note that we already determined the sign of J .

Using the obtained values of a and c , the mean orientation angle ϕ and the coefficient p can be calculated from (C.23) and are denoted $\tan 2\phi_1$ and p_1 . Equation (C.24) also provides a solution for ϕ and p denoted $\tan 2\phi_2$ and p_2 . Finally, we have to choose a best parameter set from the eight possible combinations.

$$S_i = \begin{pmatrix} a_i & c_i \\ c_i & 1 \end{pmatrix}, \phi_i, \sigma_i \quad i = 1 \dots 8 \tag{C.33}$$

There are several conditions to achieve this as follows. Several combinations of parameters can be eliminated because they violate some constraints on the parameters. For example, if the calculated orientation angle ϕ is a complex number, the candidate parameter set should be eliminated.

Ideally, the two methods of calculating $\tan 2\phi$ and p should be consistent for a candidate parameter set yielding

$$\begin{aligned}
\tan 2\phi_1 &= \tan 2\phi_2 \\
p_1 &= p_1
\end{aligned} \tag{C.34}$$

However, in practice this will not be the case. Thus we define two indices as follows.

$$\begin{aligned}\Delta \tan 2\phi &= \sqrt{(\tan 2\phi_1 - \tan 2\phi_2)^2} \\ \Delta p &= \sqrt{(p_1 - p_1)^2}\end{aligned}\tag{C.35}$$

The parameter set which minimizes these indices should be chosen as the optimal solution. In Appendix B, the characteristic equation of (C.5) is derived in (B.3). This provides another criterion for choosing the optimal parameter set. Specifically, the correct parameter set should make the characteristic equation zero. This implies the following evaluation function, which should be minimized to select the optimal parameter set.

$$\Delta\lambda = \sqrt{\sum_{i=1}^3 \left\{ -\lambda_i^3 + \frac{1}{8} \cdot f_1 \lambda_i^2 + \frac{1}{8^2} \cdot f_2 \lambda_i + \frac{1}{8^3} \cdot f_3 \right\}^2}\tag{C.36}$$

Unfortunately, these mathematical conditions may not be enough to uniquely determine the parameter set in practice. In this case, additional physical conditions should be used. For example, if it is already known that the observed area is covered by cylinder-like scatterers, the scattering matrix should have the form

$$S = \begin{pmatrix} a & 0 \\ 0 & 1 \end{pmatrix} \quad a < 1, c \approx 0\tag{C.37}$$

Or, as shown in (3.69),

$$S = \begin{pmatrix} 0 & 0 \\ 0 & 1 \end{pmatrix} \quad a \approx 0, c \approx 0.\tag{C.38}$$

As an application of this direct inversion theory, the following two-component decomposition technique is proposed. Suppose we add another scatterer to the observation described in (C.3), then we have

$$C_m = |b_{gen}|^2 C + C_{other}.\tag{C.39}$$

There are 5 unknown parameters to be fixed as

$$|b_{gen}|^2, S = \begin{pmatrix} a & c \\ c & 1 \end{pmatrix}, \sigma, \phi . \quad (\text{C.40})$$

By determining $|b_{gen}|^2$, the rest of the parameters are immediately found using the direct inversion technique. A similar approach to ANNEED can be used, as shown in Figure C.1.

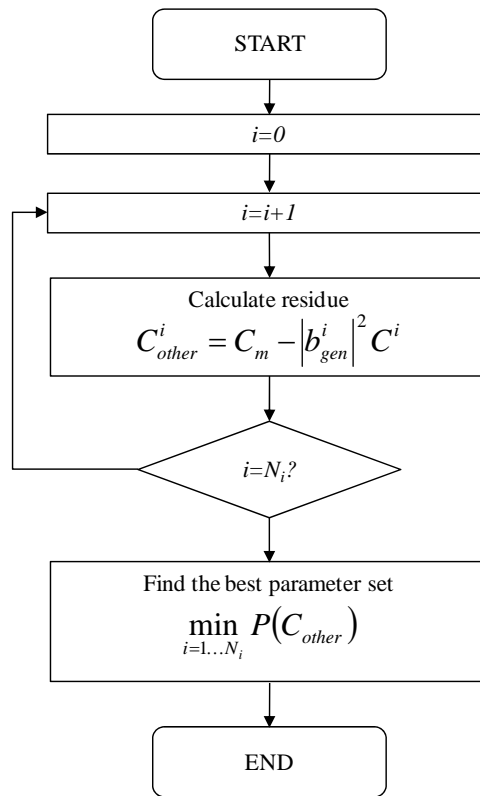


Figure C.1: Flowchart of the two-component decomposition using the direct inversion technique of the general covariance matrix

An algorithm is applied to the Black Forest image which was used in Chapter 3. Figure C.2 displays pixels at which the algorithm cannot find solution. Since the generalized volume scattering component is valid only for a cloud of symmetrical scatterers, the model has no solution when the area is dominated by other scatterers such as bare surface.

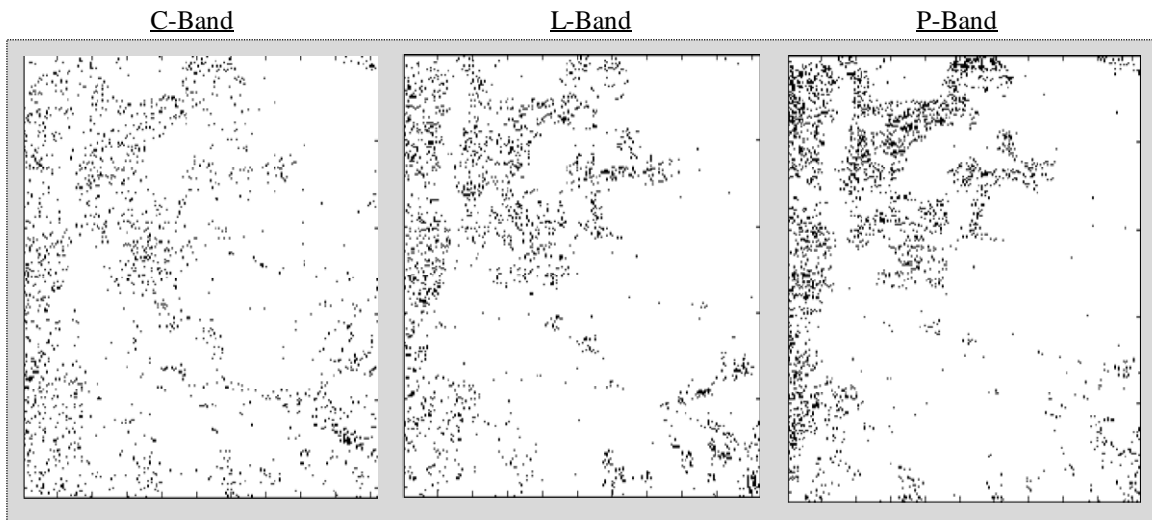


Figure C.2: Pixels with no solution are displayed at the three wavelengths: C-band (left), L-band (center), and P-band (right). Black: no solution, white: with solution. The results are obtained from the Black Forest image used in Chapter 3.

It is clear that the pixels without solution correspond to cropland, and the contrast of this area is increased as the wavelength increases. This tells us that the most of the pixels without solution are found at the places where the ground scattering is dominant.

Figures C.3, C.4, and C.5 show maps of the mean orientation angle and randomness at C-band, L-band, and P-band, respectively.

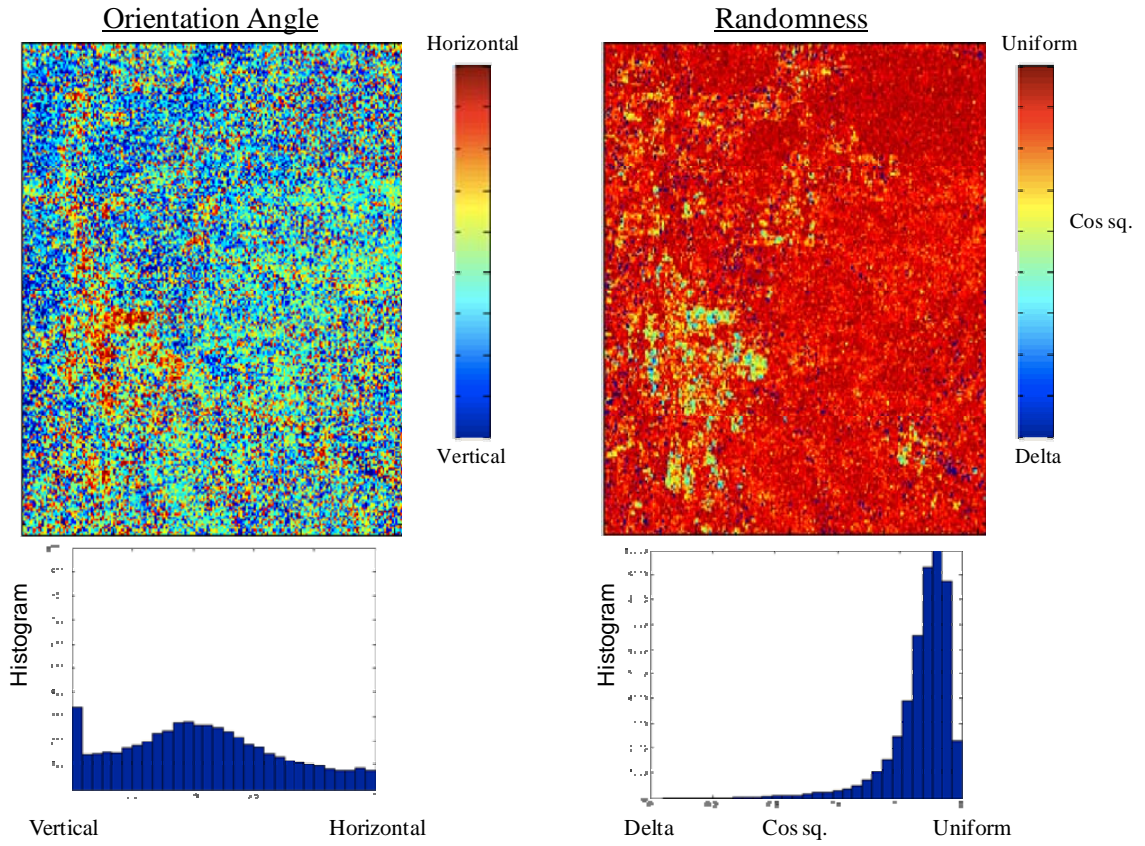


Figure C.3: Maps of the mean orientation angle (left) and randomness (right) using the two component decomposition model for the C-band Black Forest image

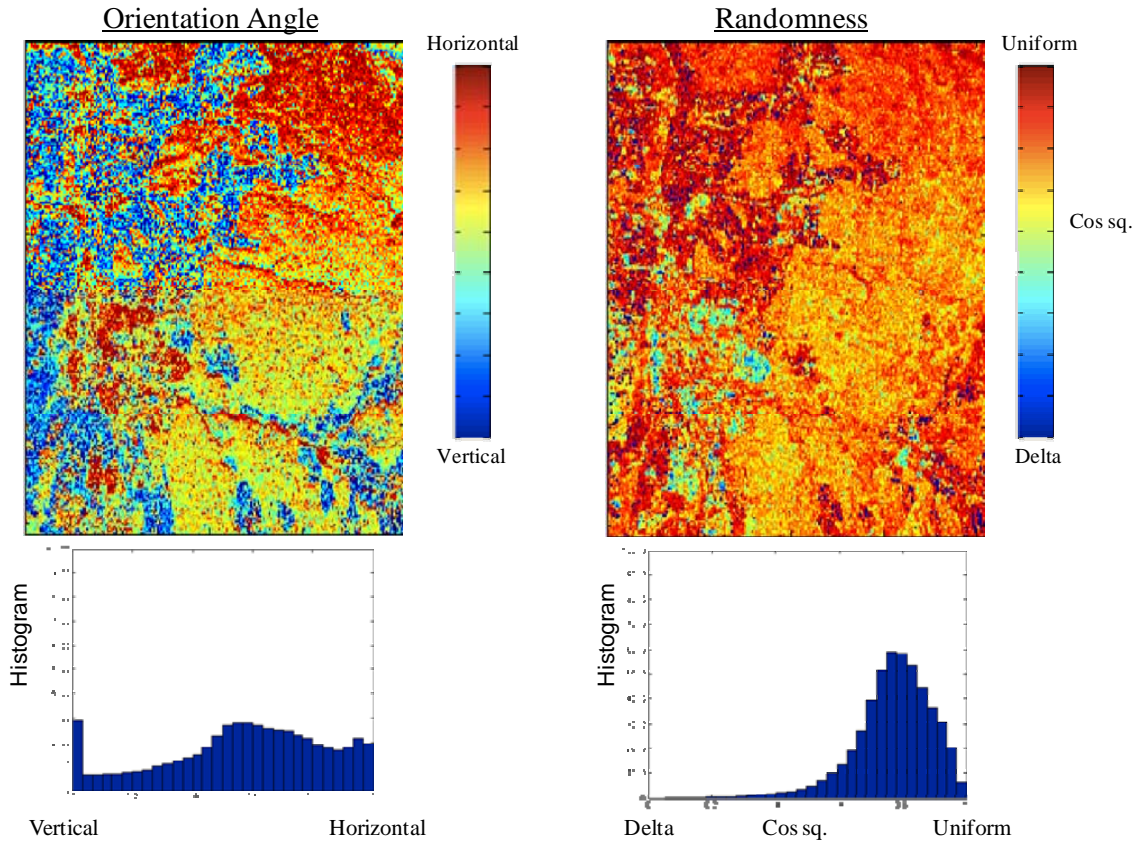


Figure C.4: Maps of mean orientation angle (left) and randomness (right) the two component decomposition model for the L-band Black Forest image

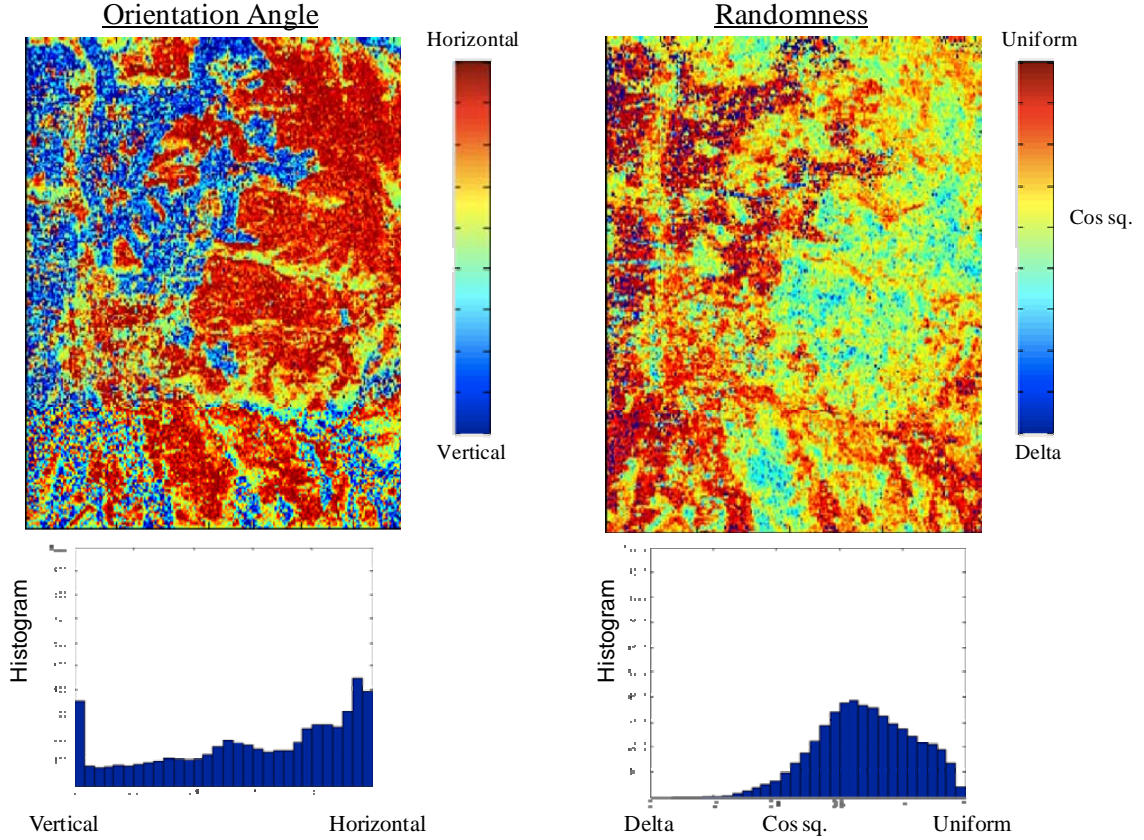


Figure C.5: Maps of mean orientation angle (left) and randomness (right) the two component decomposition model for the P-band Black Forest image

Comparing these images with the results in Chapter 3 using ANNED, the orientation angle map shows more variation, and the randomness map shows similar texture in the forested area. We do not discuss these results in this thesis, and further investigation is needed to physically interpret the results obtained from this purely mathematical algorithm.

To avoid pixels without solution, one may add another component to (C.39) as

$$C_m = |b_{gen}^1|^2 C_1 + |b_{gen}^2|^2 C_2 + \dots + |b_{gen}^n|^2 C_n + C_{other} . \quad (C.41)$$

As you see, the ANNED model in (3.74) is just one specific form of (C.41).

Appendix D

The Appearance of a Cloud of Randomly Oriented Dipoles

In this section, we will discuss how randomly oriented thin cylinders on the ground appear at the receiver.

The geometry of a single oriented dipole on the ground and a definition of this orientation angle at the receiver are shown in Figure D.1.

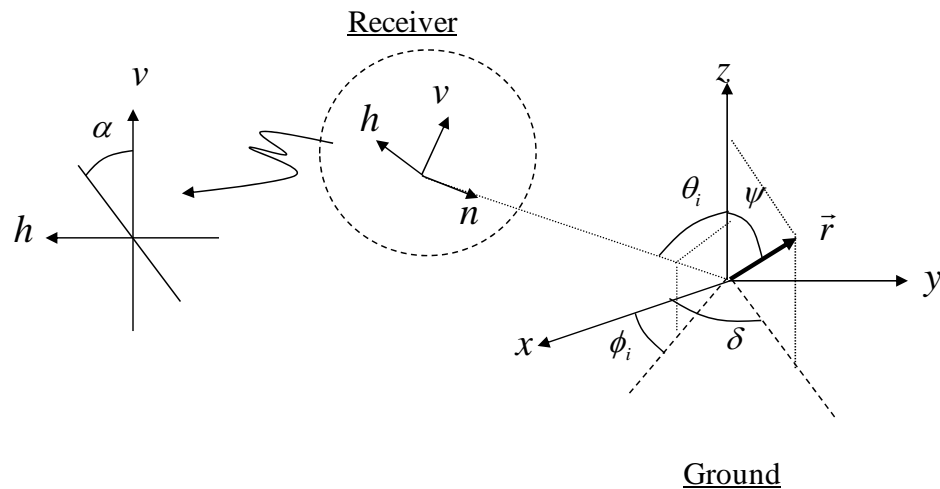


Figure D.1: Geometry of an oriented dipole on the ground and a definition of the mean orientation angle at the receiver

The α can be interpreted as the rotation angle of the target about the line of sight. From the geometry, the orientation angle at the receiver is mathematically expressed as

$$\alpha = \tan^{-1} \frac{h}{v} \quad (\text{D.1})$$

where h and v are given by

$$\begin{pmatrix} n \\ h \\ v \end{pmatrix} = \begin{pmatrix} \sin \theta_i & 0 & -\cos \theta_i \\ 0 & 1 & 0 \\ \cos \theta_i & 0 & \sin \theta_i \end{pmatrix} \begin{pmatrix} -\cos \phi_i & -\sin \phi_i & 0 \\ \sin \phi_i & -\cos \phi_i & 0 \\ 0 & 0 & 1 \end{pmatrix} \vec{r} \quad (\text{D.2})$$

$$\vec{r} = \begin{pmatrix} \sin \psi \cos \delta \\ \sin \psi \sin \delta \\ \cos \psi \end{pmatrix}$$

The orientation angle at the receiver depends on the incidence angle. From these expressions, we can numerically generate a cloud of dipoles with a specific distribution on the ground σ_{ground} , and then project them to the polarimetric plane at the receiver. The randomness at the receiver σ_{rec} can be obtained by examining the standard deviation of the projected cylinders in terms of orientation angle α . The results, with various incidence angles, are shown in Figure D.2, with the mean orientation angle fixed at zero ($\psi_0=0$).

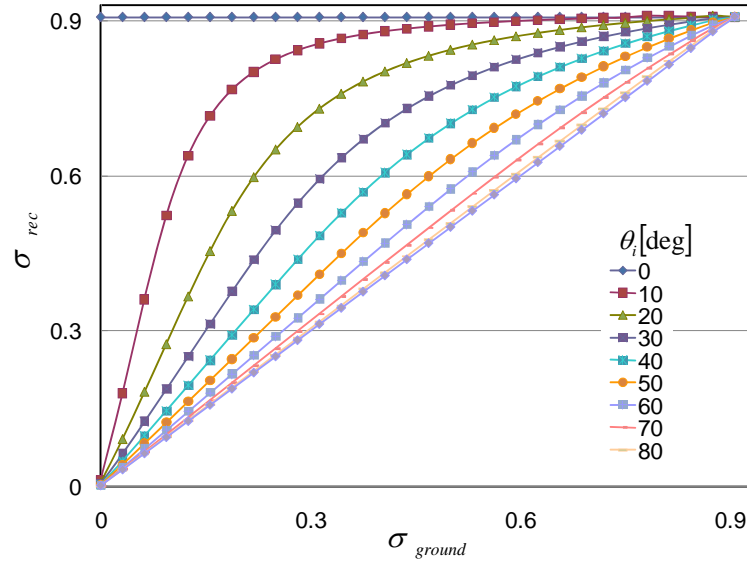


Figure D.2: Randomness at the receiver corresponding to that on the ground with various incidence angles

BIBLIOGRAPHY

- [1] G. M. Hornberger, J. P. Raffensperger, P. L. Wiberg, and K. N. Eshleman, *Elements of Physical Hydrology*, Baltimore, MD: The Johns Hopkins University Press, 1998.
- [2] S. O. Rice, "Reflection of electromagnetic waves from slightly rough surfaces," *Commun. Pure Appl. Math.*, vol. 4, pp. 351–378, 1951.
- [3] A. K. Fung, Z. Li, and K. S. Chen, "Backscattering from a randomly rough surface," *IEEE Trans. Geosci. Remote Sensing*, vol. 30, pp. 356–369, Mar. 1992.
- [4] J. Shi, J. Wang, A. Y. Hsu, P. E. O'Neil, and E. T. Engman, "Estimation of bare surface soil moisture and surface roughness parameter using L-band SAR image data," *IEEE Trans. Geosci. Remote Sensing*, vol. 35, no. 5, Sep. 1997.
- [5] I. Hajnsek, E. Pottier, and S. R. Cloude, "Inversion of surface parameters from Polarimetric SAR," *IEEE Trans. Geosci. Remote Sensing*, vol 41, no 4, Apr. 2003.
- [6] Y. Kim and J. van Zyl, "A time series approach for soil moisture estimation," *Proc. of IGARSS06*, Denver, CO, Jul. 2006.
- [7] M. C. Dobson and F. T. Ulaby, "Active microwave soil moisture research," *IEEE Trans. Geosci. Remote Sensing*, vol. GE-24, no. 1, Jan. 1986.
- [8] P. C. Dubois, J. van Zyl, and T. Engman, "Measuring Soil Moisture with Imagin Radars," *IEEE Trans. Geosci. Remote Sensing*, vol 33, no. 4, Jul. 1995.
- [9] Y. Oh, K. Sarabandi, and F. T. Ulaby, "An empirical model and an inversion technique for radar scattering from bare surfaces," *IEEE Trans. Geosci. Remote Sensing*, vol. 30, no. 2, Mar. 1992

- [10] R. T. Watson, I. R. Noble, B. Bolin, N. H. Ravindranath, D. J. Verado, and D. J. Dokken, *Land use, land-use change and forestry*, Cambridge, UK: Cambridge University Press, 2000.
- [11] E. Ezcurra, *Global Desserts Outlook*, Nairobi, Kenya: DEWA, UNEP, 2006
- [12] A. Freeman and S. L. Durden, "A three-component scattering model for Polarimetric SAR data," *IEEE Trans. Geosci. Remote Sensing*, vol. 36, no. 3, pp. 963–973, May 1998.
- [13] Y. Yamaguchi, T. Moriyama, M. Ishido, and H. Yamada, "Four-component scattering model for polarimetric SAR image decomposition," *IEEE Trans. Geosci. Remote Sensing*, vol. 43, no. 8, Aug. 2005.
- [14] W. Wagner, G. Lemoine, and H. Rott, "A method for estimating soil moisture from ERS scatterometer and soil data," *Remote Sensing of Environment*, vol. 70, pp. 191–207, 1999.
- [15] J. J. van Zyl, "On the importance of polarization in radar scattering problems," *Ph.D. dissertation* California Institute of Technology, Pasadena, CA, (*Caltech Antenna Lab. Rep. 120*), 1985.
- [16] S. L. Durden, J. J. van Zyl, and H. A. Zebker, "Modeling and Observation of the radar polarization signature of forested areas," *IEEE Trans. Geosci. Remote Sensing*, vol. 27, no. 3, May 1989.
- [17] F. T. Ulaby and C. Elachi, *Radar polarimetry for geosciences applications*, Norwood, MA: Artech House, 1990.
- [18] E. Krogager, "A new decomposition of the radar target scattering matrix," *Electron. Lett.*, vol. 26, no. 18, pp. 1525–1526, 1990.

- [19] J. S. Lee, E. Krogager, T. L. Ainsworth, and W. M. Boerner, "Polarimetric analysis of radar signature of a manmade structure," *IEEE Trans. Geosci. Remote Sensing*, vol. 3, no. 4, Oct. 2006.
- [20] S. R. Cloude, "Uniqueness of target decomposition theorems in radar polarimetry," in *Direct and Inverse Methods in Radar Polarimetry, Part 1, NATO-ARW*, W. M. Boerner et al., Eds., Norwell, MA: Kluwer, pp. 267–296, 1992.
- [21] S. R. Cloude and E. Pottier, "A review of target decomposition theorems in radar polarimetry," *IEEE Trans. Geosci. Remote Sensing*, vol. 34, no. 2, Mar. 1996.
- [22] J. J. van Zyl and Y. Kim, *Synthetic aperture radar polarimetry*, Hoboken, NJ: John Wiley & Sons, in preparation.
- [23] R. Touzi, "Target scattering decomposition in terms of roll-invariant target parameters," *IEEE Trans. Geosci. Remote Sensing*, vol. 45, no. 1, Jan. 2007.
- [24] J. S. Lee, M. R. Grunes, T. L. Ainsworth, L. J. Du, D. L. Schuler, and S. R. Cloude, "Unsupervised classification using polarimetric decomposition and the complex Wishart classifier," *IEEE Trans. Geosci. Remote Sensing*, vol. 37, no. 5, Sep. 1999.
- [25] J. J. van Zyl, "Unsupervised classification of scattering behavior using radar polarimetry data," *IEEE Trans. Geosci. Remote Sensing*, vol. 27, no. 1, Jan. 1989.
- [26] J. J. van Zyl, "The effect of topography on radar scattering from vegetated areas," *IEEE Trans. Geosci. Remote Sensing*, vol. 31, no. 1, Jan. 1993.
- [27] M. Borgeaud, R. T. Shin, and J. A. Kong, "Theoretical models for polarimetric radar clutter," *Journal of EM Waves and Applications*, vol. 1, pp. 73–91, 1987.
- [28] J. J. van Zyl, "Application of Cloude's target decomposition theorem to Polarimetric imaging radar data," *Radar Polarimetry*, vol. SPIE-I748, pp. 184–212, 1992.

- [29] S. Chandrasekhar, *Radiative Transfer*, Mineora, NY: Dover, 1960.
- [30] F. T. Ulaby, K. Sarabandi, K. C. McDonald, N. W. Whitt, and M. C. Dobson, *Michigan microwave canopy scattering model (MIMICS)*, Rep. 022486-T-1, Radiation Laboratory, University of Michigan, Jul. 1988.
- [31] C. Elachi and J. van Zyl, *Introduction to the physics and techniques of remote sensing*, Hoboken, NJ: John Wiley & Sons, 2006.
- [32] S. Saatchi and J. van Zyl, "Estimation of canopy water content in Konza Prairie grassland using synthetic aperture radar measurements during FIFE," *Journal of Geophysical Research*, vol. 100., no. D12, pp. 25,481–25,496, Dec. 1995.
- [33] H. C. van de Hulst, *Light scattering by small particles*, Mineola, NY: Dover, 1957.
- [34] G. T. Ruck, D. E. Barrick, W. D. Stuart, and C. K. Krichbaum, *Radar Cross Section Handbook*, NY: Plenum Press, 1970.
- [35] C. F. Bohren and D. R. Huffman, *Absorption and scattering of light by small particles*, NY: John Wiley & Sons, 1983.
- [36] A. Ishimaru, *Wave propagation and scattering in random media*, NY: IEEE Press, 1978.
- [37] F. T. Ulaby, K. R. Moore, and A. K. Fung, *Microwave remote sensing: Active and passive, Volume II: Radar remote sensing and surface scattering and emission theory*, Dedham, MA: Artech House, 1982.
- [38] J. D. Silverstein and R. Bender, "Measurements and predictions of the RCS of Bruderhedrals at millimeter wavelengths," *IEEE Trans. Antennas and Propagation*, vol. 45, no. 7, Jul. 1997.

- [39] J. R. Wang and T. J. Schmugge, "An empirical model for the complex dielectric permittivity of soils as a function of water content," *IEEE Trans. Geosci. Remote Sensing*, vol. GE-18, no. 4, Oct. 1980.
- [40] M. T. Hallikainen, F. T. Ulaby, M. C. Dobson, H. A. El-Rayes, and L. K. Wu, "Microwave dielectric behavior of wet soil – Part I: Empirical models and experimental observation," *IEEE Trans. Geosci. Remote Sensing*, vol. GE-23, no. 1, Jan. 1985.
- [41] M. C. Dobson, F. T. Ulaby, M. T. Hallikainen, and H. A. El-Rayes, "Microwave dielectric behavior of wet soil – Part II: Dielectric mixing models," *IEEE Trans. Geosci. Remote Sensing*, vol. GE-23, no. 1, Jan. 1985.
- [42] N. R. Peplinski, F. T. Ulaby, and M. C. Dobson, "Dielectric properties of soils in the 0.3 – 1.3-GHz Range," *IEEE Trans. Geosci. Remote Sensing*, vol. 33, no. 3, May 1995.
- [43] B. Brisco, T. J. Pultz, R. J. Brown, G. C. Topp, M. A. Hares, and W. D. Zebchuk, "Soil moisture measurement using portable dielectric probes and time domain reflectometry," *Water Resources Research*, vol. 28, no. 5, pp. 1339–1346, May 1992.
- [44] F. T. Ulaby and M. A. El-Rayes, "Microwave dielectric spectrum of vegetation – Part II: Dual-dispersion model," *IEEE Trans. Geosci. Remote Sensing*, vol. GE-25, no. 5, Sep. 1987.
- [45] A. Freeman, "Fitting a two-component scattering model to polarimetric SAR data from forests," *IEEE Trans. Geosci. Remote Sensing*, vol. 45, no. 8, Aug. 2007.
- [46] J. J. van Zyl and Y. Kim, "Estimation soil moisture for vegetated terrain," *Proc. of IGARSS04*, Anchorage, AK, Sep. 2004.

- [47] M. A. Tassoudji, K. Sarabandi, and F. T. Ulaby, "Design consideration and implementation of the LCX polarimetric scatterometer (POLARSCAT)," *Rep. 022486-T-2*, University of Michigan, Radiation Laboratory, Jun. 1989.

- [48] J. J. van Zyl and Y. Kim, "A quantitative comparison of soil moisture inversion algorithms," *Proc. of IGARSS01*, Sydney, Australia, Jul. 2001.

- [49] J. J. van Zyl, M. Arii, and Y. Kim, "Requirements for Model-Based Polarimetric Decompositions," *Proc. of IGARSS08*, Boston, MA, Jul. 2008.